1-1-2016

Design, Analysis, Optimization and Control of Rotor Tip Flows

Cis Guy M De Maesschalck
Purdue University

Graduate School Form
30 Updated 12/26/2015

PURDUE UNIVERSITY
GRADUATE SCHOOL
Thesis/Dissertation Acceptance

This is to certify that the thesis/dissertation prepared

By Cis Guy M De Maesschalck

Entitled

Design, Analysis, Optimization and Control of Rotor Tip Flows

For the degree of Doctor of Philosophy

Is approved by the final examining committee:

Guillermo Paniagua
Chair

Tom I. Shih

Ilias Bilionis

Ali A. Ameri

Jay P. Gore

Francesco Contino

Nicole L. Key

Laurent Bricteux

Wolfgang Schroder

To the best of my knowledge and as understood by the student in the Thesis/Dissertation Agreement, Publication Delay, and Certification Disclaimer (Graduate School Form 32), this thesis/dissertation adheres to the provisions of Purdue University's "Policy of Integrity in Research" and the use of copyright material.

Approved by Major Professor(s): Guillermo Paniagua

Approved by: Jay P. Gore 11/28/2016

Head of the Departmental Graduate Program Date

DESIGN, ANALYSIS, OPTIMIZATION AND CONTROL OF ROTOR TIP FLOWS

A Dissertation

Submitted to the Faculty

of

Purdue University

by

Cis Guy M. De Maesschalck

In Partial Fulfillment of the

Requirements for the Degree

of

Doctor of Philosophy

December 2016

Purdue University

West Lafayette, Indiana

To those who found their way to this book...

ACKNOWLEDGMENTS

This PhD project was a Joint research effort to obtain the Doctoral Degree at the Vrije Universiteit Brussel (Belgium, 2012-2016) and Purdue University (United States, 2015-2016) under the supervision of Prof. Guillermo Paniagua and Prof. Chris Lacor. This work was made possible in cooperation with the von Karman Institute for Fluid Dynamics (Belgium) and thanks to the financial support of the Agency for Innovation by Science and Technology (IWT) in Belgium, Fulbright in the United States and the Belgian American Educational Foundation.

Firstly, I would like to thank my supervisor Guillermo Paniagua and Chris Lacor for their continuous technical, administrative but also personal support and advice throughout the entire course of the PhD.

I'd also want to express my gratitude to all the jury members for going through my thesis dissertation and their useful suggestions for improvement: Dr. Ali Ameri, Prof. Ilias Bilionis, Prof. Laurent Bricteux, Prof. Francesco Contino, Prof. Jay Gore, Prof. Nicole Key, Prof. Rik Pintelon, Prof. Lincy Pyl, Prof. Wolfgang Schroeder and Prof. Tom Shih.

A special thanks goes to Sergio with who I spent countless hours (re)building the CT3 or discussing CFD results to make DAOCROTIF a success. I'm also particularly grateful for all the help of Pierre Londers in the lab and the support of Prof. Tom Verstraete on the numerical side.

Those four years wouldn't have been the same without the encouragements of all the friends back in Belgium in Kortrijk, in Brussels at the VKI, in the US at Purdue (with a special mention of the 'European crew' in Zucrow) and all the fellow 'Fulbrighters' I had the honor to meet throughout the United States, providing

an ever welcome escape from the engineering world, immersing in a multicultural environment.

I'll have certainly forgotten people, but those who are not mentioned but came this far to read this, certainly deserve a good Belgian beer!

Last but not least, I'd like to thank my parents, sisters and family for always being there for me and their endless support throughout all my 'endeavors'.

TABLE OF CONTENTS

LIST OF TABLES

LIST OF FIGURES

Figure Page

NOMENCLATURE

Roman symbols

a	Speed of sound
ap	Axial position of purge slot
B	Body force
C	Chord
C_p	Heat capacity
D	Substantial derivative
F	Force
gf	Gap fraction of purge slot
h	Rotor tip clearance height
Δh	Enthalpy difference
H	Channel height, Blade span
H	Total enthalpy
L	Length
M	Momentum
m	Massflow
n	Intensive property
Nu	Nusselt number
p	Apparent order
P	Pressure, Power
$pchip$	Piecewise Cubic Hermite Interpolating Polynomial
Pr	Prandtl number
Q	Heat transfer

Re	Reyolds number
r_p	Degree of reaction $(P_2 - P_3)/(P_1 - P_3)$
s	Specific entropy
S	Source of error, Total entropy
T	Temperature, Torque
tc	Tip clearance
u	Peripheral velocity
U	Peripheral velocity, Unbalance
V	Absolute velocity, Volume
y^+	Dimensionless first cell size
W	Relative velocity
w	Overtip gap channel width
z	Axial coordinate

Greek symbols

α	Absolute flow angle
α	Relaxation factor
β	Relative flow angle
γ	Heat capacity ratio
γ	Radial purge injection angle
η	Efficiency
θ	Boundary layer momentum thickness
θ	Tangential coordinate
κ	Thermal conductivity
μ	Dynamic viscosity, mean level
μ_t/μ_l	Turbulent to laminar viscosity ratio
ρ	Density
τ	Shear stress

ϕ	Flow Coefficient $(V_{2ax} + V_{3ax})/2U$
ϕ	Swirl angle
φ	Injection angle
ψ	Stage loading $(\Delta H/U^2)$
ω	Aerodynamic losses
ω	Rotational speed [rad/s]

Sub- and Superscripts

0	Total quantity, absolute condition
$0r$	Total quantity, relative condition
1	Plane 1: Stator inlet
2	Plane 2: Stator-rotor interface
3	Plane 3: Turbine stage outlet
abs	Absolute
AD	Adiabatic
AVE	Average
ax	Axial
$corr$	Corrected
def	Deformed part
is	Isentropic
ISO	Isothermal
op	Operational
m	Mainstream
man	Manufacturing
r	Radial component
rel	Relative quantity
RMS	Root mean square
rot	Rotor

s	Static quantity
sh	Shroud
st	Stator
t	Tangential component
t	Turbulent property
w	Wall

Acronyms

ANN	Artificial Neuron Network
BL	Boundary Layer, Baseline
BPF	Blade Passing Frequency
CAD	Computer Aided Design
CADO	Computer Aided Design and Optimization tool
CV	Control Volume
DE	Differential Evolution
DoE	Design of Experiments
DNS	Direct Numerical Simulation
EA	Evolutionary Algorithms
FE	Finite Element
FFT	Fast Fourier Transform
GA	Genetic Algorithms
GCI	Grid Convergence Index
HP	High Pressure
HPT	High Pressure Turbine
HT	Heat Transfer
LE	Leading Edge
LES	Large Eddy Simulation
NGV	Nozzle Guide Vane
NSGA	Nondominated Sorting Genetic Algorithm

OTL	Overtip Leakage
PS	Pressure Side
RANS	Reynolds-averaged Navier-Stokes
RPM	Rounds Per Minute
SCM	Stochastic Collocation Method
SS	Suction Side
SST	Shear Stress Transport
TE	Trailing Edge
TLV	Tip Leakage Vortex
UPV	Upper Passage Vortex
VKI	Von Karman Institute

ABSTRACT

De Maesschalck, Cis Guy M. PhD, Purdue University, December 2016. Design, Analysis, Optimization and Control of Rotor Tip Flows. Major Professor: Guillermo Paniagua, School of Mechanical Engineering.

Developments in turbomachinery focus on efficiency and reliability enhancements, while reducing the production costs. In spite of the many noteworthy experimental and numerical investigations over the past decades, the turbine tip design presents numerous challenges to the engine manufacturers, and remains the primary factor defining the machine durability for the periodic removal of the turbine components during overhaul. Due to the hot gases coming from the upstream combustion chamber, the turbine blades are subjected to temperatures far above the metal creep temperature, combined with severe thermal stresses induced within the blade material. Inadequate designs cause early tip burnouts leading to considerable performance degradations, or even a catastrophic turbine failure. Moreover, the leakage spillage, nowadays often exceeding the transonic regime, generates large aerodynamic penalties which are responsible for about one third of the turbine losses. In this view, the current doctoral research exploits the potential through the modification and optimization of the blade tip shape as a means to control the tip leakage flow aerodynamics and manage the heat load distribution over the blade profile to improve the turbine efficiency and durability.

Three main design strategies for unshrouded turbine blade tips were analyzed and optimized: tight running clearances, blade tip contouring and the use of complex squealer-like geometries. The altered overtip flow physics and heat transfer characteristics were simulated for tight gap sizes as low as 0.5% down to 0.1% of the blade height, occurring during engine transients and soon to be expected due to recent de-

velopments in active clearance control strategies. The potential of fully 3D contoured blade top surfaces, allowing to adapt the profile locally to the changing flow conditions throughout the camberline, is quantified. First adopting a quasi-3D approach and subsequently using a full 3D optimization. For the industrial rub-safe squealer profiles featuring cavities separated by upstanding rims, a topology-like multi-objective 3D optimization strategy is used to identify so far undiscovered, optimal blade tip profiles. Furthermore, the additional potential of the widely adopted shroud coolant injection just upstream of the rotor blade is examined. Specifically, the possibility of combining the beneficial effect of the purge flow in the overtip region while minimizing the detrimental influence on the upper passage vortex is explored. Eventually, a high-speed rotating turbine facility at the von Karman Institute was redesigned, allowing simultaneous testing of multiple distinct blade (tip) profiles mounted in separate sectors around the rotor annulus. Important considerations related with the balancing and precise clearance design are highlighted, arising from the complexity of such rainbow-rotor configuration. Moreover, approaches are described to integrate Reynolds-Averaged Navier-Stokes simulations to a priori estimate the errors induced by the finite spatial sampling and inherent limited sensor bandwidth.

This research effort provided new insights into the overtip flow topology and aerothermal characteristics, identified new design strategies to create future turbines with enhanced aerodynamic efficiencies and reduced thermal loads, and paved the way for an elaborate experimental validation in a rotating turbine facility, at engine-matched conditions.

CHAPTER 1. INTRODUCTION

1.1 Turbine Tip Leakage Flows and Design strategies

Developments in turbomachinery focus on efficiency and reliability enhancements, while reducing the production costs (through weight reduction and the use of standard materials), Fig. 1.1. In spite of the many noteworthy experimental and numerical investigations over the past decades [6–8], the turbine tip design continues to present numerous challenges to the engine manufacturers, and remains the primary factor defining the machine durability for the periodic removal of the turbine components during overhaul [9]. Due to the hot gases coming from the upstream combustion chamber, the turbine blades are subjected to temperatures far above the metal creep temperature. The induced tip leakage flows in shroudless turbine configurations are the source of significant heat loads onto the rotor components and give rise to severe thermal stresses inside the blade material [10]. Inadequate designs cause early tip burnouts leading to a considerable performance degradation, or even to a catastrophic turbine failure. Moreover, the leakage spillage generates large aerodynamic penalties which are responsible for about one third of the turbine losses [11] and enhances significantly the non-uniformities in the rotor exit flow field ingested by the following stage.

Over the years, several distinct tip design strategies have been proposed to mitigate the detrimental effects of the tip flow on the overall turbine performance and durability [12, 13]. While shrouded configurations (Fig. 1.2) generally achieve higher efficiencies, most engine manufacturers adopt shroudless designs for their high-pressure turbine stages due to the reduced mechanical loads and complexity to cool down the casing [14]. Typical industrial unshrouded solutions comprise the use of tight run-

This Chapter contains small parts adopted from De Maesschalck et al. [1–5]

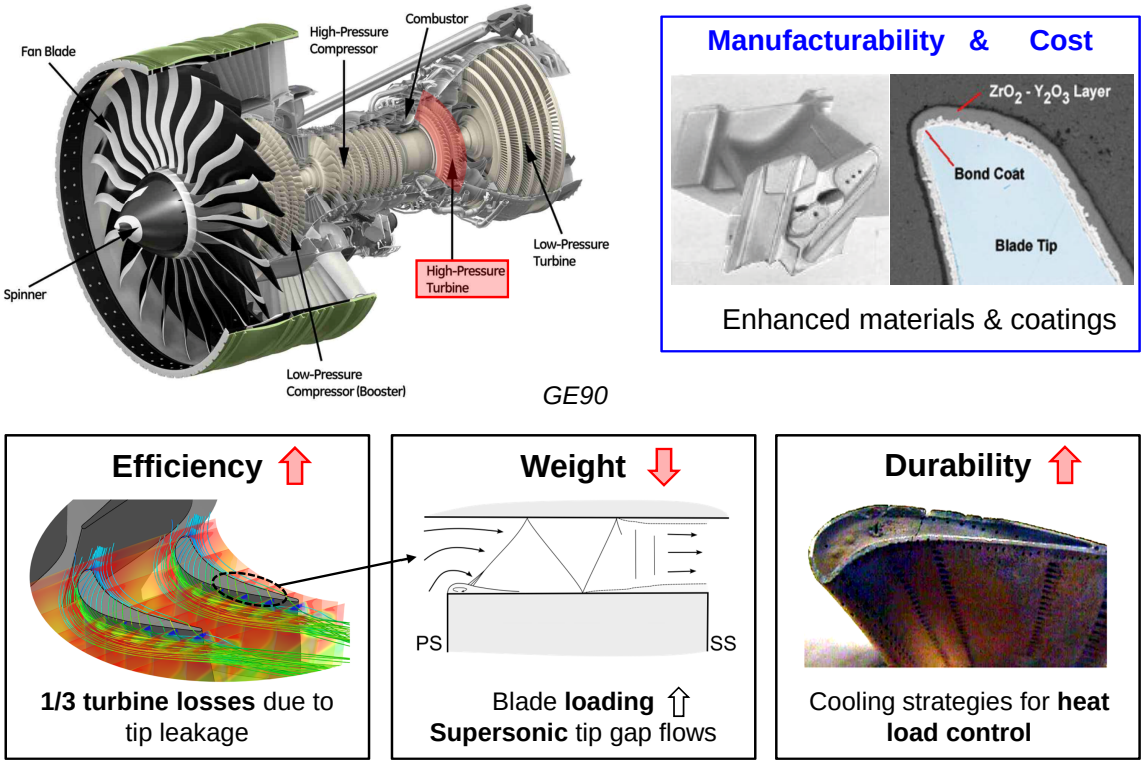

Figure 1.1: The high pressure turbine design challenges.

ning plain tips, squealer type designs or more sophisticated partial shroud (winglet) configurations (Fig. 1.2).

Early studies on flat tip designs in a low speed environment [15, 16] have revealed the conventional subsonic overtip flow topology. When the fluid enters the gap region near the pressure side, a separation bubble and vena contracta are created. After reattaching onto the blade tip and enhancing locally the heat transfer [17], the flow mixes and eventually leaves the tip gap at the suction side to form the leakage vortex further downstream. An elaborate review of the aerodynamics and heat transfer aspects in such conditions is presented by Bunker [18]. Due to its subsonic nature, the losses are mainly massflow driven. Hence, smaller running clearances, a reduction in the discharge coefficient or a lowered driving pressure beneficially affects the overall efficiency. While one tries to maximize the blade loading and the discharge coefficient

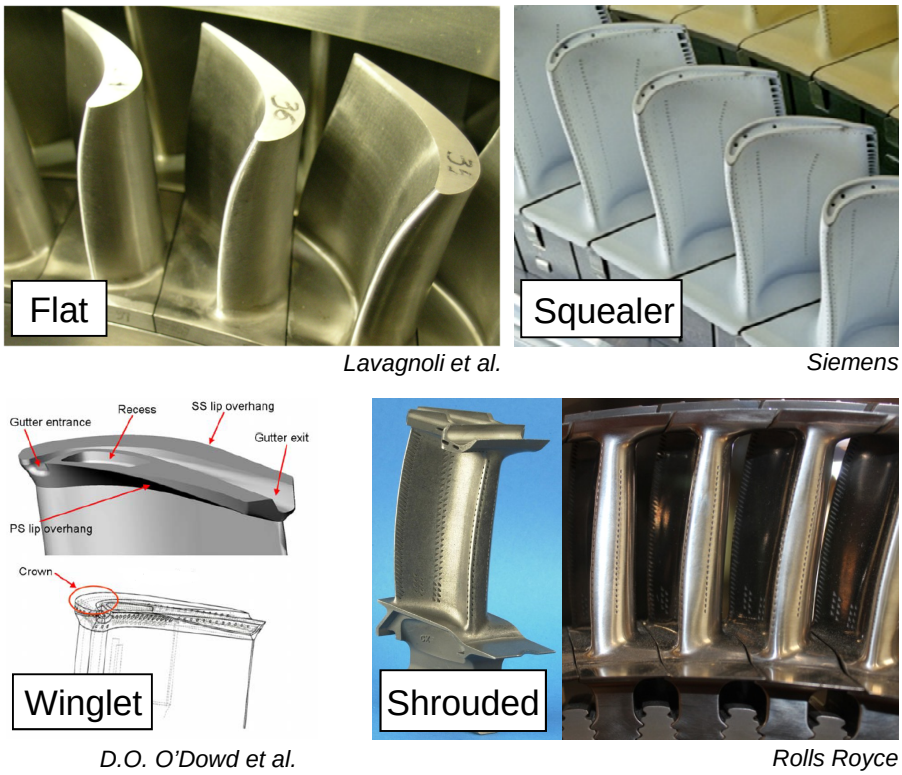

Figure 1.2: Examples of the commonly adopted turbine tip design strategies.

is mainly determined by the entrance geometry, it is especially the rotor gap size which plays a major role and continues to decrease due to the recent developments towards an accurate control of the clearance levels and effective strategies during engine transients (e.g. active clearance control, rub-in techniques [19], etc) [20, 21].

In this view, (partial) squealer configurations have been proposed which adopt upstanding rims to squeeze and guide the leakage flow [22]. One of the first numerical studies comparing flat tip designs and a squealer configuration was carried out by Ameri et al. [23]. Squealer geometries are nowadays the most prevalent design, additionally allowing to rub the casing in transient conditions [9]. Several experimental investigations both in low speed [24–26] as well as in a high-speed environment (Key and Arts [27]) demonstrated the benefits of such rim-type geometries on the aerodynamic efficiency. Additionally, experimental studies by Nasir et al. [25] and

Kwak et al. [28] and the elaborate numerical investigation by Krishnababu et al. [29] state reduced heat transfer levels compared to a flat tip.

In order to diminish the leakage massflow even further, a winglet type shape could be used to reduce the pressure difference across the tip gap [30–34]. The aerothermal performance of a more complex winglet shape, originally proposed by Harvey and Ramsden [35], was studied by Harvey et al. [36] and O'Dowd et al. [37]. Their investigations pointed out that such design allows to achieve an aerodynamic efficiency similar to a shrouded configuration with two fins. However, the approach results in an average heat load about three times higher compared to a flat tip geometry.

In the quest for higher power densities and weight reductions, engine manufacturers tend to continuously increase the turbine blade loadings and rotational speeds. Hence, in high-speed turbines, flow velocities exceeding the transonic regime characterize the rotor tip leakage flow, which drastically modifies the aerothermal structures within the overtip region. Although the existence of supersonic flows was already suggested in 1988 by Moore and Tilton [15] and afterwards experimentally identified through water table experiments [38, 39], only recent investigations were capable of revealing in detail the complex supersonic flow phenomena. The combined experimental and numerical work performed by Zhang et al. [40, 41], the URANS investigation of Shyam et al. [42] and DNS computations from Wheeler and Sandberg [43–45] accurately describe the high speed nature of heavily loaded blades. Shocks are originated within the tip gap channel at the flow reattachment line near the pressure side (Fig. 1.1, bottom). These shock structures propagate throughout the passage, reflect on the casing and rotor blade tip and give rise to parallel zones of high heat transfer [46]. Due to the supersonic character of the flow in the majority of the overtip region, the fluid is effectively choked, setting a limiter on the leakage mass flow rate [47]. The loss generation is therefore decoupled from the blade load which permits to further increase the work extraction at the tip section while maintaining similar aerodynamic performances.

However, considerable aerodynamic losses are associated with the supersonic nature of the flow inside the tip gap channel as well as throughout the downstream mixing. Moreover, strong variations of the heat transfer levels can give rise to high thermal stresses inside the rotor airfoil. Conventional geometries, which were shown to perform superior in subsonic regimes, might not always give satisfactory results under high-speed conditions [48]. Transonic overtip flows demand innovative rotor tip designs at the behest of enhanced engine reliability and further performance improvement [49].

Therefore, the use of contoured blade tip designs has been recently proposed to force the passage to remain choked while large flow accelerations are exploited to minimize the heat flux. Shyam and Ameri [50] suggested a diverging pathway for the tip flow which might reduce the shock strength and consequently lower the heat transfer fluctuations. More recently, Zhang and He [51] proposed to locally accelerate the flow in the front part of the blade through a convergent-divergent flowpath to significantly reduce the overall heat transfer [52].

Moreover, recent studies have emphasized the key importance of the shear force induced by relative motion of the casing [53], the significant influence of the modeled inflow boundary conditions [54], as well as the manufacturing tolerances and blade shape degradation during engine service [55] on the overall blade performance and leakage flow aerothermodynamics. Combined with the transonic nature of the overtip flow and the severe thermal loads onto the vulnerable tip section, this makes the turbine tip design one of the prime multidisciplinary challenges for the engine manufacturers nowadays.

1.2 Research Objectives

The current doctoral research exploits the potential that lies in the modification and optimization of the blade tip shape as a means to control the tip leakage flow aerodynamics and manage the heat load distribution over the blade profile to improve the turbine efficiency and durability. An overview of the project is presented in Fig. 1.3.

The research is divided into **5 main objectives**. The first three objectives focus on analyzing and optimizing three main strategies for the design of unshrouded turbine blade tips **(1,2,3)**, while the fourth objective aims to control and enhance the overtip flow characteristics in an indirect way, through the use of unsteady shroud coolant injection **(4)**. Eventually, the last objective comprises the redesign of a rotating turbine facility at the von Karman Institute for Fluid Dynamics, allowing simultaneous testing of multiple distinct blade profiles for advanced tip flow research **(5)**.

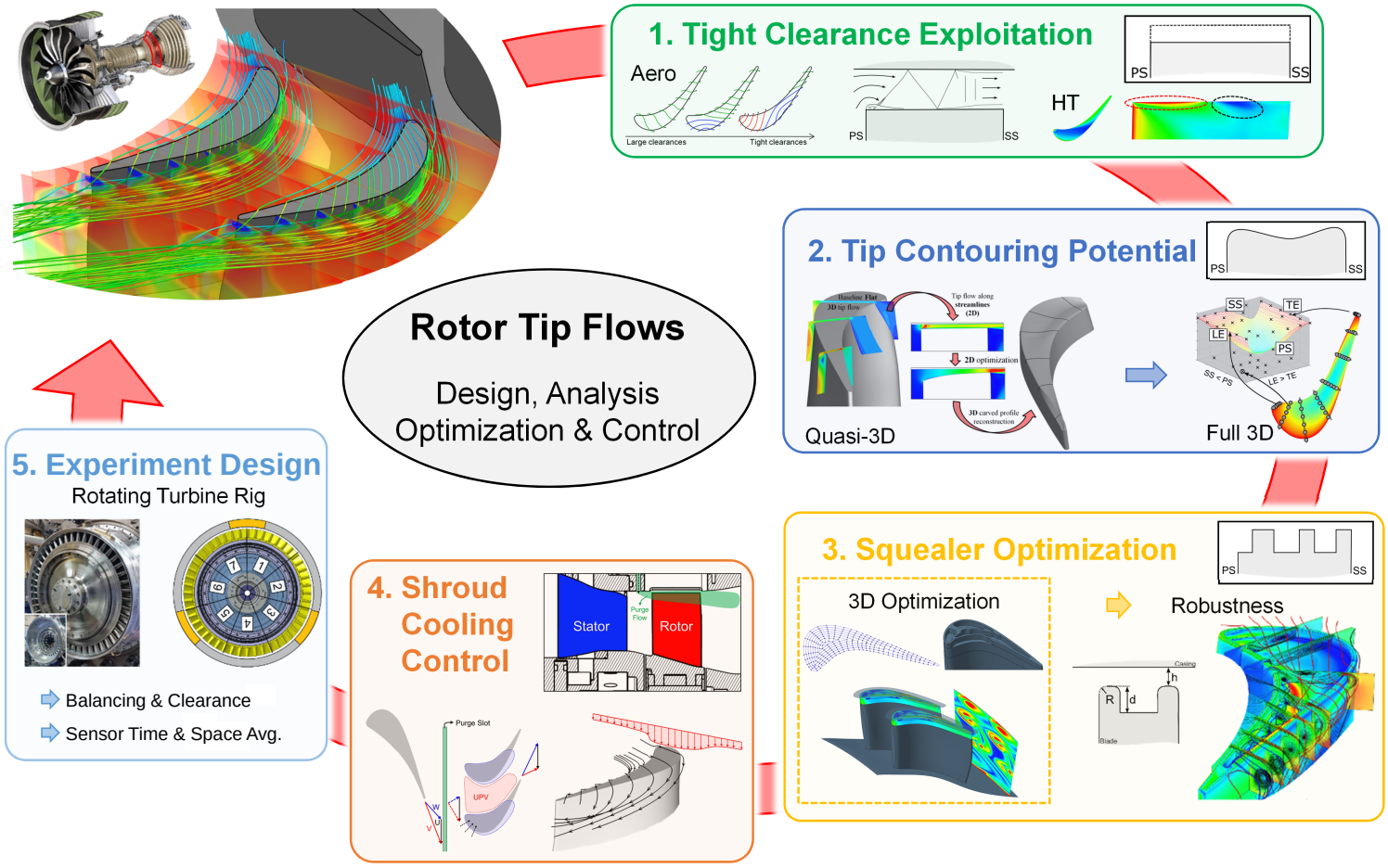

Figure 1.3: PhD Project Overview.

Exploitation of Tight Clearance Flows (1). As the aerodynamic deficit attributed to the tip leakage flow is responsible for about one third of the total turbine losses, engine manufacturers adopt many strategies to reduce the gap between the stationary and rotating turbine parts as much as possible. In this view, most of the previous studies focus on clearances above 1% of the blade span as adopted in the vast majority of the engines currently flying. However, during engine transients and due to recent developments towards a precise control of the clearance levels, further (significant) reductions of the gap size are expected in future generation engines [20].

Nevertheless, to the researcher's knowledge, no publications exist, addressing the altered physics of the overtip flows for such tight clearances below 0.5% of the turbine passage height. Therefore, the current objective aims to bridge this gap and accurately characterize the changes in both the aerodynamic as well as heat transfer aspects in these tight operating regimes. Via 3D numerical simulations over a wide range of gap heights, the aerothermal consequences in the overtip region as well as in the downstream flow field are identified.

Potential Quantification of Blade Tip Contouring (2). Conventional blade tip designs often adopt the same type of geometry across the whole blade camberline. However, the flow conditions can differ significantly along the rotor chord. While the front region is often less loaded and adopts a large blade thickness, the aft sections are typically thin and heavily loaded. Moreover, recent studies indicate a reversed flow topology near the leading edge of the blade and the existence of high supersonic overtip flows near the trailing edge. Therefore, as the existing tip geometries are not adequately designed for these altered flow topologies, a significant potential lies in the appropriate tip shaping, specifically adapted to each flow condition along the blade profile.

This objective targets to investigate such shaping and to quantify the potential for a simultaneous increase of aerodynamic efficiency while minimizing the heat transfer onto the blade top surface. First through a multi-objective quasi-3D shape optimiza-

tion and subsequent 3D verification, and eventually through a full 3D optimization, incorporating arbitrary carving of the tip surface.

Optimization of Industrial Rub-Safe Squealer-like Profiles (3). The widely adopted method of squealer-like geometries, featuring cavities separated by upstanding rims, have proven to significantly increase the aerodynamic efficiency and reduce the chances of a catastrophic event due to any accidental rubbing of the blade against the stationary shroud.

However, many of the currently investigated and industrially implemented designs remain limited to relatively simple rim configurations, e.g. a single (un)interrupted rim all over the blade tip profile, etc. Furthermore, classical tip optimization strategies are typically constrained to a specific type of geometry, narrowing the spread of shape topologies considered during the design phase significantly. This leaves a whole design space of yet unexplored types of blade tip shapes with potentially (considerably) enhanced aerothermal performances.

Additionally, the actual geometry during engine operation can differ significantly from the envisioned designed profile. Manufacturing inaccuracies, combined with the harsh turbine environment lead to relevant geometrical variations. Hence, in order to realize a proper assessment of the turbine aerodynamics, thermal loads and consequent component durability, an estimation of the performance uncertainties caused by the geometrical variability is indispensable. Moreover, to the best of the researcher's knowledge, no rigorous study on the combined geometrical effects of a squealer tip has been conducted, using non-intrusive uncertainty quantification methodologies.

In this view, to cover these important issues related to the investigation of squealer-like tip shapes, the main target of this objective is to twofold. Firstly, the quantification of the influence of geometrical uncertainties on the performance of a conventional squealer tip design. Secondly, to execute a full 3D multi-objective optimization, covering every possible rim-cavity layout using a topology-like optimization strategy to identify, so far undiscovered, optimal blade tip profiles.

Design of Tip Flow Control through Casing Cooling (4). The injection of coolant from the shroud, just upstream of the rotor blades, is commonly implemented in many engines nowadays. This purge flow does not only prevent the hot gases to be ingested outwards to less durable components but additionally ensures to cool down a part of the downstream blade tip. Moreover, this axial gap allows the application of active clearance control strategies (e.g. through the active cooling of the outer casing surface), permitting the modification of the shroud radius independently from the upstream and downstream stator ensembles.

However, this purge flow enlarges artificially the incoming boundary layer to the rotor row. In the tip region the effect can be beneficial due to the enhanced 'reversed' flow in the front part of the blade and the reduced overall amount of required purge flow to cool the tip features. In the main passage on the contrary, this increased boundary layer can give rise to an enlarged upper passage vortex, decreasing significantly the overall efficiency.

The goal of the current part of the research is to explore the possibility of combining the beneficial effect of the purge flow in the overtip region while minimizing the detrimental influence on the upper passage vortex. This is achieved through a variation and optimization of the geometrical purge slot characteristics as well as the (circumferential) purge ejection profile, in a realistic engine environment.

Conceptual Design for Advanced Experimental Tip Flow Research (5). The high-speed rotating turbine facility at the von Karman Institute for Fluid Dynamics is redesigned to allow for simultaneous testing of multiple distinct blade (tip) profiles mounted in separate sectors around the rotor annulus. Important considerations related with the balancing and precise clearance design are highlighted, arising from the complexity of the multi-sector, multi-clearance Rainbow Rotor approach.

Additionally, methodologies are developed to integrate Reynolds-Averaged Navier-Stokes simulations to a priori estimate the measurement errors induced by the finite

spatial sampling and inherent limited sensor bandwidth for space-resolved and time-resolved turbine aerothermal measurements.

This part of the research paves the way for a future, elaborate experimental validation of the superior tip geometries in a rotating turbine facility, at engine-matched conditions.

1.3 Thesis Outline

Chapter 2 describes the CFD methods and optimization platform which has been used for the numerical simulations throughout the thesis as well as a thorough aerothermal validation of the adopted algorithms. **Chapter 3** is entirely dedicated to the exploitation of tight clearance flows while **Chapter 4** quantifies the potential of blade tip contouring through a quasi-3D optimization and a full 3D verification. The full 3D multi-objective optimization of both carved tip profiles and industrial rub-safe designs is described in **Chapter 5**, targeting enhanced aerodynamic efficiency and reduced tip heat loads. **Chapter 6** presents the results of a detailed numerical analysis of the performance robustness of a conventional squealer-type profile due to geometrical variations arising from the manufacturing tolerances and engine operation. **Chapter 7** presents the scaling of a high pressure turbine stage from a lab environment up to real engine conditions and subsequently the analysis and optimization of the purge flow, aiming to control and enhance the overtip flow characteristics in an indirect way. **Chapter 8** describes the experimental redesign of the rotating turbine facility. Considerations related with the balancing and precise clearance design of the rainbow-rotor approach are described, and methodologies are proposed to adopt CFD simulations to estimate the measurement errors induced by the finite spatial sampling and inherent limited sensor bandwidth. Eventually, the results of this PhD research are summarized and the main conclusions are outlined in **Chapter 9**.

CHAPTER 2. NUMERICAL METHODS AND VALIDATION

This section provides additional background on the numerical methods adopted throughout this doctoral thesis.

The first part (2.1) describes the unstructured and structured grid generation, the employed CFD solvers and the postprocessing tools. Section 2.2 presents the results of a thorough aerothermal validation of the used numerical tools and the last part of this chapter (2.3) summarizes the key optimization strategies.

2.1 CFD Methods

2.1.1 Grid Generation

This thesis uses both structured and unstructured meshes for the simulation of the turbomachinery components, depending on the complexity of the geometrical features. Specifically, structured multi-block meshes were used in chapter 3 and 7 while chapters 4, 5 and 6 required the flexibility of unstructured grids.

All structured meshes are generated using Numeca AutoGrid5$^{\text{TM}}$, a particularly powerful and automated grid generator, specifically tailored for turbomachinery applications. The mesh is created through a specification of the meridional flow path characteristics and the 2D mesh topology on spanwise surfaces. For the latter blade-to-blade mesh, the default O4H multi-block structure is adopted. This topology consists of five blocks: an O-mesh surrounding the blade (skin mesh) and four H-blocks upstream and downstream as well as on the pressure and suction side. The mesh inside the tip gap uses a butterfly topology and employs a non-matching boundary to connect the larger amount of cells contained along the suction side as opposed to the

This Chapter contains small parts adopted from De Maesschalck et al. [1–5]

pressure side. Where necessary, additional mesh alterations are performed through Numeca IGG^{TM}.

Numeca Hexpress^{TM} created all unstructured grids for this dissertation. Hexpress is capable of generating body-fitted fully hexahedral unstructured meshes on complex arbitrary geometries. After loading the CAD geometry, the grid generation starts with the creation of an initial mesh, uniformly discretizing the entire computational domain. Subsequently, the mesh size is refined based on adaptation levels specified for certain volumes, surfaces or curves, dividing the block size in every dimension with a factor of two. Eventually, the mesh is snapped onto the surfaces, optimized and a high-quality boundary layer is inserted through its advanced smoothing capabilities. Hexpress can be automatized to run in batch through python scripts which has been used for the implementation of the optimization routines.

For each distinct project within this manuscript, grid independence studies have been performed to verify the mesh resolution.

2.1.2 Solver

The development of high-fidelity CFD methods has made significant progress in the last decades, supported by the ever-growing availability of computational power, throughout the entire range from the conventional cost-effective RANS simulations via more accurate Large Eddy Simulations (LES) up to Direct Numerical Simulations (DNS), implemented with higher order schemes and hybrid combinations thereof [56, 57]. However, due to the high Reynolds numbers and the excessive required computational resources for the more scale resolving CFD techniques, the Reynolds-Averaged Navier-Stokes solvers still remain the workhorse for the majority of design problems in the turbomachinery industry. Therefore, as the work described in the current doctoral thesis was eventually based on roughly 2000 three-dimensional simulations, the RANS method was employed to assess the aerothermal performance of the turbine components.

The solver Numeca FINE/Turbo^{TM} is adopted for all structured numerical simulations while for the cases meshed with unstructured grids, Numeca FINE/Open^{TM} is used. Both density based, finite volume CFD solvers have been validated in section 2.2 and are successfully used by several research groups to model the aerothermal flows in turbomachinery components and more general aerospace applications [58–63].

While both solvers are inherently different, the majority of the numerical strategies and schemes are identical and gives rise to particularly resembling results when solved using a similar grid resolution (cfr. section 2.2). For more information about the precise implementation and description of the solvers, the reader is referred to references [64] for FINE/Open and [65] for FINE/Turbo. However, some indispensable details about the adopted numerical techniques are outlined below.

Turbulence Modeling. Two different turbulence models were used throughout this thesis dissertation: the one-equation Spalart-Allmaras [66] and Menter's two-equation k-ω SST turbulence model [67].

Both models rely on a first order closure based on the Boussinesq hypothesis that the Reynolds Stresses can be modeled through a linear constitutive relationship with the mean flow strain, using the concept of the turbulent eddy viscosity μ_t. The turbulent heat diffusion term is modeled through an introduction of the turbulent thermal conductivity κ_t, calculated from the eddy viscosity via the turbulent Prandtl number Pr_t.

The Spalart-Allmaras model [66] is based on the resolution of an extra transport equation for the turbulent eddy viscosity and is implemented employing the improvements by Ashford and Powell [68]. This model was only used for the projects which showed to require additional robustness of the numerical scheme (e.g. chapter 6). The additional modifications to the production term related with the system rotation and streamline curvature proposed by Shur and Spalart [69] and Shur et al. [70] are not used. However, the standard Spalart-Allmaras model was carefully validated without

the latter amendments and has been proven to be sufficiently accurate (cfr. section 2.2).

The k-ω SST turbulence model [67] blends the Wilcox k-ω model near boundary layers and free-shear layers with the standard k-ϵ model in a k-ω formulation to resolve the main stream. The latter model has shown improved accuracy, particularly in highly vortical flows and the prediction of heat transfer. This strategy has been used for the vast majority of the simulations.

Spatial and Pseudo-Time Discretization. The pseudo-time integration is performed using an explicit 4-stage Runge Kutta scheme to march the governing equations towards the steady state solutions. For all simulations, a second-order central spatial discretization scheme was adopted, including the Jameson-Schmidt-Turkel type dissipation, formulated as a blend of the second and fourth-order differences of the conservative variables [71].

Fluid Model. All working fluids are simulated as 'real gases', or more accurate, as thermally perfect gases. This includes the heat capacities and γ to be dependent on the temperature, essential for simulations at engine conditions where typically large (absolute) temperature drops are created. The dynamic viscosity is computed through the Sutherland law.

In true (aircraft) engine environments, the combustion gases entering the turbine stage contain additional components related with the full/partial combustion reaction. The mixtures of combustible and inert gases with a variety of compositions can cover a wide range of heating values and densities, therefore altering the overall operation of the turbine stage. The combustible components can contain methane and other low molecular weight hydrocarbons, carbon monoxide, hydrogen. The most important inert elements are nitrogen, carbon dioxide and water vapor [72, 73]. However, for simplicity and consistency throughout this dissertation, only dry air was considered as the working medium.

Simulations in the Rotating Frame and Rotor-Stator Connections. The stationary vane and the rotating blade are each simulated in their own frame of reference. The governing equations are solved for the relative velocity components and additional source terms are introduced to account for the contribution of the coriolis and centrifugal forces in the case of rotating frames.

The connection between stationary and rotating domains was for this thesis always calculated through the commonly adopted 'mixing plane approach', exchanging the circumferentially averaged flow quantities across the different domains, guaranteeing the conservation of mass flow, momentum and energy through a flux-based algorithm.

Multigrid. In order to promote fast convergence, a multigrid strategy (3 or 4) was adopted for all simulations. The coarser structured grids are obtained through a drop of nodes in every direction while the unstructured meshes use an agglomeration strategy to create the different coarser discretizations.

Boundary Conditions. In the majority of the simulations throughout the thesis, total pressure and temperatures as well as relative flow angles are imposed at the inlet. The turbulent quantities for both the one and two-equation models are derived from the combination of the expected or measured turbulent intensity and length scales. At the outlet, the static pressure is assumed to be uniform in the tangential direction and is allowed to vary in the radial direction following the radial equilibrium equation imposing a specified pressure value at midspan.

Near Wall Modeling. All simulations were performed using a low-Reynolds approach. Therefore, the first cell size was chosen to give rise to y^+ values ($\frac{u_\tau y}{\nu}$) well below unity (generally below 0.5) to ensure a proper resolving of the aerothermal boundary layer.

Computational Power. For the CFD simulations performed throughout this thesis dissertation, high performance computing clusters at the von Karman Institute

and Purdue University were used. Typical 3D CFD computations of the turbine stage (e.g. 5M-9M cells) were run on 10-16 cores (depending on the cluster architecture) and take about 10-16 hours to converge. The 2D simulations were performed on a single core. The 3D optimizations were typically run using 100 - 350 cores simultaneously for 2 to 8 weeks per optimization.

2.1.3 Processing

The majority of the CFD postprocessing and extraction of the relevant flow and surface quantities has been performed with Numeca CFView^{TM}. Further advanced analysis of the data was done through Matlab^{TM} or Tecplot^{TM}.

2.2 Solver Validation

The CFD solvers (Numeca FINE/Open and FINE/Turbo) have been validated through a high-speed cascade experiment of a cooled turbine blade tip (section 2.2.1), as well as in a fully rotating environment (section 2.2.2), based on tests in the compression tube facilities of the von Karman Institute. Eventually, both the Spalart Allmaras model and the SST prove to perform particularly well in the estimation of the aerothermal signatures on the different turbine components. Therefore, the SST model, known for its strengths in the prediction of highly vortical flows, will be chosen for the majority of the simulations in this dissertation.

2.2.1 Validation through a High-Speed Cooled Turbine Tip

A detailed validation was performed on a stationary, cooled, highly loaded, high-pressure turbine with a squealer tip design. Both the blade and casing pressure distributions and heat transfer were measured by Hofer et al. in a transient wind tunnel at the von Karman Institute for Fluid Dynamics and reported by Naik et al. [74–76].

The simulated test article contains a central coolant plenum, feeding 16 pressure side cooling holes and 4 dust holes ejecting through the cavity floor [77], Fig. 2.1(a). An unstructured hexahedral grid of 17 million cells was generated using Numeca Hexpress (Fig. 2.1(b)), adopting a similar topology as used throughout the dissertation. The experimentally measured radial profiles of the upstream total pressure ($\sim$0.99 bar) and temperature ($\sim$402K), including the boundary layer, were applied at the inlet [78] together with fixed values for the turbulent quantities representing the measured 0.8% of turbulent intensity [75]. At the exit of the computational domain, an average downstream static pressure is imposed, resulting in an overall total-to-static pressure ratio of 2.14. All walls were set isothermal and the coolant injection is specified through the massflow ($\sim$0.25% of the mainstream flow) and a static temperature at ambient conditions.

The cases were solved with Numeca FINE/Open, using a second order central discretization scheme adopting both the SST and Spalart Allmaras (SA) turbulence model.

The resulting conditions targeted a high Reynolds number of $9 \cdot 10^5$ and mainstream Mach numbers up to 1.4 with overtip flow velocities exceeding Mach 1.6.

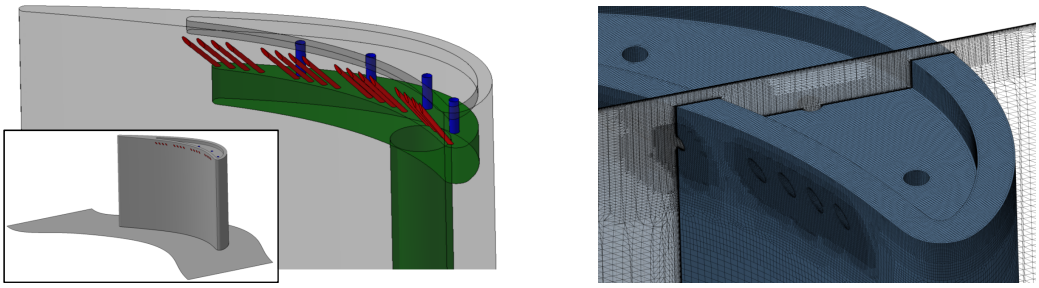

(a) (b)

Figure 2.1: Cooled turbine tip geometry for the solver validation (a) and hexahedral mesh (b).

Fig. 2.2 illustrates the comparison of the pressure measurements on the blade and the overtip casing for the SST (a) and SA (b) turbulence model. Fig. 2.2-top presents the isentropic Mach number distribution at 96.77% of the blade span (right above the pressure side coolant holes) and Fig. 2.2-bottom shows the Mach number along 6 distinct positions A to F on the casing surface. The estimated blade loading and shroud pressure distribution are in particularly good agreement with the experiments for both the subsonic and supersonic regions and even the high Mach numbers in the after portion of the blade (reaching values up to 1.6) are well predicted. Note that the small wiggles on the pressure side are due to the local coolant ejection right below the CFD extraction line.

A comparison of the Nusselt numbers on the blade tip cavity floor and overtip shroud is reported in Fig. 2.3 for the SST (a) and SA (b) turbulence model. All Nusselt numbers are calculated adopting the same reference values as the experiments were processed. As the heat transfer measurements were performed using thin film

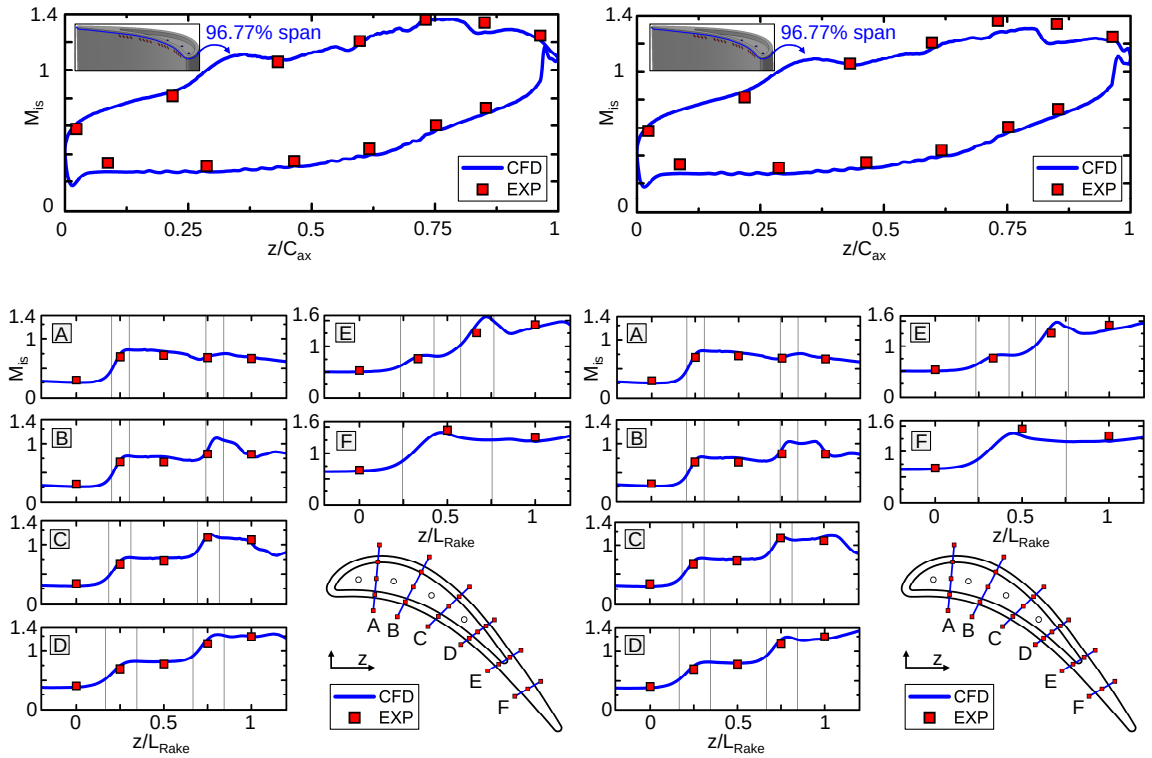

(a) SST. (b) SA.

Figure 2.2: Aerodynamic validation of the Numeca solver through high-speed experiments of a cooled turbine tip with two turbulence models.

gauges with a sensing length of about 4mm [76], both the area-average Nusselt number (symbols) as well as the minimum and maximum levels along the thin film surface (vertical lines) are presented. One can observe that the trends and distribution of heat transfer are well captured by both models, considering the complexity of the heat load signature imposed by the transonic leakage flow pattern combined with the effects of the cooling discharge (cfr. contours of Nusselt number distribution).

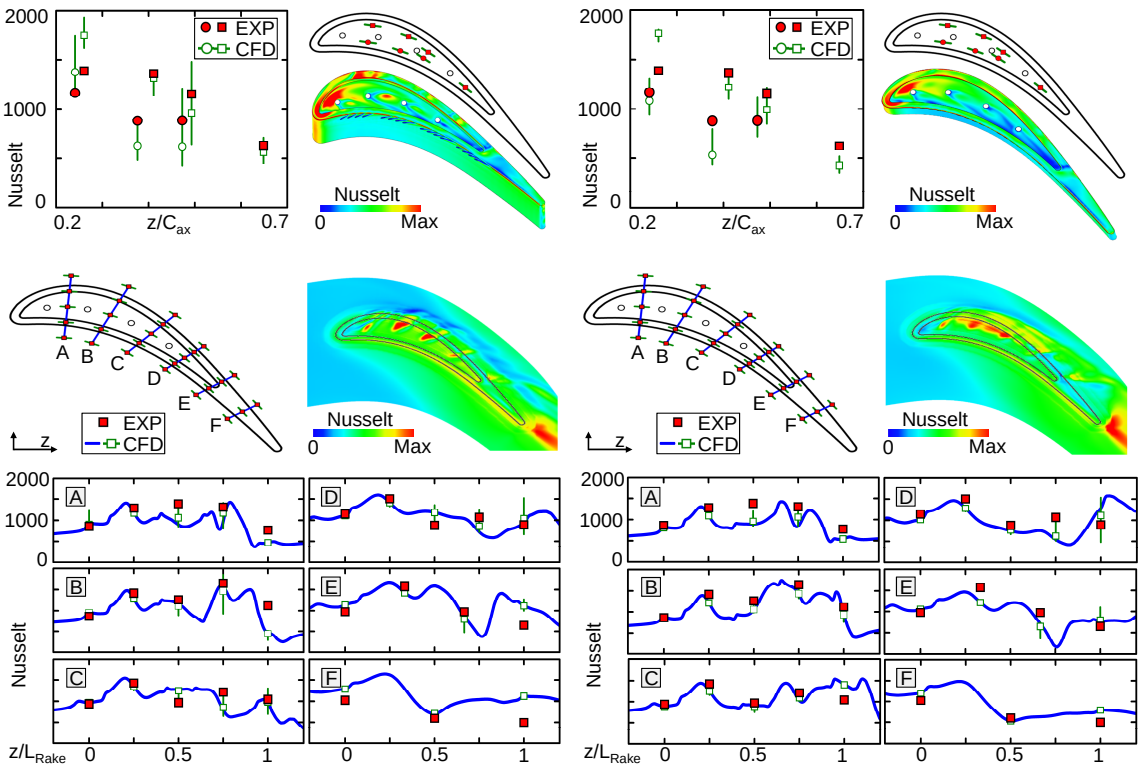

(a) SST. (b) SA.

Figure 2.3: Heat transfer validation of the Numeca solver through high-speed experiments of a cooled turbine tip with two turbulence models.

2.2.2 Validation in a Rotating High-Pressure Turbine Environment

Additional validations of the solver have been performed using pressure and heat transfer data from different experimental campaigns in the rotating high-pressure turbine facility at the von Karman Institute [79].

Stator Vane. A first case adopts the pressure data on an uncooled, restaggered version (2 deg.) of the cylindrical vane originally studied by Denos et al. [80] and Sieverding et al. [81]. This configuration allowed the investigation of strong left and right running shocks originating from the stator trailing edge and serves hereby to validate the solver's capability to capture the supersonic flow topology as well as the

shock reflections on the aft suction side. The eventual CFD results were compared against the experimental data of Paniagua et al. [82] ('nominal pressure ratio').

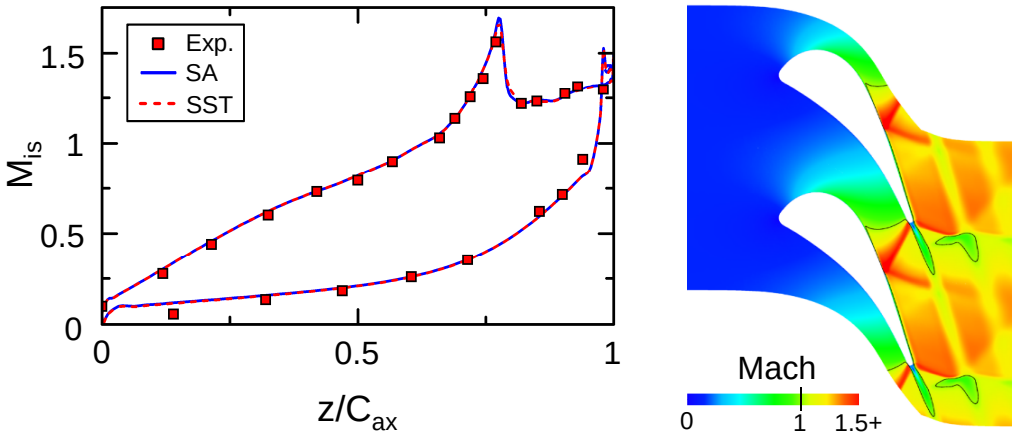

Figure 2.4: Solver validation using a restaggered stator vane with strong shocks [82].

The simulations of the stator vane were performed using a fine, structured grid (∼4 million cells and over 110 radial divisions), created with Numeca AutoGrid5. All boundary conditions (i.e. upstream total quantities and downstream static pressure) were imposed as measured during the experimental campaign and the structured solver Numeca Fine/TURBO was used with two different turbulence models: SA and SST. From the isentropic Mach number at mid-span as presented in Fig. 2.4, one can notice that both the SA and SST turbulence models are capable of predicting the overall blade loading as well as the strength and positioning of the TE shock.

Rotating Blade. A second validation case is based on the pressure and heat transfer data on the rotating turbine blade measured by Didier et al. in the same compression tube facility [83].

For this validation, a structured grid was created for the entire stage using Numeca AutoGrid5, containing a total of 9.3 million cells of which 5.8 contained in the rotor domain. The case was solved with both FINE/Turbo as well as FINE/Open.

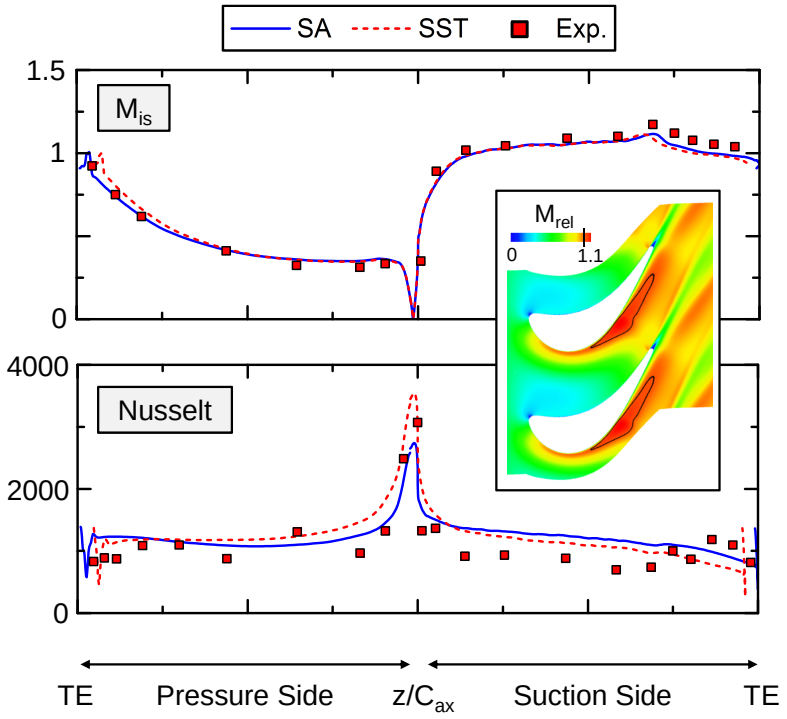

Figure 2.5: Aerothermal solver validation on a rotating turbine blade.

However, as the results for the two solvers showed to be quasi-identical, only the values for the structured solver (FINE/Turbo) are presented hereunder.

Fig. 2.5 depicts the measured isentropic Mach and Nusselt number distributions at 50% of the rotor blade span, together with the numerical predictions using two turbulence models, Spalart Allmaras and the k-ω shear-stress transport. The simulations show a good agreement with the experimental isentropic Mach number distribution. The heat transfer trends are also well captured over both suction and PS. The computational fluid dynamics predictions with fully turbulent boundary layer overestimate the front-mid SS where the boundary layer is expected to be laminar or transitional. A better match is observed on the aft suction surface, where the boundary layer is expected to be turbulent.

2.2.3 Validation Conclusion

The Numeca FINE RANS-solvers have proven to be capable of predicting the aerodynamic phenomena and heat transfer signatures in a high speed environment. Both stationary and rotating, as well as in the main passage and the tip region.

As the SST turbulence model demonstrated slightly better results overall, and due to its known strengths in the presence of highly vortical flows and the prediction of heat transfer, this two-equation model will be the preferred method throughout the dissertation. However, for some cases (mostly due to numerical stability issues), also the one-equation SA model will be adopted for its enhanced robustness (still used by other research groups on the topic; e.g. Zhang et al. [40] or Wheeler et al. [46]).

2.3 Optimization Strategies

The optimization routines which are used for the different projects within this dissertation are part of an in-house code developed at the von Karman Institute for Fluid Dynamics called 'CADO' (Computer Aided Design and Optimization) [84, 85].

This tool is specifically designed for the enhancement of turbomachinery components and has been proven successful for the multi-disciplinary optimization of radial compressors [86, 87], turbochargers [61], fan blades [60] and even internal cooling channels [88] or liquid-metal pumps [89].

The implemented optimization strategies all use the concept of Evolutionary algorithms (EA), created in the 1960s by Holland [90] and Rechenberg [91]. These algorithms are based on the theory of Darwinian evolution where populations of individuals evolve inside a design space and adapt to the imposed environment through the use of several mechanisms such as selection, crossover and mutation. Individuals with an enhanced 'fitness' will have a larger probability to survive, get reproduced, and to be part of the final set of optimal solutions.

These 'zero-order' evolutionary algorithms have several advantages over higher order methods such as gradient-based techniques. They are capable of finding global optima in a discontinuous or noisy design space and don't have the risk of getting trapped into a local optimum. However, often at the cost of a larger eventual number of required high-fidelity evaluations.

While in the past decades many different evolutionary strategies were developed (e.g. particle swarm optimization [92], ant colony optimization [93], etc...), throughout this dissertation, only two widely used types of Evolutionary Algorithms are adopted: Differential Evolution (DE) and Genetic Algorithms (GA). Additionally, for the quasi-3D optimization (Chapter 4), a '2-level' optimization strategy was employed including an artificial neural network (ANN) surrogate model.

2.3.1 Genetic Algorithms, Differential Evolution and NSGA-II

The optimization strategies attempt to find a solution for the (multi-objective) minimization problem:

$$min(f_i(\mathbf{x})) \qquad i = 1..l \tag{2.1}$$

subject to

$$g_j(\mathbf{x}) \leq 0 \qquad j = 1..m \tag{2.2}$$

$$h_k(\mathbf{x}) = 0 \qquad k = 1..n \tag{2.3}$$

where $\mathbf{x}$ indicates the vector containing the bounded design variables of the specific parametrization.

The optimization starts with the creation of an initial database of geometries, each characterized through their own design vector $\mathbf{x}$. Subsequently, $f_i(\mathbf{x})$ is evaluated for every single 'individual', which can be a CFD simulation, FEM , etc.... The way this first 'population' evolves throughout the generations, by means of crossover and mutation, is precisely what is determined by the Differential Evolution technique (originally developed by Price and Storn [94, 95]) or the Genetic Algorithm.

An overview of both techniques as well as the ranking mechanism is presented in figure 2.6.

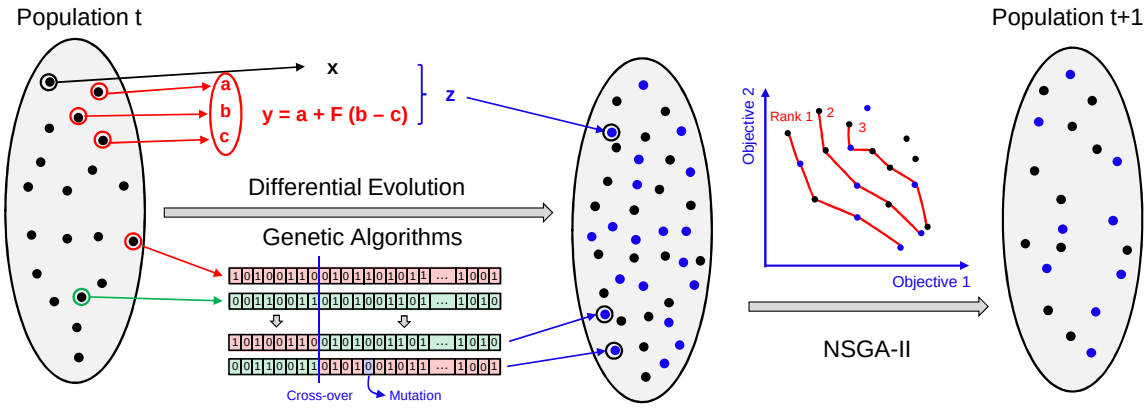

Figure 2.6: Differential Evolution, Genetic Algorithm and NSGA-II optimization strategy.

Genetic Algorithms. In the case of the genetic algorithms, the design vector comprises a string of binary elements. Two 'parents' are selected from the current population which are recombined using one or multiple crossover locations. Additionally, the mutation parameter controls an extra random swapping of distinct binary elements (e.g. 1 out of 200). The eventual combination of the crossover and mutation process generates the eventual 'children'.

Differential Evolution. While the GAs use binary strings to characterize each individual, DE adopts a vector of real numbers bounded by a lower and an upper limit. In order to create the next population, the DE selects three additional parameter vectors ($\mathbf{a}$, $\mathbf{b}$ and $\mathbf{c}$) for every original individual $\mathbf{x}$ (whereby $\mathbf{a} \neq \mathbf{b} \neq \mathbf{c} \neq \mathbf{x}$). A trial vector $\mathbf{y}$ is created:

$$\mathbf{y} = \mathbf{a} + F \cdot (\mathbf{b} - \mathbf{c}) \tag{2.4}$$

where F ($\in$ [0,2]) is a defined constant which controls the differential variation added to the vector $\mathbf{a}$. The latter process is often referred to as the 'mutation' step. Eventually, the final candidate vectors $\mathbf{z}$ (i.e. 'children') are created as a component-wise combination of the original individual $\mathbf{x}$ and the trial vector $\mathbf{y}$:

$$z_i = \begin{cases} y_i & if \quad r_i \leq C \\ x_i & if \quad r_i > C \end{cases} \tag{2.5}$$

where r_i ($\in$ [0,1]) is a uniformly distributed random variable and C ($\in$ [0,1]) is the user-defined crossover constant.

Additionally, the current implementation of CADO does not take a random selection of the vectors $\mathbf{a}$, $\mathbf{b}$ and $\mathbf{c}$ as is commonly done in GA's [96, 97]. Instead, the selection of parents is based on their distance in the objective space and favors the selection of $\mathbf{a}$, $\mathbf{b}$ and $\mathbf{c}$ close to the individual $\mathbf{x}$. This technique was originally introduced by Rai [98] and avoids that in the final stages of the optimization, the differential variation ($\mathbf{b}-\mathbf{c}$) and the eventually created trial vector $\mathbf{y}$ could still give rise

to large variations in the design space in the case of a multi-objective optimization. Opting for the closer individuals, the behaviour of a single-objective optimization is mimicked where the differential variation reduces in magnitude throughout the process.

NSGA-II. The new individuals, created either through the GA or DE, are subsequently added to the current population which results in a new population size twice as large. In order to reduce the population back to its original dimensions, CADO adopts the **N**ondominated **S**orting **G**enetic **A**lgorithm-**II** (NSGA-II) proposed by Deb et al. [99] (Fig 2.6-right). This algorithm first ranks the entire population by consecutive identifications of the Pareto front and maintains the individuals with the lowest rank (Fig. 2.6). The selection of the eventual individuals from the last rank (which fills up the populations size) is based on the crowding distance, selecting the design vectors that maximize the spread along the objective space. This technique eventually allows to bring the population back to its original size from which the creation crossover/mutation process can be re-initiated.

2.3.2 Surrogate Models

A way to reduce the eventual amount of time-consuming high-fidelity evaluations is the use of surrogate models. Such techniques are often referred to as 'Metamodel Assisted Evolutionary Algorithms' [100–103]. The basic idea behind this strategy is an optimization in two-levels, illustrated in Fig. 2.7a. During the first level (the 'Generation Loop'), only a surrogate model is used to evaluate the performance of a large number of individuals generated by the DE. This metamodel is in essence a mathematical interpolator and thus provides fast but less accurate estimations of the performance. This model is trained, based on the performance of the individuals that have already been evaluated by the high fidelity tool (e.g. CFD evaluation, etc...). The training consists of the determination of the internal parameters of the metamodel to achieve a minimum error for its performance prediction. After a specific

number of generations of the DE, the performance of the prime individuals, estimated through the surrogate model, is verified through the accurate evaluation method. These performances are consequently added to the database and the metamodel can be trained again (the 'Iteration Loop'). This results in a self-learning system which makes the metamodel predictions more accurate after each iteration.

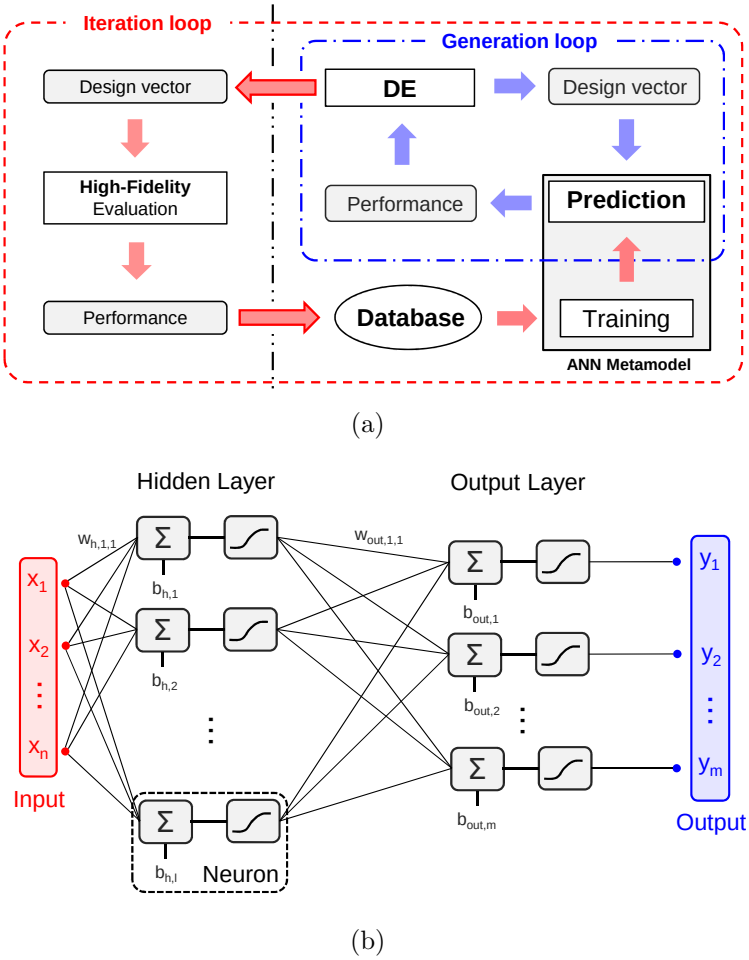

Figure 2.7: Overview of the metamodel assisted differential evolution strategy (a) and structure of an artificial neural network (b).

For the work in this dissertation, only an Artificial Neural Network is used as metamodel [104, 105]. However, many other variations of ANN (e.g. Radial Basis Function Networks,...) and different types of surrogate models have been created and

successfully applied in optimization frameworks over the past decades (e.g. Kriging [106, 107],...).

An overview of the internal structure of such Artificial Neural Network is presented in Fig. 2.7b. The input data (x_i) passes through several elementary units called 'neurons', to eventually predict the output quantities of interest y_i. Both the hidden layer as well as the output layer use a weighted recombination (w) of the input variables combined with a bias b and a subsequent application of a non-linear activation transfer function (here the sigmoidal function) to create the output for each neuron. All model constants are trained using a separate Differential Evolution optimization on its own.

CHAPTER 3. EXPLOITATION OF TIGHT CLEARANCE FLOWS

3.1 Tight Clearance Flows

The inevitable clearance between stationary and rotating parts in any fluid machinery gives rise to leakage flows. In modern gas turbine engines, the existing gap between the rotor airfoil tip and shroud is responsible for about one third of the total aerodynamic losses [11]. Therefore, engine manufacturers attempt to curtail these detrimental effects by targeting tight clearances throughout the entire operational envelope using the recent advances in active clearance control [21]. However, such tight nominal gaps can not only be found in future generation engines, but are already occurring during transient operation, mainly arising from the different thermal characteristics of the rotating components compared to the stationary casing [20]. However, the meager number of publications on this topic presents an obstacle to the understanding of such flow regimes and the exploitation of new design opportunities. To the researcher's knowledge, no publications exist in the open literature addressing the altered physics of the overtip flows for such tight clearances, particularly below 0.5% of the turbine passage height.

Therefore, the current chapter aims to fill this void via 3D numerical simulations over a wide range of clearances and describes the altered flow topology (section 3.3), identifies the effect on the near-tip heat transfer (section 3.4) and gives an overview of the aerothermal performance budget (section 3.5).

This Chapter is based on: C. De Maesschalck, S. Lavagnoli, G. Paniagua, and N. Vinha. Aerothermodynamics of tight rotor tip clearance flows in high-speed unshrouded turbines. *Applied Thermal Engineering*, 65(12):343 - 351, 2014. [1]

3.2 Numerical Methodology

3.2.1 Computational Domain and Mesh

Figure 3.1a presents the cross section of the investigated turbine stage, containing 42 stator vanes and 64 rotor blades. This geometry was selected as to be representative of modern gas turbine technology for aero-engines and power generation [108]. In order to allow a sufficient development of the flow, the outlet of the computational domain was placed 2 chord (denoted as C) lengths downstream of the trailing edge of the rotor blade. The stationary stator passage and rotating rotor domain are connected through a mixing plane. Only one periodic section of the turbine stage is modeled (i.e. 1/42 of the stator annulus and 1/64 of the rotor annulus). A flat rotor tip geometry was considered along with five different clearances (h) between the rotor tip and the stationary shroud, ranging from 0.1% to 1.9% of the rotor channel height (H). The relevant geometrical parameters are summarized in Table 3.1.

Figure 3.1 additionally displays the structured grids created with Numeca AutoGrid5, dividing the stator vane and rotor blade computational domain radially into 61 and 80 flow paths respectively. In order to be able to resolve the detailed gap flow characteristics, the clearance height was further divided radially into 33 sections (53 for the largest clearance). In the cascade plane, an O4H multiblock topology was used, consisting of five blocks: an O-mesh block surrounding the blade and captured inside four H-mesh blocks. The mesh inside the tip gap is generated using a butterfly topology (an H-block surrounded by an O-block), as visualized in Figure 3.1c. The final mesh contains 16 blocks and guarantees y^+ values between 0.05 and 0.3 in the tip region.

A grid sensitivity analysis was performed by doubling the amount of radial divisions inside the clearance and halving the first cell thickness inside the boundary layer. Further refinement of the mesh did not alter the aerothermal results in the overtip region, and hence, a final grid of approximately 2.7 - 3.1 million cells was selected with the parameters listed in Table 3.1-right.

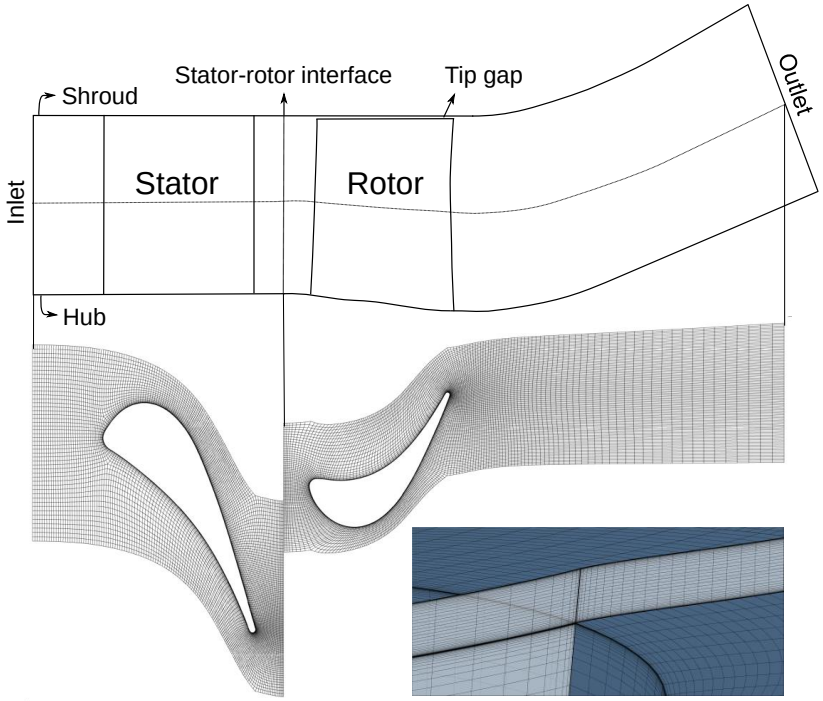

(a) Meridional view, grid at mid-span and detail of the tip gap mesh.

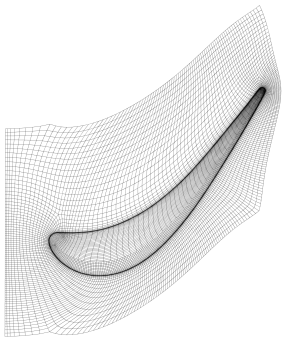

(b) Mesh of the casing surface right above the rotor tip.

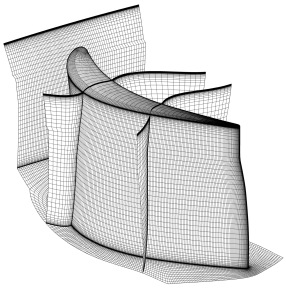

(c) Rotor blade mesh.

Figure 3.1: Turbine stage geometry and computational mesh.

Table 3.1: Summary of the turbine geometry and mesh parameters.

GEOMETRICAL PARAMETERS			MESH PARAMETERS		
	Stator	Rotor		0.1-0.2-0.4-0.9%	1.9%[1]
No. of blades	42	64	Stator divisions[2]	61	61
Inlet channel H [mm]	50.7	51.97	Rotor divisions	80 + 33 (gap)	80 + 53 (gap)
Aspect ratio (H/C)	0.704	1.053	No. of cells	2.68 x 10^6	3.1 x 10^6

3.2.2 Solver Parameters and Evaluated Cases

Steady RANS calculations were performed using the Numeca FINE/Turbo suite 8.9.2, adopting the k-ω SST turbulence model (cfr. section 2.1 and 2.2). The com-

[1]% of h/H
[2]In the radial direction

putations simulate the actual turbine conditions in terms of Reynolds and Mach numbers [108]. An axial airflow was assumed at the inlet of the turbine, imposing the total pressure ($P_{0,in}$) and temperature ($T_{0,in}$) together with a turbulence intensity of 5% [109]. At the outlet of the computational domain, the static pressure (P_s) was set at mid-height of the channel (imposing radial equilibrium) to give rise to a total-to-static pressure ratio of 2.93. The turbine rotor blade and its hub platform are rotating at 6790 RPM. On the sidewalls, periodic boundary conditions ensure that the simulation of one sector is representative of the whole annulus. To mimic the heat transfer characteristics in a true turbine environment, the gas-to-wall temperature ratio $T_{0,in}/T_w$ was set to 1.57 [110, 111]. For each evaluated rotor clearance, an adiabatic and an isothermal computation were performed. Table 3.2 summarizes the turbine operating conditions.

Table 3.2: Turbine operating conditions.

$P_{0,in}/P_{s,in}$	2.93	-
$T_{0,in}/T_w$	1.57	-
α_{in}	0	deg.
Inlet turbulence intensity	5%	-
Rotational speed	6790	RPM
M_{tip} peripheral Mach[3]	0.78	-
Mid-gap Reynolds[4]	350-14000	-

3.3 Identification of a Novel Overtip Flow Topology

3.3.1 Aerodynamics of a Reversed Tip Flow

Fig. 3.2 shows the streamlines in the middle of the gap together with the tip surface pressure contours for the different clearances, decreasing from left (h/H = 1.9%) to right ($h/H = 0.1\%$). For the two largest clearances (i.e. 0.9% and 1.9% of the blade span), the tip leakage flow shows a conventional flow pattern with streamlines

[3]Based on a_{exit}
[4]Isothermal, based on W and h

crossing the blade tip region from pressure to suction side, driven by the differential blade loading across the tip gap. For such clearances, the flow angle across the gap can be predicted using the strategy developed by Heyes and Hodson [112]. However, at clearances lower than 0.9% a striking feature is observed: a part of the flow enters the gap from the suction side and bends back to leave the gap again at the suction side. For the two smallest clearances, the flow direction over the front part of the blade profile is fully reversed, even though the driving pressure gradient is still directed in the opposite direction, from the pressure to the suction side.

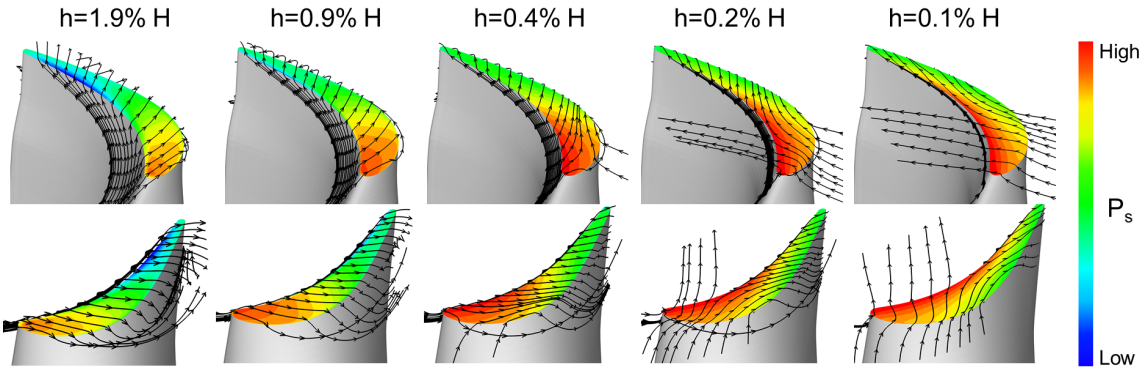

Figure 3.2: Representation of the streamlines entering the tip region in the middle of the gap and static pressure distribution on the tip surface. View from the blade pressure side (top) and suction side (bottom).

3.3.2 Relation with the Incoming Boundary Layer

This novel flow behavior is induced by the effect of the casing proximity which becomes significant only at very tight clearances. The fluid near the casing has a quasi-zero velocity in the absolute frame of reference due to the presence of the inlet velocity boundary layer. In the rotating frame this corresponds to a relative velocity nearly equal in magnitude to the rotor tip's absolute peripheral velocity, but opposite in direction, i.e. from the blade suction side to the pressure side. Fig. 3.3a shows the tangentially (massflow) averaged aerodynamic and thermal boundary layer profiles

close to the casing endwall, 10% $C_{ax,rot}$ upstream the rotor LE. These profiles were hardly affected by the gap size; the maximum variation in temperature and velocity between the lowest and highest clearance remains below 1% at the considered radial positions. Therefore, only the radial profiles for the largest gap are displayed in the figure. The flow exits the stator vane with a total absolute velocity V to which a tangential component V_t corresponds. As the flow approaches the rotating blade, the fluid heading towards the tip gap is subjected to a momentum component generated by the relative movement of the casing endwall in the rotating from of reference, causing the fluid to cross the overtip gap from the suction towards the pressure side. The casing effect on the clearance flow becomes more significant as the tip gap gets tighter.

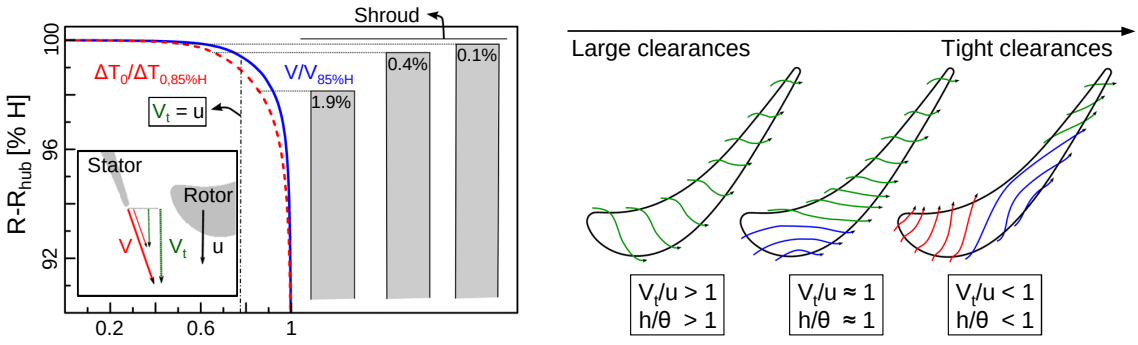

(a) (b)

Figure 3.3: (a) Aerodynamic and thermal boundary layer 10% $C_{ax,rot}$ upstream of the rotor LE; (b) effect of clearance height on overtip flow topology.

Additionally, Fig. 3.3a shows that at a clearance of about $h/H = 0.55\%$, the absolute tangential velocity approaching the rotor leading edge is balancing the peripheral velocity u. As the tip clearance grows beyond that, the tangential velocity of the fluid entering the rotor gap becomes higher than the rotor peripheral speed. Hence, the relative movement of the rotor casing is not sufficient to counteract the effect of the blade loading which pushes fluid over the tip from the pressure side to the suction

side. This case describes the physics of tip leakage flows at relatively 'large' tip gaps, as commonly found in gas turbine engines and reported on in scientific publications.

However, when the local tangential flow momentum at the rotor tip gap inlet and the blade tip peripheral speed are of comparable magnitude (the ratio V_t/u is close to unity), parts of the overtip gap flow cannot travel across the entire airfoil thickness. Hence, the fluid enters the gap suction side, moves along the channel and exits again at the airfoil suction side further downstream. This scenario has been observed for the investigated tip clearances smaller than 0.5% of the channel height, as shown in Fig. 3.2. This flow pattern is particularly evident near the leading edge of the rotor blade, where the pressure differential between the pressure and the suction side is weak.

As the clearance is reduced further below 0.2%, the fluid above almost the whole blade tip surface undergoes fully reversed flow ($V_t/u < 1$). An explanatory sketch representing the three distinct overtip flow topologies is provided by Fig. 3.3b. The momentum thickness θ of the airfoil inlet boundary layer (0.55% of the blade span) can also be used to estimate the clearance size for which reverse flow starts to appear on the tip surface. For large clearances ($h/\theta > 1$), the fluid ingested by the rotating gap has enough momentum to cross the tip channel. When the gap gets smaller ($h/\theta < 1$), reverse flow over the rotating tip surface is observed.

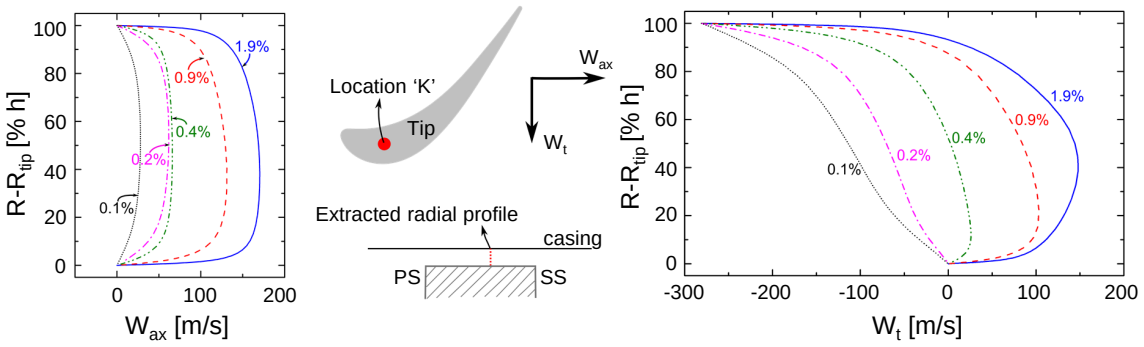

Figure 3.4: Radial distribution, within the tip gap, of the axial (left) and tangential (right) components of the flow velocity in the rotor frame of reference for the investigated clearance heights.

In dry air (Pr $\approx$ 0.7) the thermal boundary layer has a comparable extent as the aerodynamic boundary layer and hence, in the case of tight clearances, both the velocity and the thermal field are heavily influenced by the characteristics of the incoming boundary layer outside the gap. Fig. 3.4 displays the distribution along the radial direction of the flow velocity in the rotor frame of reference within the gap, extracted at a location 'K', taken at 40% of the distance from the suction to pressure side. The velocity in the rotor frame of reference was decoupled into a pressure driven component along the machine axis (W_{ax}, Fig. 3.4-left), and a component in the tangential direction (W_t, Fig. 3.4-right) which includes the effect of the casing relative movement (u = -280 m/s). The smaller the clearance is, the smaller the (signed) tangential component of the velocity vector becomes, and thus the influence of the casing increases. Nevertheless, a significant portion of the flow presents a negative tangential component along the radial direction, which moves from the suction towards the pressure side of the blade (reverse flow).

3.4 Influence of the Clearance on the Near-Tip Heat Transfer

Fig. 3.5a presents the heat transfer over the rotor domain's most relevant regions, namely the tip, shroud and suction side as sketched in Fig. 3.5b, for all the investigated clearances. The first and second column present respectively the heat transfer to the tip and shroud for the isothermal cases. From a comparison of the aerodynamic flow topology (Fig. 3.2) against the heat load contours, it can be concluded that enhanced heat transfer levels are found in the regions where the fluid enters the tip gap. For the largest clearances this happens in the proximity of the airfoil leading edge and pressure side, while for tighter clearances zones of high heat transfer appear on the near-tip suction side surface. Fig. 3.5c shows the heat transfer onto the blade tip and shroud together with the Mach number isolines and density gradient contours in the tip channel for the 1.9% case, at the cut section 'A' of Fig. 3.5b. Through the turning of the flow around the entrance corner of the flat tip, a separation bubble

is formed, which effectively creates a throat. At the reattachment point of the flow on the tip surface a region of high heat transfer is found. In the region close to the throat (characterized by $M_{rel} \approx 1$), the heat transfer on the shroud is significantly altered due to the sudden decrease in boundary layer thickness combined with the acceleration of the flow. In the aft part of the blade for the two largest gap cases, a sonic throat is created at the maximum bubble height and the flow is further accelerated up to supersonic velocities with Mach numbers above 1.4. Consequently, at the reattachment point, a shock originates and propagates back and forth between the tip and casing (Fig. 3.5c). When the shock impinges on the shroud, the boundary layer separates, creating a zone of lower heat transfer downstream.

The third column of Fig. 3.5a shows the heat load on the upper part of the blade suction side (from 75% to 100% of the blade height). For the two largest clearances ($h/H > 0.5\%$), the suction side leakage vortex, indicated with an arrow, enhances the heat transfer onto the blade surface. For the highest clearances, due to the faster gap exit flow, the leakage vortex size is larger, with its core located further away from the blade surface. As a consequence, the heat transfer levels for a clearance of $h/H = 1.9\%$ are slightly lower (-2%) and the region of enhanced heat transfer extends towards a lower radius compared to the case where $h/H = 0.9\%$. For lower clearances ($h/H < 0.4\%$) the tip leakage vortex has almost fully vanished and no large heat transfer levels are observed in the aft part. On the contrary, a zone of high heat transfer emerges near the tip surface between 25% and 40% of the $C_{ax,rot}$ due to the 'scraping' of the boundary layer and fluid ingestion into the suction side marked as zone 'C' in the figure. The zones labeled 'D' exhibit low levels of heat flux and are located at the inflection point of the streamlines that enter from the suction side and also exit at the suction side.

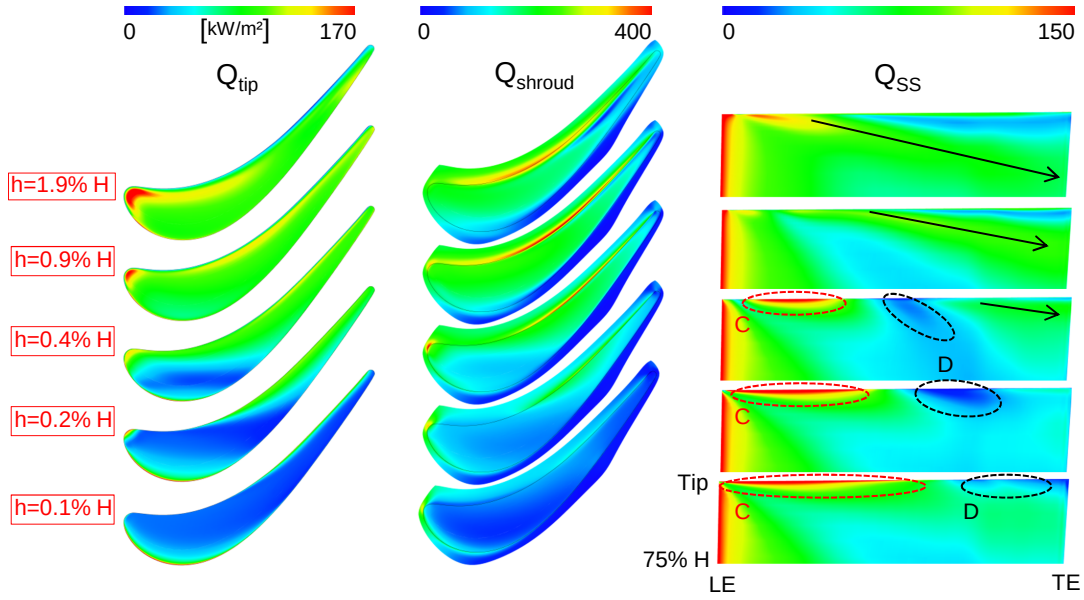

(a) Heat flux onto the tip, shroud, and upper part of the blade suction side

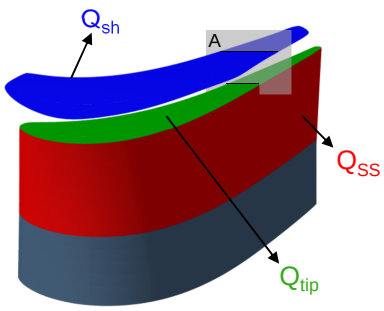

(b) The extraction zones

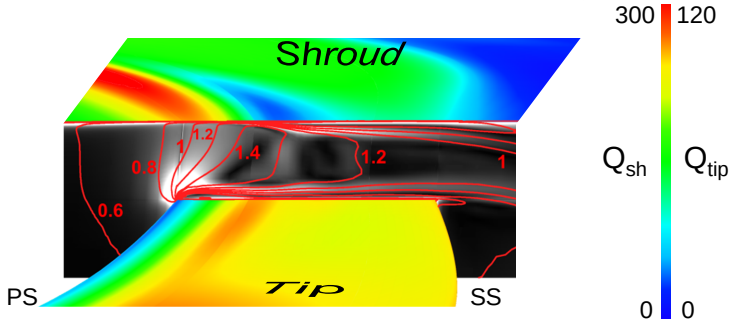

(c) Mach contours and density gradient at cut section 'A' together with tip and shroud heat flux

Figure 3.5: Heat transfer signatures for the 5 different clearances.

3.5 Aerothermal Performance Budget

3.5.1 Downstream Field and Overall Aerodynamic Performance

The clearance between the rotating blade and the stationary casing induces a leakage flow traveling over the tip, resulting in a loss of the potential work that could be extracted by the rotor and hence, a decrease in efficiency. Consequently, keeping the rotor clearance as tight as possible is of utmost importance to limit the leakage

massflow and the induced aerodynamic losses. The aerodynamic losses are shown in Fig. 3.6a, where the relative total pressure contours are presented in a cutting plane located at 95% of the rotor's axial chord ($C_{ax,rot}$). The clearance flow creates a leakage vortex near the suction side which causes a considerable entropy rise. There is a significant reduction of the leakage vortex size with decreasing clearance height. This effect is also visible in the circumferentially averaged relative total pressure values downstream of the rotor (Fig. 3.6b-left). The tip leakage flow governs the pressure levels even down to about 60% of the blade height. While the vortex for the largest clearance penetrates the passage up to 25% of the blade height and gives rise to a spanwise-averaged pressure deficit of over 15%, the vortex in the $h/H = 0.4\%$ case has almost vanished and its core barely affects the overall total pressure losses. Moreover, the leakage vortex alters significantly the exit flow swirl (Fig. 3.6b-right) which will be felt by the following turbine stage. Lowering the clearance from 1.9% to 0.4% of the blade span reduces the absolute outlet flow angle variations in the upper half of the passage by more than a factor of two.

Fig. 3.6c displays the (total-to-total) efficiency of the turbine stage in function of the clearance. The efficiency has been evaluated using different approaches. Conventionally, in the absence of heat transfer, the aerodynamic efficiency is assessed through the ratio of the extracted power (i.e. total temperature drop) to what would be isentropically possible across the same total pressure ratio. This performance is further on called the adiabatic efficiency η_{AD}. The adiabatic efficiency for the design point is η_{AD}=91.1%, while the experimental adiabatic efficiency was 91.8%, with an estimated bias error of 1.1% [113]. However, for investigations performed at isothermal conditions (e.g. experiments in transient rigs [114–116] or design and optimization studies) the heat dissipated to the endwalls must be considered, e.g. by subtracting the energy lost through heat transfer from the actual drop in total enthalpy across the stage (η_{ISO}). Atkins and Ainsworth [117] recently proposed a comprehensive estimation ($\eta_{ISO,corr.}$) of the adiabatic efficiency through a non-adiabatic simulation or

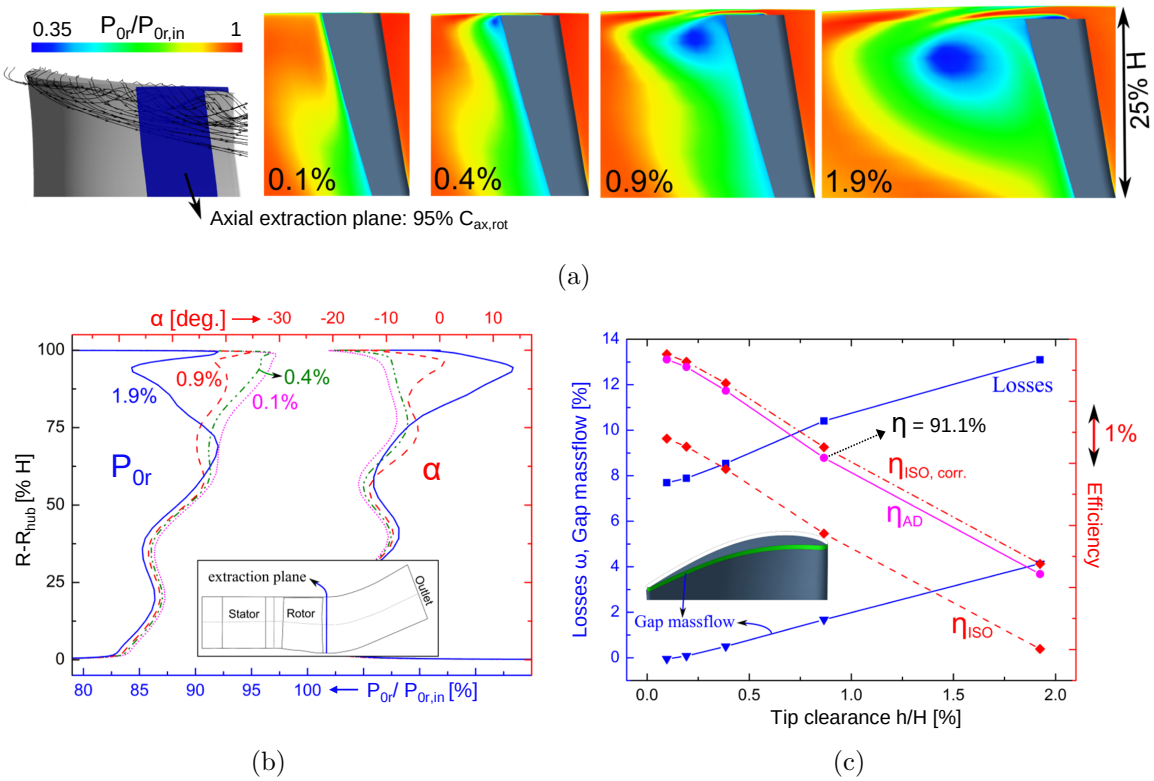

Figure 3.6: Aerodynamic performance for different clearances: (a) contours of P_{0r} at 95% $C_{ax,rot}$; (b) pitchwise-averaged P_{0r} and absolute flow angle downstream of the rotor; (c) losses, efficiency and pressure-side gap mass flow.

experiment by taking into account the temperature at which the heat transfer takes place for the entropy creation:

$$\eta_{ISO,corr} = \frac{\dot{P}_{shaft} + \dot{Q}_{stage}}{\Delta h_{0,is}} - \frac{T_{0,3}}{\Delta h_{0,is}} \left[\frac{\dot{Q}_{st}}{T_{0,1}} + \frac{\dot{Q}_{rot}}{\frac{1}{2}(T_{0,2} + T_{0,3})} \right] \tag{3.1}$$

Where $\dot{P}$ represents the extracted power, $\dot{Q}$ the heat flux levels onto the different parts of the stage and $\Delta h_{0,is}$ the istentropically possible enthalpy difference. In this case, the modified approach of Atkins and Ainsworth allows one to predict the adiabatic efficiency η_{AD} from isothermal evaluations with a difference below 0.17%, while the conventional approach gives rise to an error of about 1.3%. Examining the efficiency

for the adiabatic case (η_{AD}), an efficiency gain of 2% can be noticed for every 1% decrease in clearance, consistent with what has been found in the literature [14].

Fig. 3.6c also shows the rotor (mass flow averaged) aerodynamic losses ω (defined as the drop in relative total pressure across the rotor row normalized by the difference between the total relative and static pressure downstream the rotor) and the amount of leakage mass flow passing through the pressure side section. Both trends are similar and illustrate the essentially mass flow-driven loss mechanism. Moreover, for very tight clearances (e.g. 0.1% and 0.2% of the blade span), the mass flow going through the gap becomes considerably small and even negative. This can be explained through the reversed flow (cfr. Fig. 3.2), which (over)compensates for the flow entering through the pressure side section of the gap.

3.5.2 Stage Heat Transfer Breakdown

Fig. 3.7a presents the distribution of the heat transfer onto the different turbine parts for a tip clearance of $h/H = 1.9\%$. The first bar considers the whole stage, the second bar only the rotor domain and the third bar shows how the heat load is distributed over the rotor blade. Even though the wetted surface of the stator is similar to that of the rotor, the stator extracts 60% more heat than the rotor section due to the higher driving temperature difference. Within the rotor section, the airfoil contributes about 66% of the total heat transfer. Of this, 6% goes to the tip surface while the rest is almost equally distributed amongst the different pressure and suction side surfaces.

Fig. 3.7b illustrates the effect of the clearance on the rotor heat flux across the surfaces of interest, namely the upper part of the rotor blade, the tip surface, and the shroud. The heat load onto the other surfaces (PS and SS) showed almost no variation with clearance ($< 3\%$). One can observe a significant decrease in blade tip and shroud heat transfer in the gap region (the same zones as presented in Fig. 3.5a), due to the combined effect of the ingested low energy fluid and the low aspect ratio of the gap

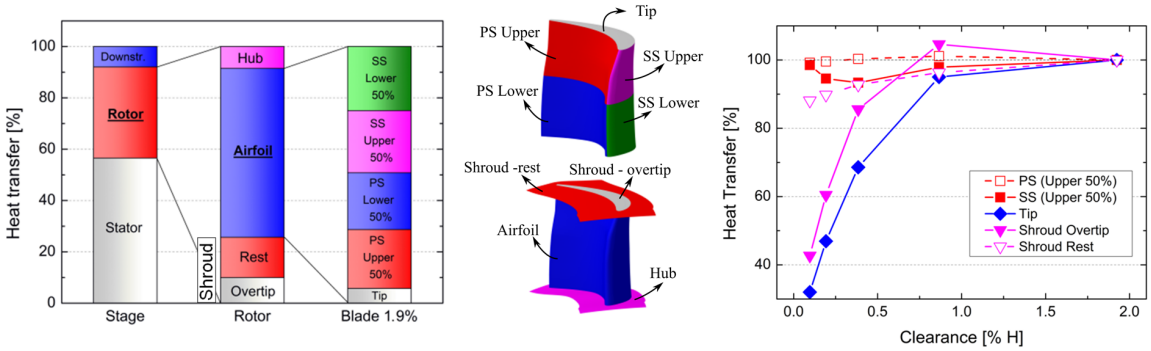

Figure 3.7: Turbine heat transfer budget: (a) breakdown for the entire stage; (b) heat transfer levels on the rotor surfaces as a function of the tip clearance, normalized by the heat transfer for the h=1.9% H case.

channel. Hence, for the largest clearance, the tip and shroud heat transfer is more than twice the value for the lowest gap size. However, the overtip shroud component shows a peak value at $h/H = 0.9\%$ while the tip heat load shows a monotonic increase with the gap height. This is due to the reduced heat transfer on the shroud in the case of the highest clearance, where a significant flow detachment takes place (cfr. Fig. 3.5), resulting in lower heat transfer levels in the aft part of the blade. The heat transfer to the pressure side remains practically unchanged (variations $< 2\%$), while the suction side reveals a minimum (-7%) for $h/H = 0.4\%$. This is the clearance size at which the leakage vortex is diminished significantly (which is the main reason for the heat transfer at higher clearances) while the high heat transfer levels due to the scraping of the boundary layer (important for very low clearances) are not yet significant.

3.6 Conclusions

This chapter presented an elaborate numerical investigation of a high-speed gas turbine stage, operating in the as-yet uninvestigated tight running regime (tip clearances less than 0.5% of the blade span).

At such narrow clearances, the streamlines in the tip gap reveal a reversed flow (i.e. from the suction side to the pressure side) due to the low-momentum and -energy fluid from the upstream boundary layer ingested through the gap suction side. The precise reversed flow regime can be related to the momentum thickness of the incoming boundary layer and the local tangential fluid velocity when compared to the tip gap size and blade peripheral speed respectively.

Heat transfer distributions show enhanced levels on the shroud and tip where the fluid enters the gap. In the suction side near-tip region, the influence of the leakage vortex is predominant for clearances above 0.5%. However, for lower gap sizes, an important zone of high heat transfer emerges at 25% $C_{ax,rot}$ due to the scraping of the boundary layer. The dependency of the heat load on clearance size show different trends for the suction side and tip surface, with a minimum at $h/H = 0.4\%$ in the former and a maximum at $h/H = 0.9\%$ in the latter. The aerodynamic (adiabatic) efficiency proved to be mainly driven by the leakage mass flow and was predicted accurately from isothermal calculations with an error lower than 0.17% following the correction approach of Atkins and Ainsworth.

The results of this numerical effort showed a novel change in the aerothermal characteristics in the overtip region for tight clearances and provide new physical insights, indispensable to design efficient rotating machines adopting small leakage paths.

CHAPTER 4. POTENTIAL QUANTIFICATION OF BLADE TIP CONTOURING

The first section (4.1) will introduce the blade tip carving concept and its potential to locally adapt the top profile to the changing overtip flow along the blade camberline. Subsequently, a quasi-3D optimization of the blade tip shape for 5 different flow regimes will be presented in section 4.2. Eventually, the carving methodology is verified through the construction of fully three-dimensional contoured blades in section 4.3.

4.1 Blade Tip Shape Carving

4.1.1 Concept

Conventional blade tip designs usually adopt the same type of geometry along the whole blade camberline. However, the flow conditions can differ significantly along the rotor chord. While the front region is often less loaded and has a large blade thickness, the aft sections are typically thin and heavily loaded. Consequently, a potential performance gain can be expected when the separate blade tip sections are adapted to the local flow topology.

This Chapter is based on:

C. De Maesschalck, S. Lavagnoli, and G. Paniagua. Blade tip shape optimization for enhanced turbine aerothermal performance. *ASME Turbo Expo 2013 Proceedings*, GT2013-94754. [118]

C. De Maesschalck, S. Lavagnoli, and G. Paniagua. Blade tip shape optimization for enhanced turbine aerothermal performance. *Journal of Turbomachinery*, **136**(4):041016, October 2013. [2]

C. De Maesschalck, S. Lavagnoli, and G. Paniagua. Blade tip carving effects on the aerothermal performance of a transonic turbine. *ASME 2013 Turbine Blade Tip Symposium Proceedings*, TBTS2013-2028. [119]

C. De Maesschalck, S. Lavagnoli, and G. Paniagua. Blade tip carving effects on the aero-thermal performance of a transonic turbine. *Journal of Turbomachinery*, **137**(2):021005, September 2014. [3]

However, the design of a full 3D rotor tip section with an optimal aerothermal performance might only be achieved through a complex and computationally expensive optimization procedure (e.g. chapter 5). Furthermore, any successful optimization of a 3D tip surface would require at least a preliminary knowledge of the optimal tip contours at a number of tip flow regimes. The impact of numerous geometrical and turbine parameters involved in the tip flow problem should be previously assessed to limit the optimization design space and guarantee an efficient parametrization of the tip contour [120]. Unfortunately, this information is a priori not available, and additional understanding of the flow physics and heat transfer mechanisms in the overtip gap region is still needed.

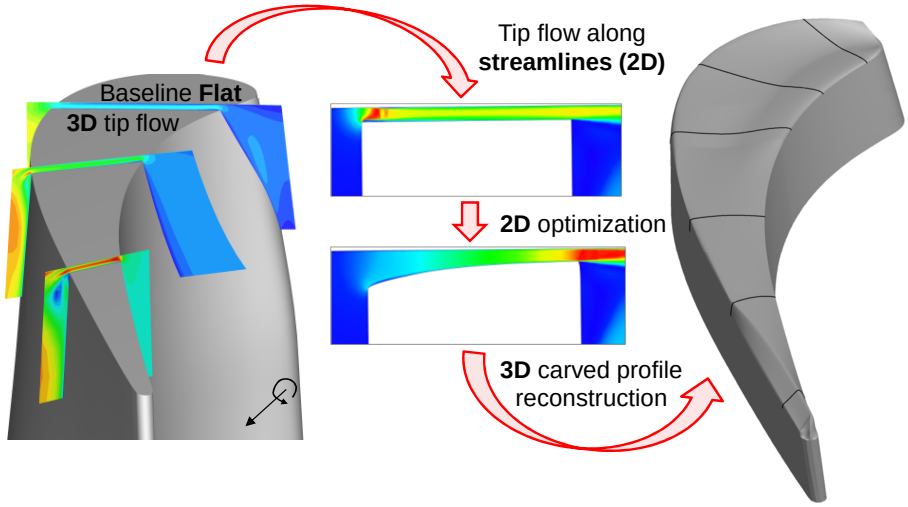

Figure 4.1: Tip carving design methodology.

Therefore, a design methodology is proposed (and used in section 4.2) to study the rotor tip leakage flow for contoured tip geometries, which greatly simplifies the investigation of blade tip shape optimization. The design methodology, illustrated in Fig. 4.1, assumes that the tip leakage flow is two-dimensional in the overtip gap region. This approach allows us to represent the real three-dimensional overtip cross flow as a composition of discrete 2D flow snapshots along the machine axis. In this way, the complexity of the overtip leakage flow simulation is substantially reduced,

an optimization procedure could efficiently be applied and an optimal flow topology can be created at every section (e.g. 6) along the overtip streamlines.

In an early design stage, the required overtip flow characteristics could be predicted using theoretical models based on the tip gap pressure ratio along the rotor chord using a known static pressure distribution around the blade. Additionally, for conventional clearances, the flow direction can be estimated using simplified models of the overtip flow direction, e.g. developed by Booth et al. [121] or Heyes and Hodson [112], and adapted to compressible flow and applied to the current turbine stage by De Maesschalck [122].

As a consequence, once one knows the overtip flow topology, i.e. the blade loading and width-to-gap ratio, the obtained set of superior 2D profiles can be blended together into a, potentially optimal, fully carved 3D blade tip shape (see section 4.3).

4.1.2 Assumption of 2D Tip Gap Flow

The fundamental assumption behind this design approach is that the flow streamlines do not change direction in the overtip region. Therefore, the validity of this 2D flow hypothesis was assessed using a numerical simulation of a 3D high pressure turbine stage. The results of the transonic HP turbine stage simulations of chapter 3 were used at a moderate clearance level of 0.9%. The full description of the numerical setup can be found in section 3.2.

Fig. 4.2a displays a top view of the streamlines entering the overtip gap together with contours of the relative flow angle β in the mid-gap section. The validity of the two dimensional flow assumption was verified quantitatively inside the tip channel at three axial locations along the tip camberline. At these locations, 2D cutting planes are generated in such a way that they are parallel to the leakage flow at the camberline. Fig. 4.2b presents the deviation ($\Delta\beta$) of the clearance flow from the plane direction. Values equal to zero degrees represent the case when the idealized 2D overtip flow representation would actually reproduce the real 3D flow topology.

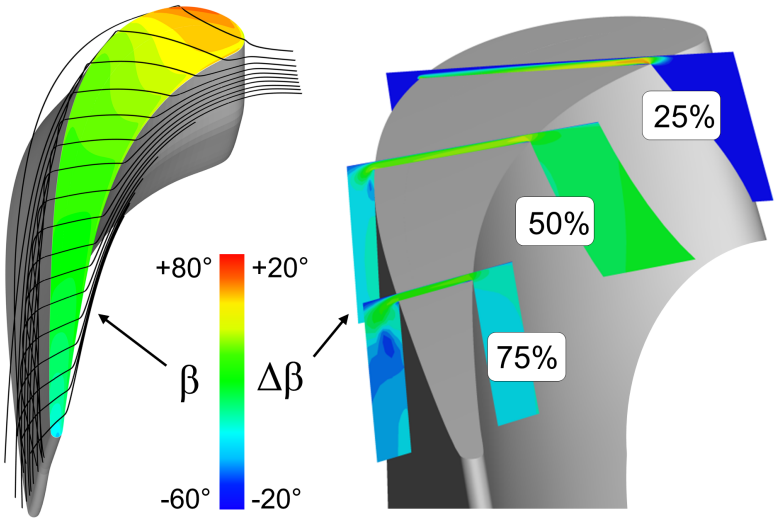

Figure 4.2: Assessment of the 2D overtip flow assumption using 3D CFD.

Overall, it can be noticed that the largest portion of the fluid keeps parallel to the cutting plane direction when it crosses the tip gap. Only a small portion of the flow shows a deviation from the plane direction induced by the proximity of the tip and casing endwalls. The smallest deviation from the 2D assumption ($\Delta\beta < 5$ deg.) is found in the rear part of the blade profile (75% $C_{ax,rot}$). In this part of the blade the tip gap flow is driven by the largest pressure differences over a relatively short channel (low thickness to gap ratios) and is likely to be choked for HP rotors with transonic exit flow [47]. The flow variations from the imposed 2D plane direction become more and more significant for planes closer to the blade leading edge. In reality, the flow structure in the first half of the blade is intrinsically three-dimensional and the tip gap flow is typically subsonic in the frontal region of the blade tip.

Therefore, the present design approach is not intended to be quantitatively accurate but should still provide correct guidelines for the design of optimal tip shapes over a wide range of tip flow regimes normally encountered in HP rotors.

4.1.3 Tip Flow Regime Selection

The design approach employed here targets the optimization of blade tip profiles using a 2D representation of the overtip gap flow. The physics of high-speed overtip gap flows have shown to be dictated by the driving pressure difference between the pressure and suction side on one hand and the tip channel geometry on the other hand [46]. Every case can therefore be characterized by a certain pressure ratio across the gap (noted as an equivalent isentropic Mach number, M_{is}) and a width to gap height ratio (w/h).

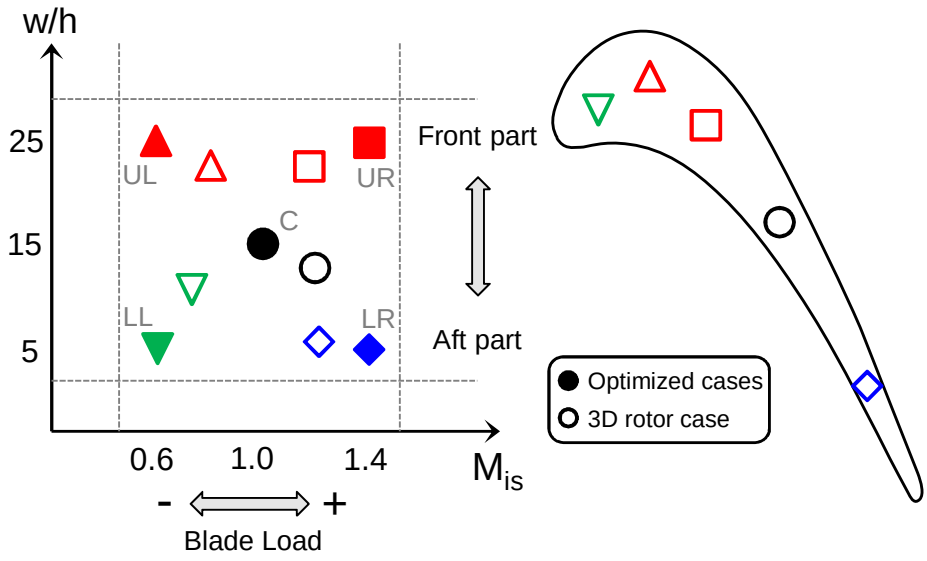

Figure 4.3: Illustration of the investigated tip gap flow regimes and corresponding application to a 3D HP turbine blade.

In order to select relevant optimization cases, typical gap flow scenarios found along the rotor blade tip surface are presented in Fig. 4.3. Fig. 4.3 shows the tip leakage flow evolution from the leading to trailing edge of the evaluated 3D HP rotor (empty marks) compared with the selected overtip flow regimes for the optimization (filled marks). Eventually, three gap exit Mach numbers (M_{is} = 0.6, 1.0, 1.4) and three width to gap size ratios (w/h = 5, 15, 25) were chosen. In a conventional turbine design, the front part of the rotor has a low blade load and a thick transversal section

(upper left part of the graph, Fig. 4.3), giving rise to a fully subsonic flow within the tip gap. The aft part of the rotor is highly loaded and overtip flow velocities can reach the supersonic regime over a small blade width (lower right part of the graph, Fig. 4.3). For the sake of simplicity, the five optimized cases will be labeled throughout the dissertation according to their relative position in the plot of Fig. 4.3 (C=Central, UL=Upper Left, UR=Upper Right, LR=Lower Right, LL=Lower Left).

All the simulations were performed at a fixed tip clearance of 1% of blade span with the tip Reynolds number varying between $0.27{\cdot}10^5$ and $1.64{\cdot}10^5$, based on the blade width and the gap exit velocity.

4.2 Quasi-3D Optimization of Tip Contouring

4.2.1 Numerical Methodology

2D Tip Shape Parametrization

A proper parameterization of the tip gap geometry is of paramount importance for the quality of the optimization output. Fig. 4.4 shows the adopted parameterization of the blade tip shape that consists of two quadratic (left and right blue lines) and one cubic Bezier curve (middle red line). Parametric Bezier curves use Bernstein polynomials as a basis to model smooth curves with control points. Due to the simplicity and strong coupling with the underlying polygon of control points, Bezier curves are commonly used in computer graphics and shape definitions for optimization routines [123]. In this case, the three Bezier curves are constructed through 8 control points which are defined by 6 design parameters.

The profile can adapt within a design domain which is bounded by the blade thickness, on the upper side by a minimum tip clearance $\mathrm{tc_{min}}$ and on the lower side by a fixed maximum deformation length $\mathrm{L_{def}}$. The latter sets the maximum extent of the profile deformation in the radial direction and was chosen to be two times the minimum tip clearance. The range over which the different parameters can span is defined by the maximum allowed deformation length. Moreover, additional constraints are set to prevent the creation of unphysical geometries, ensure the tip profile manufacturability and discard geometrical features that could undermine the blade structural integrity. The control point B can move horizontally from 1% up to 25% of the blade width, and vertically from $\mathrm{L_{def}}$ up to the $\mathrm{tc_{min}}$. Point A can only move vertically, keeping the horizontal position of this point fixed to ensure the continuity of the first derivative at the pressure side of the blade. Consequently, control point C is constructed to provide continuity of the first derivative at point B and to be close to a continuity of the second derivative there. Similarly, point E can move horizontally from 75% up to 99% of the blade width, while the location of

point D is defined according to the location of point E and F. The wide variety of profiles that can be generated is illustrated in Fig. 4.4, bottom.

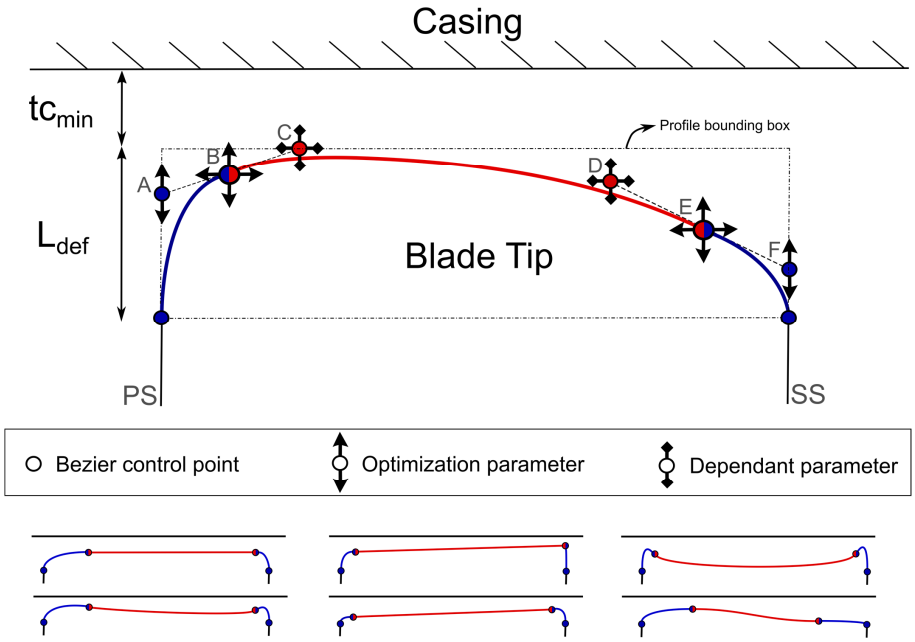

Figure 4.4: The parametrization of the blade tip geometry (top) and possible 2D tip shapes in the design domain (bottom).

High-Fidelity Tip Flow Evaluation

Accurate tip flow simulations were performed using the computational domain shown in Fig. 4.5. This domain consists of a rectangular inlet and a radiused outlet plenum, connected by the tip channel. This geometry models the 2D representation of the overtip leakage (OTL) flow along a streamline where the fluid flows from an inlet plenum (PS) through the tip gap driven by the pressure differential with the suction side. The width and height of the inlet plenum are 100 times the minimum tip gap size (i.e. 1% of the blade span). The outlet plenum is sized as one third of the inlet plenum dimensions. The latter criterion ensures no influence of the outlet plenum size on the overtip flow characteristics. A fixed total temperature and total

pressure were imposed at the inlet section. A static pressure boundary condition is imposed at the domain exit. The lower boundary of the inlet plenum is an inviscid wall while the other walls are set as viscous surfaces. An isothermal wall boundary condition is employed on the tip and casing surfaces to retrieve the heat fluxes. The wall temperature was set to 75% of the total inlet temperature.

A fully unstructured grid is created using Numeca Hexpress (Fig. 4.5). The minimal amount of cells inside the gap in the streamwise direction is set to 100 and the minimum amount of cells in the vertical direction inside the gap before an extra boundary layer refinement is done was fixed to 50. The final mesh features approximately 70,000 cells with y^+ values in the order of 0.1 in the tip channel to accurately resolve the local flow structures and the heat transfer. Both the dimensions of he computational domain as well as the mesh size are the result of a sensitivity study [122].

The steady-state RANS equations are solved in Numeca FINE/Open using the k-ω SST turbulence model [67] and a multigrid approach to accelerate convergence. The numerical flow quantities are eventually extracted and visualized using Numeca CfView.

Optimization Strategy

The adopted method is an in-house developed optimization code of the Von Karman Institute (VKI) using 'Differential Evolution' (DE) 'Evolutionary Algorithms' (EA) [86, 88], described in section 2.3. The basic idea behind this routine is a two-level optimization (section 2.3.2, Fig. 2.7) where in the first level (the 'Generation Loop'), only a metamodel is used to evaluate the performance of a large number of individuals (in this case tip geometries) generated by the DE. In this research, an Artificial Neural Network (ANN) metamodel is used which is trained, based on the performance of the individuals that have already been evaluated by the high fidelity tool (CFD). The training consists of the determination of the internal parameters of

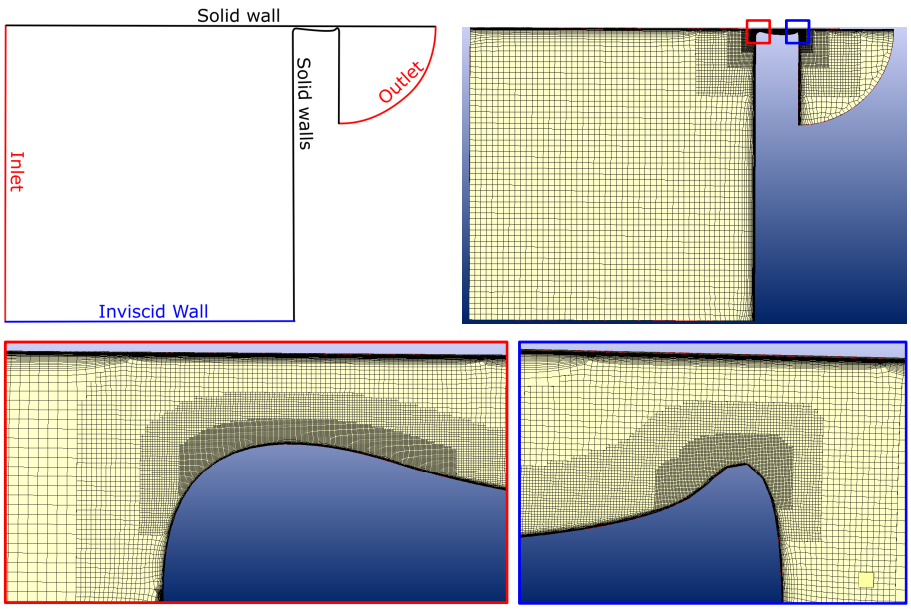

Figure 4.5: The computational domain (upper left) and grid (upper right) together with two details of the mesh in the tip gap region (bottom).

the ANN to achieve a minimum error for its performance prediction. After a specific number of generations of the DE, the performance of the prime tip profiles, estimated through the metamodel, is verified through the accurate evaluation method. These performances are consequently added to the database and the ANN metamodel can be trained again (the 'Iteration Loop'). This results in a self-learning system which makes the metamodel predictions more accurate after each iteration. The use of such metamodel requires an initial database which contains individuals who are already evaluated with high fidelity. This performance database (Design of Experiments, 'DOE') is created using a fractional factorial approach [124], maximizing the amount of information contained in a limited number of designs.

For this project, a multi-objective optimization is performed, i.e. the tip profile optimization targets both the increase of the aerodynamic performance and the reduction of the surface thermal loads. This means that the population evolves every iteration towards a population where the individuals lay on a Pareto front (e.g. Fig. 4.7). The Pareto front contains individuals for which one of the performance parame-

ters cannot be enhanced without deteriorating the other ones. Table 4.1 summarizes the main settings used in the current optimization for the five flow cases defined in Fig. 4.3.

Table 4.1: The optimizer settings.

Parameter					
No. of DoE samples			65		
No. of DE generations			1000		
Population size			40		
Mutation constant			0.6		
Crossover constant			0.8		
No. of CFD Evaluations per iteration			5		
	LL	LR	Central	UL	UR
No. of iterations	92	82	79	90	100

Aerothermal Performance Assessment

The criteria to evaluate the performance of a certain tip design must represent a measure of the heat load levels generated at the tip channel surfaces and of the aerodynamic loss associated with the tip leakage flow.

The first performance parameter represents the heat load. Since the shroud and the tip are vulnerable to failure due to the high thermal loads, both quantities need to be taken into account (see Fig. 4.6). It is important to evaluate not only the mean heat flux levels, but also the heat flux variations along the tip and casing surface. The average thermal loads impose the amount of cooling air to guarantee acceptable metal temperatures, while fierce unsteady heat transfer fluctuations may cause high-cycle thermal fatigue issues and strong thermal stresses which can lead to early blade tip failures.

The contribution of the mean heat transfer level to the heat load performance parameter is described by the total heat flux (Q^{AVE}), the magnitude of the heat transfer variations is evaluated by the RMS of the heat flux field (Q^{RMS}). The combination

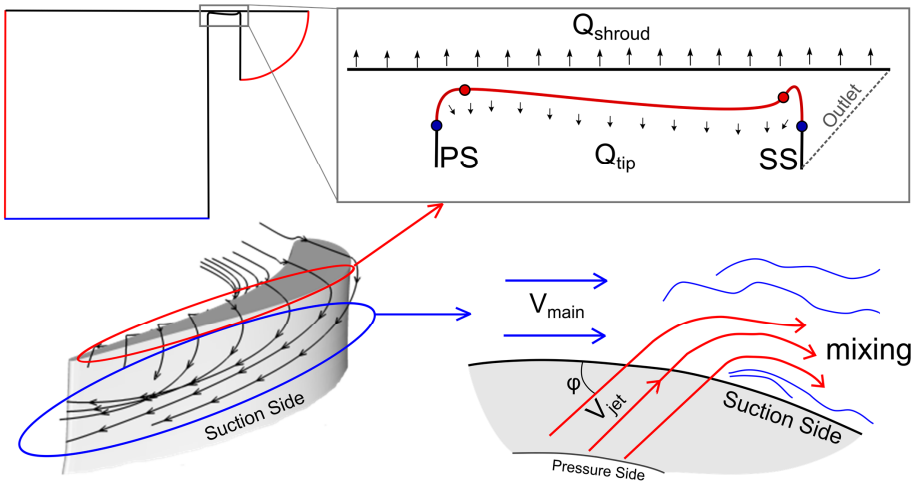

Figure 4.6: Evaluation of the performance parameters.

of both terms for the tip and shroud walls yields the overall performance parameter that budgets the heat load:

$$HT = \alpha\left(A_{sh}Q_{sh}^{AVE} + B_{sh}Q_{sh}^{RMS}\right) + \beta\left(A_{tip}Q_{tip}^{AVE} + B_{tip}Q_{tip}^{RMS}\right) \tag{4.1}$$

The weight factors α and β indicate the relative importance of the heat load generated on the shroud compared to the heat load experienced by the blade tip. The factors A and B weight the influence of the average and fluctuating heat flux on the global heat transfer parameter. It should be noted that since the computational domain is in the rotating frame of reference, the predicted (steady) heat flux spatial variations along the (stationary) casing correspond in reality to unsteady fluctuations periodic with the blade passage events. In this investigation, the heat load on the tip and shroud are assumed to be equally important. The tip section is generally more sensitive to large heat flux variations, therefore large peaks in the heat transfer should be reduced to a minimum. The selected weighting factors are summarized in Table 4.2.

The aerodynamic parameter accounts for the loss generated by the tip leakage flow. These losses can be quantified in terms of entropy production and are classified into

Table 4.2: Weight factors for the heat transfer performance.

Parameter	Tip	Shroud	**Parameter**	
A	0.3	0.5	α	1
B	0.7	0.5	β	1

two main categories: losses that are produced inside the gap and the losses generated by the mixing of the tip leakage flow with the mainstream. The contribution to the aerodynamic performance parameter of the gap loss is calculated by evaluating the entropy difference (Δs_{gap}) between the domain inlet and the exit of the tip gap region as defined in Fig. 4.6.

The rise in entropy produced by mixing of the leakage flow with the mainstream is estimated using the simplified theory of Shapiro [125]. The mixing process is modeled assuming the injection of a jet at a certain angle φ in a mainstream flow at a different velocity V_m, Mach number M_m and total temperature $T_{0,m}$ [11]:

$$\Delta s_{mixing} = C_p \left[\left(1 + \frac{\gamma - 1}{2} M_m^2 \right) \frac{T_{t,tip} - T_{t,m}}{T_{t,m}} + (\gamma - 1) M_m^2 \left(1 - \frac{V_{tip} cos(\varphi)}{V_m} \right) \right] \quad (4.2)$$

The jet flow quantities are mass flow averaged at the gap exit plane (Fig. 4.6). The mainstream flow values are taken to be the isentropic quantities calculated from the boundary flow conditions imposed in the 2D case. Based on 3D CFD simulations of the rotor stage, the injection angle φ generally varies between 50 deg and 90 deg. For this investigation, an average fixed value of 70 deg was assumed.

The global loss parameter is computed as the combination of the losses inside the gap (Δs_{gap}) and the losses due to the mixing (Δs_{mixing}) and can be expressed in terms of the total specific entropy rise Δs:

$$Loss = \dot{m}_{tip}(\Delta s_{gap} + \Delta s_{mixing}) = \dot{m}_{tip} \Delta s \quad (4.3)$$

4.2.2 Results

For all five tip flow regimes the optimization process was successful and individuals with superior aerothermal performances were found to lie on a Pareto front (Fig. 4.7).

Tip shapes that offer the best potential to minimize the loss parameter, the heat transfer or offer a trade-off in terms of aerothermal performance were selected for each tip gap regime from the database generated by the optimizer algorithm. The aerodynamics and the heat transfer associated to these superior geometries are investigated to explain the physics behind the enhancement of the tip gap flow.

The discussion will first focus on the results of the central case. Subsequently, the low and high speed flow regimes are presented and the flow analysis is carried out through visualization of the Mach number and turbulent production in the tip channel. Emphasis on the potential gain offered by tip shaping is given by comparison of the aerothermal performance budget of the best tip profiles against the flat tip configuration.

Central Case

The objective space for the central case is shown in Fig. 4.7, including the performance evaluation of a entirely flat tip. For ease of interpretion, both the loss parameter as well as the heat transfer parameter are non-dimensionalized using their respective flat-tip values. The geometries of the initial database (DOE) are characterized by a large scatter of the aerothermal performance. As the optimization proceeds, tip profiles are generated with both reduced loss and heat transfer parameters. Eventually, the optimized tip geometry population converges towards a Pareto front.

The Pareto front of Fig. 4.7 shows that a number of optimized tip geometries can offer ameliorated aerodynamic and heat transfer performances compared to the conventional flat tip case (blue square). The distribution of the tip profile performances shows that a significant reduction of the heat transfer parameter can be achieved by

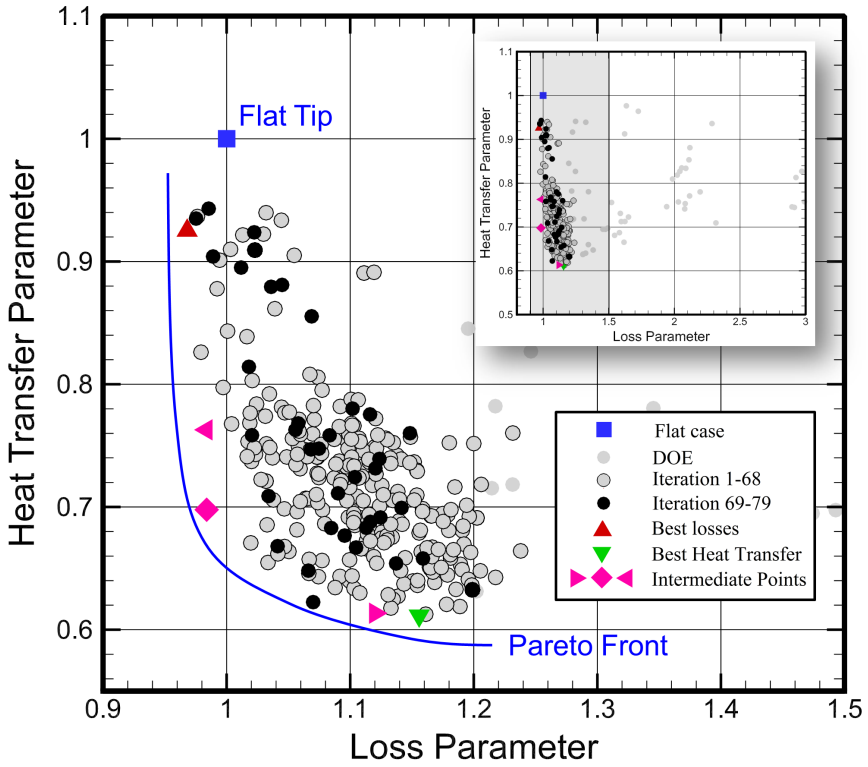

Figure 4.7: 2D objective space for the optimization of the central case and zoom into the relevant area.

tip shaping (∼40%), while only a little margin exists to decrease the losses associated with the flat tip geometry.

In order to analyze the flow topology involved with the optimization of the central case, a set of four tip shapes on the Pareto front was evaluated (Fig. 4.7): a nearly flat tip shape for the lowest losses, two geometries with intermediate performance and one case with the best heat transfer configuration. The gap flow structure on the selected tip profiles can be seen in Fig. 4.8a. This figure displays contours of the gap Mach number for the four geometries, together with the variation in turbulent viscosity in the tip gap for the best aerodynamic and intermediate profiles. The tip profiles are optimized for a M_{is}=1 and a blade width to height ratio of 15. At these conditions the flow reaches the transonic regime within the tip gap as shown by the middle-gap Mach number evolution of Fig. 4.8b-top.

Superior aerodynamic performance can be achieved by reducing the mass flow ingested by the tip channel and by concurrently minimizing the entropy production associated to the gap flow (see eq. 4.3). During the optimization process the new generations of tip profiles tend to adopt the smallest clearance necessary to minimize the mass flow inside the tip channel. The most efficient way to decrease further the gap mass flow is to create a throat at the channel entry through a sharp inlet corner. The tip boundary layer separates in the gap entry region and a small recirculation bubble is formed. This flow structure serves to lower the discharge coefficient by limiting the effective area of the gap orifice (top profile in Fig. 4.8a). However, the separation bubble gives rise to additional mixing losses induced by an increase of turbulence production [126], Fig. 4.8a. Through radiusing of the pressure side corner (e.g. the two intermediate cases), the bubble height reduces and a larger mass flow enters the gap. However, the corner radiusing has a beneficial effect on the aerodynamics since the specific entropy rise in the gap is attenuated. Fig. 4.8b-bottom displays the performance budget associated with the best tip geometries (here only the mid-bottom intermediate profile (diamond symbol) is considered) relative to the performance of the flat tip. The bar plot shows that the loss parameter is mostly controlled by the gap mass flow and to a less extent by the gap entropy generation and mixing loss. The effect of the tip geometry on the relative (to the flat tip case) variation of mass flow and entropy rise is illustrated in Fig. 4.9. The flat tip configuration guarantees a low gap mass flow (large bubble height), but is not optimal in terms of gap loss generation. The best aerodynamic performance is achieved by the tip profile with a small pressure side corner radius which helps to maintain a large bubble height (only 2% of mass flow more than the flat tip case) while keeping a low gap loss level. However, any further reduction in tip gap loss (through optimum radiusing) is overcompensated by the large increase in mass flow which deteriorates the overall loss parameter. On the contrary, the mixing losses are rather insensitive to the gap mass flow as the structure of the exit flow is largely

determined by the gap pressure ratio and the outlet gap area (sonic flow speeds at the gap exit).

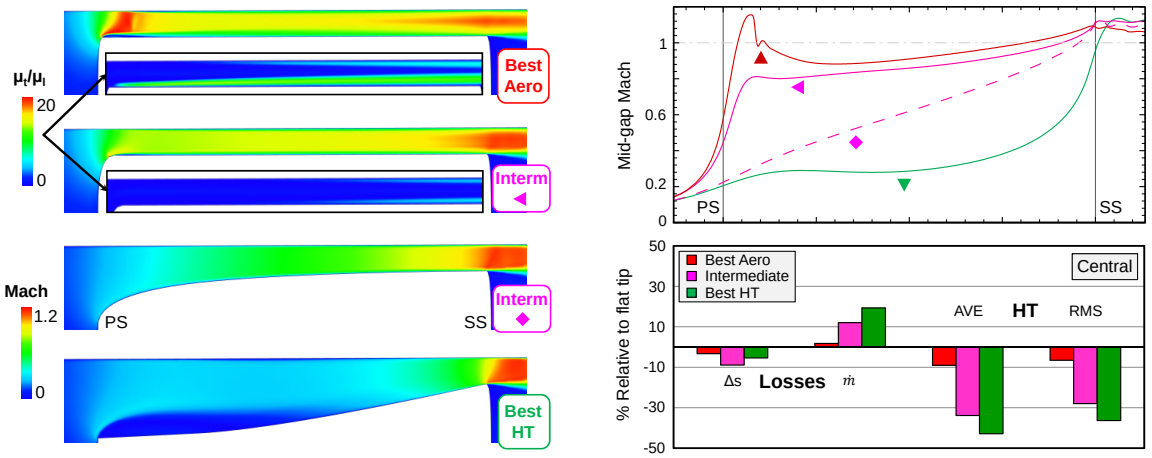

(a) (b)

Figure 4.8: Mach number and turbulent viscosity contours (a), mid-gap Mach number evolution (b-top) and performance budget (b-bottom) of optimal tip profiles for the central case.

The performance balance in Fig. 4.8b-bottom shows that significant improvement in the heat transfer parameter can be achieved by tip contouring at the price of a relatively small loss penalty. When the geometric throat is situated at the entry gap section (flat tip or small radius pressure side corner), the flow undergoes a strong acceleration over a short length around the tip separation bubble (Fig. 4.8b-top, upper and mid-upper profiles). Downstream of the bubble, the flow speed variation along the blade width is very moderate and sonic velocities are reached near the gap exit. The low acceleration rates combined with high levels of turbulent mixing results in large surface heat transfer as already observed by Wheeler et al. [46]. Based on this consideration, it is not surprising that the flat tip geometry presents the largest heat transfer parameter (see the Pareto front in Fig. 4.7). In order to minimize the heat flux levels, the tip shape must be contoured such as to maximize the local pressure gradients over the blade width. The management of the tip and shroud heat transfer is achieved by moving the minimum channel area towards the suction side

corner. This situation can be observed for the intermediate and the best heat transfer tip geometries (Fig. 4.8a). In the upper intermediate case the separation bubble is almost vanished, the sonic throat is located at the gap exit and the boundary layer development along the channel ensures a continuous acceleration. However, this gap configuration implies a detrimental effect on the aerodynamics since the exit sonic throat cannot be exploited to reduce further the discharge coefficient. For the lower intermediate case, the tip profile assumes the shape of a subsonic nozzle with a large pressure side corner radius (convex curvature) which guarantees a smooth and constant flow acceleration from M∼0.2 up to M∼1 along the tip channel, Fig. 4.8b-bottom.

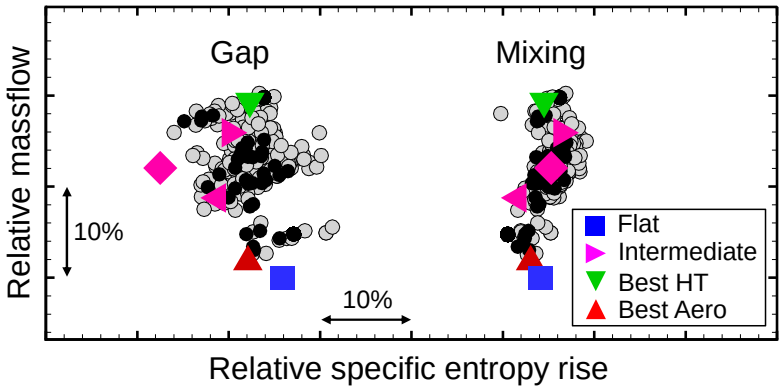

Figure 4.9: Specific entropy variation versus gap mass flow relative to the flat tip geometry.

The largest reduction in wall heat flux is obtained by a convergent nozzle with a concave tip wall curvature and a sharp inlet corner (bottom profile of Fig. 4.8a). This geometry generates a large flow recirculation in the front part of the channel which helps to insulate the tip surface. Downstream of the reattachment point the flow accelerates up to the exit section. The convergent nozzle tip shape (concave curvature) offers a potential reduction of the average heat flux levels up to 43% with respect to the flat tip profile. Additionally, the subsonic nature of the flow is characterized by low heat transfer fluctuations within the gap, opposed to the larger pressure gradients found in transonic tip flows with intense shock-boundary layer

interactions (best aerodynamics case). The heat flux variations for the superior heat transfer profile were observed to drop by 36% compared to the flat tip value, Fig. 4.8c.

Lower Left Case

This overtip flow regime simulates a thin rotor section subjected to a low blade load. All the optimized tip shapes that lied on the final Pareto front were characterized by a knife-edged profile. This tip geometry guarantees the concurrent betterment of the aerodynamic and heat transfer parameters with respect to the flat tip case. The Mach number contour plots in Fig. 4.10a display the flow structure of the flat tip (left plot) and of the optimized knife-edged tip (right plot). Since no significant difference was observed among the best individuals in terms of tip shape or flow structure, only the intermediate optimized geometry is reported in Fig. 4.10a.

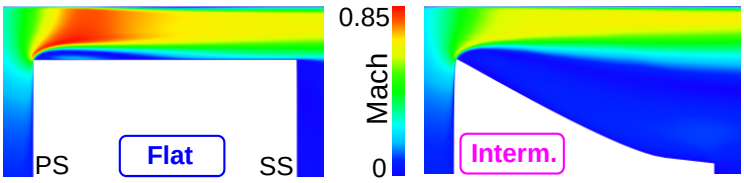

(a)

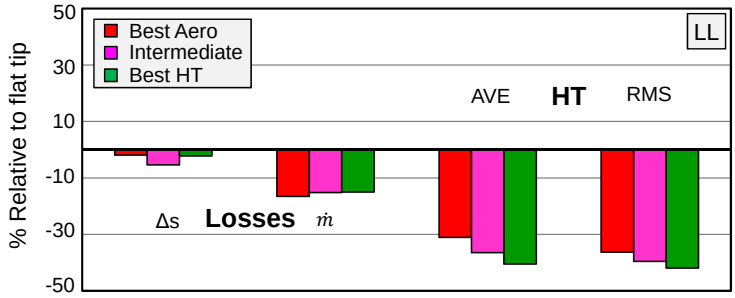

(b)

Figure 4.10: Mach number contours for the flat tip geometry and intermediate optimum shape (a). Performance budget of optimal tip profiles for the lower left case (b).

The flow field remains fully subsonic within the gap for all tip shapes. Therefore, the aerodynamic losses are mainly driven by the amount of ingested mass flow. As shown by Booth [127] for an unshrouded blade configuration, a knife-shaped profile provides an effective way to reduce the tip gap discharge coefficient. The performance budget in Fig. 4.10b indicates that an additional 15% reduction in mass flow could be attained using the knifed-edge geometry instead of the plain tip profile. On the other hand, the results point out that there is little room for further aerodynamic improvement through the reduction of the gap and mixing losses. Moreover, the knife-edged geometry causes the flow to completely detach from the tip surface providing a beneficial thermal insulation effect in this area, that causes a significant reduction in the heat transfer parameter (between 30% and 40% of the flat tip value). This configuration is also frequently used as a sealing mechanism in shrouded bladings [128].

Upper Left Case

This situation is representative of a lowly loaded front section of a turbine blade. Similarly to the previous cases, the Mach number and the turbulent contours plots are presented in Fig. 4.11a for three superior tip shapes. The geometry which performs the best in terms of losses presents a squealer-like configuration. A long separation bubble is created by a sharp pressure side corner which also serves to increase the bubble height, thus the gap discharge coefficient diminishes. Due to the relatively large blade width, the flow eventually reattaches on the tip wall and smoothly reaccelerates up to the suction side edge, driven by the gap pressure difference and the convergent geometry in the aft part of the channel. This geometry can be regarded as to be similar to a squealer-like tip treatment where the rim width is sufficiently small to avoid the flow reattachment and provide a further reduction in mass flow. On the other hand, this profile has very poor thermal performances, even worse than in the case of a flat tip gap (see Fig. 4.11b).

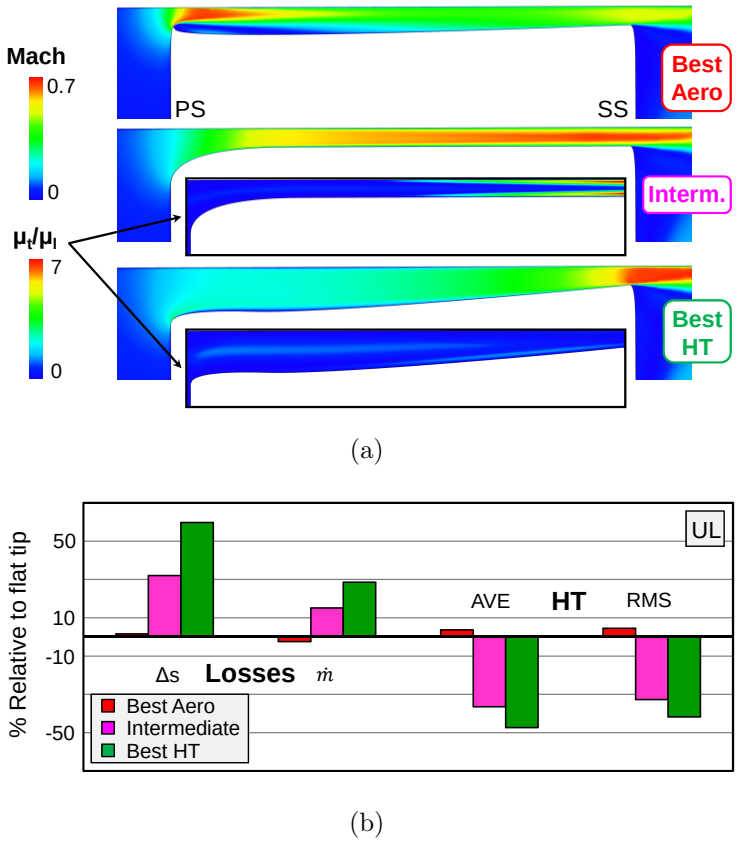

Figure 4.11: Mach number and turbulent viscosity contours (a) and the performance budget (b) of three optimal tip profiles of the upper left case.

As already observed for the central tip flow regime, the most effective way of reducing the overtip heat transfer is to shape the tip wall as a convergent nozzle with concave curvature. This allows abating the total heat transfer levels by as much as 50% compared to the flat tip case.

Upper Right Case

This case is the first of two optimizations performed on a highly loaded tip section ($M_{is} = 1.4$) characterized by supersonic flow velocities within the channel. The Mach number contours, shroud heat transfer and budgeting of the performance are

presented in Fig. 4.12a and b respectively for the tip channel with a width-to-gap ratio of 25.

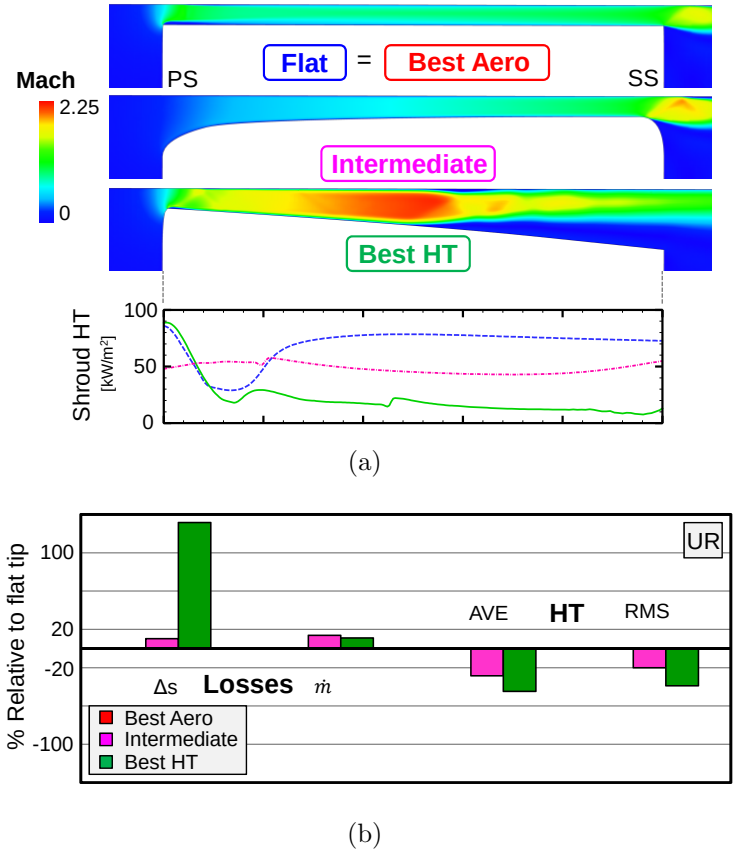

Figure 4.12: Mach number contours (a-top), shroud heat transfer evolution in the tip gap (a-bottom) and the performance budget (b) for three optimal tip profiles of the upper right case.

The results of this optimization case revealed that actually the flat tip geometry offers superior aerodynamic performance even though the separation bubble size is significantly reduced by the transonic flow speed and additional shock losses affect the tip channel (Fig. 4.12a, top). The sonic throat is located near the pressure side corner and the flow velocity keeps below Mach 1 in most part of the gap channel. Only a slight reacceleration is observed in the gap exit region. The flat tip channel flow results in a reduction in gap mass flow of 14% compared to the intermediate profile with a convergent passage geometry. The tip shape with the lowest heat

transfer parameter uses a sharp inlet curvature to generate a small separation bubble in the pressure side corner. This sealing mechanism is more efficient than the one adopted by the intermediate tip profile to reduce the mass flow ingestion. However, the divergent passage causes an overexpansion of the fluid to supersonic speeds (M > 2) and the flow undergoes a recompression process along the duct to readapt to the exit flow conditions. Consequently, the entropy production rises tremendously due to the strong shock activity within the channel (Fig. 4.12b).

From a heat transfer point of view, the analysis of the optimized profiles indicates that at high blade loads it is advantageous to steeply accelerate the flow to supersonic speeds in the tip gap, rather than maintaining a subsonic flow in the channel with the throat located near the suction side region (see the intermediate case). Expansion of the gap flow to supersonic speed provides an additional drop of the heat transfer levels by 16% with respect to the intermediate tip profile. The origin of the thermal benefit is explained by presenting the heat transfer evolution on the shroud wall (Fig. 4.12a-bottom). Both the flat tip and the optimized tip cases with divergent gap geometry show a heat transfer reduction due to the steep flow acceleration downstream of the corner separation bubble. Thanks to the strong flow acceleration to supersonic velocities, the heat transfer in the rest of the channel remains significantly lower than for the flat and convergent tip shapes.

Lower Right Case

This case is representative of a highly aft-loaded thin turbine blade. The large pressure ratio set across the tip gap induces a supersonic flow regime within the tip channel. Fig. 4.13a shows the predicted Mach number distribution of two tip profiles with superior aerodynamic (left plot) and thermal performances (right plot) respectively.

Excellent aerodynamic performances are achieved by adopting a tip profile with a sharp pressure side corner and a diverging tip passage with a smooth convex cur-

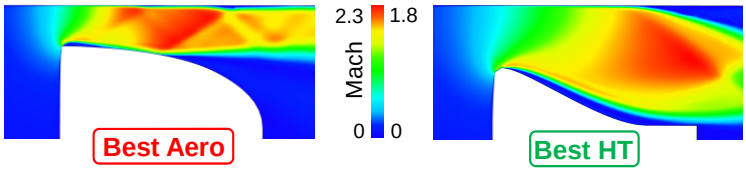

(a)

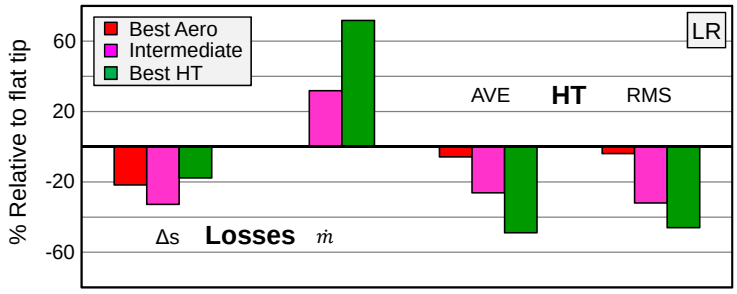

(b)

Figure 4.13: The Mach number contour (a) and the budgeting compared to the flat tip (b) for the lower right case.

vature. The budget of the aerothermal performance presented in Fig. 4.13b shows that this tip profile ingests the same mass flow as the flat tip geometry. The sharp pressure side edge generates a separation bubble whose height is of similar magnitude to the one featured by the flat tip profile. Downstream of the reattachment point, the flow expands along the diverging tip channel and eventually separates from the tip surface. This mechanism allows the gap static pressure to adapt to the imposed back pressure. Even though the separated region has a detrimental effect on the aerodynamic performance, the total entropy production is reduced by 22% with respect to the flat tip case, at the price of a slight increase (6%) in heat transfer parameter.

A tip profile with a rounded pressure side knife followed by an open tip channel provides the best geometry for thermal performances. Downstream of the pressure side rim, the flow separates and the bubble length covers almost the entire tip wall. Due to the area increase along the tip gap, the flow accelerates to supersonic speeds within the channel. For this profile both the tip and shroud average heat drop by 50% compared to the flat tip case. Furthermore, this tip shape allows for an effi-

cient expansion process within the gap resulting in entropy generation levels similar to the ones found for the best aerodynamic profile. However, since the minimum clearance is not reached, the gap mass flow is considerably higher than for the optimum aerodynamic profile. Therefore, a significant increase in aerodynamic penalty is observed.

Tip Flow Regime Comparison

Fig. 4.14 presents a comparison of the aerodynamic and heat transfer performances of the optimal tip shapes identified for each investigated flow regime. The aerothermal parameters of the optimal profiles are normalized by the values predicted for the corresponding flat tip geometry.

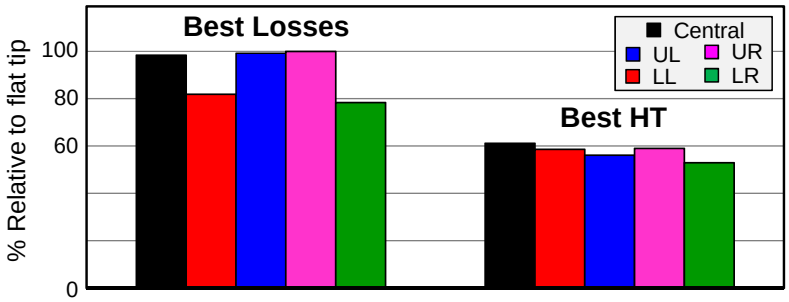

Figure 4.14: Aerodynamic and heat transfer parameters for each tip flow regime relative to the flat tip case.

The right part of Fig. 4.14 clearly shows that a significant betterment of the overtip heat transfer can be obtained through appropriate tip contouring at all tip flow conditions. The optimization results suggest that a potential reduction of 40% in total heat load can be targeted for every simulated flow regime. The abatement of the heat transfer levels is generally achieved through continuous acceleration of the flow within the tip channel and by application of contoured profiles.

For a relatively thin blade (case LL and LR), tip contouring can provide up to 20% loss reduction compared to a conventional flat tip. This aspect is of particular

interest for the optimization of HP turbine rotors which are typically highly loaded in the aft part of the profile. The optimization results showed that the aerodynamic performance of relatively thick blades can potentially be enhanced by 1-2% through a slight radiusing of the pressure side corner or by adopting a squealer-like geometry, depending on the blade load. Although this might appear as a small change compared to the heat transfer situation, it should be noted that the penalty associated to the tip leakage flow usually accounts for about one third of the overall stage loss.

The results of the optimization process are used to investigate the effect of the gap flow regime onto the aerodynamic performance of optimized tip shapes for a fixed blade width.

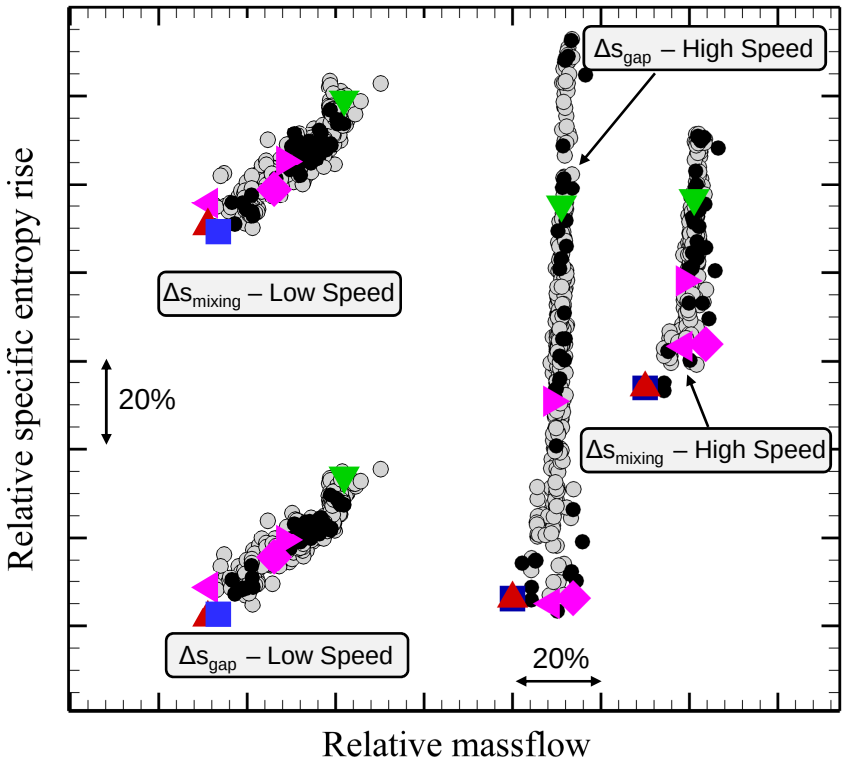

Figure 4.15: Specific entropy rise versus gap mass flow, relative to the flat tip case for large blade width ($w/h = 25$) at low ($M_{exit} = 0.6$) and high ($M_{exit} = 1.4$) speeds.

As shown in Equation (4.3), the specific entropy rise can be decoupled into the losses generated inside the gap and losses due to the mixing with the mainstream.

Both contributions (i.e. respectively Δs_{gap} and Δs_{mixing}) for each of the simulated tip profiles with the largest width to height ratio (w/h=25, case UL and UR) are plotted against the gap massflow in Fig. 4.15. The different quantities are normalized by the performance of the corresponding flat tip geometry. It is important to note that similar trends as the ones displayed in Fig. 4.15 were also observed for the low width-to-gap ratio cases which are therefore not reported.

In the subsonic regime (Fig. 4.15, left) both the loss contributions show a strong correlation with the amount of mass flow ingested by the tip gap. On the contrary, when the tip gap flow becomes transonic or supersonic, the specific entropy production shows a larger scatter and the effect of the massflow rate has almost vanished. Interestingly, the relative difference in loss generation between the best aerodynamic profile and the one with best thermal performances in the high speed case is about two to three times larger than the difference observed in the subsonic case.

The present comparison helps to emphasize the high potential of tip-shaping for the high speed regimes. In contrast to the subsonic speed case where efficient tip designs can be achieved through minimization of the effective throat size (i.e. reducing the mass flow), high speed gap flows also demand for an efficient design of the tip channel contour.

4.3 3D Verification of Contouring Potential

In this section, the previously obtained optimal 2D profiles will be used to construct a fully carved 3D profile in order to verify the quasi-3D optimization approach.

4.3.1 Creation of the Fully 3D Carved Blades

Computational Domain and Tip Geometries

The numerical study replicates the high-speed turbine rotor previously installed at the von Karman Institute compression tube rig and studied in chapter 3. The high-speed rotor operates at a Reynolds number of 550,000 with an exit relative Mach number of 0.9. Relevant specifications of the meshed rotor blade are listed in Table 4.3 and further details on the baseline rotor geometry are given in [108]. The computational domain models a single airfoil with periodicity along the tangential direction. The inlet is positioned about one rotor chord upstream of the rotor leading edge (LE) and the outlet section extends 2 axial rotor chords downstream of the blade trailing edge. A sketch of the computational domain is shown in Fig. 4.16.

Table 4.3: Main turbine specifications.

Parameter		
Reynolds number based on rotor outlet	-	5.5 x 10^5
Blade count	-	64
Design rotational speed	rpm	6790
Design tip clearance h (% of span)	-	1%
Rotor pressure ratio ($P_{0,in}/P_{s,out}$)	-	2.91
Tip peripheral speed	m/s	280
Tip absolute inlet Mach number, M_{in}	-	1
Tip relative outlet Mach number, $M_{r,out}$	-	0.9
Rotor relative inlet flow angle	deg.	∼32
Rotor relative exit flow angle	deg.	∼-62
T_{gas}/T_w	-	∼1.6

Four different tip shapes were analyzed. The performance of two conventional blade tip shapes, a flat tip ($FLAT$) and a squealer type geometry (SQ), are compared

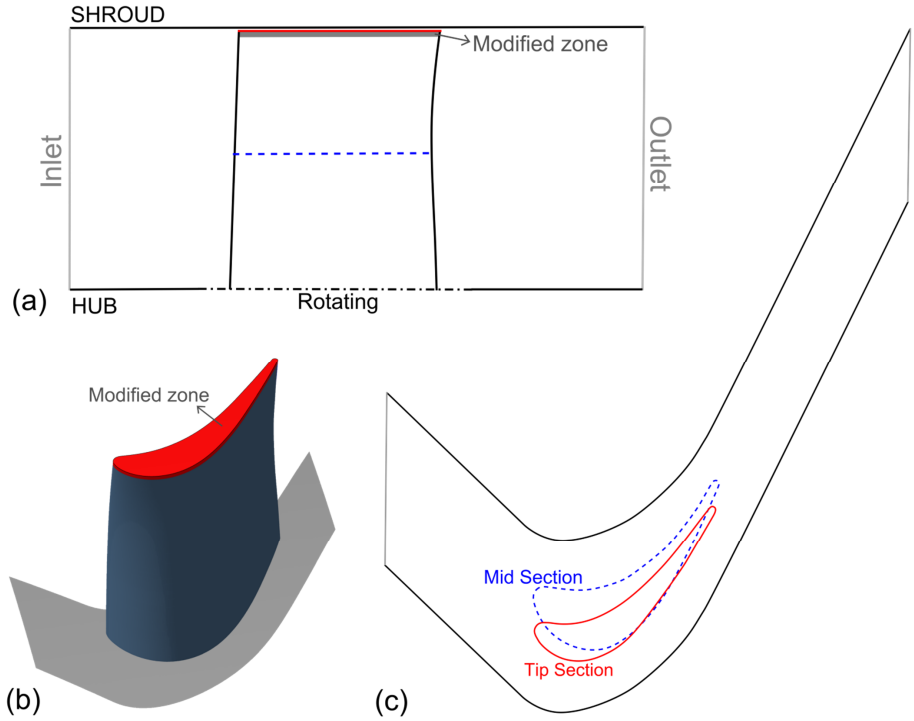

Figure 4.16: Detailed view of the computational domain.

with the two fully contoured designs (*HT* and *AERO*). All the investigated tip designs were run at the same minimum clearance, i.e. 1% of the blade height (h). For the carved geometries, the tip shape was only modified over a height equal to 2% of the blade span (Fig. 4.16b), identical to what was allowed throughout the quasi-3D optimization (section 4.2).

Fig. 4.17 displays a detailed view of the investigated tip geometries including the successive cross sections sliced up along the rotor airfoil chord (a, b, c, ..., f). The squealer type geometry is representative of commonly used industrial designs, a trade-off between mechanical durability, machinability and aerodynamic performance. The rim length and cavity depth are set as 1.2 and 2.4 times the minimum clearance respectively.

A convergent section from pressure to suction side characterizes the front part of the *HT* design. Close to the leading edge (profile 'a' in Fig. 4.17) the contraction mainly takes place in the last 50% of the tip gap. A smooth convergent passage

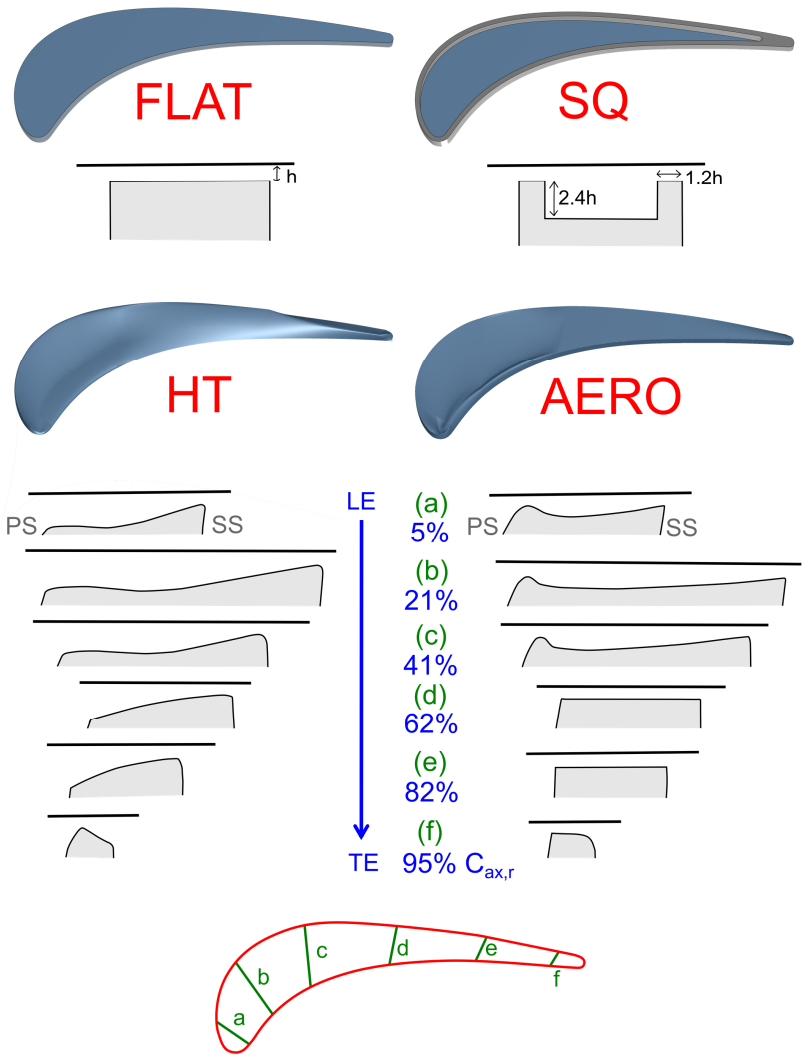

Figure 4.17: Geometrical cut sections for the evaluated tip shapes.

is chosen for the mid part of the blade; while in the aft section of the blade, a convergent-divergent nozzle is created throughout the over tip passage.

By contrast, the *AERO* design presents in the front part a first throat near the pressure side. This is followed by a divergent and slowly converging passage. The blade's mid section adopts a nearly flat shape, which then evolves towards a fully divergent passage in the aft section. All the optimal tip profiles used to construct the

two carved blade tip geometries assume the minimum tip clearance at least at one point along the 2D section.

The prospective aero-thermal performances of the carved three-dimensional tip geometries are summarized in Table 4.4. The table presents the relative variations of the 2D optimal profiles relative to the flat tip, considering the losses ($\Delta\omega$), tip and shroud heat transfer (ΔQ_{tip} and ΔQ_{sh}). The entire length of the pressure side rim (PS rim length) was used to weight the contributions of the optimized 2D tip profiles to the global performances of the reconstructed 3D geometry. Sections a, b and c, are located in the 40% front part of the pressure side rim, therefore their performance gains are weighted 40%. In turn, section f, occupies 26% of the rear pressure side, therefore, the 2D loss and heat load contributes 26% to the overall figure of merit listed in the row with the 3D blade data. The *HT* rotor is expected to deliver a significant reduction in heat transfer (ΔQ_{tip} ∼-38%) compared to the 3D flat tip blade, at the price of poor aerodynamic performance ($\Delta\omega$=+2.4%). The performance budget anticipates that the *AERO* airfoil will perform similarly to the *FLAT* tip with just a tiny gain in aerodynamic loss ($\Delta\omega$=-0.5%) and almost no variation in thermal loads.

Table 4.4: Performance breakdown for 2D optimal profiles from section 4.2 [2], and expected output for the reconstructed 3D carved blades (bold).

	HT				**AERO**			
Tip shape	PS length[1]	$\Delta\omega^2$	ΔQ_{tip}	ΔQ_{sh}	PS length[1]	$\Delta\omega^2$	ΔQ_{tip}	ΔQ_{sh}
a+b+c	40%	+1.3%	-25.6%	-55.0%	40%	-0.1%	+4.9%	+2.7%
d+e	34%	+2.5%	-33.3%	+13.7%	42%	-0.2%	-3.3%	+1.7%
f	26%	+4.1%	-63.7%	-30.4%	18%	-2.2%	-9.1%	-1.7%
3D blade	-	**+2.4%**	**-38.0%**	**-25.1%**	-	**-0.5%**	**-1.1%**	**+1.5%**

[1]Percentage of the total PS rim length.
[2]Loss variation with respect to the *FLAT* tip design.

Mesh and Solver Settings

Due to the complexity of the overtip geometry, the computational domain was discretized with an unstructured hexahedral mesh using Numeca Hexpress. To accurately retrieve the spatial distribution of the heat transfer, a total amount of cells between 11.9 and 13.6 million was utilized. Over 100 span-wise divisions were made along the rotor blade channel height. To sufficiently resolve the overtip flow, a minimum amount of about 40 cells was imposed in the gap radial direction. To ensure an accurate prediction of the wall heat transfer, the first cell thickness was selected to result in y^+ values below 0.5.

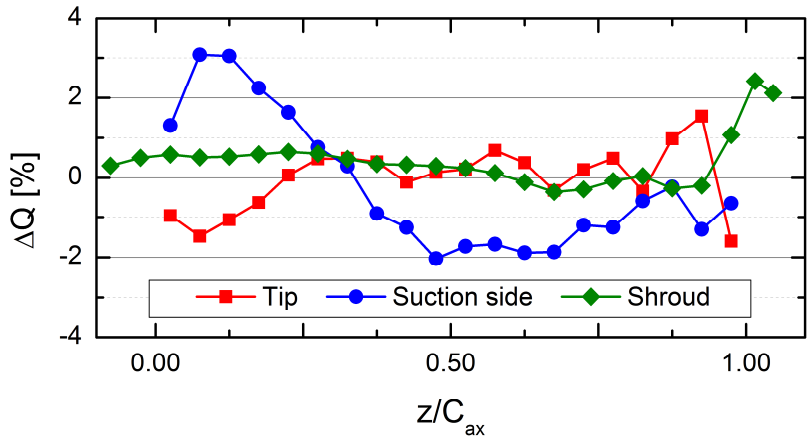

Figure 4.18: Difference in heat transfer (ΔQ) onto the tip, SS (upper 25%) and the shroud between the medium and fine mesh solution.

To ensure grid insensitivity, 2 additional grids were created for the *HT* profile: a 'coarse' (5.8 million cells) and 'medium' (7.8 million cells) grid besides the used 'fine' grid (12.4 million cells). Fig. 4.18 shows the difference in heat transfer (ΔQ) along the rotor axial chord between the medium and fine mesh solution (in % of the fine grid prediction). These differences give rise to a total difference in heat load of 0.009%, 0.38% and -0.37% for the tip, shroud and upper 25% of the blade suction side respectively. Table 4.5 presents the grid convergence index (GCI) and apparent order (p), evaluated through the standard procedure reported by Celik et al. [129], for the

relevant aerodynamic parameters. The approximate relative error e_a is also reported in Table 4.5, i.e. the difference between the medium and the fine grid solution in percentage of the fine grid solution. Based on this analysis, the finest grids were deemed to be sufficiently accurate and thus, these settings were adopted to construct similar meshes for the *AERO*, *FLAT* and *SQ* profiles. Fig. 4.19 shows a detail of the unstructured meshes employed for this investigation.

Table 4.5: Grid convergence study.

	ω	Massflow	$T_{0,50\%}$	P_{0r}
p	3.39	0.55	12.43	0.43
GCI^{21}_{fine} (%)	5.32	0.13	0.002	2.83
e^{21}_a (%)	2.89	0.009	0.007	0.16

The total flow quantities (P_0 and T_0) and the flow angle were imposed at the domain inlet together with the turbine static back pressure at the outlet plane. The steady state RANS equations were solved using the Numeca FINE/Open suite, adopting the Spalart-Allmaras model for the turbulence closure (cfr. section 2.1). The validation of the solver can be found in section 2.2. Additionally, the unsteady effects due to stator-rotor interactions [42] or non-uniform inlet flow fields [130] were neglected in the current numerical experiments.

The inlet turbulent viscosity was set such that the inlet μ_t/μ_l was about 100. All the simulations were performed with isothermal walls at a gas to wall temperature ratio ($T_{0,in}/T_w$) of 1.57. Data reduction of the numerical database was eventually carried out with Numeca CFView and Tecplot.

4.3.2 Verification of the Quasi-3D Approach

The carved blade tip profiles were built optimizing the flat tip streamlines. The three-dimensional blade tip shape was therefore reconstructed assuming that the over-tip leakage flow still maintains a pronounced two-dimensional structure along the

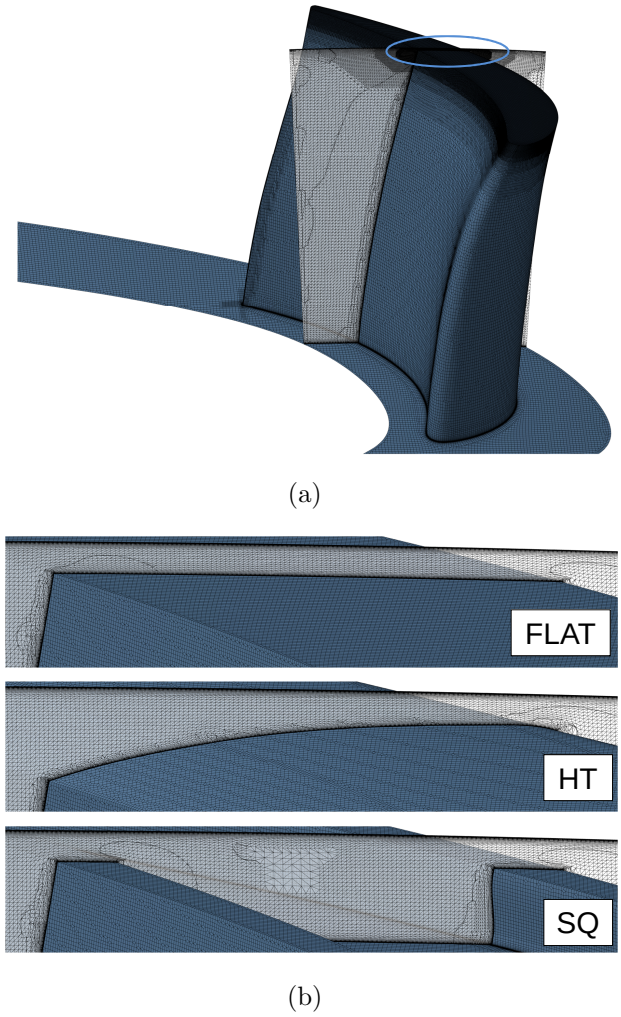

(a)

(b)

Figure 4.19: (a) Flat-tip rotor geometry and computational grid and (b) detail of the unstructured overtip mesh for different tip designs.

overtip gap streamlines. Fig. 4.20 compares the flow direction (relative flow angle, β) in the mid-gap plane for the investigated geometries. In particular, Fig. 4.20a displays the flow angle evolution along the tip camberline. The optimized carved 3D tip geometries (*AERO* and *HT*) exhibit a flow angle distribution along the machine axis very similar to the baseline flat tip design (*FLAT*). For the *AERO* profile, the flow direction appears to be offset by about 10 degrees in the front part of the blade, while in the rear part the flow angle distributions are matched (from $z/C_{ax,rot}$= 60% onwards). For the *HT* shape, the angle deviates about 30 degrees from the flat tip

case near the leading edge, but after 25% $z/C_{ax,rot}$, a quasi constant shift around 15 degrees is maintained. The contour plots in the overtip mid-gap (Fig. 4.20b-left) demonstrate that flow angle variations along streamlines that traverse the flat tip gap are low, i.e. in the order of 10 deg.

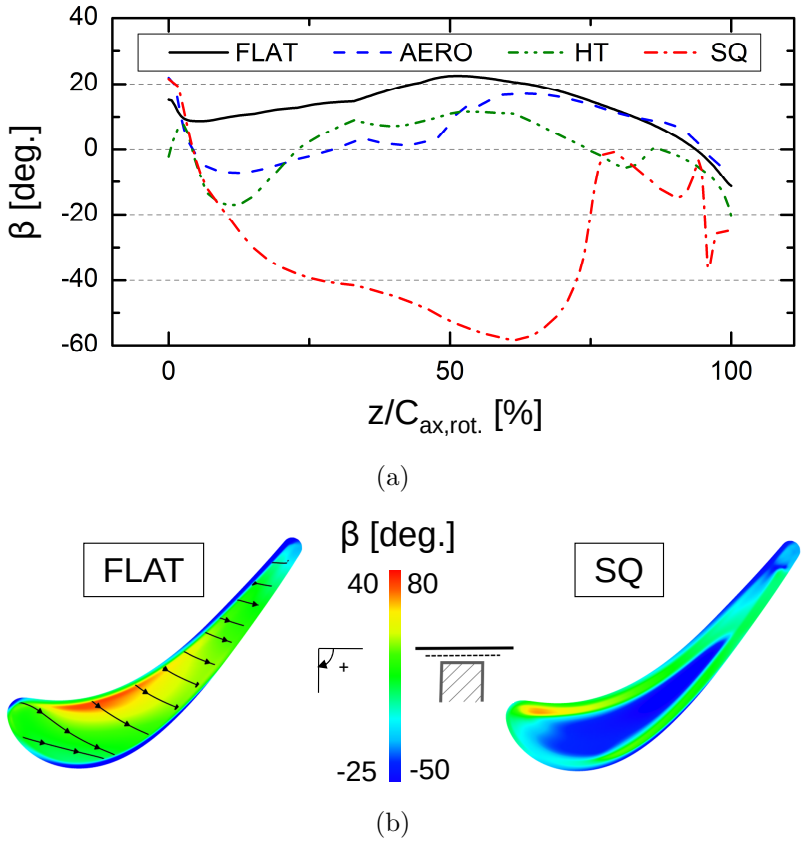

Figure 4.20: Midgap flow angle for the four investigated tip geometries: (a) variation along the midgap camberline and (b) contours of midgap flow angle for the flat and squealer blade tip designs.

By contrast, the flow angle evolution in the squealer tip configuration manifests a large discrepancy against the baseline flat tip case. Both the trends as well as the flow angle levels differ significantly along the entire blade chord. The flow angle immediately drops downstream of the blade leading edge and reaches a minimum value of almost -60 degrees at 60% of the axial chord. In the aft part of the squealer blade, between 70% of the axial chord and the trailing edge, the flow angle resembles

the *FLAT* design and exhibits smaller angle variations. The mid-gap flow angle contours for the squealer geometry (Fig. 4.20b-right) reveals the three-dimensional nature of the overtip gap flow introduced by the cavity.

Fig. 4.20 demonstrates that the streamline paths are generally maintained with respect to the plain blade tip geometry, which was used as baseline for the tip contour optimization. However, when the baseline tip geometry features complex 3D effects (e.g. squealer tip) associated to dominant 3D flow structures, the quasi-2D streamline approach is not anymore appropriate to model and optimize the overtip flow passage.

4.3.3 Overtip Flow Field

Fig. 4.21 presents the flow velocity field in the mid gap section for the different investigated cases. The contours show the relative Mach number distribution combined with Mach 1.0 and 1.2 isolines to highlight the supersonic regions. Additionally, the streamlines of the particles entering the overtip region in the middle of the gap are drawn to illustrate the leakage flow direction.

The overall flow pattern determined by the carved and flat tip geometries reveals similar features to the ones previously observed in the overtip flow angle evolution (Fig. 4.20). On the contrary, the streamlines for the squealer tip highlight a complex three-dimensional flow topology [22], generated as the fluid is entrained into the squealer cavity across the pressure side rim, while being accelerated. Due to the relative casing motion, the flow jet bends downwards heading towards the cavity floor, while a recirculating vortex develops attached to the pressure side rim. Due to the suction side rim and the effect of the relative casing movement, the flow aligns with the blade camberline before being compressed and ejected over the suction side rim to generate the tip leakage vortex. From 75% of the $C_{ax,rot}$, the cavity vortex fills up the whole squealer bath. There, the tip leakage traverses the rotor blade aligned with the axial direction driven by the gap pressure difference, producing a flow direction similar to the flat tip configuration. The described flow topology serves

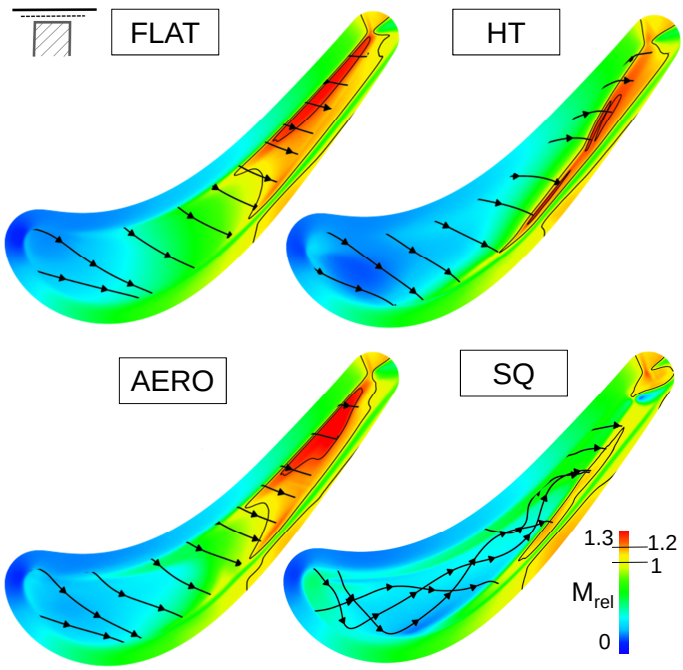

Figure 4.21: Relative Mach number distribution in the midgap section with overtip flow streamlines.

to explain the flow angle evolution in the front part of the squealer blade and the sudden angle increase observed around 70% of the blade camberline, Fig. 4.20a. This observation is in agreement with the flow velocity rise in the overtip channel of the rear blade part, Fig. 4.21.

The front part of the *AERO* profile adopts a contoured rim at the pressure side (Fig. 4.17, at sections a, b and c), which mimics a squealer tip section. Similar to the *SQ* profile, the flow detaches as it enters the tip gap from the pressure side rim, and is then pushed downwards by the relative casing motion. Lower relative flow angles are therefore observed in the mid-gap compared to the flat tip design as illustrated in Fig. 4.20a. The same conclusion can be drawn for the near leading edge region of the *HT* case, where the flow is entrained at the suction side, where it encounters a squealer-like rim.

Just downstream the PS rim in the front section of the contoured *AERO* case, the profile features a convergent channel from the PS to SS edge (squealer-like front-central part). This geometry promotes a slight smooth flow acceleration within the clearance over a larger portion of the front blade compared to the flat tip design. The *HT* profile on the contrary adopts in the mid-chord region a fully convergent channel from the PS to the SS. The flow only gets choked at the SS edge and therefore the gas velocity at the tip gap inlet (subsonic) is reduced compared to the tip entry speed found in the other tip profiles where the throat is located near the PS, Fig. 4.21. Additionally, due to the absence of a separation bubble at the PS rim, the effective overtip throat size is increased. Therefore, a larger mass flow crosses the overtip channel and the leakage fluid jet exits the tip suction side at increased velocities.

The Mach number distribution in the middle of the clearance for the flat and carved tip profiles shows that a considerable part of the aft overtip region operates in the supersonic regime. Indeed, the flat-tip overtip flow is choked at about 60% $C_{ax,rot}$, revealing gas velocities beyond M_r=1.2 over large regions of the tip channel. For the *AERO* case, a similar supersonic zone is present. However, due to the divergent channel in the aft part, the flow accelerates even further resulting in an extended supersonic flow region zone. The shaped geometry of the *HT* profile guarantees gradual and controlled flow acceleration all over the axial chord, and the gap passage becomes choked slightly upstream compared to the *FLAT* and *AERO* blades. Similarly, due to the overexpansion around the SS edge and to the presence of the divergent channel in the last section, the flow accelerates to Mach numbers above 1.2 as it exits the tip region. For the *SQ* geometry on the contrary, sonic velocities are confined only to a small region above the rear blade suction side where the flow is suddenly accelerated by the abrupt contraction imposed by the rim seal. The gap outlet jet velocity is significantly reduced with respect to the plain tip geometries.

4.3.4 Heat Transfer Signature

Fig. 4.22 compares the averaged heat flux in the carved tip profiles against the conventional flat and squealer tip geometries, onto the rotor tip (Fig. 4.22a), shroud (Fig. 4.22b) and suction side (Fig. 4.22c). The numerical data reported in the graphs are pitch-wise-averaged at discrete stations along the blade chord to yield values representative of the heat transfer evolution along the machine axis, and normalized by the total average heat load onto the flat tip. Additionally, the heat load distribution to the blade tip, rotor shroud and upper 25% suction side are presented in Fig. 4.23 for the investigated tip profiles.

On the tip surface, Fig. 4.22a, the squealer design unveils the highest average heat flux levels in the blade frontal part and over a limited region in the aft part. High levels of heat flux in the front part of the blade are generated by impingement of the vortical flow from the pressure side rim onto the tip cavity floor. In the rear part of the blade, enhanced thermal loads are found on the suction side rim of the squealer seal. Combined with a larger total wetted area (about 33% more than in a plain tip in the upper 2% of the blade span), the squealer geometry is subjected to significantly higher overall heat loads which demands for increased cooling rates.

The *AERO* tip design shows slightly larger heat transfer rates compared to the flat tip in the front-central part of the blade between 15% and 40% $C_{ax,rot}$ (Fig. 4.22a). A small recirculation bubble establishes downstream of the contoured pressure side rim forcing the flow to impinge on the tip endwall (Fig. 4.23). In the mid section, the *AERO* profile evolves towards a flat-like tip resulting in comparable heat load levels. However, the tip heat transfer is reduced near the blade TE (75%-100% $C_{ax,rot}$). In this region, downstream of the PS separation bubble created by the sharp PS edge, the fluid is accelerated along the divergent tip passage imposed by the carved profile up to the SS exit.

Overall, the *HT* profile demonstrates an abatement of the heat transfer levels over the entire rotor tip compared to a flat tip design, with reductions as large as

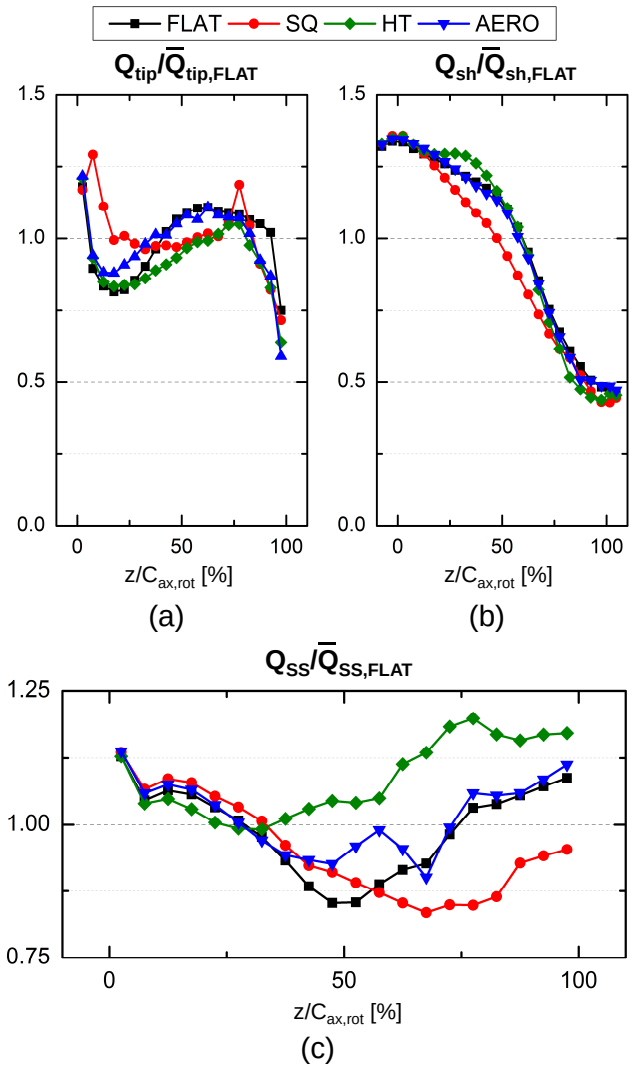

Figure 4.22: Tip (a), shroud (b), and upper 25% SS (c) heat transfer along the machine axis (fraction of flat tip average heat load (W/m^2)).

10% along the rotor chord. Between 25% and 70% of the rotor axial chord the HT design offers the best thermal performance compared to the other three investigated tip geometries. Additionally, the *HT* profile also serves to reduce the heat flux peaks observed in the LE region of the *FLAT* and *AERO* designs. However, the extent of the 'sweet' spot region in the front part of the blade [18] is reduced for both carved profiles with respect to the flat tip case as illustrated in Fig. 4.23. In the rear part the

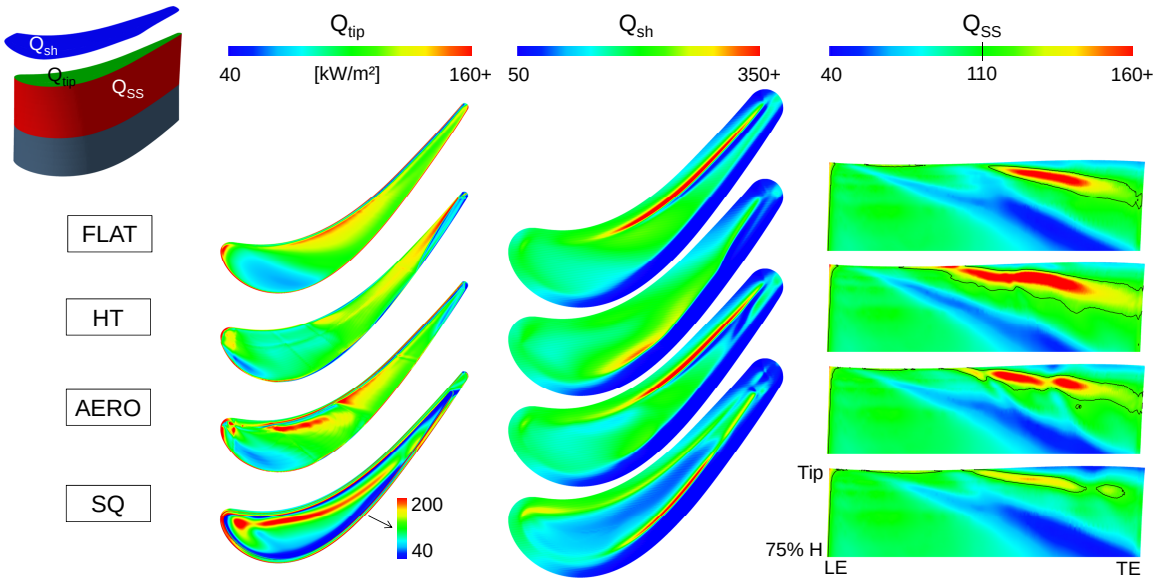

Figure 4.23: Heat transfer distribution onto the blade tip, shroud and upper 25% of the rotor SS.

HT blade presents tip heat transfer distributions similar to the *AERO* case, which result from analogous diverging tip shape designs.

On the stationary casing endwall, the pitchwise averaged heat transfer diminishes along the rotor chord by about 100%, Fig. 4.22b. This evolution is caused by the absolute flow temperature drop across the turbine as work is being extracted from the fluid. The squealer seal configuration (*SQ*) presents the lowest casing heat flux levels, furthermore a decrease of about 15% compared to the other tip geometries can be observed in the central region of the blade passage ($25\% < z/C_{ax,rot} < 75\%$), Fig. 4.23. The results suggest that the time-average casing heat transfer processes are mainly dependent on the sealing mechanism design (i.e. plain or squealer cavity geometry). Only minor differences in the casing thermal loads were detected when comparing the *AERO* and *FLAT* tips. By contrast, the *HT* profile contributes to a slight increase of the casing heat transfer in the mid-chord region (from 25% of $C_{ax,rot}$ to 45% of $C_{ax,rot}$) as enhanced heat flux levels are generated in the proximity of the tip suction side (Fig. 4.23). However, the *HT* design proves to reduce the heat

load slightly in the aft part, $z/C_{ax,rot} > 75\%$ (Fig. 4.22b). More importantly, the casing heat transfer contours in Fig. 4.23 show that the HT profile generates a more uniform thermal field compared to the other investigated tip shapes. In particular, the HT tip profile in the mid and rear part of the rotor chord helps to suppress the large casing heat fluxes associated to the flow acceleration around the sharp PS edges ($AERO$ and $FLAT$ tips) and to avoid the heat flux peaks at the SS rim observed in the SQ case. Thus, the HT design is capable to damp significantly the unsteady heat transfer peaks that the casing endwall undergoes at each blade passing event.

Fig. 4.22c presents the evolution along the machine axis, of the heat flux averaged over the upper 25% of the blade suction side. In the first 30% of the axial chord, the blade tip shape has a weak influence on the heat flux although the HT carved profile helps to reduce the heat load levels up to 10% with respect to the squealer design (see also contours in Fig. 4.23). Further downstream, the suction side heat transfer becomes strongly dependant on the overtip shape, which affects the aerodynamics of the tip leakage vortex and the development of the upper passage vortex. The heat transfer variations exhibit very similar trends over the rotor axial length. The suction side heat load decreases starting from the blade LE until the spillage flow, which has crossed the overtip gap, penetrates into the suction side blade passage. The average heat transfer then begins to rise up to the blade TE. For the HT profile the minimum suction side heat transfer is found at $z/C_{ax,rot}$=30%. The SQ tip geometry shows the lowest heat transfer levels up to the blade TE, and the effect of the tip leakage vortex on the SS heat transfer becomes significant only in the rear blade passage starting from $z/C_{ax,rot}$=65%. The $AERO$ and $FLAT$ tip shapes present an intermediate situation where the minimum suction side heat transfer is found around mid-chord. However, in the case of the $AERO$ profile, the rise in heat transfer in the aft part is not monotonous. The sudden drop in heat load at around $z/C_{ax,rot}$=70% is due to the abrupt variation in the tip shape profile occurring at around this axial position (Fig. 4.17, i.e. from squealer-like to flat).

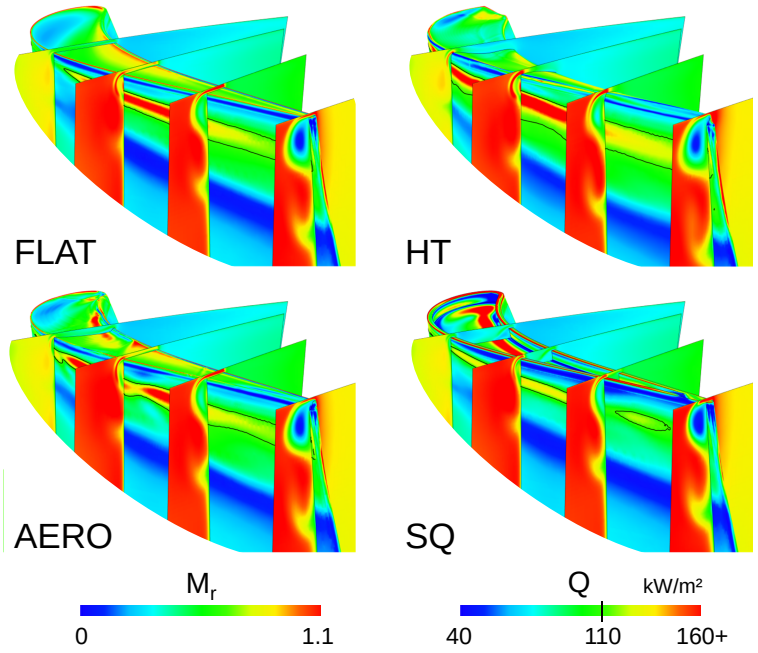

Figure 4.24: Relative Mach number contours in four planes normal to the blade SS and rotor heat transfer.

To further illustrate the coupling of the overtip flow and rotor passage aerodynamics with the heat transfer, Fig. 4.24 presents the relative Mach number contours in four planes perpendicular to the blade suction side, together with the blade surface heat flux. The design of the front tip section is fundamental to control the development of the passage vortex inside the rotor passage. The tip leakage flow generated in the frontal part of the *HT* rotor has slightly the highest SS exit velocities. Thus, the passage vortex that forms at the blade LE is pushed downwards and its size increases more rapidly than for the other three tip shapes, which is related to the reduction in the heat transfer displayed by the HT profile in the front SS, Fig. 4.22c.

Regions of enhanced heat transfer can be found where the tip leakage vortex impinges on the suction side after rolling off from the overtip gap (Fig. 4.23 and Fig. 4.24). The rim-type design (*SQ*) reduces the overtip mass flow and suction side exit velocities. Consequently, the tip leakage vortex core is weaker and closer to the blade wall, leading eventually to a reduction of the suction side heat transfer of more than

10% compared to the flat tip. The *HT* shape allows for higher spillage mass flows compared to the other plain tip shapes due to the absence of a sharp edge separation bubble at the minimum clearance tip section. A strong tip leakage vortex builds up along the rotor passage and the resulting vortical flow structure impinges with higher momentum onto the blade suction side. This consequently generates a wider region of enhanced heat transfer compared to the other evaluated cases from about 30%$C_{ax,rot}$ up to the blade TE, Fig. 4.23.

The squealer tip design offers the best sealing strategy to simultaneously limit the momentum of the tip leakage fluid and reduce the heat loads in the aft part of the rotor suction side.

4.3.5 Global Rotor Performance

Fig. 4.25 describes the rotor outlet flow field with contour plots of relative total pressure and of vorticity magnitude for the upper 50% of the rotor span. The outlet conditions are evaluated in a plane located 50%$C_{ax,rot}$ downstream of the rotor trailing edge. To allow for a direct comparison amongst the different cases, two isolines are drawn. The total pressure contours provide an estimate of the overall aerodynamic losses, while the vorticity field represents the flow non-uniformity at the inlet of a downstream turbine stage.

Distributions of the pitch-wise averaged relative total pressure and vorticity, normalized by the flat tip average value are presented in Fig. 4.26. The radial profiles depict the penetration of the tip leakage and highlight the difference in secondary flow structures for the four tip designs. Overall, the results show that only minor dissimilarities exist in the rotor exit flow field between the four simulated tip profiles (Fig. 4.25) and that blade to blade variations are limited to the upper 50% of the rotor span (Fig. 4.26). The overall outlet flow field is essentially unaffected by the tip geometry but some distinct flow features are observed.

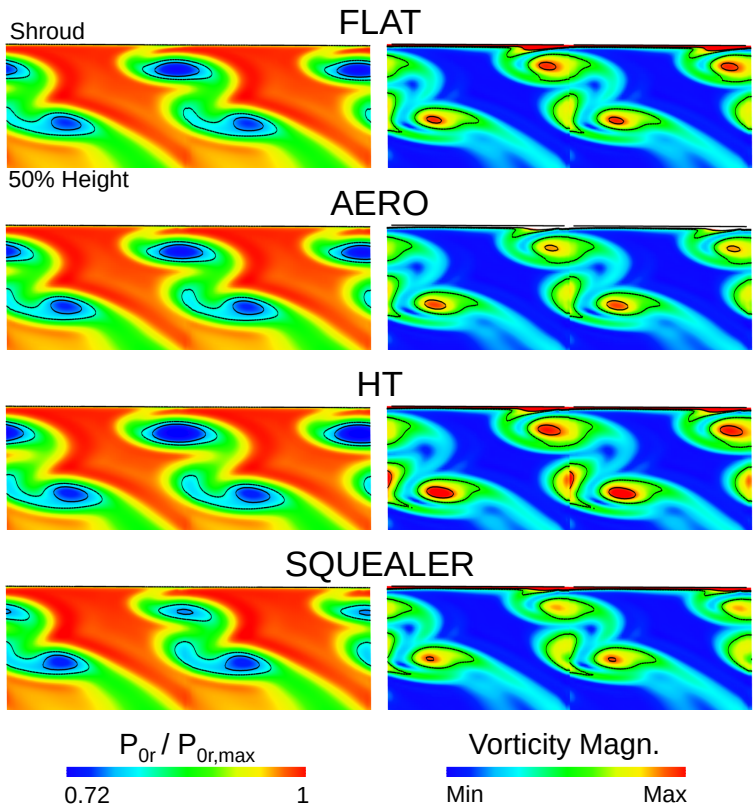

Figure 4.25: Total pressure and vorticity magnitude contours for the four tip geometries, $0.5C_{ax,rot}$ downstream of the rotor trailing edge.

The squealer tip seal mechanism contributes to significantly reduce the intensity of the downstream vortical structures: the tip leakage vortex and, to a lesser extent, the upper passage vortex intensity are diminished in comparison to the flat and carved tip rotors. The squealer geometry serves to reduce the jet flow speed at the suction side rim outlet. As such the strength of the tip leakage vortex is weakened as it develops along the rear blade suction side (Fig. 4.24, Fig. 4.25-right, Fig. 4.26-right) and also the associated pressure deficit is significantly attenuated (Fig. 4.25-left,Fig. 4.26-left). The total pressure contours in Fig. 4.25 show that the *AERO* tip shape offers a slight aerodynamic benefit over the conventional *FLAT* tip configuration to control the tip leakage vortex core intensity. On the other hand, the radial distributions of Fig. 4.26 quantify such performance variation as negligible. Interestingly, the tip

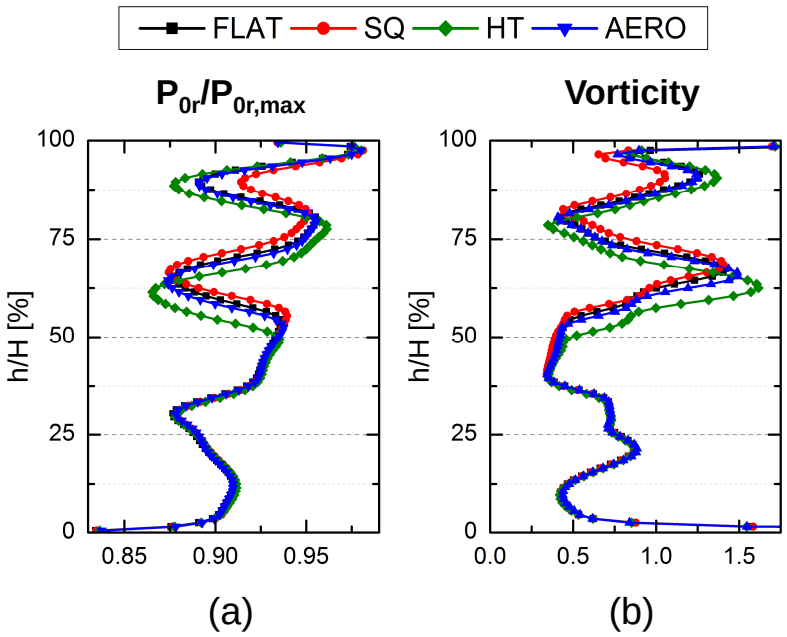

Figure 4.26: Pitchwise-averaged radial distributions of relative total pressure and vorticity magnitude (normalized by the flat tip average), $0.5C_{ax,rot}$ downstream of the rotor trailing edge.

geometry has little impact on the locus of the leakage vortex core (identified by the total pressure drop around h/H=0.88 in Fig. 4.26a), while the effect on the upper vortex position appear to be more pronounced depending on the tip shape. These observations are confirmed by the evolutions of the secondary flow pattern along the four rotor blades shown in Fig. 4.24, which also demonstrates the large influence of the tip design in the front part of the airfoil where the vortical fluid structures are originated. The shaped *AERO* profile exhibits pressure loss levels similar to the *FLAT* tip design case. This is in agreement with the observation that the upper passage structure is akin for the two blade tip designs, Fig. 4.24-left. Interestingly, the largest pressure deficits associated to the upper passage vortex are generated by the squealer and the HT rotor tip geometries. However, the main driver for the aerodynamic loss parameter is the tip leakage vortex. The squealer design generates the most uniform flow field at the turbine stage outlet (Fig. 4.26-right). The vorticity

distributions prove the inadequacy of the *HT* blade tip shape to control the strength of the secondary flow structures.

Fig. 4.27 summarizes the overall aero-thermal performance of the investigated blade tip configurations with respect to the absolute values predicted for the *FLAT* tip design. The bar plot reports the variation in relative total pressure loss ω (evaluated $50\%C_{ax,rot}$ behind the rotor trailing edge), the total tip heat transfer Q_{tip} (integrated over the top 2% of the blade span), the total shroud heat transfer Q_{sh}, and the suction side heat transfer Q_{SS} (integrated over the upper 25% of the blade span).

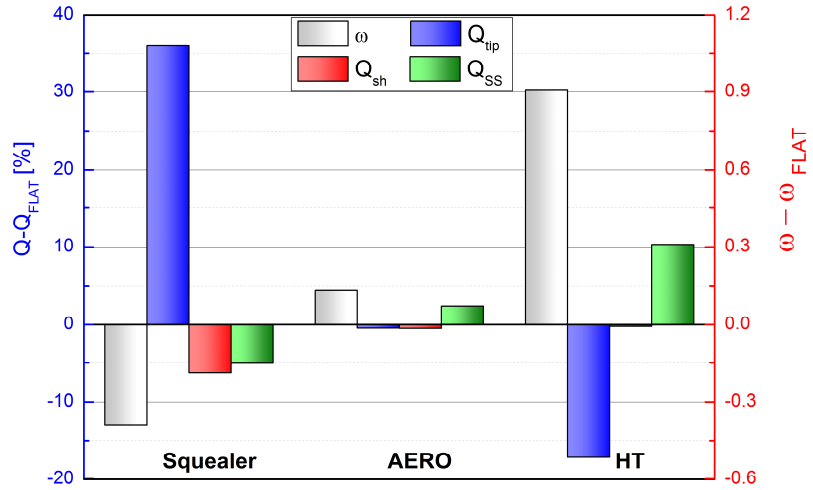

Figure 4.27: Overall performance comparison against a flat tip configuration.

The squealer design presents the best aerodynamic performance ($\Delta\omega$=-0.39%) mainly due to the potential of the overtip gap cavity to significantly reduce the strength and size of the tip leakage vortex with respect to the other investigated tip designs. The *AERO* blade tip maintains a similar performance compared to the flat tip geometry ($\Delta\omega$=+0.13%). While the *AERO* contoured tip proved to be superior to the flat tip design in controlling the overtip spillage flow, the *FLAT* tip shape is advantageous in reducing the detrimental impact of the upper passage vortex on the turbine aerodynamics. The *HT* tip profile presents high pressure losses ($\Delta\omega$=+0.91%). This result supports the consideration that the overtip aerodynamics

required for enhanced tip thermal performance might not be compatible with rotor tip designs for improved aerodynamic performance and a compromise needs to be sought.

The squealer-type blade scores poorly in terms of total heat load budget along the tip. The heat flux to the tip surface in the presence of a squealer cavity is increased by over 35% considering now also the larger exposed surface. On the contrary, both the *HT* as well as the *AERO* contoured tips are capable of reducing the thermal load onto the blade tip wall. The *HT* design manages to lower the tip heat transfer by nearly 18%. The *HT* carved tip geometry features a plain tip profile (with no recessed cavities) that relaxes the tip cooling requirements and limit the issues associated to the coolability of complex small geometrical details (e.g. squealer rims). On the contrary, the squealer design helps to decrease the average casing endwall heat transfer (ΔQ_{sh}=-6.3%), while the use of carved tip shapes shows almost no change with the respect to the reference flat tip geometry. Both the *AERO* and the *HT* tip profiles expose higher levels of heat transfer on the rotor suction side compared to the flat tip (respectively about +2% and +10%), in contrast with the reduced heat transfer levels predicted for the squealer suction side (ΔQ_{SS}=-5%).

In general, the actual aerothermal performances of the 3D carved airfoils are in agreement with the prospective estimates based on the 2D tip optimization output (Table 4.4). On the other hand, the expected reduction in tip and shroud heat transfer for the *HT* blade was largely overestimated. The cause for this can be attributed to the effect of the relative casing movement on the endwall heat transfer (not considered in the precedent 2D numerical optimization), which counterbalances the positive effect of tip contouring. The carved *AERO* geometry, designed for best aerodynamics, exhibits a small increase in pressure losses with respect to the flat tip. Such results can be justified first of all, by the rather small expected gain, few tenths, therefore susceptible to be spoiled in the 3D profile reconstruction. Secondly, the prediction of the mixing losses implemented in the 2D optimization procedure lacked

the modeling of the complex 3D flow interactions between the tip leakage and the local mainstream flow.

4.4 Conclusions

A novel quasi-3D strategy to identify rotor tip profiles with optimal aerothermal performances is presented in this chapter and verified in 3D.

The design methodology is based on the overtip gap flow analysis of 2D planes along streamlines which reduces the complexity of the leakage flow simulations significantly. A numerical multi-objective optimization of the tip shape was performed using differential evolution algorithms combined with a surrogate model. The 2D tip geometry was optimized for five gap flow regimes relevant to modern HP turbines varying the blade load and the width-to-gap ratio.

The geometry of superior tip profiles was found to vary considerably among the distinct tip flow conditions. Tip shapes which perform better at low speed are not optimal for supersonic gap flows. Loss production in the subsonic regime is mainly driven by the amount of gap mass flow and improvements rely on minimizing the gap throat. At high speed, the specific entropy generation has a larger impact on the overall gap losses, which are less mass flow dependent. Appropriate tip-shaping can provide loss abatement up to 20% compared to conventional flat tip geometries. On the heat transfer side, the flat tip profile performs very poorly and optimized tip shapes offer a potential reduction of the thermal loads by 40% at all tip flow conditions. Management of the wall heat fluxes is achieved through local flow acceleration and control of the boundary layer status.

In order to verify the quasi-3D approach, the aerothermal performances of two fully carved 3D turbine rotor tips were compared against two conventional geometries: a flat and squealer tip geometry. Analysis of the flow direction in the middle of the clearance reveals that the transonic flowpaths for the carved design are generally maintained and only marginally modified compared to the flat tip. However, the identified complex 3D flow structures for the squealer type illustrate the limits for the applicability of the current quasi-3D streamline approach. The aerodynamic and heat transfer parameters of the 3D carved blades were found in agreement with the

expectations inferred from a weighted performance budget of the discrete 2D optimal tip profiles.

Both of the carved profiles proved to reduce its tip heat load (even up to a decrease of 18% with a smoother distribution), alas at the price of a slight increase (2-10%) in thermal load on the, less critical, upper quarter of the blade SS. On the contrary, a squealer type geometry, even though achieving a pressure loss abatement of 0.39%, performs poorly from a thermal point of view and enhances the total integrated tip heat transfer with 36%. The shroud heat flux does not reveal substantial changes differentiating the simulated profiles and mainly depends on the driving temperature potential. Investigation of the downstream aerodynamics shows a decreased leakage and passage vortex strength for the squealer case. The effect of tip carving was shown for one case to slightly reduce the leakage vortex strength while maintaining a similar upper passage vortex signature.

This part of the dissertation served to quantify the influence of the blade tip contouring on the physics of the overtip rotor flow, the near-tip heat transfer processes and the development and interactions of the rotor secondary flow structures. The current chapter illustrated that a good potential lies in the design of enhanced carved tip profiles exploiting further the three-dimensional nature of the overtip leakage flow to reduce the heat transfer on the whole rotor airfoil while targeting aerodynamic performance improvements by using a full 3D design optimization strategy (i.e. chapter 5).

CHAPTER 5. FULL 3D OPTIMIZATION OF CARVED AND INDUSTRIAL RUB-SAFE PROFILES

5.1 Three Dimensionality and a Holistic Approach

The previous chapter demonstrated the performance gain that could be achieved through the use of carved blade tip profiles, constructed based on a simplified quasi-3D approach. Therefore, a potential for further aerothermal enhancements exists when using a fully three-dimensional optimization strategy, capable of capturing the complex behaviour of the overtip leakage flow and its interaction with the mainstream structures.

However, while the contoured geometries have proven to offer considerable reductions in heat transfer, it are the squealer geometries which are the widely adopted sealing mechanism in the industry due to their enhanced aerodynamic performances. These profiles have the extra advantage of reducing the chances of a catastrophic event caused by any accidental rubbing of the blade against the casing. Unfortunately, many of the currently implemented designs remain limited to relatively simple rim configurations. A holistic approach has not been extended yet to the design of the turbine tip section which leaves a whole design space of unexplored shapes with potentially (considerably) enhanced aerothermal characteristics. In order to overcome the limitations entailed with conventional optimization approaches (generally restricted to a single specific type of geometry), a topology-like optimization strategy was implemented.

This Chapter is based on:

C. De Maesschalck, S. Lavagnoli, G. Paniagua, T. Verstraete, R. Olive, and P. Picot. Heterogeneous optimization strategies for carved and squealer-like turbine blade tips. *ASME Turbo Expo 2015 Proceedings*, GT2015-42983. [131]

C. De Maesschalck, S. Lavagnoli, G. Paniagua, T. Verstraete, R. Olive, and P. Picot. Heterogeneous optimization strategies for carved and squealer-like turbine blade tips. *Journal of Turbomachinery*, June 2016. [4]

This technique, well established for treating structural design problems [132], enables the generation of unconventional and non-intuitive designs.

This chapter presents the results of two novel, heterogeneous multi-objective optimization methodologies, exploring of a broad range of both carved and squealer-like tip configurations.

5.2 Turbine Environment

The investigated rotor is part of a modern high pressure turbine stage, operating at a Reynolds number of 2.4 x 10^5 and an exit relative Mach number ($M_{r,exit}$) of 0.73. Relevant specifications of the rotor blade are given in Table 5.1.

Table 5.1: Turbine specifications.

Parameter		
Reynolds number (rotor outlet and $C_{ax,rot}$)	-	2.4 x 10^5
Exit relative Mach number ($M_{r,exit}$)	-	0.73
Blade count	-	48
Corrected speed (RPM/$\sqrt{T_{0,in}}$)	-	281
Tip gap - design	% of span	1.38%
Tip gap - tight	% of span	0.85%
Rotor pressure ratio ($P_{0,in}/P_{s,out}$)	-	2.2
$T_{0,gas}/T_w$	-	∼1.47
$T_{0r,gas}/T_w$	-	∼1.33

A periodic section of the blade row is modeled while only the top 6% of the rotor span is allowed to change shape (Fig. 5.1). The simulated geometry is divided into 2 subdomains: one 'downblock' that does not change during the optimization and an 'upperblock' that is meshed according to the requirements of the particular tip design under consideration. For the current optimization, an uncooled geometry was considered. However, the dimensions of the tip parameterized features were constrained based on real-engine manufacturing capabilities, minimum requirements for mechanical strength and demands for the installation of coolant holes in a later design stage.

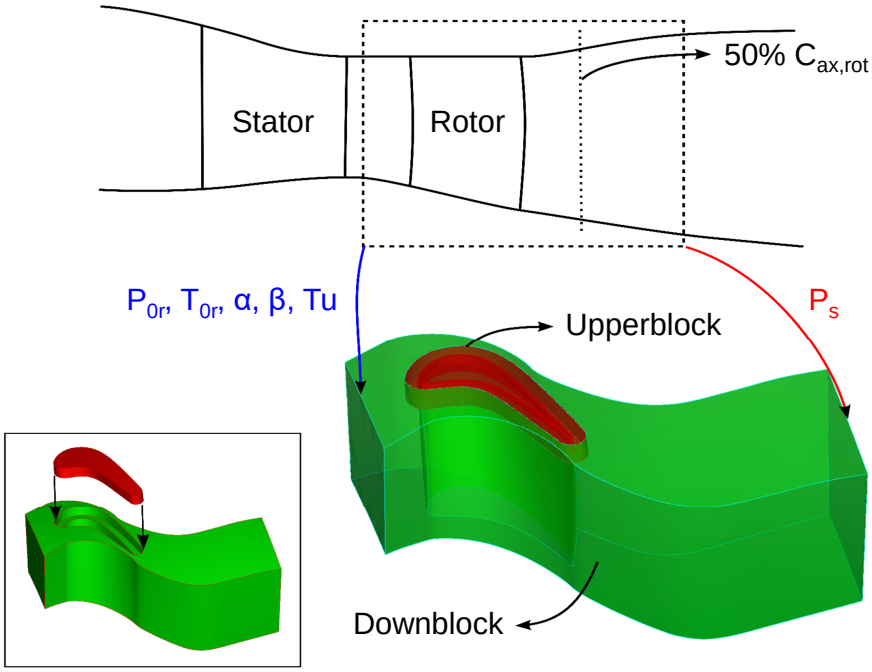

Figure 5.1: Computational domain.

A full hexahedral mesh is subsequently generated by means of Numeca Hexpress, separately for the down- and upper-blocks. A thorough grid sensitivity analysis has been conducted in order to assess the optimal mesh properties that were then applied to all the geometries generated during the optimization. The simulations for the sensitivity study were performed by increasing the mesh density isotropically for one of the blocks while keeping the same grid resolution in the other one. Fig. 5.2a presents the influence of the grid density on the efficiency for a single squealer configuration. The lower and left axis of Fig. 5.2a and Fig. 5.2b refer to the down-block refinement (blue curves with square labels), while the right and upper axis define the upperblock mesh resolution (red curves with circular labels). One can observe that refining the upperblock beyond 2 million cells does not improve the estimation. However, grid refinement of the downblock reveals a clear asymptotic trend. It is important to note that all the profiles are evaluated with the same downblock mesh in the optimization loop. Hence, the same efficiency offset associated with the downblock

grid will equally affect each tip configuration, ensuring a valid comparison among different profiles. Fig. 5.2b illustrates the influence of the discretization levels for both blocks on the tip heat transfer (compared to the finest grid solution) in the case of three tip arrangements: a flat tip, a single squealer and a complex squealer configuration. Refinement of the downblock (with a simple squealer) does not provide significant variations in the tip heat transfer ($\Delta Q_{tip} < 1\%$). On the contrary, the tip heat transfer is more sensitive to the upperblock mesh resolution as can be expected. However, the error between the finest and the 2nd finest grids remains relatively small, below 1.5% for every investigated tip shape.

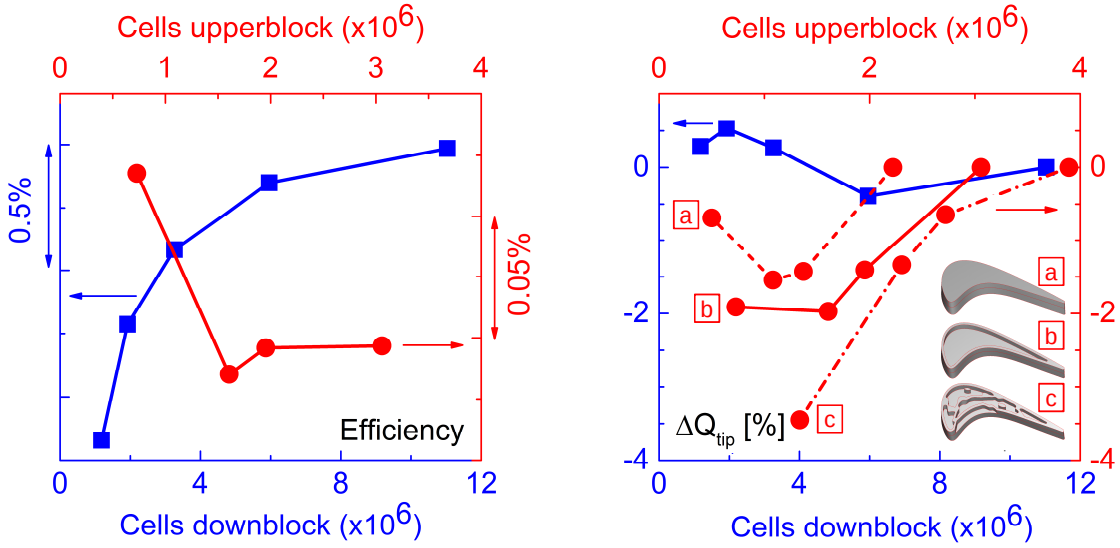

(a) Effect on rotor efficiency.

(b) Effect on tip heat transfer.

Figure 5.2: Grid sensitivity analysis.

Based on the outcome of the grid-dependency study, the computational domain was meshed using the grid settings of the 2nd finest grid: the downblock mesh counts about 6 million cells while the upperblock can contain between 1.5 up to 3 million cells, depending on the specific tip design. The main passage includes over 140 spanwise divisions and a minimum of 40 grid points inside the tip gap. These mesh settings are comparable to values used in previous numerical investigations where a satisfactory

resolution of the tip flow region was obtained [29, 46]. The first cell size was set such that the y^+ values remain below 0.2 along all solid surfaces to accurately resolve the complete aerothermal boundary layer.

The steady-state simulations were performed by means of Numeca FINE/Open using the k-ω SST model for the turbulence closure [67]. In order to simulate correctly the tip flow problem [54], pitchwise-averaged radial profiles of relative total pressure, total temperature, flow angles and turbulent quantities were extracted from the NGV exit plane of a full stage calculation (see Fig. 5.1) and imposed at the rotor inlet. At the domain exit, the static pressure was set to satisfy the radial equilibrium for a total to static pressure ratio of 2.20. The solid walls were isothermal in order to retrieve the heat flux at an engine representative gas to wall temperature ratio of about 1.5.

5.3 Parametrization and Geometry Generation

Two distinct parametrizations were developed during this investigation, each targeting a different type of profiles. The first parametrization creates smoothly carved blade tip surfaces using a shape optimization methodology, while the second parametrization encompasses squealer-like tip designs by means of a topology-like strategy.

5.3.1 Carved Tip Designs

The parametrization for the carved tip optimization aims to cover a wide range of smoothly contoured tip profiles. The full procedure is illustrated in Fig. 5.3 and consists of a general rectangular Bezier control surface [123], which is mapped onto the tip profiles. The tip surface is discretized in 8 predefined sections along the rotor camberline where the tip contouring can be adjusted separately by means of 6 control points, equally spaced from PS to SS (Fig. 5.3). In this way, a rectangular Bezier surface is constructed through 48 control points (6 x 8) that set the radius evolution over the complete tip surface. Each control point is a design variable for the optimization and can take a value ranging from 0, when located at the maximum

deformation depth, up to 1, when the point reaches the minimum tip clearance. To reduce the amount of design variables and to ensure the tip manufacturability, the profiles of the leading edge (LE) and trailing edge (TE) sections are forced to lie on a straight line and their definition only requires 4 (2 x 2) design variables. In this way, the shape parametrization counts a total of 40 design parameters. By means of Matlab, the rectangular Bezier surface is subsequently mapped onto an auxiliary surface that extends slightly beyond the tip contour (see Fig. 5.3, bottom left). Eventually, the blade is cut with the generated surface resulting in the final contoured tip shape (through Numeca IGG and Gambit). The maximum deformation depth was set to 5.6% of the blade span (about four times the design tip clearance). This range was judged sufficient to allow for a significant influence on the overtip flow field with a minimum deformation of the overall blade profile. Moreover, the use of such a Bezier surface guarantees that the final surface will not exceed the minimum clearance nor deform the profile outside the prescribed deformation region.

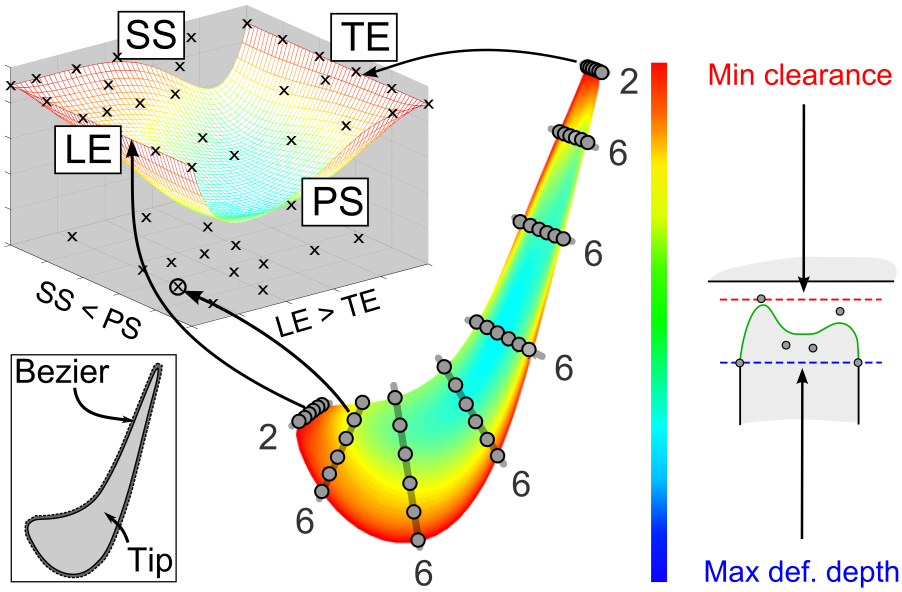

Figure 5.3: Illustration of the carved tip parametrization.

5.3.2 Squealer-like Tip Design

This type of tip parametrization is inspired by a topology-based optimization rather than a pure shape optimization [133]. Although seldom applied to fluid machinery design, these topology optimization techniques have already shown promising results in a number of alternative applications (e.g., cars [134], microfluidic mixers [135], or complex duct flows [136]). The goal of the current parametrization is to enable the creation of a very wide range of squealer-like designs, which shall consist of an arbitrary amount of rims which separate one or multiple cavities. Hence, the tip surface has been divided in about 200 different blocks (see Fig. 5.4a). Each block can be either up (and so it becomes part of a rim) or down (which makes it part of a cavity floor), Fig. 5.4b. The minimum dimensions of the blocks are set based on real-engine manufacturing capabilities and requirements dictated by the mechanical strength and coolability. The cavity depth was set to 4.5% of the blade span, about three times the design tip clearance. The reference squealer design adopts one single rim along the tip outer profile with a thickness of about 2% of the blade span. The real blade tip corner radius was not modeled and all the rim blocks were defined with sharp edges in the CFD geometry.

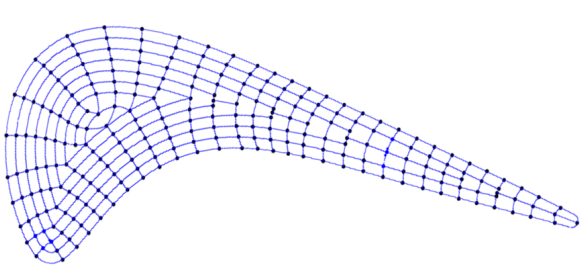

(a) Block discretization pattern.

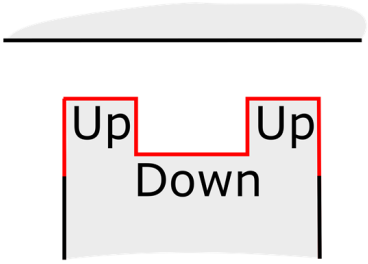

(b) Graphical example of the block-up/block-down tip surface generation.

Figure 5.4: Block discretization for the squealer-like optimization.

In order to define whether a certain block is set up or down, two different approaches were used:

The Binary Approach. This strategy uses a binary string that defines the position of every block separately (Fig. 5.5). Since the binary string contains about 200 elements there will be an equal amount of design variables.

The Level-Set Approach. In an attempt to reduce the number of optimization parameters and exclude non-relevant configurations, a level-set approach [137] was implemented. This methodology is illustrated in the top side of Fig. 5.5.

Similarly to what is done in the carved shape parametrization, the procedure starts from a general Bezier surface which is mapped onto the tip. The surface is built based on 12 sections disposed along the rotor camberline where the shape evolution from PS to SS is defined through a maximum of 8 equally spaced design parameters (8 x 12 = 96 parameters varying from 0 to 1). To discriminate whether a block is up or down, the mapped Bezier surface is evaluated at the center of every cell (Fig. 5.5, blue dots). If this value is higher than a chosen threshold (in this case the threshold is set at 0.5), the block is set to be 'up'. In the case the value is below the threshold, the considered block becomes part of the cavity floor. In general, 8 design parameters are not always necessary to define the contour from PS to SS in all the tip sections along the chord. For very thin sections of the rotor blade (e.g. the aft part of the blade), some of the Bezier control points are combined together with one design variable. The amount of design variables is reported in Fig. 5.5 next to each section. The strategy used to combine the control points is demonstrated in the top-left side of Fig. 5.5. For example, in the case the section is defined by only 5 design parameters (instead of all 8 required for a 8 x 12 Bezier surface), one variable is attributed to each of the two outer control points. The other control points are combined two-by-two, and the height of each duo is set equally through one design parameter. In case for example only 2 design variables describe the section (e.g. the last three sections near the TE), the first four control points take the value of the first design variable while the last

4 control points adopt the height set by a second design parameter. This approach brings the total amount of required design variables for the level-set approach down from 96 to 50.

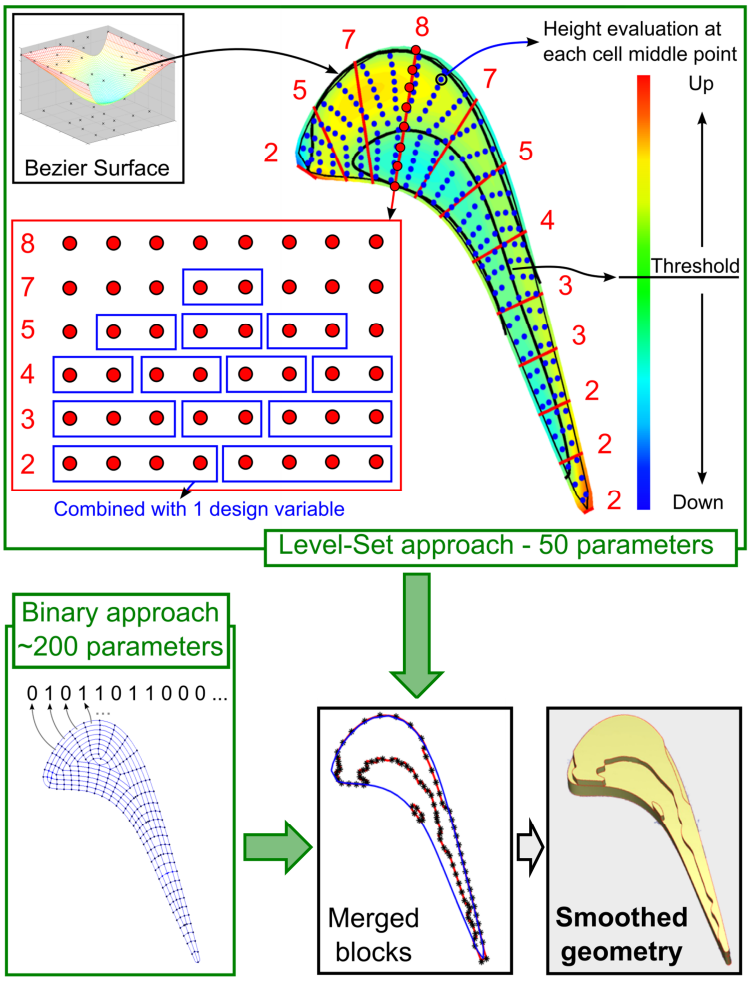

Figure 5.5: Binary and level-set approach for the squealer-like optimization.

Once the position of each of the blocks is established, the upstanding blocks are merged through a Matlab script and the edges of each of the rims are identified (Fig. 5.5). For each cell at the border of a rim, the middle point on its edge is exported and a B-Spline interpolation generates the smoothed rim sides (performed through Numeca IGG). Eventually, the rim volumes are created and merged with the rest of the blade geometry to compose the solid domain which is consequently cut away from

the upperblock to define the fluid domain (using the commercial softwares Gambit and Numeca Hexpress).

5.4 Optimization Methodology

The current study comprises a multi-objective optimization that aims at the reduction of the rotor tip thermal loads and the concurrent improvement of the rotor efficiency.

The heat transfer objective parameter is defined as the heat transfer integrated over the entire rotor surface exposed to the tip deformation (red area in Fig. 5.4b). Although the tip design also affects the heat transfer distribution on other relevant regions of the rotor blade (pressure and suction side, shroud), only the tip heat load was considered as the optimization objective being the tip the most critical area to refrigerate in a turbine blade. In order to provide an accurate assessment of the rotor heat transfer performances, the heat flux magnitude and distribution were also determined on all the other rotor surfaces and results are discussed later in this chapter.

The second objective parameter which lumps up the aerodynamic performances is the rotor efficiency η evaluated according to:

$$\eta = \frac{T\omega}{\dot{m}C_pT_{0,in}\left[1-\left(\frac{P_{0,exit}}{P_{0,in}}\right)^{\frac{\gamma-1}{\gamma}}\right]} \tag{5.1}$$

Fig. 5.6 presents a general overview of the methodology for the three types of optimizations that have been conducted: the carved tip optimization, the squealer-like optimization with the Binary approach and finally with the Level-Set approach. The in-house optimizer CADO (chapter 2.3, Fig. 5.6-top) is coupled to the evaluation routine (Fig. 5.6-bottom) which handles the sequence from the CAD generation through the meshing, the flow solving and the data post-treatment.

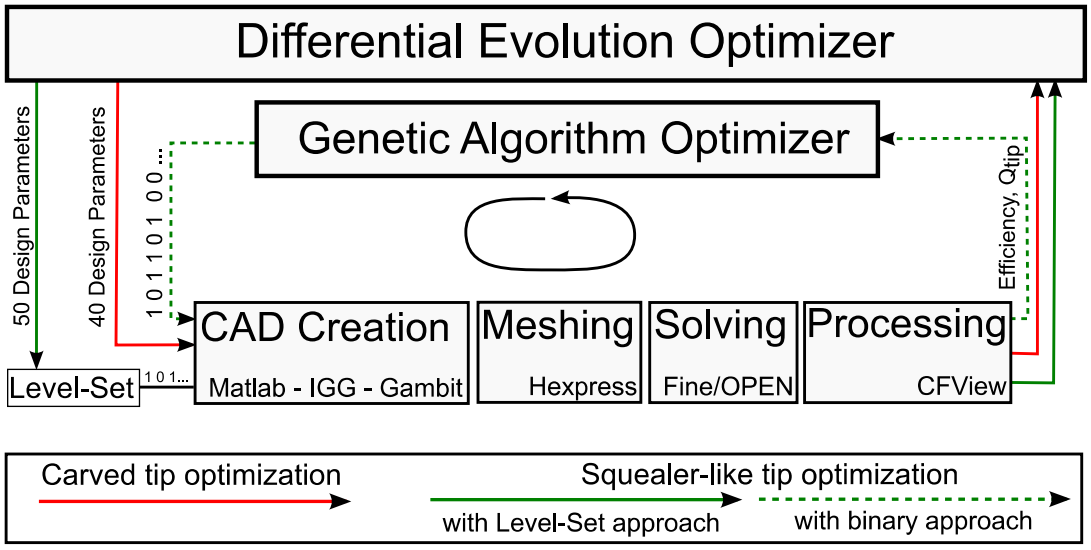

Figure 5.6: Flowchart of the optimization methodology.

The optimization was kicked-off with an evaluation of the performance of the profiles from an initial database, the DoE ('Design of Experiments'). For the current investigation, a fractional factorial approach [124] was used to select the subset of the design space to be evaluated during the DoE. Subsequently the tip profiles are ranked and the prime geometries constitute the first population. Based on the process of crossover and mutation (controlled through user-defined constants), the 'children' are generated and their design parameters are passed on to the evaluation routine (in the form of optimization parameters between 0 and 1 for the DE code and a binary string for the GA routine). Once the performances are assessed, this information is fed back to the optimizer that adds the newly evaluated children to the previous population including the 'parents'. Eventually this enlarged database is ranked and the prime individuals compose the next population. From the latter population, new children are created through the aforementioned recombination procedure and the iterative loop continues until no significant improvements in the Pareto front can be

noticed anymore. The latter Pareto front contains the individuals for which one of the performance parameters cannot be enhanced without deteriorating the other.

For the GA optimization, the crossover likelihood was set to 0.8 and the mutation probability to 0.005 (1 out of 200, resulting in about one mutated block per new tip design). The population size was set to 20 individuals, fixing the amount of new tip designs per iteration. This number was deemed to be sufficiently large in order to capture the inherent variety contained in the final Pareto front. For the optimization of the carved tip geometry and the squealer-like optimization with the level-set approach, the DE algorithm provides the design parameters of the geometries to be evaluated. For this optimization, the cross-over and mutation constants were set respectively to 0.8 and 0.6. The population size for the carved design optimization was fixed to 20. For the optimization of the squealer-like tip with a level-set approach, a population size of 40 was imposed to allow for a larger spread in the Pareto front.

Carved Tip Optimization Sequence. The optimization of the contoured tip profiles was conducted for the two rotor tip clearances under investigation: 1.38% of the blade span (design gap case) and 0.85% of the blade span (tight gap case). The design sequence is presented in Fig. 5.7. Firstly, the DoE (129 designs) was constructed for the tight clearance case from which the DE optimization was initiated (highest ranked 20 designs). After 14 iterations (about 270 extra evaluated designs), the Pareto front was deemed to be converged and 9 optimal designs were selected and recalculated at the design tip clearance. Combined with the DoE of the design clearance, this pool of 138 tip shapes formed the basis for the 2^{nd} DE optimization. Eventually, the optimization of the rotor tip section at the design tip clearance converged after 8 iterations and about 300 designs were generated.

Squealer-Like Tip Optimization Strategy. The sequence for the squealer like optimization is illustrated in Fig. 5.8. The DoE was created first with the Level-Set approach from which the 40 best profiles were selected to initiate the population for the DE optimization. After 11 populations of 40 individuals ($\sim$540 designs), no

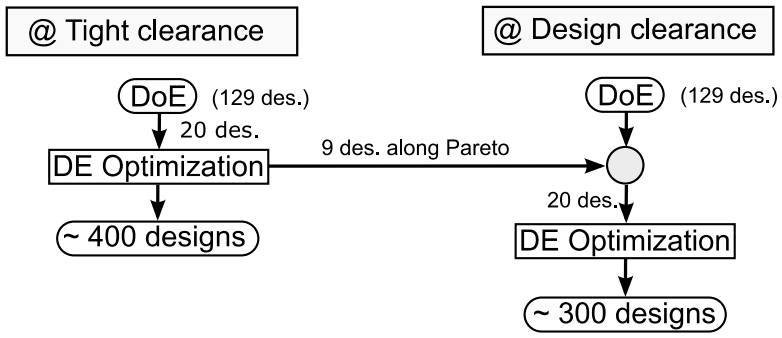

Figure 5.7: Strategy sequence for the carved tip optimization.

significant improvement could be discerned. The prime designs along the Pareto front were then combined with some additional conventional profiles. The optimization was restarted with the Binary Approach up to a total of 17 iterations employing the GA routine.

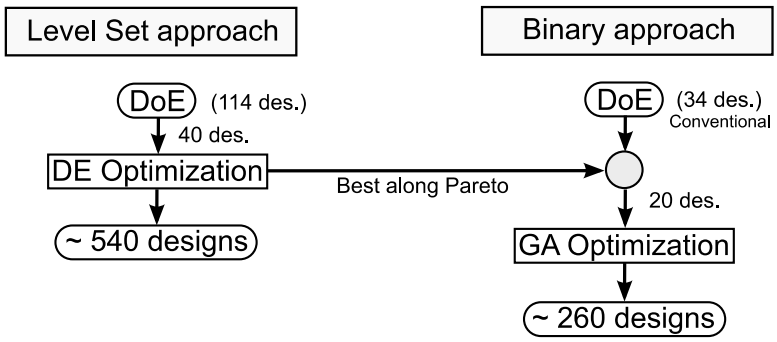

Figure 5.8: Strategy sequence for the squealer-like optimization.

5.5 Optimization Convergence and Pareto Fronts

5.5.1 Carved Tip Optimization

Fig. 5.9 presents the Pareto front for the carved tip optimization where each evaluated tip profile is identified by the two objective functions: aerodynamic efficiency and tip heat transfer. For both the design and tight clearance optimizations, the tip

heat load is normalized by the heat flux over the flat tip blade at the nominal gap. For consistency, the aerothermal performance of this flat tip profile will be used as the reference case throughout the rest of the chapter. Furthermore, the color code used in Fig. 5.9 to distinguish the different optimization strategies is also kept in the following figures.

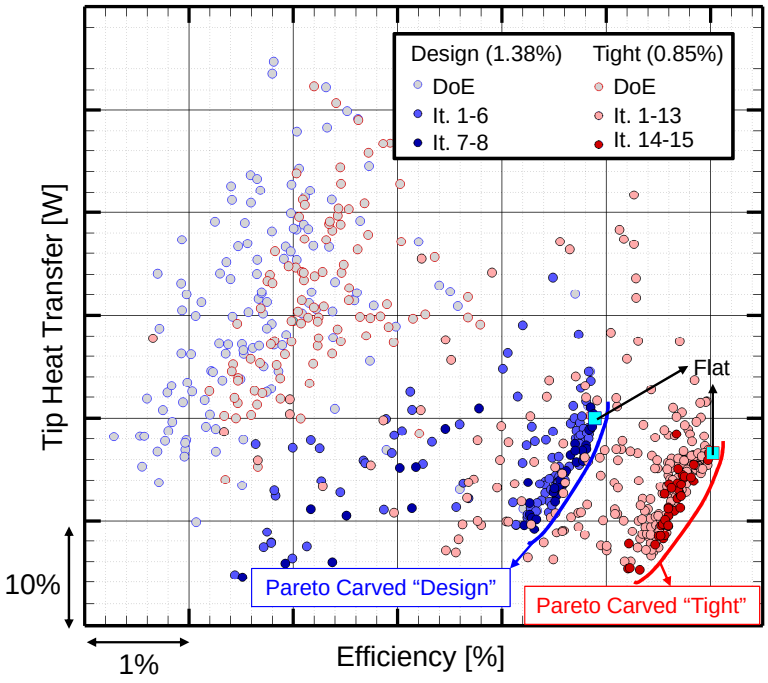

Figure 5.9: The Pareto front for the carved tip optimization at design and tight clearance.

In Fig. 5.9, the individuals generated during the DoE expose a large scatter of the performance with differences in heat transfer higher than 40% and about 4% in efficiency. As the optimization evolves, the new individuals move towards enhanced efficiencies and reduced heat fluxes. Eventually, for both tip clearance levels, the optimization was deemed converged when no significant improvements were obtained in the last 2 populations. Additionally, the location of the flat tip performances at the tight and design clearance is reported for each of the optimizations. A reduction of the gap size by 0.5% of the blade span enhances the rotor efficiency by about 1%, consistent with trends found in the literature (e.g. Yoon et al. [14]). The smaller

gap size additionally helps to reduce the total heat transfer by 4% despite the larger wetted surface. For both of the investigated clearances little to no improvement in efficiency could be obtained considering 3D carved tip profiles. However, the Pareto front indicates that the exchange rate between rotor efficiency and the tip heat load is approximately 1:20. In other words, the use of the contoured tip design strategy allows to trade a small reduction in efficiency ($\Delta\eta$ $\sim$0.5%) with a reduction in tip heat load of about 10%.

Fig. 5.10 shows the detailed convergence history of the optimization objectives as a function of the number of evaluated tip designs. The evolution of the efficiency and heat transfer parameters for the tight clearance case is displayed in Fig. 5.10a and Fig. 5.10b. Since the DoE was performed with a fractional factorial design approach employing 0.1 and 0.9 as the lowest and the highest level, the flat tip design at the minimum clearance (design variables equal to unity) was additionally included in the database prior to the optimization. The addition of the flat tip into the database resulted in a faster convergence to the maximum efficiency (Fig. 5.10a) since the conventional flat tip geometry turned out to offer superior performances. The Pareto front in Fig. 5.9 shows that the scatter of the efficiency data is above 5% in the initial population and it reduces to 1% as the optimization converges. On the contrary, the minimization of the heat transfer (Fig. 5.10b) happens more gradually and the dispersion of the individuals' performance is around 10-12% after the evaluation of 400 tip geometries (15 populations).

Once the optimization of the carved tip design is completed, the DoE is conducted at the design clearance. The lower and upper level for the tip gap size were set to 0 and 1 in order to enable the largest variability in blade tip shape. Nine designs along the Pareto front of the tight clearance were selected and evaluated at the design gap height in order to accelerate the convergence rate of the optimization. These profiles are designated by green dots in Fig. 5.10c and Fig. 5.10d. In terms of efficiency, these tip surfaces show high levels of performances and their introduction into the individual pool effectively helps the optimization algorithm to reach convergence for the rotor

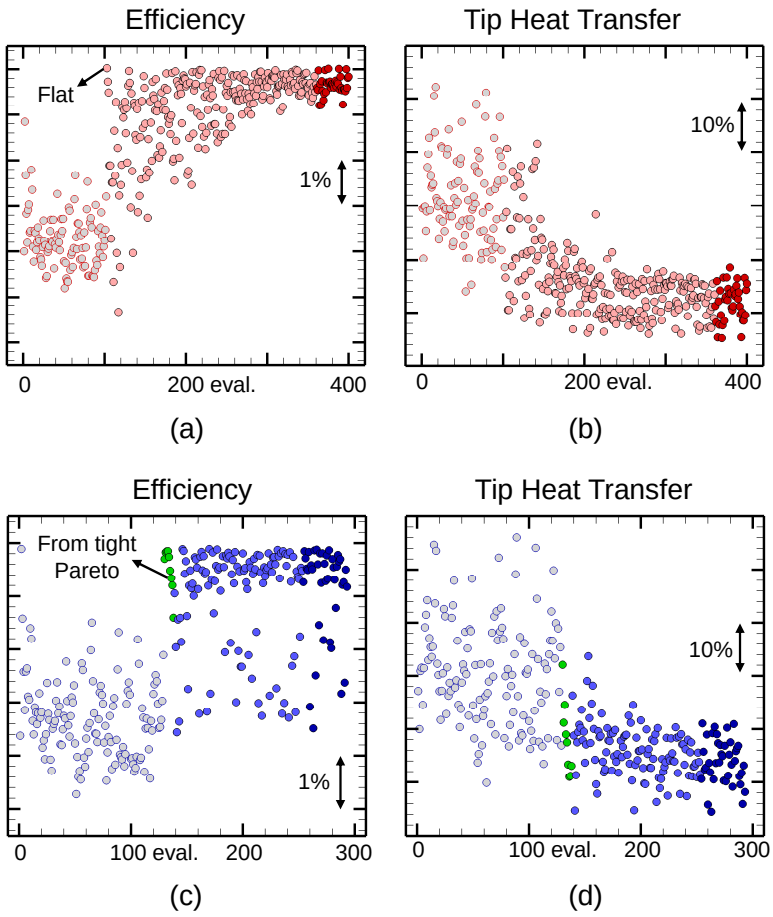

Figure 5.10: Convergence evolution of the optimization objectives for the tight clearance (red dots, (a) and (b)) and design clearance (blue dots, (c) and (d)). Colors are consistent with legend of Fig. 5.9.

efficiency. However, due to a low score in the heat transfer objective parameter, these evaluated profiles do not lay on the final Pareto front. Eventually, convergence in the heat transfer parameter was reached after 8 populations.

Fig. 5.11a presents a zoom of the Pareto front for the fully carved tip shape optimizations. Additionally, Fig. 5.11b shows the contoured surface of four optimized tip geometries selected along the Pareto lines of the two investigated tip clearance cases: profiles 'A' and 'C' represent the best compromise between aerodynamics and thermal performances, while profiles 'B' and 'D' are tip designs tailored for heat

transfer minimization. Eventually, a sketch of the tip cross section for two overtip streamlines ('1' and '2') for geometry B and D are presented.

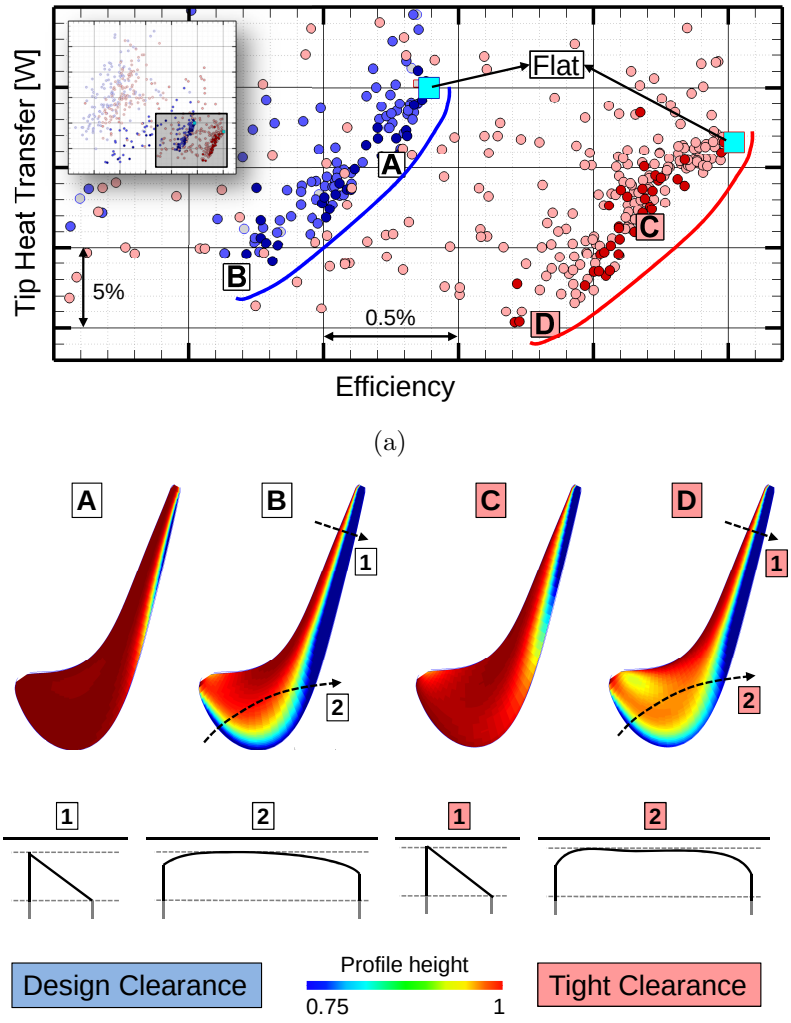

(a)

(b)

Figure 5.11: Zoom on the carved optimization Pareto front (a) and a detailed view of four optimal shapes (b).

The color bar in Fig. 5.11b ranges between 1, when the profile is at the minimum clearance, and 0.75, when the tip surface is contoured for about 25% of the deformation depth (Fig. 5.3). The results show that over most of the tip surface such deformation depth span is sufficient to obtain significant reductions in heat transfer

(Fig. 5.11b). The 25% deformation length corresponds approximately to the size of the design clearance.

The designs located in the central part of the Pareto front for both clearances (profile A and C) indicate that a divergent passage in the aft section of the blade produces an immediate reduction of the overall heat transfer by 5%. In the front section, the tight clearance profile (C) exposes a slightly larger absolute deformation with respect to the optimal profile at the design clearance (A). From the tip geometries in the lower region of the Pareto front (B and D) the low radius of the profile at the suction side extends up to the rotor leading edge. These optimal design solutions attempt to create a continuous converging-diverging flow path in the front section of the rotor blade that is beneficial to alleviate the thermal loads. Remarkably, tighter tip gaps demand more aggressive contouring (i.e., deeper blade radius variations) in the front blade region to achieve reduction in heat transfer as high as 12%.

5.5.2 Squealer-Like Optimization

The Pareto front for the squealer-like optimization is depicted in Fig. 5.12 for both the level-set optimization and the optimization based on the binary approach. Additionally, the performances of two types of conventional designs, the flat and single squealer tip geometry, are explicitly indicated in the graph. As it was done for Fig. 5.9, the performance of the flat tip design at the nominal clearance is used to normalize the heat transfer of all the individuals. Similar to the carved tip optimization, a fast advancement towards the lower right region in the objective space is obtained. However, at the end of the optimization with the level-set method, the distribution of the tip profiles along the Pareto line is characterized by discontinuities. The optimization using the binary approach succeeded in making the Pareto front denser and to generate additional tip profiles with enhanced efficiency. This improvement was achieved by including every possible binary combination into the parametrization to enable the exploration of a much larger design space.

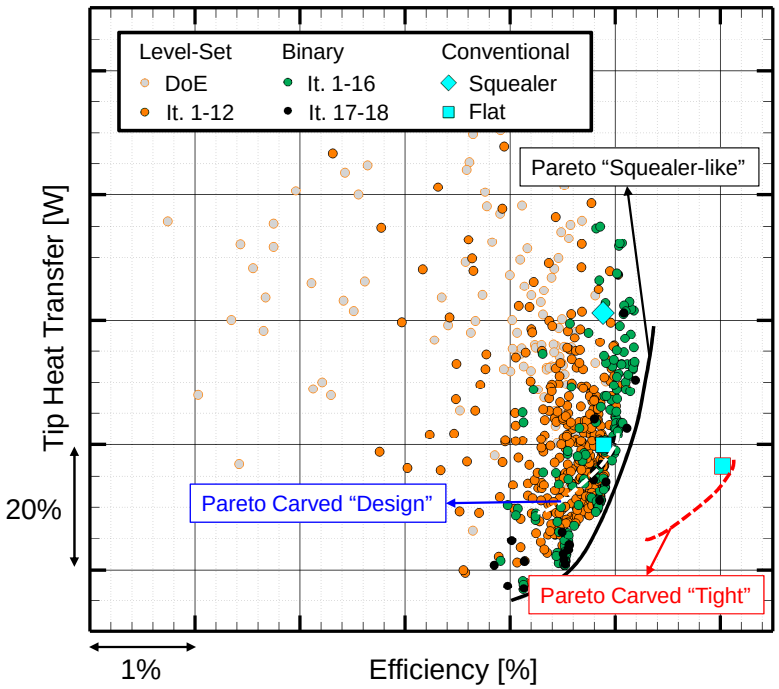

Figure 5.12: The Pareto front for the squealer-like optimizations.

The outcome of these optimizations clearly points out that the proposed design methodologies can generate a large number of tip geometries that outperform the conventional squealer and flat tip design. For this particular state-of-the-art turbine blade, there exist tip configurations that would allow a reduction in the tip heat load by 10% compared to a flat tip and nearly by 30% in comparison with a squealer design, while preserving the aerodynamic performance. Other superior tip geometries provide an increase of the rotor efficiency by 0.3% in combination with a 10% drop in the total heat transfer when compared to the squealer tip configuration. Fig. 5.12 additionally displays the Pareto fronts for the two carved tip optimizations represented by dashed lines. Overall, the squealer-like Pareto spans an efficiency range of 1%, similarly to what was observed for the carved tip designs. On the contrary, the corresponding tip thermal loads exhibit a much large scatter ($\sim$40%) with respect to the Pareto line predicted for the contoured tip optimization. The exchange rate between the efficiency and the tip heat flux for the squealer-like optimal profiles ($\Delta\eta$=1% yields

ΔQ=40%) is twice the exchange rate associated with the carved tip design strategy ($\Delta\eta$=1% yields ΔQ=20%). In other words, the squealer-like configuration is likely to offer a stronger reduction in heat load at the price of smaller aerodynamic loss.

Similar to Fig. 5.10, Fig. 5.13 presents the convergence evolution for the squealer-like optimization. Consistent with Fig. 5.12, the grey dots present the DoE, the orange ones the created individuals adopting the level-set approach and the green/black dots the tip profiles generated with the binary approach. In terms of efficiency (Fig. 5.13a), one can note that the binary approach realizes quite fast the last percent-points of improvement by allowing every single block to vary independently. On the heat transfer side (Fig. 5.13b) many profiles with reduced heat transfer levels were created throughout the last 200 evaluations and served to make the Pareto front more continuous.

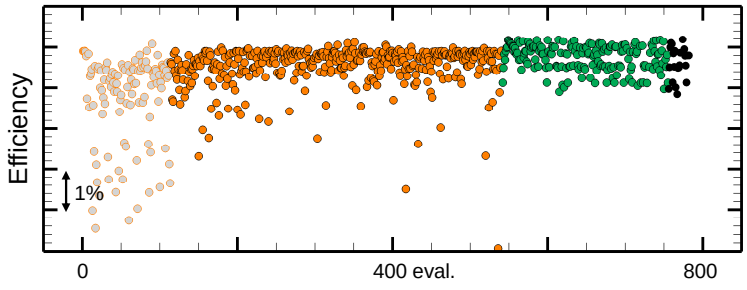

(a)

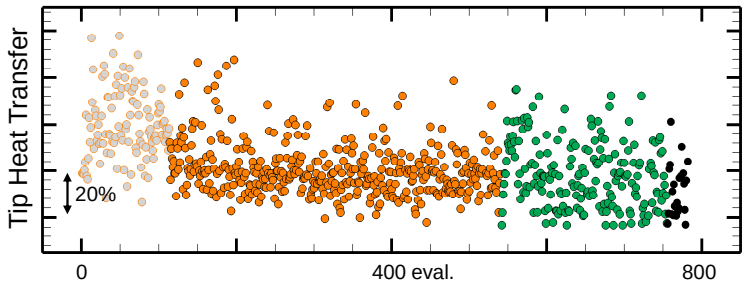

(b)

Figure 5.13: Convergence evolution of the objectives throughout the squealer-like optimization: Efficiency (a) and Tip heat transfer (b).

5.6 Aerodynamic Performance and Flow Field

Fig. 5.14 presents the blade torque as a function of the turbine massflow for every evaluated tip design. On the bottom right of Fig. 5.14, the same plot has been constructed, colored by the efficiency levels. The latter figure locates the high performing individuals in the upper left region of the graph. Comparison among the optimal individuals obtained with the carved tip optimization indicate little variations in turbine power extraction for the same pressure loading across the rotor row. Reducing the clearance on the other hand decreases the massflow almost by 1.5% while preserving the blade torque. As a consequence, the total temperature drop across the rotor slightly increases together with a higher flow turning. The Pareto front of the squealer-like optimization shows a much larger scatter. Blade to blade variations of about 4% in massflow and almost 3% in torque extraction can be observed, generally exceeding the values for the carved rotor shapes. Moreover, on the efficiency plot, two distinct zones of high efficiency are identified. The bottom ellipse generally encloses designs with a closed aft part while the zone with a larger torque and massflow mainly consists of profiles adopting an open configuration near the trailing edge.

The downstream flow vorticity of the upper 50% of the blade channel (massflow-averaged in the plane $0.5C_{ax,rot}$ downstream of the rotor trailing edge, Fig. 5.1) is plotted in Fig. 5.15 against the efficiency objective. The distribution of the carved tip profiles reveals a general trend where an increase of 1% in efficiency corresponds to a decrease by 15% in vorticity. The scatter of the carved tip data suggests that a contoured tip design offers limited control on the rotor outlet flow field once the maximum efficiency is attained. This is the evidence that only one particular pattern of tip surface shape provides the best aerodynamic performance.

Similarly as for the other aerodynamic quantities, the Pareto front of the squealer-like designs shows a scattering about 3 times as large as for the carved optimization at the same design clearance. The squealer design approach clearly provides various effective solutions to control to a greater extent the interaction of the overtip

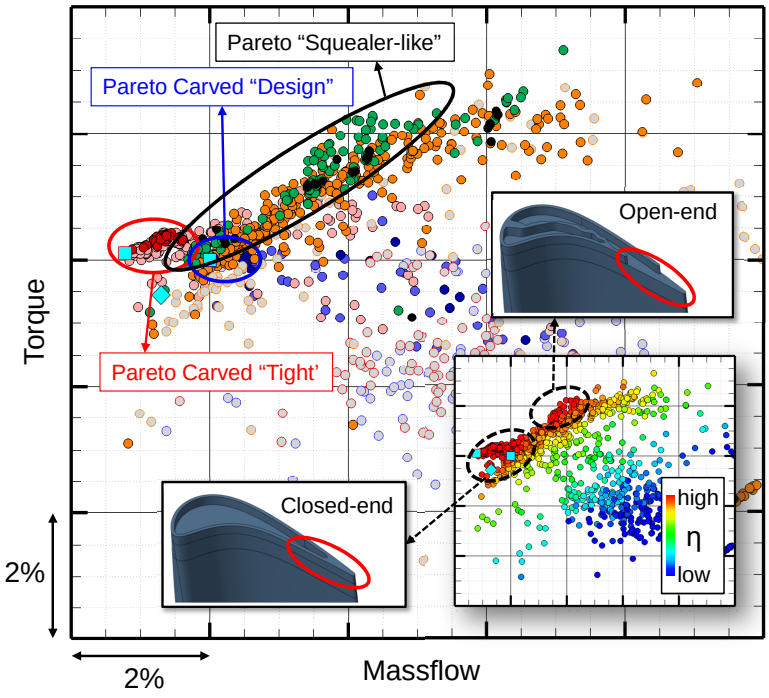

Figure 5.14: Blade torque versus the massflow for every evaluated profile.

spillage fluid with the main stream flow without significant impact on the overall rotor efficiency.

The three profiles (‘A’, ‘B’ and ‘C’) highlighted in Fig. 5.15 give an indication of the wide variety of tip geometries and downstream flow structures that were achieved throughout the optimization. The flat tip, denoted with ‘B’, shows an established downstream vortex pattern consisting of the overtip leakage vortex (TLV) which is clearly separated from the upper passage vortex (UPV). Tip geometry ‘A’ on the contrary adopts a small suction side rim and a fully opened back end. This configuration imposes a large fraction of gap massflow to accelerate rapidly inside the tip channel. As a consequence, the fluid exit velocity is increased and the tip leakage vortex is bent further towards the direction of the rotational speed (compared to a flat tip). Tip shape ‘C’ exposes one of the lowest vorticity magnitudes among the optimal squealer-like designs. This profile features a version of a PS squealer. The PS rim serves to cut the flow like a knifed edge, reducing the effective gap throat

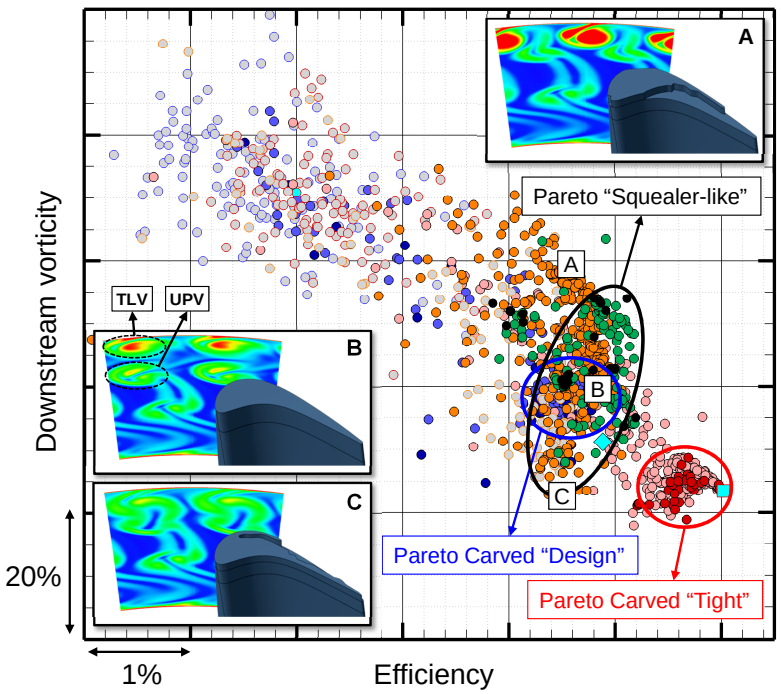

Figure 5.15: Downstream vorticity in the upper 50% of the blade span against the efficiency.

and thus the overtip massflow. However, since only a small fraction of the SS edge is protected by a rim, the rotor efficiency is reduced in comparison to the conventional full squealer blade. The rotor exit flow field of blade 'C' experiences the merging of the tip leakage vortex with the upper passage vortex. Because of the SS opened rim, the interaction between the UPV and the TLV starts further upstream inside the blade passage. At the rotor outlet, the merged vortical structure spreads over a wider portion of the blade channel when compared to the vorticity field predicted for blade tip 'A' and 'B'. The increased size of the single vortex is due to the earlier start of the UPV-TLV mixing process. As the two vortices are counter-rotating, the resulting vorticity strength at the rotor outlet is however weakened.

5.7 Heat Transfer Characteristics

Fig. 5.16 shows the relation between the total integrated heat transfer and the heat load per unit of area. While the first one gives an indication of the total amount of coolant required for refrigeration of the tip area, the second quantity represents the actual thermal loads that drive the local metal temperature. In this view, the current optimization strategy proves to be an effective tool to manage the tip thermal gradients by offering extended control on the tip heat load distribution, a requisite to design improved cooling schemes.

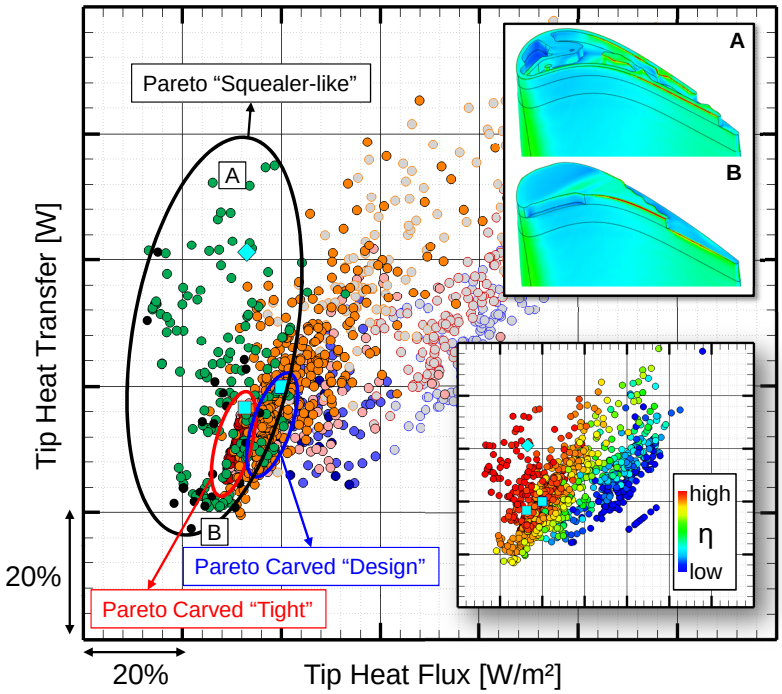

Figure 5.16: Total tip heat transfer [W] versus the surface-averaged heat load [W/m^2].

The carved tip optimizations for both clearance sizes show similar limits of their Pareto front where the area averaged tip heat transfer varies less than 10%. The tip heat flux of the optimal profiles at tight clearance is approximately 10% lower than the levels found for blade tip shapes running at the design clearance. In general, this can be explained by the variation in the average tip gap size rather than by a direct

influence of the tip surface shape. On the contrary, the squealer-like profiles present a large variety of thermal performances, with variations as high as 40% in tip heat transfer and heat flux for similar aerodynamic performances (Fig. 5.16, bottom right). The average heat load per unit area is generally lower in the case of rim-type designs compared to the contoured ones, mainly because of the wider wetted area. Two profiles 'A' and 'B' are shown in detail in Fig. 5.16. While both geometries present a comparable tip heat transfer, the total heat load differs by almost 60% of the flat tip heat flux. Such a large variation in tip thermal load discloses a drawback of complex squealer configurations with multi-cavity arrangements where a much larger surface is inevitably exposed to the hot spillage gas. Multi-cavity tip layouts (blade tip 'A') also promote increased heterogeneity and interaction of the flow structures within the squealer bath. The contour plots of blade tip heat transfer shown in Fig. 5.16 prove how the augmented cavity flow activity associated with tip profile 'A' results in large heat transfer variations over the rotor tip surface. Less extreme squealer designs such as blade tip 'B' alleviate the tip thermal loads by minimizing the generation of separated regions and impinging jet flows in the tip channel. Areas of high thermal exchange are confined in the proximity of the outer rim edges.

In this view, it is not sufficient to consider only the total heat measurement, but the average heat transfer must also be taken into account to correctly identify the actual thermal forcing. Another important aspect to assess is the occurrence of potential 'hot spots' induced by a particular tip configuration. From a qualitative point of view, one indication of the presence of large temperature gradients on the tip surface can be given by the RMS of the heat transfer distribution. In Fig. 5.17 the total tip heat flux is plotted against the associated heat transfer RMS. A higher RMS value is an indication that large thermal gradients are likely to be generated into the metal blade if not appropriately compensated by effective cooling schemes.

The squealer-like tip geometries manifest again a broader scatter of the RMS values compared to the carved tip geometries and a general trend cannot be distinguished. Fig. 5.17 shows the surface heat flux distribution for two profiles 'A' and

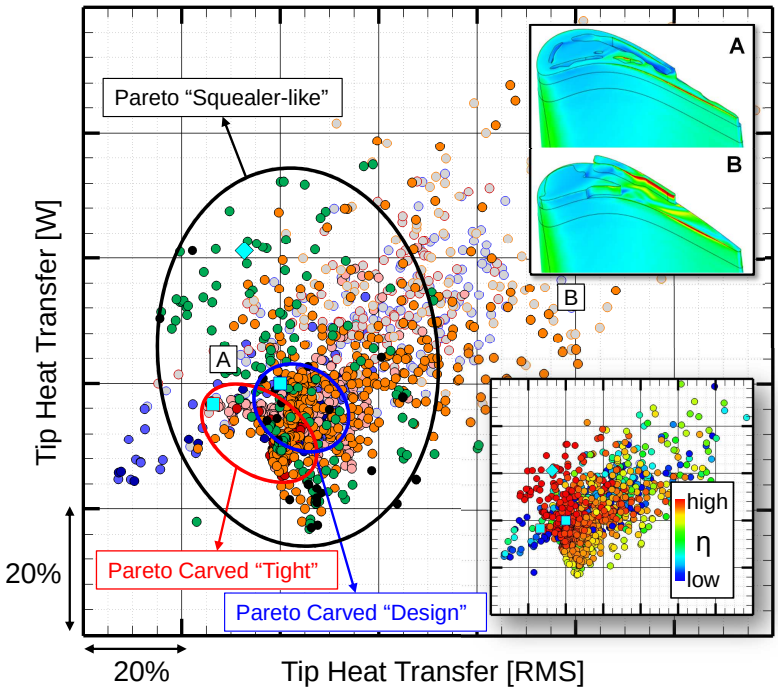

Figure 5.17: Tip heat transfer [W] in function of the heat load RMS value.

'B' that have similar tip heat transfer levels, but differ significantly in terms of RMS value ($> 60\%$ of the flat tip RMS value). Profile 'A' exposes a more uniform tip heat flux distribution (low RMS) compared to profile 'B', and the highest heat flux peaks remain confined on a small region in the proximity of the aft PS edge. On profile 'B' spread zones of high heat transfer are visible on the aft blade rims and cavity floor, which makes this tip design more susceptible to thermal fatigue issues. Wide apertures in the outer seal rims (profile 'B') are particularly detrimental for the heat transfer performance. The tip leakage flow enters the open tip channel in the front suction side and accelerates within the squealer cavity. A strong fluid interaction takes place between the high-speed jet in the squealer bath and the spillage flow that crosses the blade tip at the rotor mid-chord pressure side. The mixing of the two fluid streams generates local hot spots on the mid-chord cavity floor and on the inner surface of the SS rim. On the contrary, a continuous seal rim running along the external

blade perimeter (blade tip 'A') prevents the creation and the consequent interaction of high-momentum hot streams within the squealer channel.

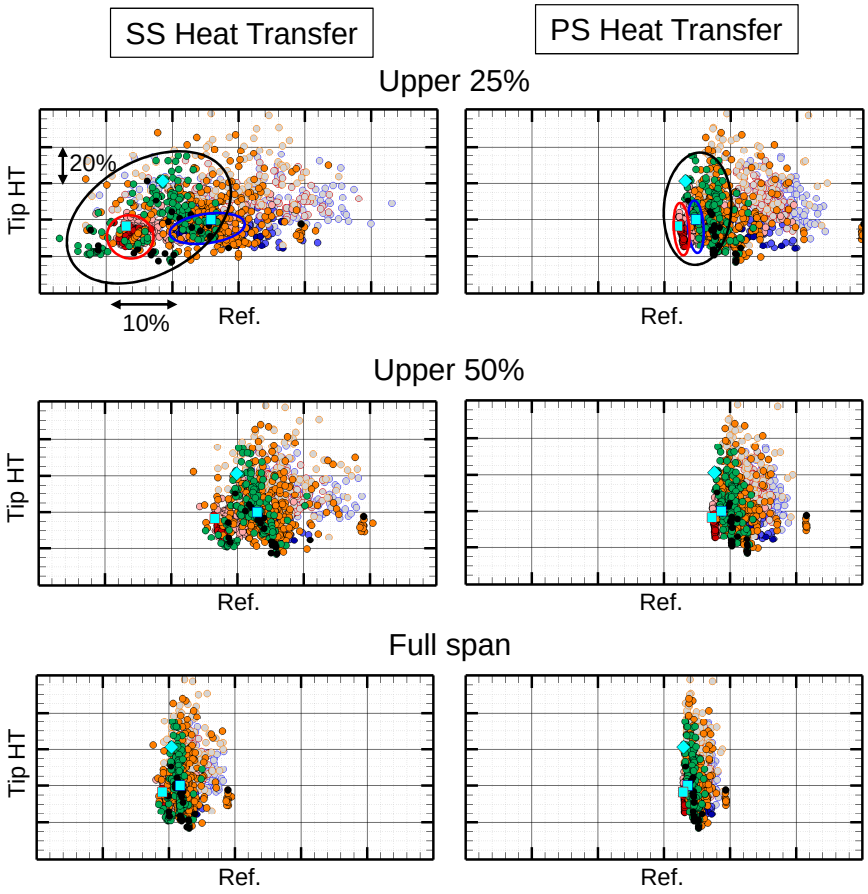

Figure 5.18: Heat transfer to the SS and PS for the upper 25%, upper 50% and the full blade span.

In order to quantify up to what extent the tip design influences the rotor blade thermal loads, Fig. 5.18 plots the tip heat transfer optimization objective (vertical axis, 'Tip HT') against the heat transfer onto the rotor SS and PS surfaces (horizontal axis). For comparison purposes, the same reference heat transfer value ('Ref') normalize both the pressure and suction side heat transfer data. The graphs on the upper part of Fig. 5.18 display on the horizontal axis the heat transfer on the upper 25% of the blade span. The middle and bottom plots report the heat transfer over the upper 50% and the entire blade height respectively. On the upper 25% of the blade

span, the suction side heat transfer varies up to 50% depending on the tip design. On the contrary, the heat transfer on the upper 25% of the pressure side is less sensitive to the specific tip geometry and the performance scatter is reduced to about 25%. Most of the variability in suction and pressure side thermal loads can be attributed to those profiles with large tip clearance that were simulated during the initial phases of the optimization (e.g. the numerous DoE samples on the right side of Fig. 5.18-top). A more intense tip leakage flow is associated with larger tip gaps which in turn plays a role on the flow pattern in the near-tip blade pressure side. The profiles that lie on the Pareto front (identified by the colored ellipses in Fig. 5.18) show less pronounced variations in heat transfer on both the blade pressure side ($\sim$10% for the squealer-like geometries, $\sim$2-3% for the carved tip designs) and suction side (about 25% for the for the squealer-like geometries, $\sim$10% for the carved tip profiles). As it can been deduced from Fig. 5.18-bottom, the effect of the tip leakage flow structure on the whole blade heat transfer is less strong and variations below 15% for the SS and below 8% for the PS can be attributed to the rotor tip configuration. Individuals with the lowest tip heat transfer or superior aerodynamic performance showed large variability in the SS and PS heat transfer levels. Overall, the near-tip heat transfer data did not reveal any clear correlation with optimal blade tip geometries.

5.8 Conclusions

This chapter introduced two novel optimization strategies for the design of the blade tip section of unshrouded turbine rotors with enhanced aerothermal performances. A first strategy evaluates fully three-dimensional contoured blade designs based on a general Bezier surface (40 parameters) mapped onto the tip geometry. The optimization was performed at two different tip clearances using a Differential Evolution algorithm. The second methodology uses an approach similar to a topology optimization strategy where the tip area was divided in about 200 distinct blocks which can be either part of an upstanding rim or be set down to constitute the cavity floor. This strategy allowed to generate almost every possible rim-cavity layout during one single optimization. In total, around 700 carved tip profiles and 800 squealer-like geometries were evaluated during 4 consecutive multi-objective optimizations which targeted the simultaneous increase of the aerodynamic efficiency and the reduction of the overtip heat load.

The results show that a flat tip represents a prime design choice in terms of efficiency for the investigated turbine hardware when the optimization space is limited to the carved tip shape approach. However, the Pareto front for these optimizations revealed the possibility of an immediate heat transfer reduction of 5% through the creation of a diverging passage in the aft part of the blade. Further heat transfer reduction is accessible by reducing the suction side tip radius up to the blade leading edge region. Interestingly, tip profiles running at a tight clearance require a more aggressive tip contouring than what is demanded by geometries at the design clearance to achieve the same heat transfer enhancement.

The final Pareto front for the squealer-like tip optimization showed additional aerodynamic improvements and a reduced sensitivity of the efficiency compared to the contoured blade design approach. The exchange rate between the aerodynamic performance and the tip heat flux for the squealer-like optimal profiles was proven to be twice as high as for the carved tip design strategy.

Variability in massflow and power extraction remains fairly low for the contoured profile optimization. On the contrary, the squealer-like designs along the Pareto front show almost 4% scatter in massflow and 3% in torque, with significant variations in the rotor exit flow field structure. Two distinct zones of high aerodynamic performance were identified corresponding to blades with a closed and fully opened aft-section.

The comparison of the area averaged heat load and its RMS value showed that while the heat flux in the case of the rim-type designs tends to be generally lower due to the larger wetted area, the occurrence of hot spots is considerably increased. The influence of the tip shape is most significant on the upper 25% of the blade span and strongly depends on the tip leakage vortex physics. The tip design can account for variations in heat transfer up to 50% on the near-tip suction side and up to 25% on the near-tip pressure side.

One of the most important conclusions of this investigation was the demonstration of the two novel optimization strategies to uncover unexplored types of turbine tip geometries. The analysis of the generated tip profiles shows that the final tip geometry selection should not only result from a trade-off between efficiency enhancement and tip heat transfer reduction, but must take into account a combination of additional aerodynamic parameters (e.g. the rotor outlet flow field) and thermal aspects (e.g. presence of hot spots, coolability issues). The optimization results illustrated that a significant number of new heterogeneous tip geometries exist that can offer increased aerothermal performances, beyond the standards of prevalent conventional tip designs adopted in modern gas turbine engines.

CHAPTER 6. AEROTHERMAL FIELD OF SQUEALER-LIKE PROFILES AND PERFORMANCE ROBUSTNESS

6.1 Operational and Manufacturing Variabilities

The actual tip profile in operation may differ significantly from the optimal designed geometry. Manufacturing tolerances as well as engine operation effects (e.g. transients, erosion, oxidation, creep, rubbing, foreign object damage) can lead to considerable shape alterations [9, 139]. However, the influence of these uncertainties is rarely the subject of academic studies and their actual impact on the aerodynamics and heat transfer remains vague.

Lattime and Steinetz [21] quote that axisymmetric clearance changes of 0.03 in. are not uncommon during take-off for large commercial engines (e.g. 1.5% of a typical blade span) and can reach even larger values when flight-induced asymmetric loads are included. Clearance measurements by Glezer [140] on the first stage of a mid-size industrial turbine showed gap variations between 2.2% and 0.6% of the blade span during engine transients. Hershey et al. [141] present a 20 mils change of the tip gap during transients (e.g. about 1% of a representative rotor height). Additionally, Bunker [142] quotes the variations of the aerodynamic profile shape and the thermal barrier coating thickness due to manufacturing inaccuracies to be ± 0.05 mm in the case of a large heavy frame gas turbine.

Recently, non-intrusive probabilistic uncertainty methodologies such as polynomial chaos expansion and stochastic collocation methods [143] have received an increasing interest [144]. These methods allow to propagate large uncertainties through

---

This Chapter is based on:

C. De Maesschalck, C. Lacor, G. Paniagua, L. Lavagnoli, A. Remiot, and Bricteux L. Performance robustness of turbine squealer tip designs due to manufacturing and engine operation. In *ISABE 2015 Conference Proceedings*, number ISABE2015-20205. [138]

complex models while requiring singlificantly less simulations compared to conventional Monte Carlo methods. Considering the relatively high computational cost of turbomachinery computational fluid dynamics, these efficient techniques offer opportunities to include a-priori known uncertainties already from an early design phase, or test a-posteriori the robustness of the design outcome [145]. Such assessment, indispensable for a proper reliability evaluation [142,146], could additionally be used to justify discrepancies between numerical predictions and experimental data [147,148]. Nevertheless, these methods are not widely adopted (yet) in the gas turbine community [149], except for rare examples [150]. Moreover, to the best of the researcher's knowledge, no rigorous study on the combined geometrical effects of a squealer tip has been conducted using such non-intrusive uncertainty quantification methodology.

Therefore, the current chapter presents the results of an extensive numerical study, investigating the robustness of a squealer tip design to manufacturing tolerances and operational degradation, adopting the stochastic collocation method. This part of the research provides a deeper insight into the distinct geometrical influences on the aerothermal characteristics and reliability of the turbine rotor and quantifies confidence intervals for the heat transfer signatures and aerodynamic flow properties.

6.2 Numerical Methodology

The simulated blade row subject of this robustness analysis is the same high pressure turbine stage as adopted during the 3D optimization (cfr. Chapter 5). The most important specifications are presented in Table 5.1. Additionally, the 2-block strategy for the computational domain was employed (see Fig. 5.1), allowing the need to only change the upperblock for every evaluated case.

A fully hexahedral mesh is generated through Numeca Hexpress, separately for both subdomains. Fig. 6.1 shows the results of a grid sensitivity study, focusing on the overtip heat transfer characteristics of interest. For this study, a general squealer design with sharp rim edges was used, adopting gradual isotropic refinements (while

maintaining the mesh density for the other domain constant). Fig. 6.1 presents the variability of the heat transfer onto the tip (solid lines) and the overtip casing (dashed lines) compared to the finest grid solution. The lower and left axis refer to the influence of the down-block refinement (blue curves with square labels) and the upper and right axis to the upperblock resolution (red curves with round markers). The influence of the downblock resolution on the tip and shroud heat transfer is limited: less than 0.4% between the two finest grids. The influence of the upperblock is more pronounced but still limited to 1.5% between the two finest grids.

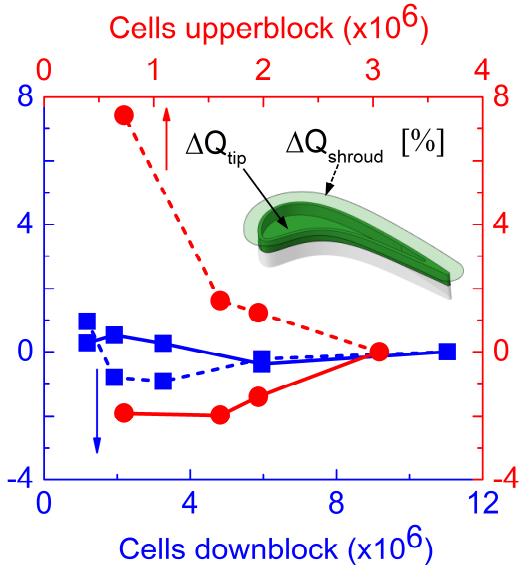

Figure 6.1: Mesh sensitivity analysis: effect on tip (solid lines) and shroud (dashed lines) heat transfer.

Therefore, the computational grid settings were chosen to be identical to the one during the optimization, i.e. the 2nd finest mesh (cfr. section 5.2, Fig. 5.2). However, additional refinements were included here to capture accurately the rim corner radii. This results in a significant increase of the average total amount of cells for the upperblock mesh from about 2-3 million, up to 5-6 million. Together with the downblock, containing 6 million grid points, final grid sizes of 11-12 million cells are obtained. The blade span of the main passage is divided into roughly 140 radial

divisions while the tip gap height has been discretized with about 40 cells. The first cell size was fixed such that the y^+ values remain below 0.2 along all solid surfaces to accurately resolve the entire aerothermal boundary layer. A view of the final mesh for the baseline squealer design and a zoom into the overtip region can be seen in Fig. 6.2.

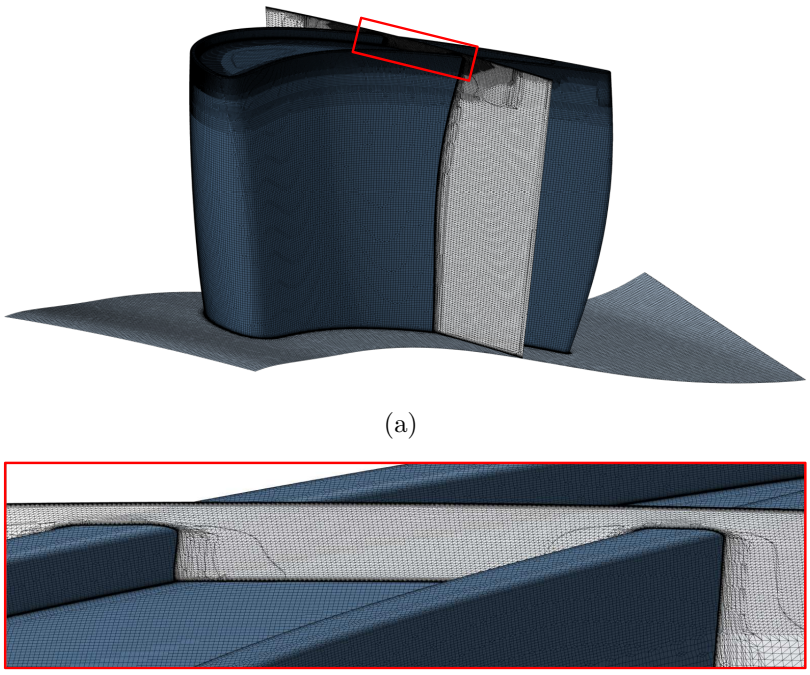

(a)

(b)

Figure 6.2: Full rotor mesh (a) and zoom of the tip gap region (b).

The simulations were performed with Numeca Fine/OPEN, adopting a 3-step multigrid approach to accelerate convergence. Dry air was selected as the working fluid, modeled as a thermally perfect gas. Specifically, temperature-dependent profiles for the heat capacity, thermal conductivity and dynamic viscosity [151] were employed. The turbulence closure was obtained through the Spalart Allmaras model [66], implemented including the improvements described by Ashford and Powell [68].

The same boundary conditions were adopted as for the 3D optimization (Table 5.1): at the rotor inlet the pitchwise averaged radial profiles of relative total pressure,

temperature, flow angle and turbulent quantities, and a static pressure at the downstream end of the computational domain, satisfying the radial equilibrium condition.

6.3 Robustness Assessment

6.3.1 Geometrical Variability

Fig. 6.3a shows the investigated squealer tip geometry, widely used in the industry, consisting of an upstanding rim all along the pressure and suction side which creates a central cavity. Ideally, the turbine operates at a predefined design clearance (i.e. the distance between the rotating blade and the stationary shroud) and the top edges of the squealer rims are sharp. However, these rim edges are prone to wear due to the extremely harsh pressure and temperature operating conditions, which results in the radiusing of the top rims during engine service [55, 152]. Moreover, unintentional rubbing of the blade tip against the non-rotating casing may cause scraping of the squealer rim and consequently give rise to a reduction of the cavity depth. Lastly, during engine transients, the tip clearance undergoes large variations induced by the different thermal dilatation rates of the rotating and stationary components.

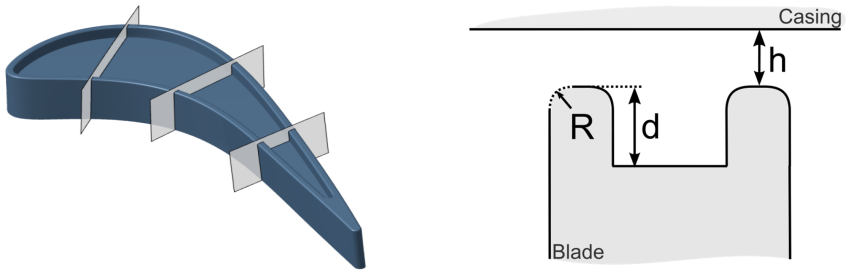

(a) (b)

Figure 6.3: Squealer design (a) and investigated tip parameters (b).

The three distinct features of the squealer tip geometry (radius 'R', cavity depth 'd' and clearance height 'h') are presented in Fig. 6.3b. The baseline squealer geometry adopts a design clearance of 1.38% of the blade span. The rim thickness and

cavity depth are 1.23 and 2.5 times the design clearance respectively (i.e. 1.7% and 3.4% of the blade span), resulting in a cavity depth to rim thickness ratio of 2. The baseline radius is 25% of the rim thickness. The parameter variabilities are considered representative of the profiles' degradation during engine operation and typical manufacturing errors [21, 140–142]. The latter are summarized in Table 6.1, reported as percentage of the blade span or rim thickness. All uncertainties are assumed to have a normal distribution.

Table 6.1: Investigated parameter variations.

Parameter	[%]	Baseline (μ)	$\sigma_{\text{op.}}$	$\sigma_{\text{man.}}$
Tip clearance '**h**'	Blade span	1.38	0.45	0.17
Cavity depth '**d**'	Blade span	3.40	1.19	0.08
Corner radius '**R**'	Rim thickness	25	10	-

6.3.2 Stochastic Collocation

For this work, the Stochastic Collocation Method (SCM) has been used to assess the eventual uncertainty on an output quantity $y(\mathbf{x},\xi)$ due to a set of known geometrical input variabilities.

In this case, the output quantity of interest (y) could be the heat flux at a certain location $\mathbf{x}$ inside the domain where ξ are the independent standard random variables (e.g. variations in the clearance height or cavity depth). The SCM [143] describes the stochastic response $y(\mathbf{x},\xi)$ by adopting a polynomial expansion based on the Lagrangian interpolation of the $\mathrm{N_p}$ samples at the Gaussian quadrature points:

$$y(\mathbf{x},\xi) \approx \sum_{j=1}^{N_p} y_j(\mathbf{x}) L_j(\xi) \tag{6.1}$$

Where the coefficients $y_j(x)$ are the simulation results at the interpolation points ξ_j and the Lagrangian polynomials $L_j(\xi)$ are defined as:

$$L_j(\xi) = \prod_{\substack{i=1 \\ i \neq j}}^{N_p} \frac{\xi - \xi_i}{\xi_j - \xi_i} \tag{6.2}$$

In this case, combined effects of the multiple geometrical effects are considered and the consequent multi-dimensional interpolation is performed based on a tensor product approach, adopting all N_p samples. In order to maximize the performance, the collocation points defined from the optimal orthogonal polynomials were used. In the case of a normal input distribution, the collocation points for a Lagrange interpolation of order p are the roots of the Hermite polynomial of order p+1 [153].

For the SCM [143], the first two statistical moments of the output variable, the mean μ_y and the variance σ_y^2, are analytically available in a closed form:

$$\mu_y = \sum_{j=1}^{N_t} y_j(\mathbf{x}) w_j(\xi) \tag{6.3}$$

$$\sigma_y^2 = \sum_{j=1}^{N_t} y_j^2(\mathbf{x}) w_j(\xi) - \mu_y^2 \tag{6.4}$$

where w_j are the quadrature weights corresponding to a certain collocation point. The open-source toolkit DAKOTA [154] from the Sandia National Labs has been used to calculate the latter statistical moments from the CFD simulations. Specifically, the spatial heat flux distributions and flow data extracted from the turbine domain were fed into the Stochastic Collocation module of DAKOTA to retrieve the eventual robustness intervals.

6.3.3 Investigated Cases

The simulated tip designs are summarized in Fig. 6.4. The three axes show the three different geometrical effects: the clearance gap, the cavity depth and the corner radius. The Baseline case is centered at the origin, further denoted as 'BL'. In order to evaluate the influence of the operational variabilities, 6 cases were computed,

each located at the roots of a 3rd order Hermite polynomial ($\mu \pm \sqrt{3}\sigma_{op.}$, blue labels, simulations h^+/h^-, d^+/d^- and R^+/R^-). Additionally, the combined effect of a change in tip clearance and cavity depth was investigated (red labels, simulations 1-4). The influence of the manufacturing tolerances was only assessed for the combined change in tip gap and cavity depth (green labels, a-h).

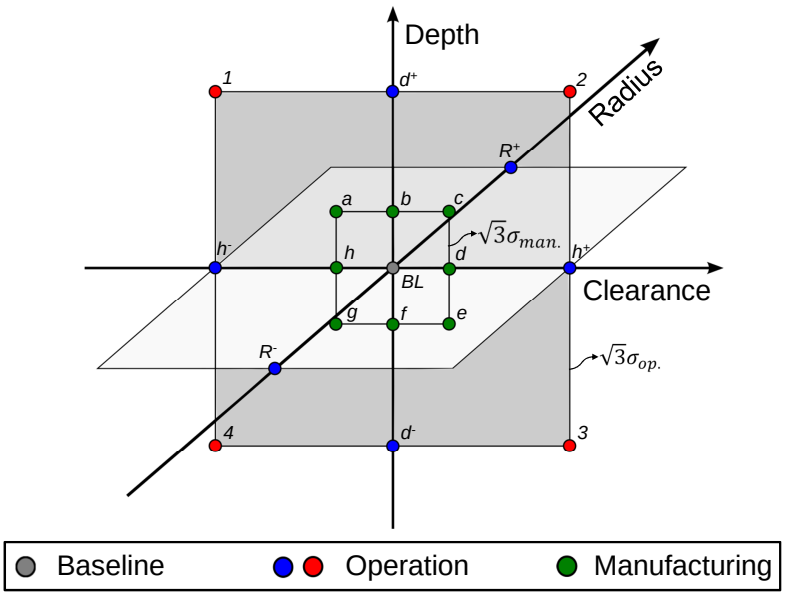

Figure 6.4: Overview of the evaluated cases.

The investigated levels of tip clearance, cavity depth and rim corner radius are summarized in Table 6.2.

Table 6.2: Characteristics of the simulated designs.

Parameter[1]	$\mu - \sqrt{3}\sigma_{op.}$	$\mu - \sqrt{3}\sigma_{man.}$	μ	$\mu + \sqrt{3}\sigma_{man.}$	$\mu + \sqrt{3}\sigma_{op.}$
Tip clearance '**h**'	0.60	1.09	1.38	1.67	2.16
Cavity depth '**d**'	1.34	3.26	3.40	3.54	5.46
Corner radius '**R**'	7.68	-	25.0	-	42.3

[1]the same percentage conventions were adopted as in Table 6.1

6.4 Results

First, the influence of the corner radius will be discussed (section 6.4.1) as well as the rotor global performance (6.4.2). Then, the overall flow topology (6.4.3), heat transfer (6.4.4) and loss production (6.4.5) will be analyzed more in detail, focusing on the combined effect of clearance and cavity depth variations.

6.4.1 Influence of the Corner Radius

Fig. 6.5a presents the influence of the corner radius on four turbine performance indicators: the turbine efficiency and the heat fluxes onto the blade tip, overtip shroud and upper 50% of the suction side. Each quantity is compared to the baseline case ('BL').

Larger radii of curvature lead to a decrease in size of the separation bubble created at the pressure side of the rim where the leakage flow enters the overtip cavity. Hence, a large amount of fluid is ingested into the tip gap [55] and the strength of the tip leakage vortex (TLV) is enhanced. Consequently, the rotor efficiency reduces almost linearly with the rim corner radius as more leakage mass flow is produced. The numerical results indicate that the rotor efficiency decreases by roughly 0.15% per 20% of corner radius increase. Both the tip and the suction side heat transfer intensify for larger rim corner radii, while the shroud heat transfer reduces.

Fig. 6.5b presents the tip heat flux for the baseline case as well as the results of the simulations performed with a smaller (R^-) and a larger (R^+) radius. We notice that the increase of total tip heat transfer is associated to the stronger vortical structure impinging on the tip cavity bath in the aft part of the blade (Fig. 6.5b, 'A'), overcompensating the slight decrease in the strength of the hot spot near the leading edge. The decrease in shroud heat transfer is mainly located at the PS entrance in the downstream half of the turbine rotor.

Even though extreme cases for the corner radius were investigated (ranging from $\sim$8% up to $\sim$42% of the rim thickness), the influence of this parameter remains

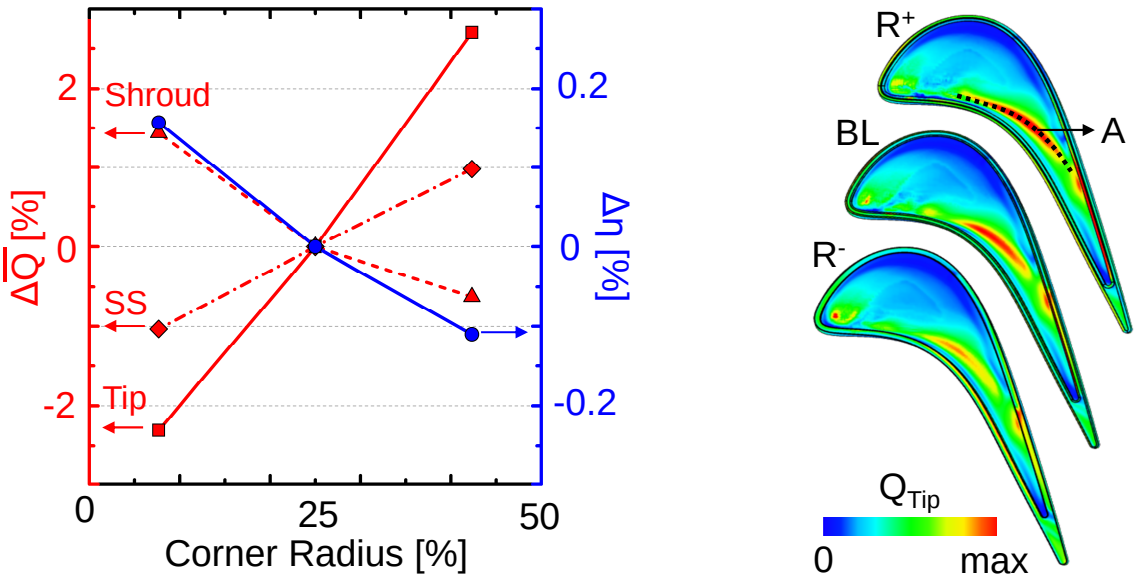

(a) (b)

Figure 6.5: Influence of the corner radius on global performance (a) and tip heat flux (b).

relatively limited (in particular concerning the heat transfer) compared to the other two geometrical effects: variations in tip clearance and cavity depth. For this reason, only the combined effect of the latter two parameters was simulated and taken into account for the total robustness quantification. However, where relevant, the influence of the corner radius will be indicated.

6.4.2 Global Performance

Fig. 6.6 shows the influence of the gap size and cavity depth on the rotor performance. The contour plots display the variation in efficiency and heat transfer onto the tip, suction side and overtip shroud relative to the BL case. The results for all the simulated cases with an adjusted clearance and/or cavity depth are included. A cubic interpolation was adopted to generate the contours and reveals the general trends associated over a wide range tip gap sizes and cavity depths.

The efficiency is primarily dominated by changes of tip clearance and it increases almost linearly, about 2% per 1% of gap size reduction, in accordance with previous studies [14]. On the heat transfer side, tight clearances are generally associated with lower thermal loads. The cavity depth has a higher impact on the rotor heat transfer levels than on the rotor efficiency. On the tip, the surface averaged heat flux is generally the highest for the baseline cavity depth. At large tip gaps, cavity depths lower or higher than the baseline value reduce the tip heat transfer by more than 5%. For clearances close to the design value, the tip heat transfer is less affected by variations of cavity depth. At tight clearances, larger depths are generally favorable to reduce the tip heat transfer.

The heat transfer on the stationary rotor shroud is found insensitive to variations of the cavity depth for tip gap sizes smaller than the design value. At increased clearances, the analysis shows that an optimum cavity depth exists that minimizes the shroud thermal load (for the present case in the range of the nominal cavity depth). However, only a potential reduction of 2-4% of the shroud heat transfer is possible through cavity depth variations.

The suction side heat transfer is primarily governed by the tip gap size and the lowest suction side heat transfer is obtained with larger depths at low tip clearances.

6.4.3 Overtip Flow Topology

Fig. 6.7 illustrates the flow topology in the overtip region while Fig 6.8 presents a broader view of the tip leakage and upper passage vortex structures together with the suction side surface streamlines. Fig 6.7 and 6.8 were constructed using the baseline case (BL).

In 6.7, the solid walls are colored by the heat flux levels while the relative Mach number distributions with streamlines are displayed on several cutting planes along the rotor camberline. Due to the size of the incoming boundary layer carrying low momentum fluid and the relative casing movement, fluid enters the blade tip chan-

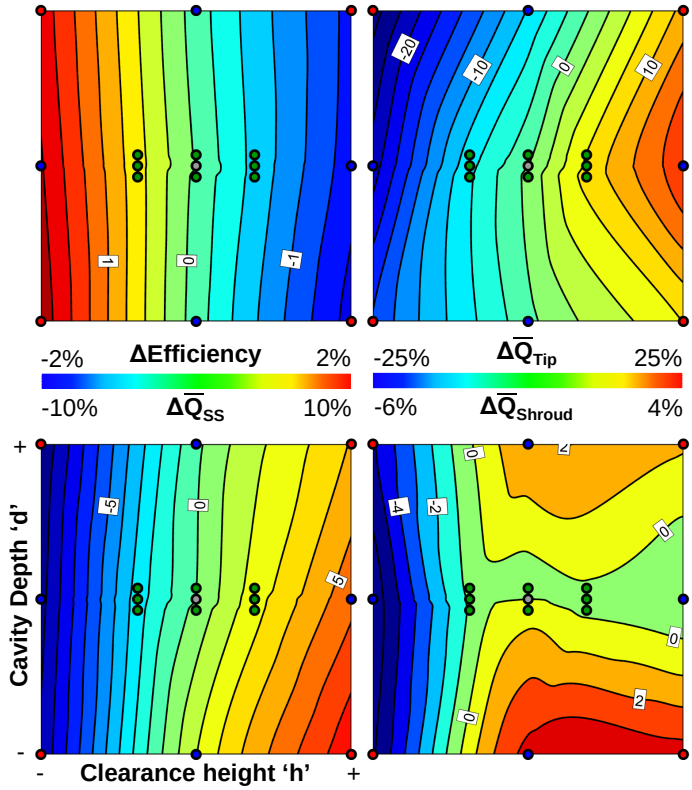

Figure 6.6: Global performance for clearance and cavity depth variations.

nel both at the pressure side (blue streamlines) as well as at the suction side (red streamlines). The flow crossing the suction side rim rolls up in a large vortex that creates a considerable zone of low heat transfer in the front section of the tip cavity. The fluid ingested inside the squealer bath turns along the blade camberline, gets pushed towards the shroud and exits the overtip region by crossing the suction side squealer (region 'A'), contributing to the formation and energization of the TLV. The distribution and the levels of suction side heat transfer are determined by the location of the initiation point of the TLV (indicated with 'B') and the location where all the fluid that entered the tip region from the suction side has exited the squealer cavity ('C'). The flow entering through the pressure side rim in the front part of the blade rolls up into a vortex, remains entrained close to the pressure side squealer and leaves the gap region in the aft section of the blade. In region 'D' (right downstream the

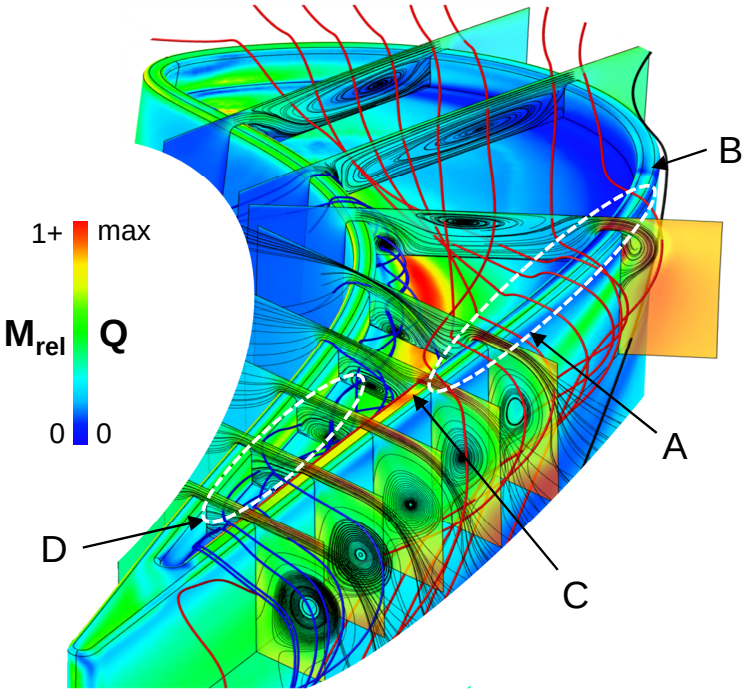

Figure 6.7: Flow topology for the baseline case with blade heat transfer and overtip Mrel contours.

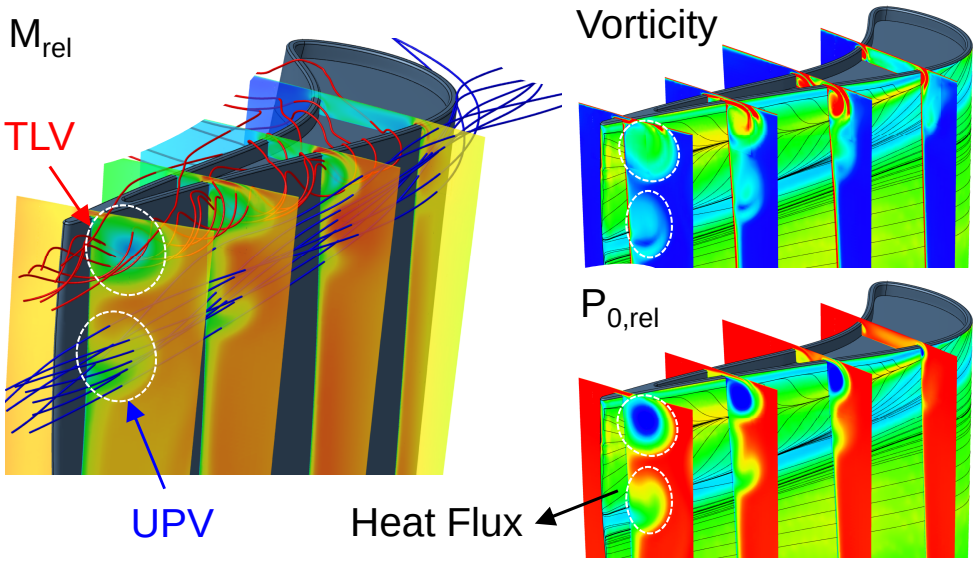

Figure 6.8: Illustration of the tip leakage and upper passage vortex structures.

switch-point 'C'), the fluid coming from the PS does not enter the cavity anymore but gets directly accelerated and ejected towards the suction side into the TLV which gathers strength as it progresses downstream towards the rotor outlet.

Fig. 6.9 illustrates the relative Mach number distribution at mid-height for all investigated cases. In the front and central part of the blade, the overtip Mach number tends to increase for larger cavity depths (in particular near the SS) and increases moderately when rising the tip clearance level. In the aft part of the blade, enlarged tip gaps induce higher overtip velocities. Interestingly, a similar trend is observed when reducing the cavity depth. The signature of the exit jet shows the propagation of the TLV into the main passage (tracked by line 'A') and its characteristics are mainly dictated by the tip gap size. The circles depict zones with a characteristic drop in Mach number, corresponding to the beginning of the region in the overtip gap where all the fluid that entered through the suction side rim has left the squealer cavity (cfr. Fig. 6.7, point 'C'). This is particularly visible for the cases where a significant amount of fluid is ingested in the overtip region, i.e. at large clearances and large cavity depths.

6.4.4 Heat Transfer Analysis

Tip

Fig. 6.10 presents the surface averaged tip heat transfer along the machine axis normalized by the heat flux of the BL case. To highlight the influences of the distinct geometrical variabilities, the simulations in which only one type of (operational) geometrical parameter was modified have been included in the plot, i.e. clearance size (h^-/h^+), cavity depth (d^-/d^+) and corner radius (R^-/R^+). Additionally, the $\pm 2\sigma$ uncertainty bands have been colored in light and dark grey to show respectively the operational and manufacturing variabilities. In order to explain the observed differences and trends in more detail, Fig. 6.11 displays the tip heat transfer distribution for all the nine cases with operational geometry changes.

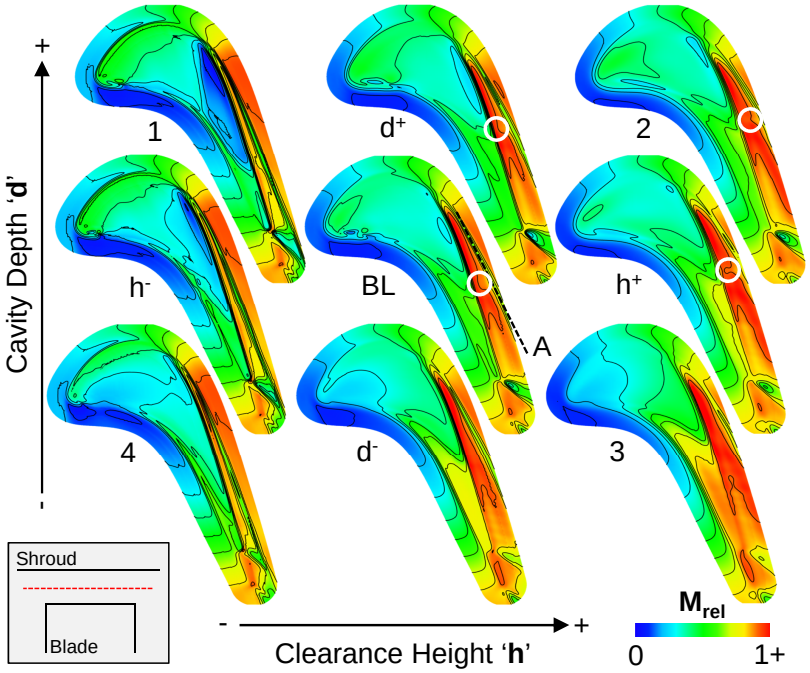

Figure 6.9: Mid-gap relative Mach number in the overtip region.

The general trend in Fig. 6.10 reveals an initial decrease followed by an increase in tip heat transfer along the rotor chord. Near the LE, the flow travels over the first part of the SS tip rim and impinges immediately onto the cavity floor (Fig. 6.11, region 'A'). This results in an enhanced heat transfer in the blade front part. Downstream the separation line with the flow coming from the pressure side (Fig. 6.11, 'B'), the overall surface heat flux decreases due to the large (slow) recirculation zone (cfr. Fig. 6.7). Eventually, the flow accelerates inside the cavity and a significant part of the heat transfer can be attributed to the impingement line of the pressure side vortex (Fig. 6.11, 'C'). Fig. 6.10 indicates that the tip clearance size is the main driver for tip heat transfer variations, accounting for fluctuations as high as ±25%. The changes due to the cavity depth are mainly located in the very front part (caused by the impingement strength of the vortex near the LE) and in the aft part. In the rear half of the blade chord, a decrease in depth lowers the absolute magnitudes of the heat transfer (e.g. Fig. 6.11, case d^- and 3), the reduced surface area brings it back

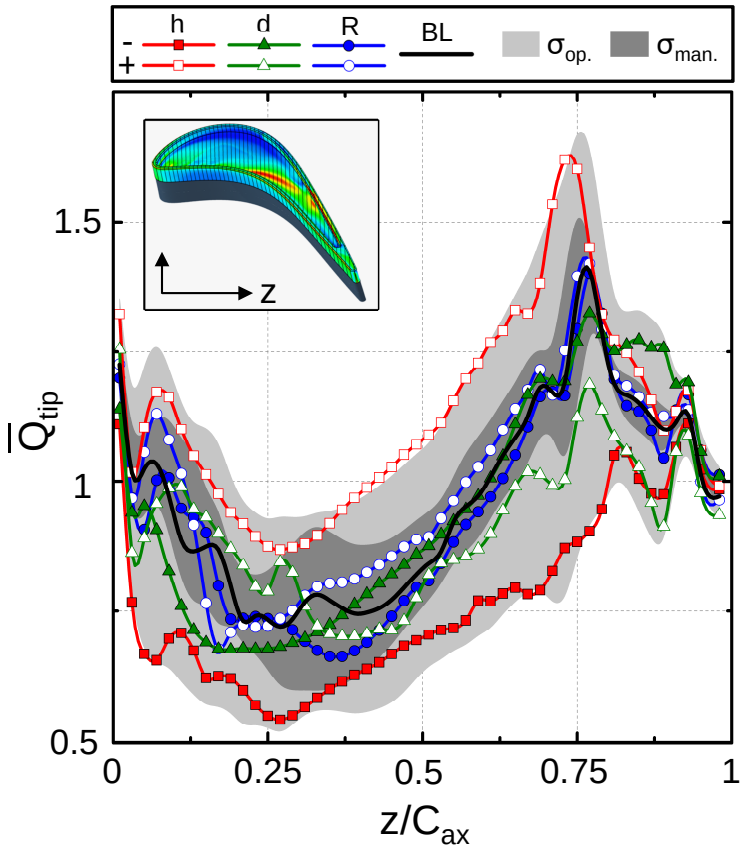

Figure 6.10: Tip heat transfer along machine axis.

to a similar level as the BL (Fig. 6.10). Increasing the depth similarly lowers the peaks by 10% in the aft part. Lastly, as indicated in Fig. 6.5, the overall sensitivity to the radius variations remains limited. However, in the central part of the blade, variations in heat transfer caused by changes in corner radius are of similar magnitude as variations induced by cavity depth modifications.

Shroud

Fig. 6.12 shows the casing heat transfer from 10% $C_{ax,rot}$ upstream of the rotor LE up to 10% $C_{ax,rot}$ downstream of the blade TE. For consistency, the same labels and color codes have been adopted as in Fig. 6.10. Up to 70% of the blade axial chord,

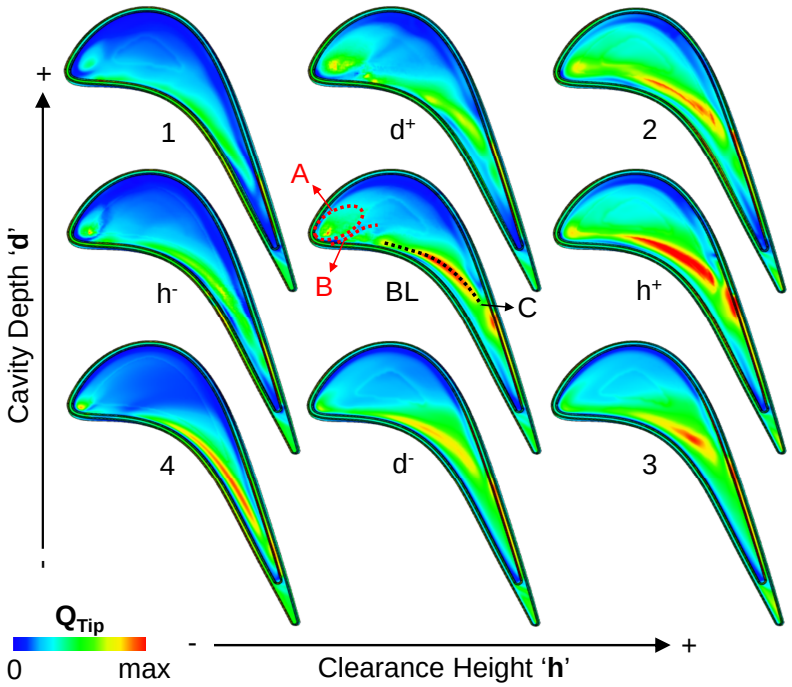

Figure 6.11: Tip heat transfer contours for clearance and cavity depth variations.

the thermal load variations remain below ±10%, mainly caused by local changes in the heat flux levels right above the rim top surfaces. However, in the blade aft part and further along the machine axis, the shroud heat transfer becomes very sensitive to tip geometry variations. In particular, the shroud heat flux exposes a distinct distribution for the tight clearance case compared to the cases operating at design and large clearances.

Fig. 6.13a illustrates the overtip shroud heat transfer for the large cavity depth at small (Case 1), baseline (Case d^+) and large (Case 2) clearances. For the tightest clearance, there is only one line of high heat transfer near the SS. However, for the two other clearances, two parallel stripes of large heat transfer emerge, aligned with the SS edge. Fig. 6.13b shows a detailed view of the overtip shroud heat transfer, together with several cuts of the relative Mach number that picture the TLV location and strength. In the case of the tighter clearance (Case 1), the TLV size is rather small and its core remains close to the SS surface. Consequently, the flow leaving

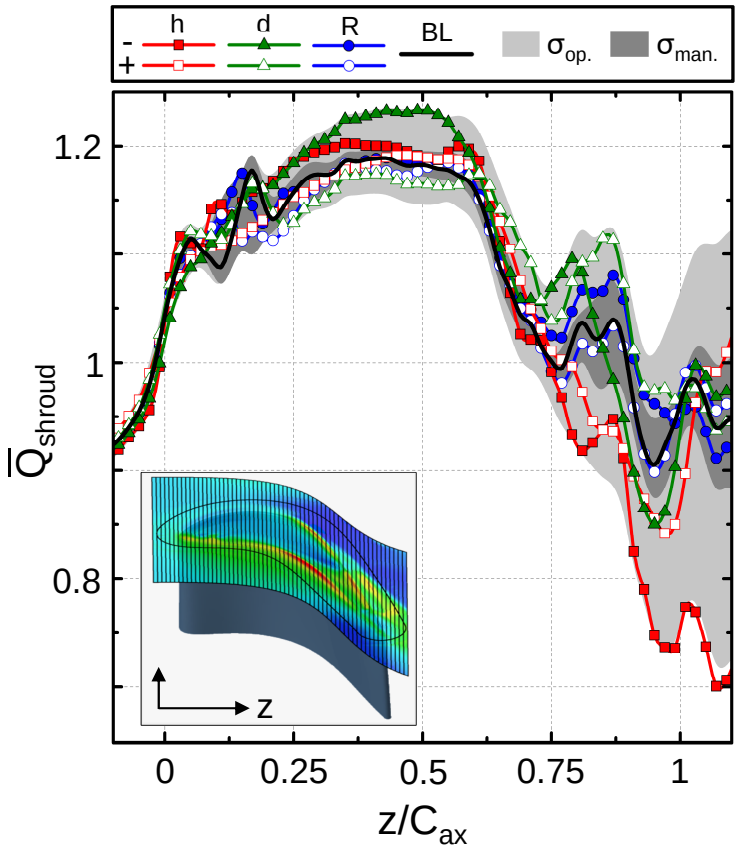

Figure 6.12: Shroud heat transfer along machine axis.

the overtip region across the SS rim bends immediately downwards and rolls up into the tip leakage vortex. For larger clearances, the vortex size is considerably more voluminous and its center is displaced further away from the SS. Therefore, the flow is contracted a first time when crossing the SS rim (first line of high heat transfer, 'A'), remains close to the shroud surface, and then is accelerated a second time ('B') when passing the vortex centerline before rolling up into the TLV.

Suction Side

Fig. 6.14a shows the surface averaged heat load onto the suction side for the upper 25% of the blade span. The presented cases and adopted symbols are identical

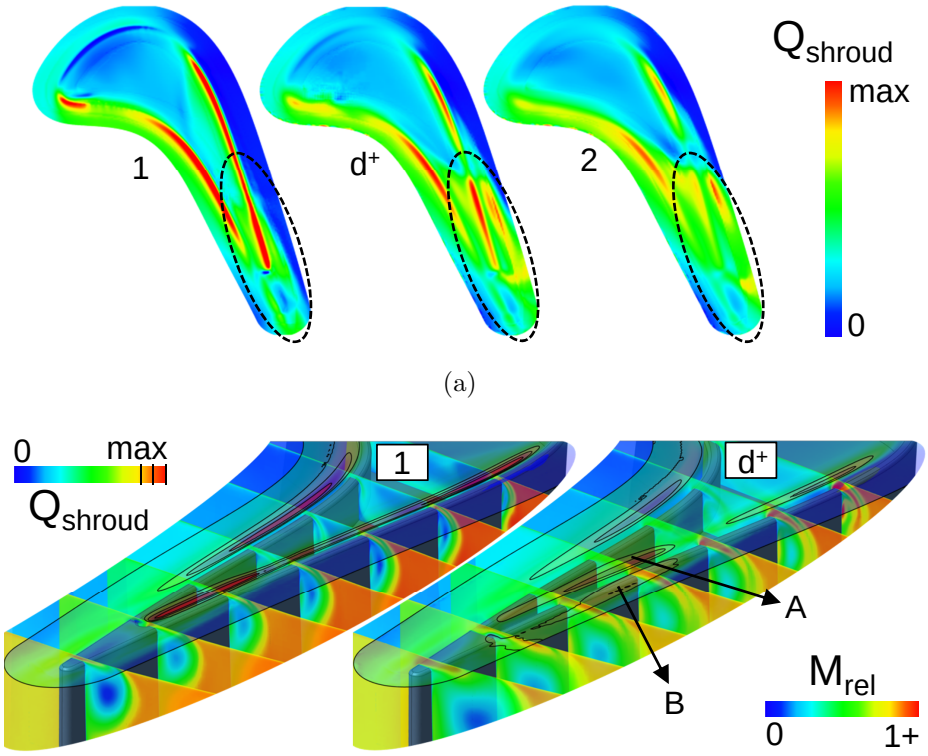

Figure 6.13: Overtip shroud heat flux for clearance variations (a) and driving vortex structures (b).

to Fig. 6.10 and Fig. 6.12. The heat transfer drops downstream of the leading edge and increases in the aft part ($z/C_{ax,rot}$ >50-65%). Interestingly, the heat transfer on the blade suction side is significantly affected by tip geometry variations over a large fraction of the blade length, with heat transfer variations as high as ±20%.

Fig. 6.14b presents the detailed heat transfer signature in the upper half of the blade suction side for the simulated case at a smaller clearance (h^-), the baseline case (BL) and a large clearance (h^+). The dashed line indicates the separation line between the emerging vortex structures and the main passage flow. These vortex structures include the upper passage vortex and the tip leakage vortex as illustrated in Fig. 6.8. The upper zone is divided into two parts, separated by another region of low heat transfer (dashed-dotted line). At the tip, the latter line coincides with the

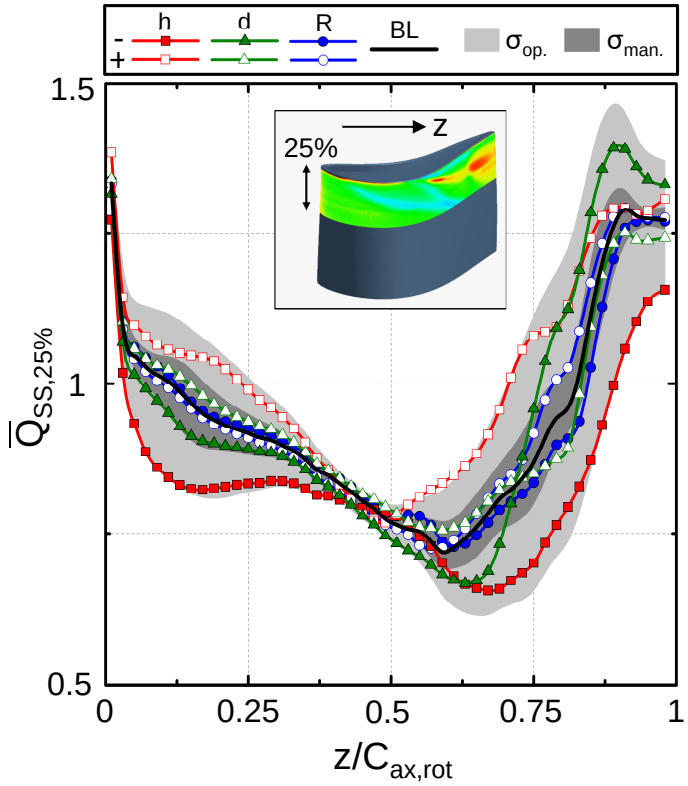

(a)

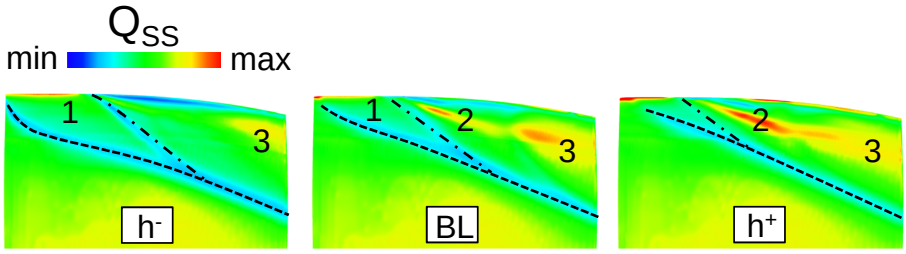

(b)

Figure 6.14: Suction side heat transfer along the rotor axial chord.

initiation point of the tip leakage vortex (i.e. point 'B' in Fig. 6.7). Consequently, the upstream region (labeled '1') is characterized by flow entering the cavity from the SS, while the downstream zones (marked '2' and '3') are characterized by fluid streams that exit the overtip region. The enhanced heat transfer in region 1 is the result of the 'scraping' of the boundary layer through the relative movement of the casing. Fluid

near the stationary shroud that does not enter the overtip gap gets pushed downwards, rolls up and merges eventually with the upper passage vortex (cfr. Fig. 6.8, blue streamlines). In the rear part of the blade, the heat transfer signature is determined by the TLV characteristics. A first region (2) can be identified, characterized by the initial development of the tip leakage vortex. A second region (3) starting at about 80% $C_{ax,rot}$ shows considerably enhanced levels of heat transfer. This hot spot is generated by the large overtip velocities reached by the flow that enters the PS, and is immediately accelerated towards the SS (Fig. 6.7, region 'D'). This leads to a sudden increase of the vortex size and strength and consequently produces a large thermal load on the suction side surface. Generally, the main driving parameter for the SS heat transfer is the clearance, where lower heat loads levels are associated with tighter gaps.

6.4.5 Loss Development and Downstream Field

In order to quantify the loss development throughout the turbine, Fig. 6.15 presents the vorticity and relative total pressure drop along the rotor axial direction (compared to the inlet and normalized by the downstream dynamic pressure measured in the BL case). For the sake of clarity, only the two cases with clearance variations are compared against the baseline simulation. The other investigated cases showed only very small differences with the BL case and are not reported. The ΔP_{0r} gives a direct indication of the loss generation across the stage. The tighter clearance induces slightly larger pressure losses in the first half of the blade. However, in the aft part, the larger size of the TLV (cfr. also the enhanced vorticity) combined with the downstream mixing overcompensates the initial trend, resulting in about 5% additional pressure losses compared to the baseline.

To investigate the effect of the tip geometry on the quality of the flow received by a downstream stator, Fig. 6.16a shows the relative total pressure drop and the flow swirl at 50% $C_{ax,rot}$ behind the rotor TE. Both clearance as well as cavity changes

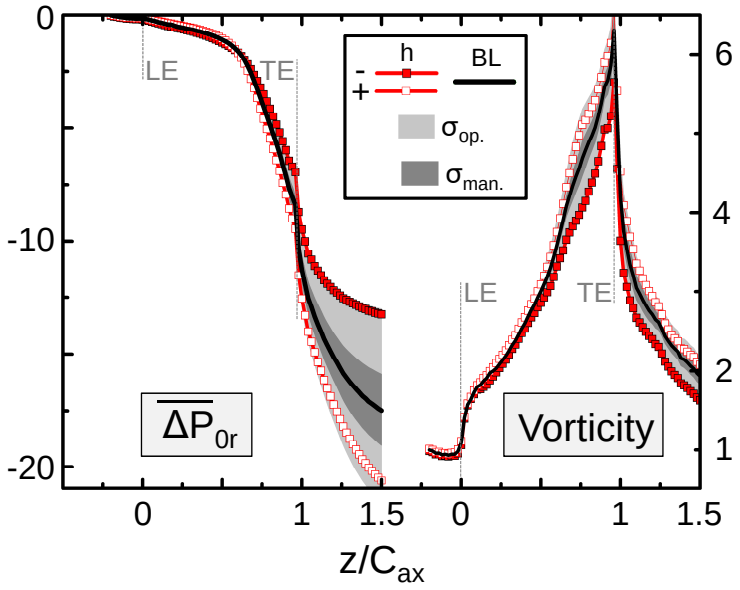

Figure 6.15: Total relative pressure losses and vorticity along $C_{ax,rot}$.

are included. The predictions indicate that the influence of tip clearance and cavity depth remains limited to the upper 50% of the blade span. Gap size variations can lead to a maximum change in flow angle of 40 degrees. The peak loss associated with the tip leakage core increases with the gap size, whereas the opposite trend is observed for the pressure loss associated with the center of the upper passage vortex. The effect of the tip clearance on the physics of the UPV and TLV is illustrated in Fig. 6.16b which shows contours of relative total pressure and the isolines help to identify the size of the vortical structures.

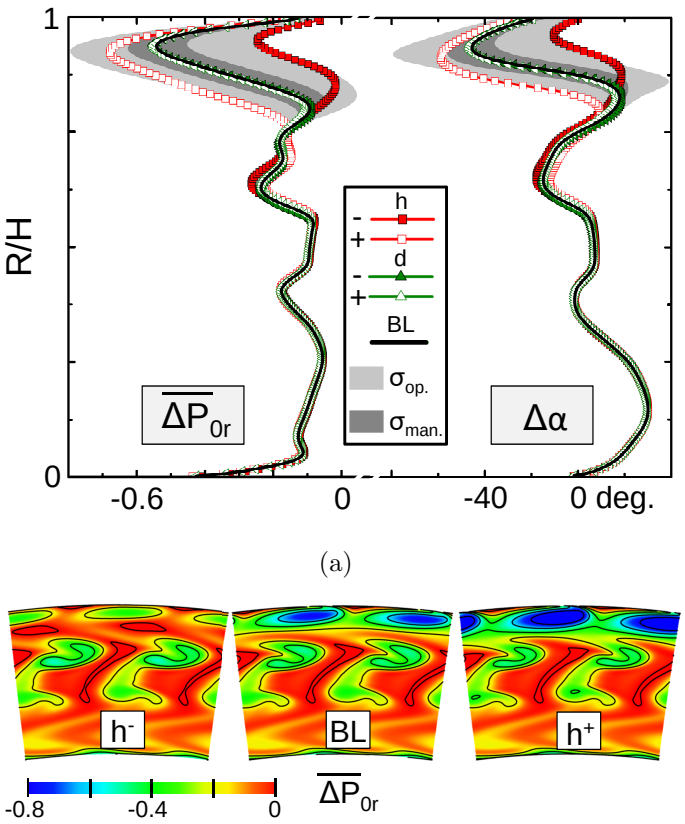

Figure 6.16: P_{0r} loss and absolute flow angle deviation 50% $C_{ax,rot}$ downstream of the rotor TE (a), P_{0r} loss for clearance variations (b).

6.5 Conclusions

Because of multiple factors the squealer tip rim corner, cavity depth and running tip clearance may vary from one rotor blade to another, during the life, and from engine to engine. This part of the research characterized the aerothermal performance of high pressure turbines under operational variability and manufacturing tolerances using advanced numerical tools. In particular, the stochastic collocation method was used to assess the robustness of the squealer tip design. Of all the different geometrical parameters considered, the corner radius has the smallest effect. The change of 40% in the corner radius caused only a change of 2% in the heat transfer and 0.15% in the

efficiency. The efficiency is primarily influenced by the clearance, a 1% variation in the tip gap results in a 2% variation in the turbine efficiency. Cavity depth variations alter the tip heat flux by more than 5% while the shroud heat flux increases by 2-4%.

Beyond the overall aerothermal performance parameters, this chapter presented a detailed characterization of the flow topology. Interestingly, a portion of the leakage flow enters the overtip region from the suction side, generating a large recirculation zone of low heat transfer in the front part of the blade. Along the suction side three distinct regions were identified: a first zone acts as an inlet whereas the two downstream zones let fluid leave the gap region. In between the latter downstream outlet zones we could observe a significant decay in the jet exit Mach number.

The detailed flow characterization was then related to the local heat flux values in function of the explored geometrical variability. The tip heat transfer distribution experiences variations of $\pm 25\%$, caused by the tip clearance change. The shroud thermal load shows considerable fluctuations in the last 30% of the rotor blade. Remarkably, the front part of the suction side is significantly altered by the geometrical changes. The downstream field is generally affected in the upper 50% of the blade height, giving rise up to 40 deg. angle deviations. Interestingly, low clearances slightly increase the upper passage vortex strength.

The present study yields insight into the robustness of squealer tip designs and points out the importance of integrating the effects of these inevitable geometry changes within the optimization strategies of future turbines.

CHAPTER 7. TIP FLOW CONTROL THROUGH CASING PURGE COOLING

This chapter first explains the additional potential of the upstream shroud purge (7.1) to enhance the overtip aerothermal characteristics. In order to have a representative case, a modern high-pressure turbine stage was scaled from lab conditions towards a real engine environment matching a business jet engine flying at cruising altitude (7.2). Section 7.3 introduces the computational model of the shroud purge flow and the overall optimization methodology is outlined. Eventually, the results and underlying flow physics are described in the last section (7.4).

7.1 The Potential of the Upstream Shroud Purge

The injection of coolant flow from the casing is implemented in the vast majority of the engines nowadays. This shroud purge flow, introduced right upstream the rotor blade leading edge, serves to prevent the ingestion of the hot gases towards the less durable components of the engine and provides additional cooling for the turbine blade tip section (Fig. 7.1a). Furthermore, the created axial gap allows the application of active clearance control strategies, permitting the modification of the shroud radius independently from the upstream and downstream components.

However, this purge flow enlarges artificially the incoming boundary layer to the rotor row. In the tip region the effect can be beneficial due to the creation of 'reversed' flow in the front part of the blade and the reduced overall amount of required coolant to lower the metal temperature of the tip features. In the main passage on the contrary, this increased low momentum fluid can give rise to an enlarged upper passage vortex, decreasing significantly the overall efficiency (Fig. 7.1b).

The work of Zlatinov et al. [155, 156] identified the beneficial effect of suppressing the tip clearance flow for a set of distinct cases with a constant purge injection geome-

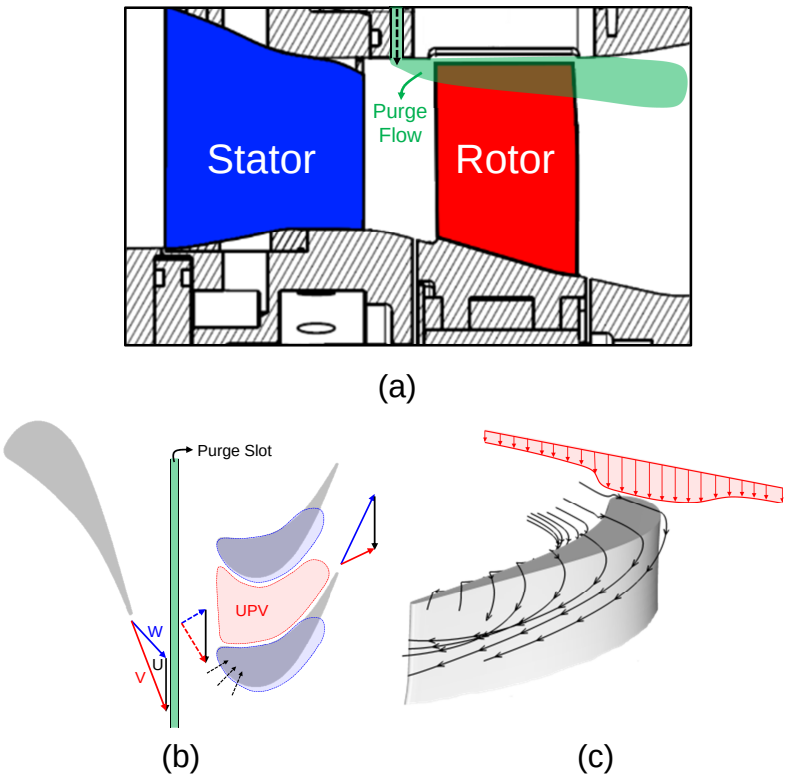

Figure 7.1: Purge flow injection location (a), a schematic of the downstream influence of the coolant flow (b) and a non-uniform ejection profile (c).

try. The additional losses were attributed to the viscous effects inside the shear layer, the interaction with the passage vortex and a change in the reaction of the turbine stage. Several other recent works by Bloxham and Bons [157], Collins et al. [158] and Tamunobere and Acharya [159] experimented with the flow injection through discrete holes on the overtip shroud to cool and additionally control the tip leakage and passage vortex.

This part of the doctoral research explores the possibility of maximizing the beneficial aerodynamic effect of the purge flow on the vortex structures, while assessing the coolant effect onto the blades tip section. This is achieved through a variation and optimization of the geometrical purge slot characteristics as well as the (circumferential) purge ejection profile (Fig. 7.1c), in a realistic engine environment.

7.2 Scaling Towards a Real Engine Environment

7.2.1 Turbine Geometry and Scaling Comparison

The turbine stage adopted for this purge cooling investigation is representative of a modern gas turbine for aero-engines and power generation and geometrically similar to the uncooled stator and rotor used for the analysis of tight clearances (Chapter 3) and the first investigation of the potential of tip shape carving (Chapter 4). The high pressure turbine characteristics are described by Sieverding et al. [81], Denos [160] and Paniagua et al [79], used for several numerical and experimental investigations.

In order to be able to perform this investigation in a relevant engine environment, the high pressure turbine stage was scaled from the existing lab operating conditions (i.e. 'cold' testing at about 480K and 6790rpm [113, 161, 162]) up to real engine conditions mimicking a medium-sized aircraft engine, powering a business jet (Fig. 7.2).

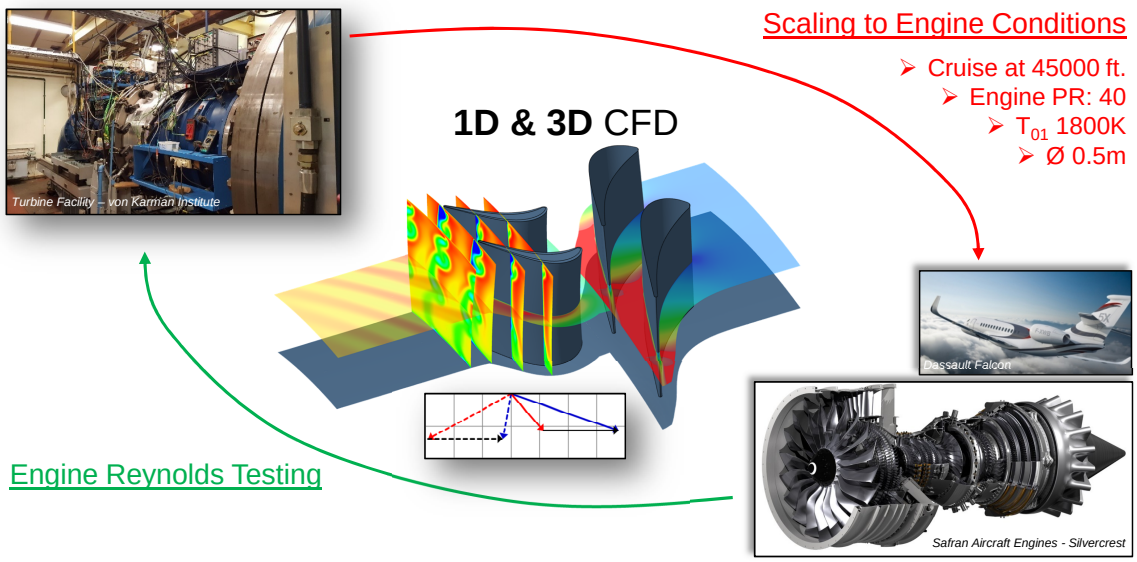

Figure 7.2: Turbine stage scaling towards engine conditions (presented engine is illustrative).

First, a 1D code was tailored based on the results of 3D CFD simulations of the turbine stage under lab conditions. The 1D routine calculates the meanline charac-

teristics of the turbine stator and rotor row based on the inlet total quantities and Mach number, degree of reaction, stage pressure ratio and rotational speed. Together with the blade and flow path measures, this code allows to generate fast and relatively accurate estimates of the stage performance. Subsequently, this 1D solver was used throughout the scaling to iterate on the optimal engine operating conditions in order to maintain the relevant non-dimensional parameters.

As a medium-size business jet engine was targeted, the stage was scaled down with a factor 1.5, resulting in a mean turbine diameter of about 0.5m. The target cruising altitude of 45,000 ft. and an overall engine pressure ratio of 40 gives rise to an upstream total pressure of 5.8 bar. Additionally, a turbine inlet temperature of 1800K [110] was assumed together with realistic turbulence levels arising from the upstream combustor. In particular, a large turbulence intensity of 25% and a length scale of the turbulent structures of 15% of the blade span were adopted [163] significantly larger than what is typically measured in 'cold' test facilities without the upstream devices (e.g. 5% turbulence intensity [109, 113]). The engine's wall temperature was set to 1200K, at a similar gas-to-wall temperature ratio of 1.5. Eventually, in order to obtain the aerodynamically similar stage, the same inlet Mach number, degree of reaction and pressure ratio were imposed. An estimate for the rpm was provided through the peripheral speed U by matching the corrected speed $U/\sqrt{T_{01}}$.

The final results for the 1D and 3D simulations (details on the numerical method are given in the next section) are presented in table 7.1 for both the 'Cold Test' as well as the 'Engine' conditions. All quantities extracted from the 3D CFD are massflow averaged values and the downstream plane is located at 0.5 $C_{ax,rot}$ away from the rotor trailing edge. Firstly, one can notice the good accuracy of the 1D meanline solver to predict the eventual 3D stage characteristics. Additionally, all Mach numbers (within 0.03) and angles (within 0.5 deg. except β_2, most likely due to the small difference in non-dimensional speed) are matched closely as well as the non-dimensional parameters. However, only the Reynolds was chosen not to be kept

and dropped with about almost a factor 3. The lab testing occurs at higher Reynolds, e.g. for larger aircraft engines or land-based turbines for power generation. As an illustration, in order to match the Reynolds Number of such engine in the von Karman Institute rotating turbine facility, one would have to operate the rig with a sub-atmospheric inlet total pressure of 0.83 bar.

Table 7.1: Comparison of the 'Cold Test' and 'Engine' turbine characteristics.

			Cold Test		**Engine**	
			1D	3D CFD	1D	3D CFD
Overall	Mean Diameter	[m]	0.74		0.49	
	P_{01}	[bar]	2.25		5.8	
	T_{01}	[K]	480		1800	
	T_{wall}	[K]	300		1200	
	RPM	[rpm]	6790		20000	
	Pressure Ratio (P_{01}/P_3)		2.92		2.92	
	Flow Coefficient ϕ		0.486	0.487	0.486	0.481
	Stage Loading ψ		1.537	1.510	1.536	1.475
	Degree of Reaction r_p		0.261	0.261	0.261	0.273
	Corrected speed $U/\sqrt{T_{01}}$		12.00		12.17	
	Absolute Stator Reynolds	[x10^3]	739	764	276	271
	Relative Rotor Reynolds	[x10^3]	449	463	162	162
	Massflow	[kg/s]	13.51	13.44	7.75	7.71
	Power	[MW]	1.44	1.40	3.17	3.03
Plane 01	M_1	[-]	0.163	0.162	0.163	0.163
Plane 02	M_2	[-]	0.982	0.992	1.009	0.994
	$M_{2,r}$	[-]	0.403	0.407	0.410	0.395
	Absolute Angle α_2	[deg.]	73.1	73.4	73.3	73.4
	Relative Angle β_2	[deg.]	44.9	44.6	45.0	42.4
Plane 03	M_3	[-]	0.378	0.393	0.388	0.401
	$M_{3,r}$	[-]	0.847	0.843	0.869	0.866
	Absolute Angle α_3	[deg.]	-11.8	-8.3	-12.2	-8.8
	Relative Angle β_3	[deg.]	-64.1	-63.1	-64.2	-63.3

7.2.2 Stage Grid Sensitivity

Before modeling the purge flow itself, 3D simulations were performed of the entire high-pressure turbine stage. These stage calculations were used to decide the spatial

discretization of the main passage regions for the eventual purge flow computations as well as to scale the turbine up to engine conditions.

Steady-state Reynolds-Averaged Navier-Stokes (RANS) simulations were performed (Numeca FINE/Turbo), adopting the k-ω SST model for the turbulence closure and a multigrid (3) solving approach to accelerate the convergence. The computational domain (Fig. 7.3) extends 2 axial chords downstream of the rotor blade to allow for a sufficient development of the downstream flow structures and the stationary/rotating interface is modeled through a mixing plane. At the inlet of the turbine stage, the total pressure and temperature, flow direction as well as the required values for the turbulent quantities (k and ϵ) are imposed while a static pressure is applied at the back end of the stage (satisfying the radial equilibrium). All walls are set to be isothermal.

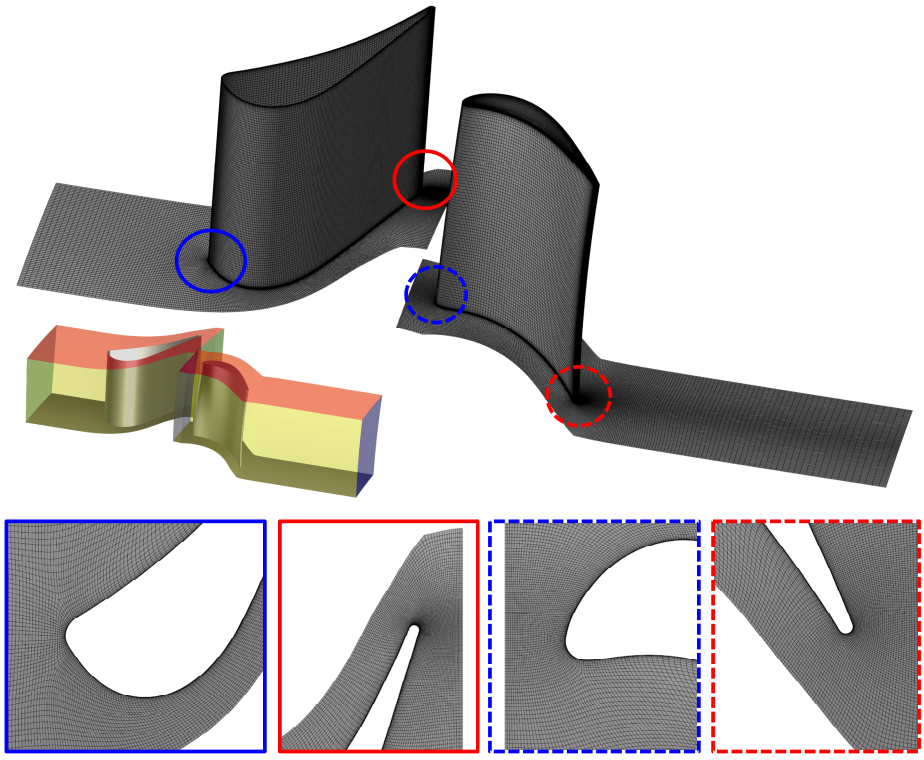

Figure 7.3: Computational domain and adopted mesh for the turbine stage calculations.

All structured meshes were created using Numeca AutoGrid 5 and adopt a multi-block strategy, i.e. without the purge flow, the grid contains 16 different blocks (Fig. 7.3). The first cell size was chosen to give rise to a y^+ well below 1 to ensure a proper resolving of the aerothermal characteristics inside the boundary layer and heat transfer signatures. For the grid sensitivity study, a total of 5 different grids were created, ranging from 2.1 (v00 - coarse) to 11.8 (v04 - fine) million cells. Every time, the cell size was refined isotropically and the amount of radial divisions for the stator and rotor varied from 77 to 133 and from 93 to 169 respectively. The coarsest grid adopts 25 cells along the tip gap height while the finest mesh divides the clearance into 45 points. Table 7.2 presents the characteristics for all generated computational grids.

Table 7.2: Grid sizes (in million cells).

	Stator	Rotor	**Total**
v00	0.708	1.440	**2.149**
v01	1.404	2.764	**4.168**
v02	2.148	4.229	**6.377**
v03	2.658	5.448	**8.106**
v04	3.816	7.965	**11.782**

The evaluation of the pitchwise averaged (relative) total pressure losses along the blade radius are summarized in Fig. 7.4 across the stator (left) and rotor (right) for all simulated meshes. One can observe only very small differences between the finest (v04) and second finest (v03) mesh, resulting in a stage efficiency difference of less than 0.06%. While here only the losses are presented, the same trend could be observed for all other aerodynamic quantities (e.g. Mach numbers, angles, etc...). Also the differences in heat transfer between v03 and v04 remain well below 2% on the casing and tip along the entire axial chord. Therefore, the v03 mesh characteristics (Fig. 7.3 and indicated in blue in Table 7.2) are eventually chosen for the purge flow optimization. The finest mesh (v04) was used to perform and evaluate the scaling.

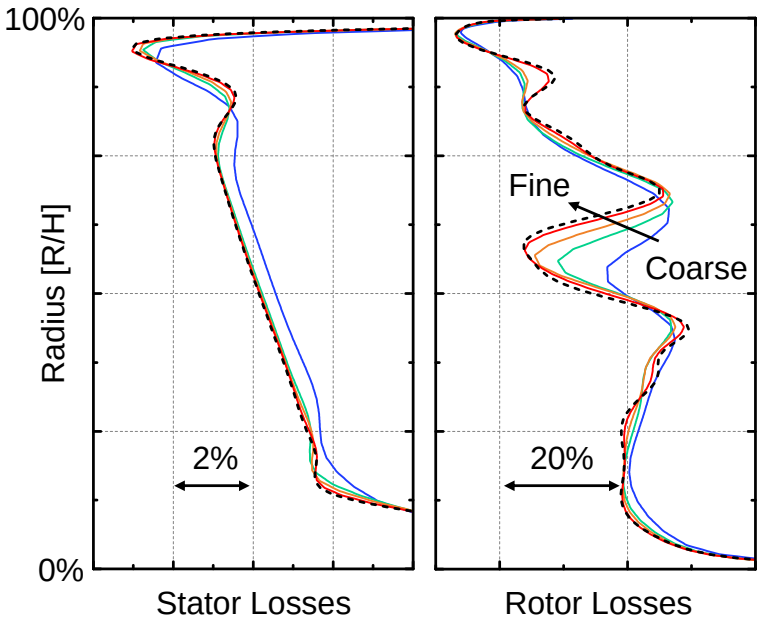

Figure 7.4: Grid sensitivity results based on the stator and rotor loss distribution.

7.3 Purge Cooling Optimization Methodology

7.3.1 Computational Model of the Shroud Purge Flow

In order to reduce the overall computational cost, the purge flow simulations only model the rotor domain, extending upstream to the axial location of the stator trailing edge and 1.5 axial chord lengths downstream of the rotor blade (Fig. 7.5a). Additionally, the commonly implemented squealer rim is adopted as the tip sealing mechanism. The tip clearance, cavity depth and rim thickness are fixed respectively at 1%, 3.4% and about 1.85% of the blade span, in accordance with industrial practice.

A detailed view of the mesh can be found in Fig. 7.5b. The rotor has a total of 169 radial divisions of which 41 inside the tip gap and 33 in the squealer bath. Additionally, the insertion of the purge slot is connected to the main passage using a matching connection with 33 cells along the axial direction adopting a hyperbolic tangent stretching function. The additional clustering of the structured grid due to

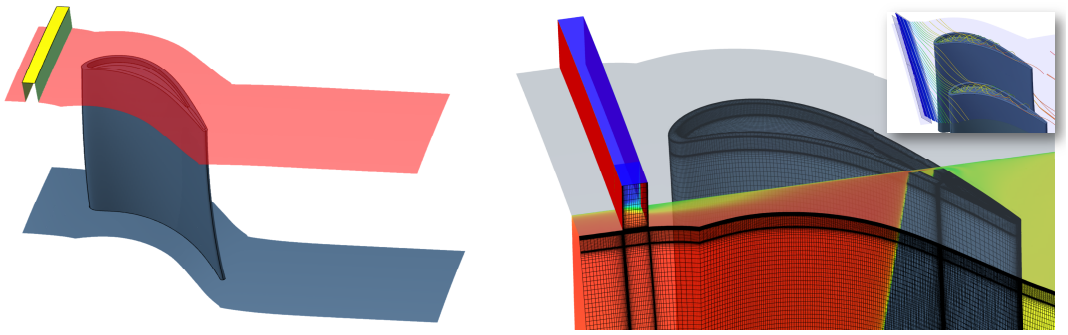

(a) (b)

Figure 7.5: The computational domain (a) and mesh (b) for the purge flow simulations.

the purge slot as well as around the tip region increases the final amount of cells from 5.4 up to 9.7 million cells.

The inlet boundary conditions for the rotor domain are extracted from the stage calculations. Specifically, the radial pitchwise averaged distributions of the relative flow angles, total temperature and pressure as well as the turbulent quantities were extracted 25% $C_{ax,rot}$ downstream the stator TE and radially rescaled to be imposed at rotor inlet. The purge inlet conditions are specified through a fixed static temperature of 830K together with the absolute velocity components. The rotational speed was set to 20,000 rpm and the same static back pressure was imposed as adopted throughout the stage calculations.

The cases were solved with Numeca FINE/Turbo using the k-ω SST turbulence model, a second order central discretization and a real gas as working fluid with temperature dependent properties (cfr. section 2.1).

7.3.2 Parametrization of the Purge Flow Characteristics

The detailed parametrization of the purge flow injection is illustrated in Fig. 7.6. The purge slot is characterized by a certain axial width, denoted as a fraction of the blade span (the 'gap fraction' *gp*) and a certain axial position between the stator trailing edge and rotor leading edge (*ap*). The purge injection is angled radially using

γ and a fixed (absolute) inlet tangential swirl along the slot direction is generated (ϕ). Eventually, the pitchwise distribution of the actual injected purge massflow is parametrized in function of the azimuthal angle θ using 5 points, interpolated using a piecewise cubic Hermite interpolating polynomial.

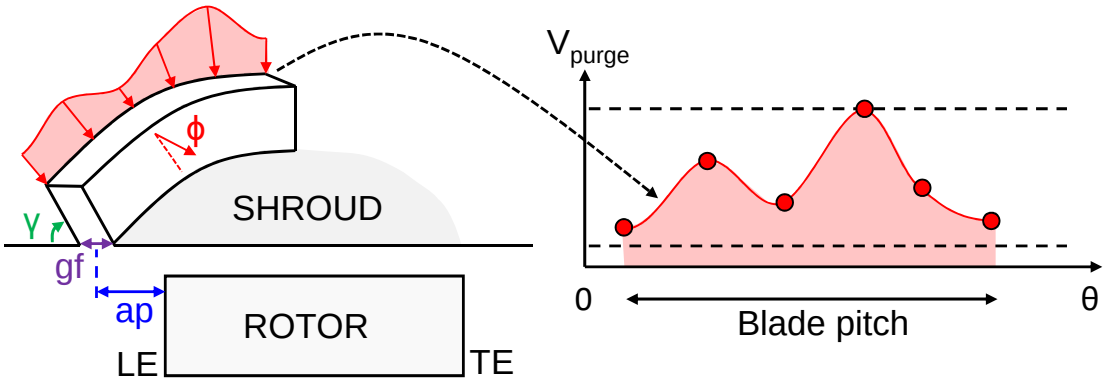

Figure 7.6: Parametrization of the purge flow injection.

The adopted limits for all variables are specified in table 7.3 and cover a wide range of purge slot geometries and flow conditions. The gap fraction gf goes from 2.5 to 9 percent of the blade span [155] and the radial injection angle γ can vary from 90 deg. (fully perpendicular), down to 10 deg., almost parallel to the mainstream. The axial position ap varies from 20 to 70 percent of the stator-rotor gap, mainly limited on the downstream end to ensure a proper meshing near the rotor LE and avoid excessive cell clustering. A swirl angle ϕ is imposed which sets the angle of the injected flow with the tangential direction, going from 0 deg. (no swirl in the absolute frame) to 70 deg., close to the maximum amount that upstream miniature stator vanes in the shroud assembly would be able to provide. Eventually, the massflow of each point of the injection distribution can be set to give rise up to 2.5% of the mainstream massflow.

Table 7.3: Purge flow parametrization characteristics.

Parameter	**Min.**	**Max.**	Units
Gap Fraction gf	2.5	9	[% span]
Injection Angle γ	10	90	[deg.]
Axial Position ap	20	70	[% of row gap]
Swirl Angle ϕ	0	70	[deg.]
Massflow Injection (x5)	0	2.5	[% of mainflow]

7.3.3 Optimization Strategy and Objectives

Routine Overview

An overview of the optimization routine is presented in Fig. 7.7. Similarly to the full 3D tip optimization strategy (cfr. Chapter 5), the differential evolution optimizer CADO is coupled to an evaluation routine, handling the sequence from the initial CAD generation based on the design parameters, all the way up to the post-processing to eventually feed the objectives back into the optimizer. First, a Matlab routine generates the coordinates of the actual purge slot and calculates the tangential distributions of the velocity components based on the given massflow percentages, actual geometry, swirl angle and the mainstream static pressure at the purge injection location. Subsequently, Numeca AutoGrid and IGG create the fully structured grid, using an identical 'template' file for all geometries. Eventually, the case is solved through Numeca FINE/Turbo and processed in Numeca CFView. The total time for the evaluation of a single individual is about 13 hours on 10 CPU's.

Objectives

The performed multi-objective optimization targets a maximization of the aerodynamic efficiency and a simultaneous minimization of the tip heat load.

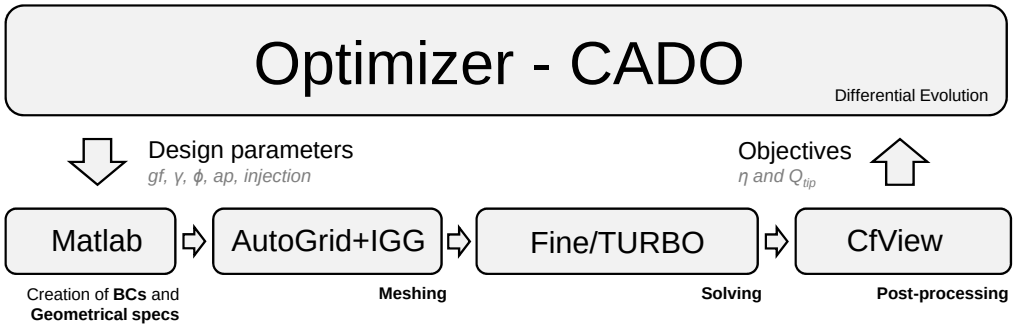

Figure 7.7: Overview of the purge optimization routines.

The efficiency definition uses the mechanical torque exerted on the blade and compensates for the additional injection of the purge flow [164, 165]:

$$\eta = \frac{T\omega}{\dot{m}_m C_p T_{0,m}\left[1-\left(\frac{P_{0,exit}}{P_{0,m}}\right)^{\frac{\gamma-1}{\gamma}}\right] + \dot{m}_p C_p T_{0,p}\left[1-\left(\frac{P_{0,exit}}{P_{0,p}}\right)^{\frac{\gamma-1}{\gamma}}\right]} \tag{7.1}$$

where the subscripts m and p respectively relate to the mainstream and purge flow quantities. Additionally, averaged values between the inlet and outlet for the heat capacity C_p and γ were used. The second, heat load objective is taken as the integrated value of the heat transfer onto the top 5% of the blade.

Besides the latter two objectives, a variety of 81 other single-valued quantities were extracted characterizing the simulated individual. Additionally, the pitchwise averaged heat transfer on the blade and shroud surfaces, radial traces of the flow quantities downstream of the turbine stage as well as the averaged aerodynamic flow properties along the machine axis were retrieved.

Optimization Sequence

An overview of the entire optimization sequence is presented in Fig. 7.8. The optimization started with the creation of an initial database (Design of Experiments,

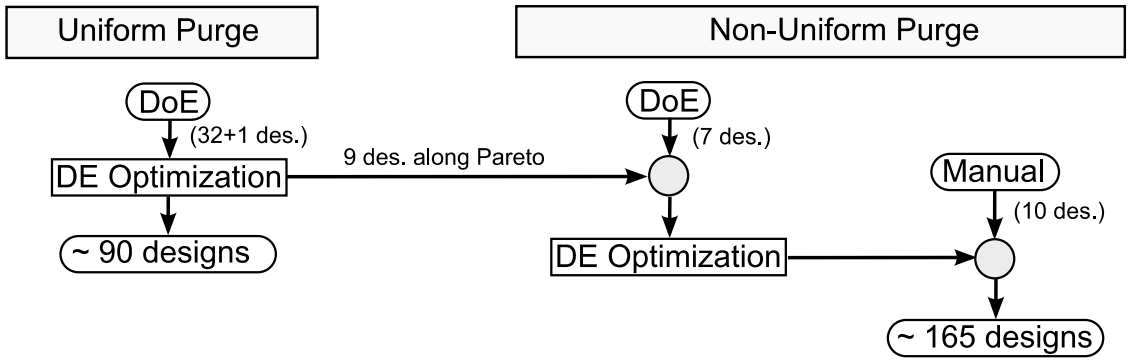

Figure 7.8: Overview of the purge optimization sequence.

'DoE'), assuming a uniform purge flow distribution. Specifically, all massflow injection coefficients were set identical, reducing the amount of design parameters from 9 to 5. The DoE in this case was created using a full factorial approach, simulating all combinatorial possibilities where each of the design parameters are set to 10% or 90% of their range (i.e. $2^5 = 32$ simulations + a central case). From this database, the uniform purge flow optimization is initiated, using the Differential Evolution optimizer with a population size of 16 individuals with a crossover and mutation constant of 0.8 and 0.6 respectively (section 2.3). After 5 iterations and a total amount of about 90 converged purge flow simulations, the Pareto front was extracted. In order to kick-off the non-uniform purge flow optimization, 9 designs along the Pareto front with a uniform distribution were chosen, combined with 7 optimal designs where non-uniformities were introduced as high as 40% of the range. Subsequently, a total of 10 iterations were run, allowing all 9 design variables to vary. Eventually 10 additional simulations were performed to study the effect of design variations on an optimal profile.

7.4 Results

7.4.1 Investigation of the Pareto Front

Fig. 7.9 presents the evolution of the Pareto front throughout the optimization iterations. Each of the axes illustrates one of the objectives: the maximization of the aerodynamic efficiency (horizontal) and the reduction of the tip heat load (vertical). The heat transfer is non-dimensionalized with the result obtained without any coolant injection, using a perpendicular purge slot in the middle of the stator-rotor gap. Similarly, the efficiency is quoted as the difference with the 'no-purge' case in percentage.

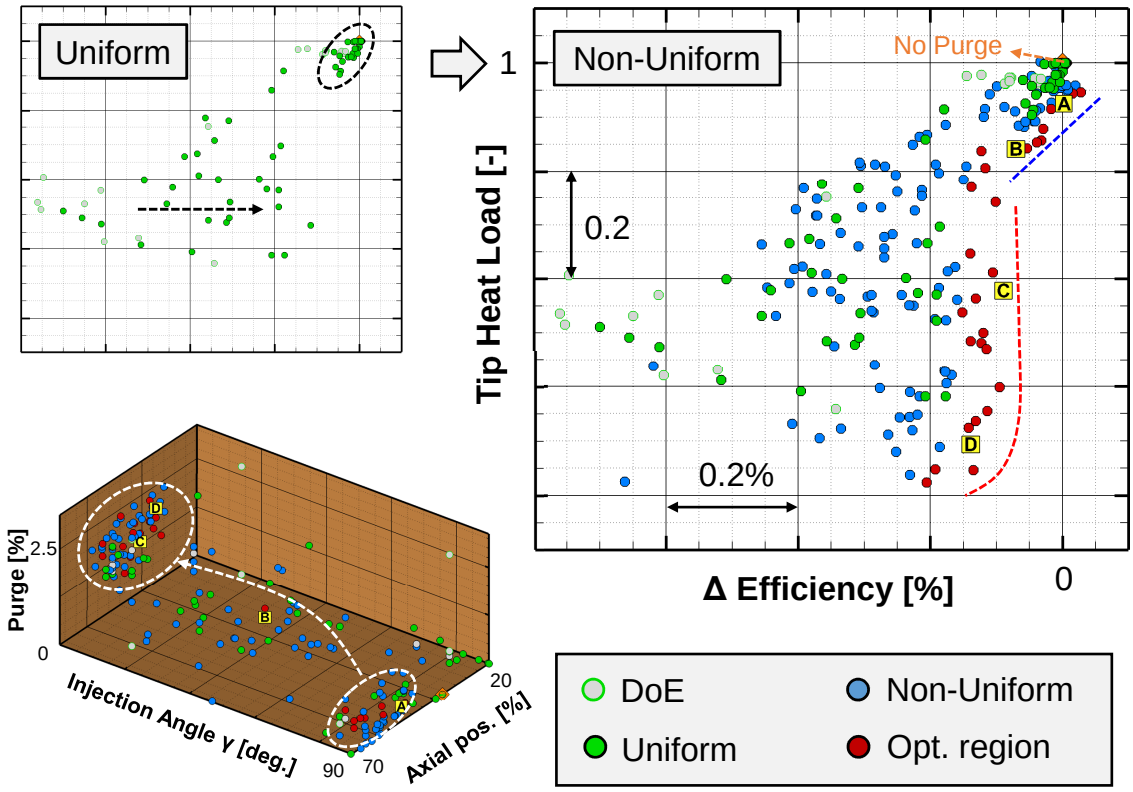

Figure 7.9: Evolution of the Pareto front throughout the optimization.

The first 33 evaluated individuals from the Design of Experiments are indicated in gray (Fig. 7.9, top left). The roughly 60 individuals generated thereafter during the differential evolution optimization adopting a uniform purge flow injection are colored in green. The Pareto front moves directly towards the right, i.e. to a lower loss regime, and a clustering of geometries can be observed on the top right. The latter region contains profiles with a low injection flow rate, generally 0.5% of the mainstream mass flow or less. The evaluated cases throughout the non-uniform optimization are colored in blue and the final (region of) optimal profiles in red (Fig. 7.9, top right). Eventually, the no-purge case is indicated with an orange diamond while four distinct profiles along the Pareto front are labeled from 'A' to 'D'. This coloring and labeling will remain consistent throughout the following sections and serves to track the optimal profiles inside the entire the design space.

The Pareto front reveals a large scattering up to 80% in heat flux, while the variations in efficiency of the optimal region remain limited to 0.2%. On the whole, negligible aerodynamic improvements are possible compared to the no-purge case and the additional introduction of a non-uniform peripheral purge flow distribution does not reveal significant opportunities. The front itself shows two distinct regions. The upper region roughly trades a reduction of 20% in tip heat load with 0.2% in efficiency (profile 'A' to 'B'). The lower region on the contrary, shows to be rather insensitive in terms of the aerodynamic performance and is able to drop the heat transfer further with almost 60%, adopting increased purge flow rates. The three-dimensional plot in Fig. 7.9 presents the most important purge flow characteristics for the entire design space. Specifically, the bottom plane illustrates the variations of the axial position of the purge slot as well as the radial injection angle while the eventual amount of purge mass flow is indicated on the vertical axis. The upper right region in the Pareto front is located in the regime of low purge mass flows, high injection angles and positioned in the downstream half of the stator-rotor gap. The second region however uses larger amounts of purge flow at very low injection angles (i.e. as parallel as possible to the

mainstream) located closer to the mid-point in between the stator trailing edge and rotor leading edge.

Fig. 7.10 presents the detailed purge flow characteristics of the four profiles indicated from 'A' through 'D', while Fig. 7.11 depicts their heat transfer signatures onto the blade tip, suction side and shroud surface.

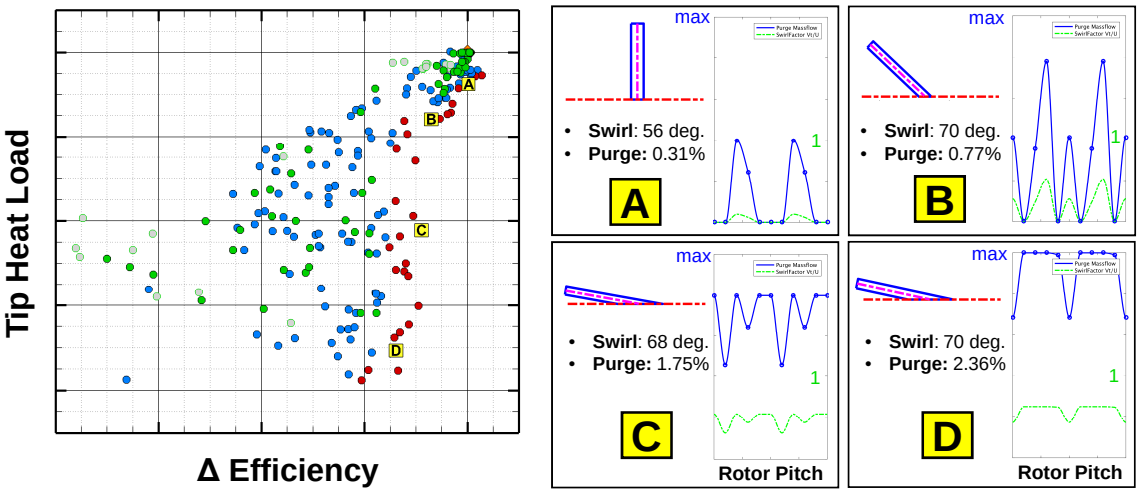

Figure 7.10: Purge flow characteristics for four distinct profiles along the Pareto front.

The geometries show a gradual inclination towards the direction of the mainstream flow for higher purge rates while maintaining a rather constant channel width (i.e. the design parameter 'gap fraction' enlarges along with lower injection angles).

Important to point out are the obtained absolute values of the swirl factor (green curves in Fig. 7.10). This factor indicates the ratio of the tangential component of the purge flow compared to the tip speed. In this project, the purge flow is injected with a constant swirl angle. This represents the real case of miniature stator vanes embedded inside the purge channel around the rotor annulus which are turning the flow into the direction of the peripheral speed. Therefore, as the mass flow distribution varies along the tangential direction, so does the swirl factor. Note that, even though close to the maximum amount of mass flow is injected for case 'D', with the highest swirl angle possible (70 deg.), only an average swirl factor of 0.5 is obtained. This means

that the flow will be picking up at about half of the tip peripheral speed and will therefore have a significant momentum directed in the relative frame of reference from the suction to pressure side.

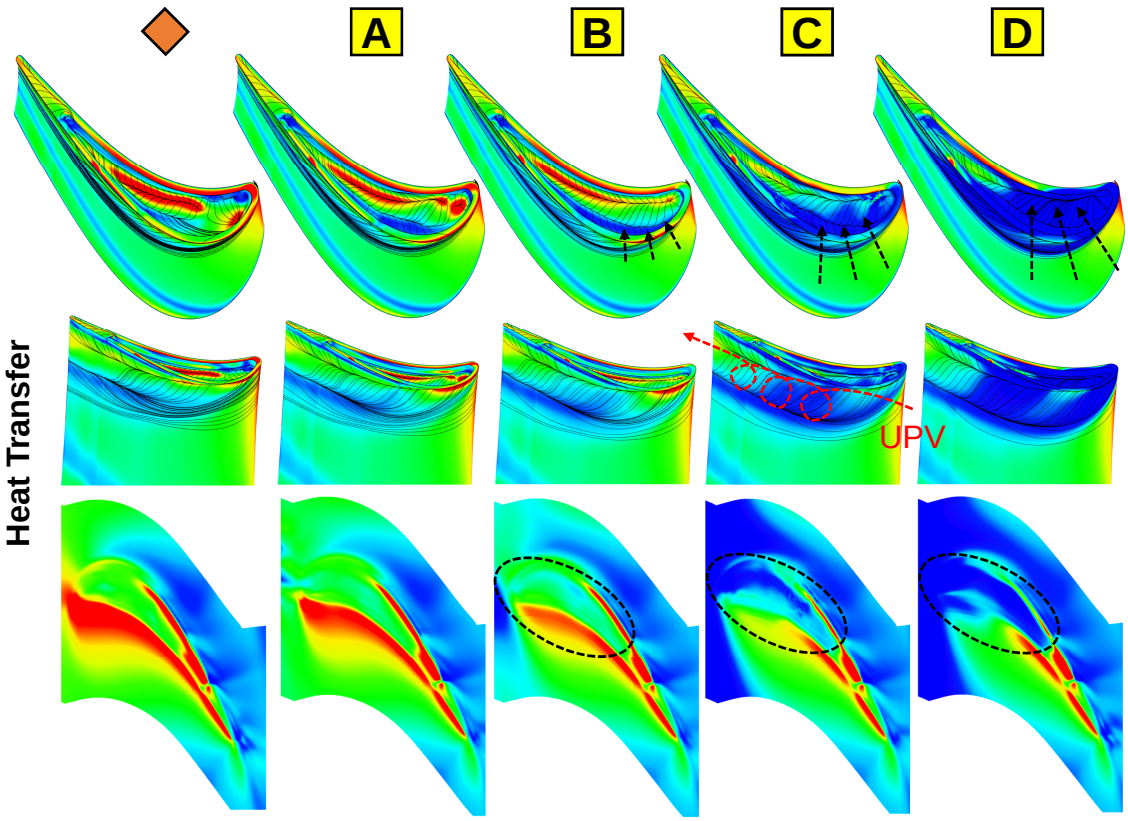

Figure 7.11: Blade and shroud heat transfer signatures for the no-purge case (diamond) and four profiles along the Pareto front ('A' through 'D').

The heat transfer contours on the tip of the blade (Fig. 7.11) illustrate the increasing amount of coolant flow entering the cavity bath through the suction side, creating a large zone of low heat transfer in the front region of the blade (cfr. black arrows). The flow that doesn't enter the overtip gap region bends downwards and rolls up into the upper passage vortex (UPV, red arrow), cooling down the upper 25% of the blades suction side. The shroud heat transfer reveals an emerging zone of low heat flux caused by the increased amount of purge flow captured inside the cavity bath. The shroud purge serves additionally to cool down the casing surface

and demonstrates reduced heat levels in the first part of the axial chord. In the downstream half, all profiles show similar distributions both in the overtip region as well as the main passage, indicating little to no effect of the upstream shroud purge.

7.4.2 Effect of the Design Parameters and Purge Flow

Fig. 7.12 illustrates the variation of the optimization parameters over the design space. The upper left plot colors the Pareto front (cfr. Fig. 7.9) by the eventual purge mass flow while the other four graphs indicate the changes of the different design parameters characterizing the purge slot.

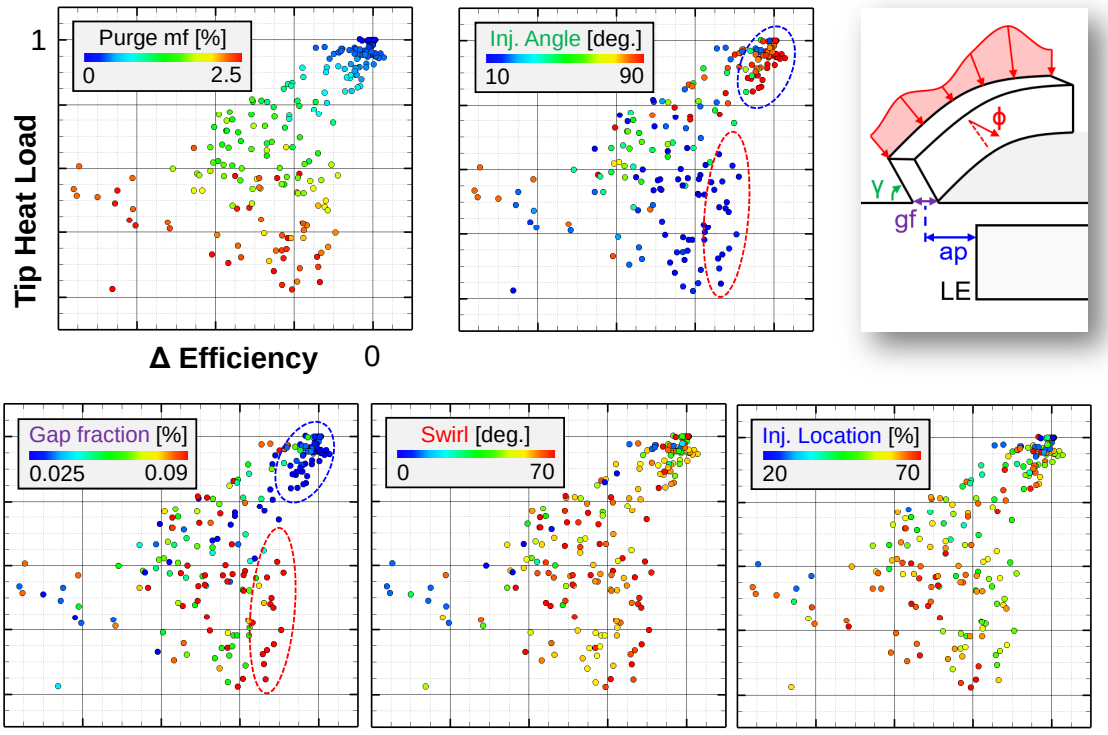

Figure 7.12: Illustration of the Pareto front colored by the different design parameters of the optimization.

The individuals in the optimal region show monotonously increasing purge flow rates when moving from the barely cooled (top right) to heavily cooled (bottom right)

part of the Pareto front. The injection angle and gap fraction reveal two distinct zones, corresponding with the previously identified regions (Fig. 7.9). The upper right region (blue circles) adopts high injection angles combined with low gap fractions while the lower region uses low injection angles with a large gap fraction (red circles). The swirl on the Pareto front is maximized and the sub-optimal individuals feature lower levels of peripheral angle. The injection location shows quite some scatter but generally remains within 40% to 60% of the rotor-stator gap as previously observed in the 3D plot of Fig. 7.9

In order to illustrate the detailed effect of the most important, driving characteristic of the purge (i.e. the eventual mass flow), Fig. 7.13 presents the two optimization objectives in function of the purge flow rate.

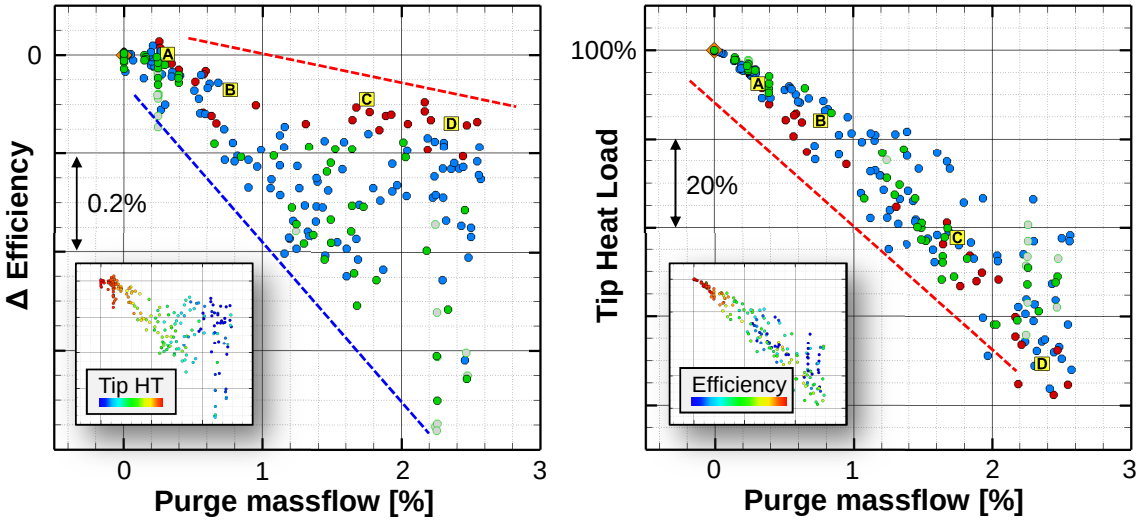

Figure 7.13: The effect of the purge mass flow on the optimization objectives.

The evolution of the efficiency with purge (Fig. 7.13-left) identifies the optimal profiles on the top part of the design space, showing the lowest sensitivity to the injected mass flow: ±0.07% of efficiency reduction per 1% of massflow (red curve). However, if one does not use a proper injection geometry, losses as high as almost 0.4% of aerodynamic performance can be observed for each percent increase of the

purge flow (blue curve). The heat transfer (Fig. 7.13-right) shows a reduction of almost 30% in tip heat load per 1% of purge flow increase (red slope).

7.4.3 Blade and Shroud Heat Transfer

The relation of the tip heat load to the heat fluxes onto the other relevant turbine surfaces is presented in Fig. 7.14. Specifically, the connection with the heat flux onto the upper 25% of the pressure and suction side as well as the shroud thermal load (from the rotor leading edge to 20% $C_{ax,rot}$ downstream the trailing edge) is illustrated.

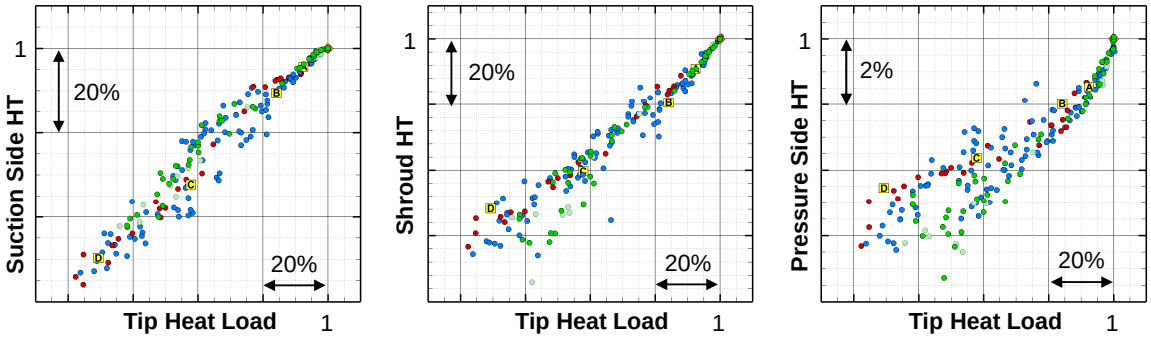

Figure 7.14: Relation of the tip heat load to the heat flux onto the upper 25% of the pressure and suction side as well as the shroud.

Both the suction side and shroud show a reduction of heat transfer of ±15% per 20% of tip heat load. The pressure side fluctuations along the Pareto front are an order of magnitude lower, i.e. about 1.5% per 20% change in tip heat transfer.

Interesting is to correlate the latter values through Fig. 7.13 to obtain the sensitivities to the actual purge mass flow. This results in a response of the shroud and suction side heat transfer of almost 23% for each percent of injected coolant massflow.

7.4.4 Aerodynamic Trends

Fig 7.15 illustrates a variety of relevant aerodynamic quantities throughout the evaluated purge flow configurations.

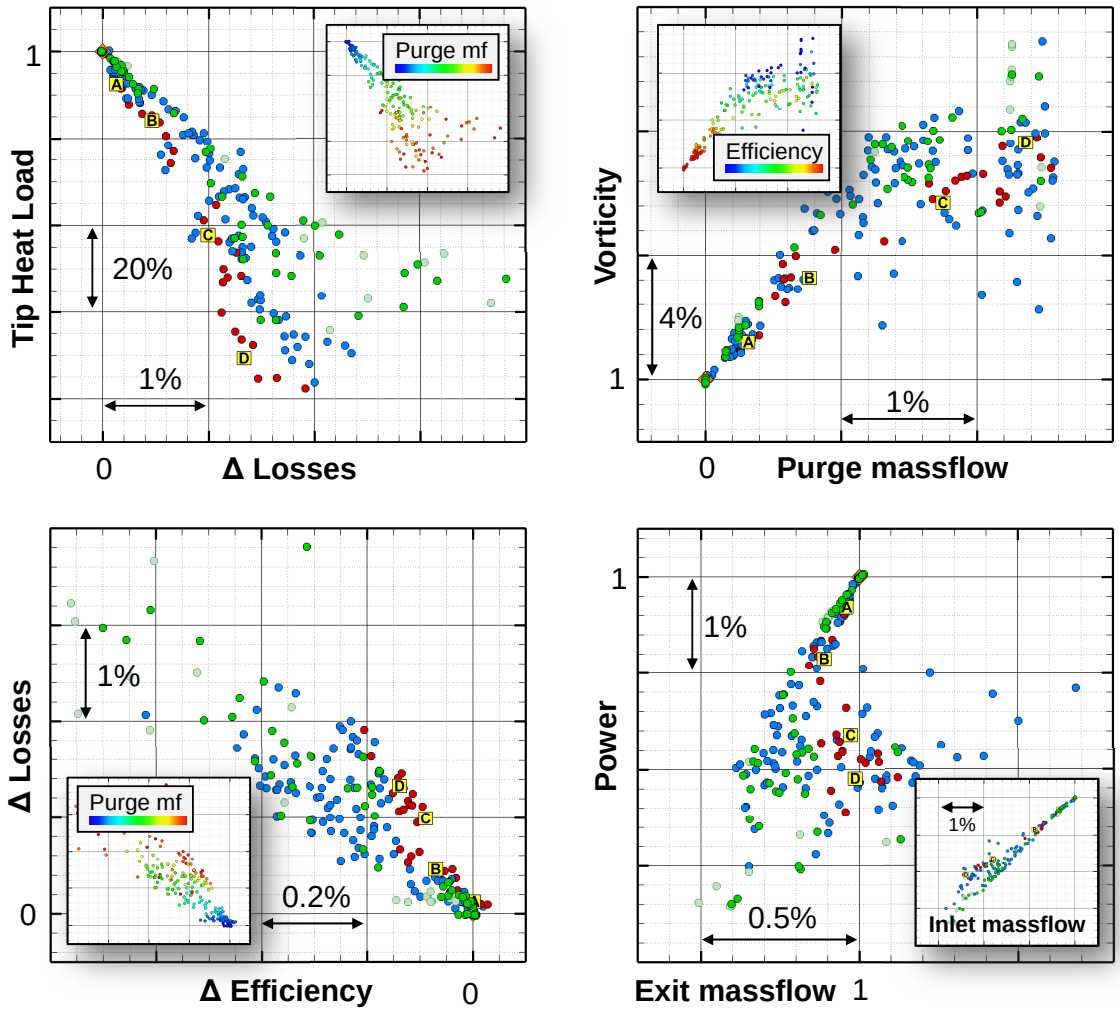

Figure 7.15: Aerodynamic trends across the entire design space.

The top left graph presents the tip heat load in function of the aerodynamic losses evaluated through the total relative pressure deficit between the rotor leading edge (downstream of the purge injection) and a plane 50% $C_{ax,rot}$ behind the rotor trailing edge. As the optimal (red colored) region constitutes also here the prime configura-

tions (i.e. low losses and low heat transfer), the efficiency and loss objective would be quasi interchangeable. The lower left figure quantifies their exact relationship, revealing a 1% increase of losses per 0.1% decrease in efficiency along the Pareto front.

The upper right graph demonstrates an increase of non-uniformity in the downstream field through enhanced vorticity magnitudes of almost 4% per 1% of injected purge mass flow.

The plot on the lower right eventually illustrates the effect on the operating point of the turbine rotor. For the optimal profiles one can observe changes in the exit mass flow of less than 0.2%. However, this results in a changing inlet flow rate, depending on the injected purge (cfr. bottom right plot). Note that throughout the optimization only the rotor was simulated adopting a constant pressure ratio across the computational domain. If one would simulate the entire stage, the injected purge creates a blockage which is going to alter the degree of reaction [155, 156]. The extracted torque reduces more than 2% between no-purge injection and the 'D' case (adopting almost 2.4% of purge flow) due to the affected blade loading in the top section (see following section).

7.4.5 Effect of Design Variations on an Optimal Profile

In order to quantify the separate effects of the design variables on a certain optimal configuration, 10 additional simulations were performed. The starting case is the configuration 'C', obtained through the non-uniform optimization. First, a quasi identical geometry was evaluated using a uniform purge injection, giving rise to the same final mass ejection as case 'C'. This reference case is presented in the Pareto front of Fig. 7.16 as a yellow square. The design features a slot with a gap fraction of 0.09 in the middle of the stator-rotor spacing and injects 1.75% of purge mass flow under an angle of 10 deg. with the mainstream flow and 70 deg. of swirl. Subsequently, 9

cases with altered design parameters were evaluated to separate the influence of the distinct purge characteristics.

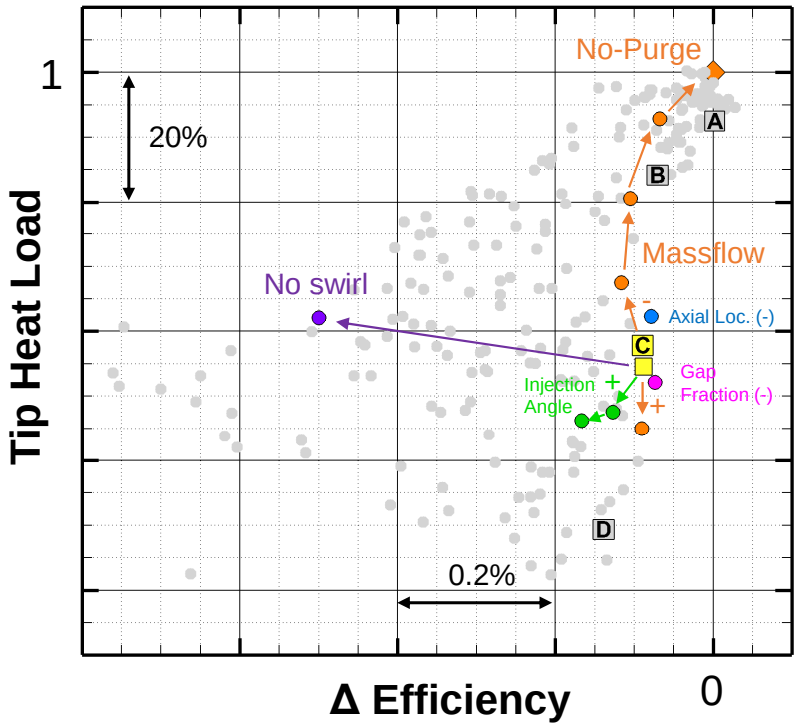

Figure 7.16: The effect of design alterations on an optimal purge injection.

Comparing the simulation 'C' and the reference case with a uniform distribution, one can conclude that the additional introduction of the non-uniformity along the purge inlet peripheral direction does not make a significant difference. A reduction of the gap fraction (-17%) and axial injection location (-20%) gives rise to a similar aerodynamic performance and shows to affect the heat transfer within ±5-10% (Fig. 7.16). Injection without any swirl significantly reduces the efficiency with 0.4%. Increasing the injection angle to 25 deg. and 45 deg. (maintaining the same channel width) shows to move the designs to a region of lower efficiency and tip heat loads. However, the main contributor is the eventual injected mass flow. Therefore, four cases were evaluated with altered flow rates, specifically 0.5%, 1%, 1.4% and 2% of

the mainstream value, resulting in a quasi vertical movement inside the Pareto front (Fig. 7.16).

To investigate the mass flow effect more in detail, Fig. 7.17 illustrates the variations in heat transfer (left) and three aerodynamic performance characteristics (right) for all purge flow rates compared to the 'no-purge' case. The evolution of the thermal load shows an average sensitivity between 20% and 30% of heat transfer reduction per 1% of purge increase. The suction side proves to be the least sensitive while the tip heat flux reveals the largest slope. The losses as well as the vorticity demonstrate an increasing trend, respectively with 1% and 6% for a 2% of coolant injection while the power drops with almost 2%.

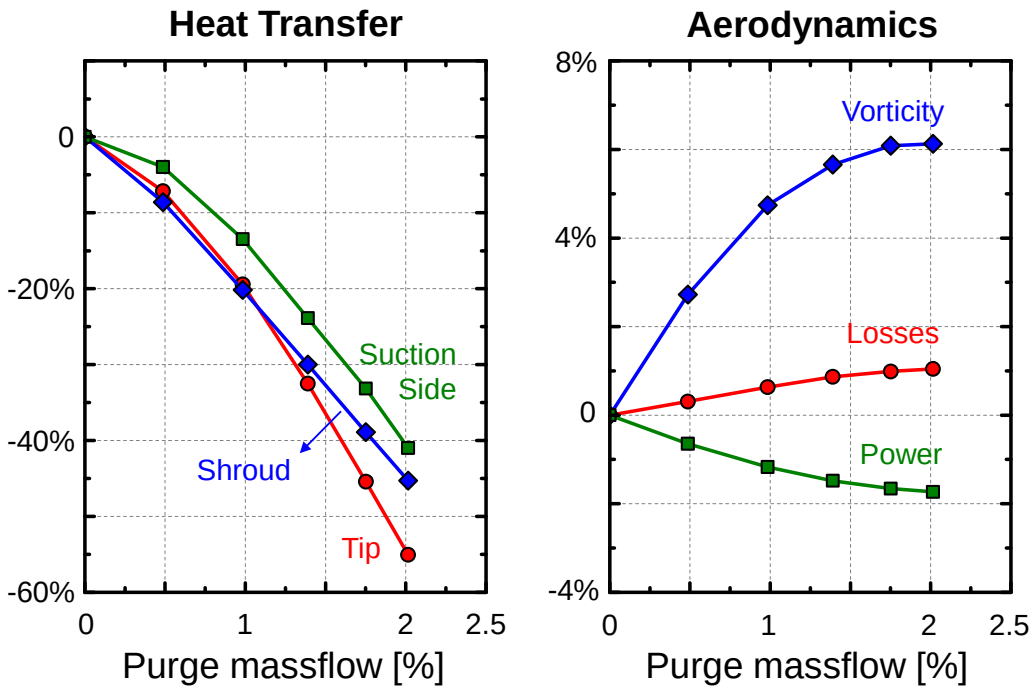

Figure 7.17: Influence of the purge mass flow injection on the heat transfer (left) and aerodynamic (right) characteristics.

Fig. 7.18 presents the evolution of the average heat flux onto the tip, shroud and upper 25% of the blade suction side along the axial chord, non-dimensionalized with the average value of the no-purge case. Additionally, the heat transfer contours for

four injection rates are added to facilitate the understanding of the observed trends. The bottom right graph illustrates the difference in static pressure (i.e. blade loading) on the upper part of the suction side compared to the no-purge case.

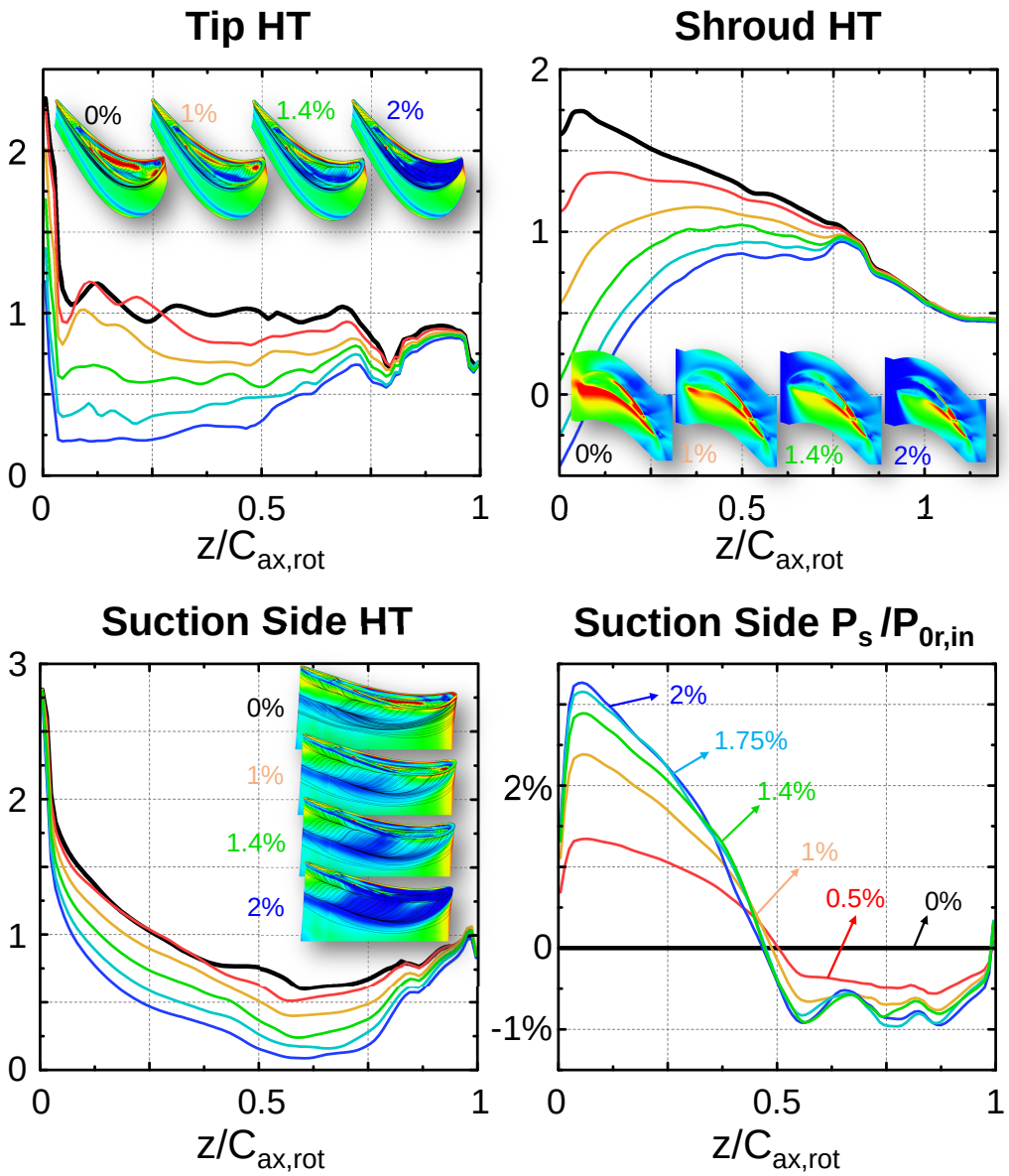

Figure 7.18: Axial evolution of the heat transfer onto the tip, shroud and suction side together with the suction side pressure.

Both the tip and shroud heat transfer show large dependencies in the first 75% of the blade axial chord and drop quasi monotonously with the injected coolant rate.

In the last 25% of the rotor as well as downstream the trailing edge, the variations are negligible. On the blade tip, the reductions are largely due to the additional amount of cold fluid entrained in the cavity bath (cfr. also Fig. 7.11), while on the shroud it is a combination of the lowered loads in both the overtip region as well as the main passage. The heat transfer onto the blade suction side on the contrary, is affected throughout the entire blade chord. In both the front part due to the early development of the passage vortex with cold purge flow and the aft part, the contours show reduced levels of heat flux.

The distribution of the static pressure along the suction side reveals an asymptotically increasing pressure in the first half of the axial chord up to about 3% while the pressure in the aft part is reduced with almost 1%. However, as the detrimental effect on the front part overcompensates the increase in loading on the downstream half, the power exhibits a decreasing trend with the purge flow rate as observed in Fig. 7.17.

7.5 Conclusions

This chapter explored the opportunity of maximizing the advantageous aerodynamic effect of the upstream shroud coolant flow onto the vortex structures, while assessing the capability of enhancing the blade tip coolability.

To generate an engine-relevant environment, a modern high-pressure turbine stage was successfully scaled from the lab towards real engine conditions matching a business jet flying at cruising altitude. First, through a 1D meanline approximation of the turbine conditions and subsequently validated using full 3D CFD simulations.

The purge flow injection was parametrized using 4 geometrical characteristics, and 5 variables describing the peripheral distribution of the upstream shroud coolant flow. A 2-stage multi-objective optimization was performed, simultaneously maximizing the aerodynamic efficiency while minimizing the tip heat load. RANS simulations were used on a 9.7 million cells grid to evaluate the performance of more than 240 different designs.

The Pareto front reveals variations in heat transfer of 80% in heat flux while efficiency variations remain limited to 0.2% among the optimal profiles. Negligible aerodynamic improvements are observed compared to the no-purge case and the additional introduction of a tangential distribution of the purge flow did not reveal significant opportunities. The Pareto front showed two distinct regions. At low purge flows, high injection angles combined with a low gap fraction are preferred, trading a reduction of 20% in tip heat load with 0.2% in efficiency. The region of the Pareto front operating at higher purge flow rates uses low injection angles with a large axial slot width. This region allows to reduce the heat transfer with over 60% and demonstrates to be rather insensitive in terms of aerodynamic performance. The efficiency of the rotor drops roughly with 0.07% for each percent of injected mass flow. However, reductions as high as 0.4% per 1% of purge are possible if one uses a sub-optimal injection geometry. The exchange rate between the tip heat load and purge flow is 30% per 1% injection, while the shroud and upper part of the suction side are less

sensitive ($\pm 23\%$). Eventually, the relative total pressure deficit across the rotor is quasi-interchangeable with the adopted efficiency definition and power variations of 2.5% are observed due the reduction of the blade loading in the front half of the rotor blade.

CHAPTER 8. DESIGN LAYOUT FOR ADVANCED EXPERIMENTAL TIP FLOW RESEARCH

This chapter presents the redesign of a high-speed rotating turbine facility at the von Karman Institute for Fluid Dynamics to allow for simultaneous testing of multiple distinct blade (tip) profiles.

In the first two sections, important considerations related with the balancing (8.1) and precise clearance design (8.2) are highlighted, arising from the complexity of the Rainbow Rotor approach. In the last three sections of the chapter, new methodologies are described to integrate Reynolds-Averaged Navier-Stokes simulations to estimate the expected measurement ranges (8.3), optimize the spatial positioning of the sensors (8.4) and a-priori predict the measurement errors induced by the inherent limited sensor bandwidth (8.5).

8.1 A Rainbow Rotor Approach for the Turbine Rig at the von Karman Institute

8.1.1 CT-3: a Transient Rotating High Pressure Turbine Rig

The turbine rig which has been remodeled is the compression tube facility of the von Karman Institute for Fluid Dynamics [79], Fig. 8.1. This short-duration, rotating

This Chapter is partly based on:

S. Lavagnoli, C. De Maesschalck, and V. Andreoli. Design considerations for tip clearance control and measurement on a turbine rainbow rotor with multiple blade tip geometries. In *ASME TurboExpo 2016 Conference Proceedings*, GT2016-56544. [166]

S. Lavagnoli, C. De Maesschalck, and V. Andreoli. Design considerations for tip clearance control and measurement on a turbine rainbow rotor with multiple blade tip geometries. In *J. Eng. Gas Turbines Power*, **139**(4), 042603. [167]

The processing of unsteady clearance traces described in the papers above is not my contribution and their results are therefore not included into the PhD dissertation. However, the interested reader is referred to the conference and journal manuscripts.

facility contains a scaled up stage of a high-pressure turbine (stator-rotor) and preserves the relevant non-dimensional parameters for a correct aerothermal performance assessment. Specifically, the Mach and Reynolds numbers established throughout the turbine stage are representative of the operating conditions of a modern gas turbine engine. The transient character of the test rig allows for accurate measurements of the blade and endwall heat transfer at engine-like gas- and coolant-to-wall temperature ratios.

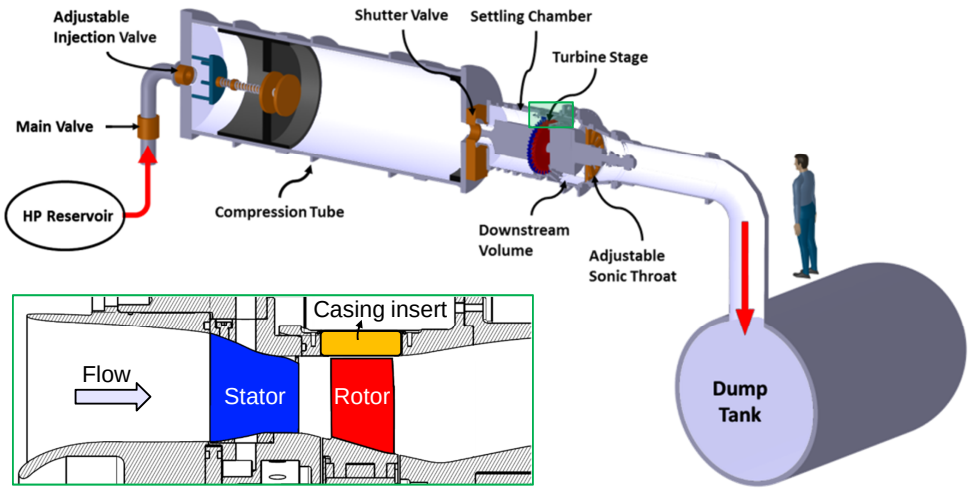

Figure 8.1: Turbine test rig layout and zoom of the flow path.

The wind tunnel consists of two volumes, initially separated by a fast-acting shutter valve (Fig. 8.1). The upstream compression tube contains a free piston while the downstream turbine stage is connected to the dump tank through a variable sonic throat. Prior to the experiments, the initial pressure in the tube is set and the test section (and dump tank) are evacuated to a pressure of about 30 mbar. During the run-up, the rotor is accelerated by means of a small air turbine. Once the rotor nearly reaches its nominal rotational speed, air from the high-pressure reservoirs is injected at the back of the piston, which forces it to slide forward, compressing the fluid upstream quasi-isentropically. When the target pressure and temperature are achieved inside the tube, the shutter valve opens. This allows the hot gas to be released into

the turbine stage towards the dump tank during an actual testing time of about 400 ms.

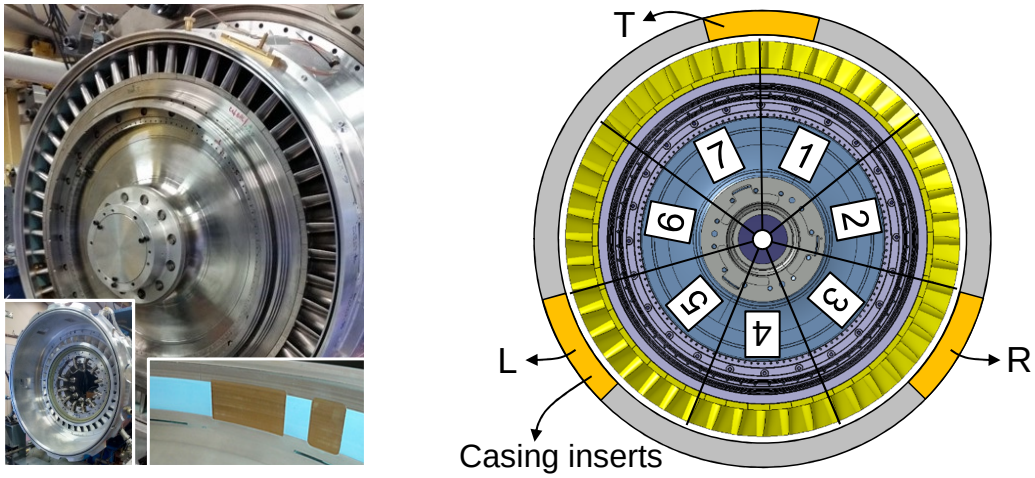

(a) (b)

Figure 8.2: View of the turbine assembly (a) and the rainbow rotor configuration (b).

For the current experimental campaign, the test section has been refurbished to hold a new high-pressure turbine stage for advanced tip flow research. Fig. 8.2a presents a view of the turbine rig where the rotor and shroud assembly is mounted on a sliding frame that moves inside a fixed stator section when the test section is sealed using hydraulic clamps (Fig. 8.2a, bottom left). The rotor and the surrounding casing ring are locked inside the same assembly to ensure that the mounting tip clearance is maintained during the closure of the test section. The inner rotor casing endwall is covered with a thin layer (2 mm) of abradable liner (Fig. 8.2a, bottom right). The liner is a two-part flame retardant epoxy produced by 3M^{TM} (Scotch-Weld^{TM} 3524 B/A AF), commonly employed in aircraft engines for void filling or as an edge-sealing compound. The abradable coating provides an effective safety measure against unexpected blade-rubbing events.

More information about the specific operation of the turbine facility can be found in [113, 161, 162, 168]

8.1.2 Rainbow Rotor Approach

The 48 installed rotor blades all adopt the same baseline geometry with an average span of about 59 mm. The operating rotational speed is 5900 rpm, resulting in a blade passing frequency of 4720 Hz. The rotor disk is divided into 7 distinct sectors. Each sector contains 6 or 7 rotor blades with an identical baseline geometry but different blade tip seal design (Fig. 8.2b). This rainbow rotor approach allows for the simultaneous testing of multiple turbine geometries, minimizes the total amount of experiments and reduces the time required to reassemble and balance the rotating elements. The overall duration and cost of the experimental campaign is considerably reduced. In the present case, the rotor tip geometries are a selection of high-performance squealer-like and contoured blade tip shapes, selected from the full 3D optimization (cfr. chapter 5 [4]).

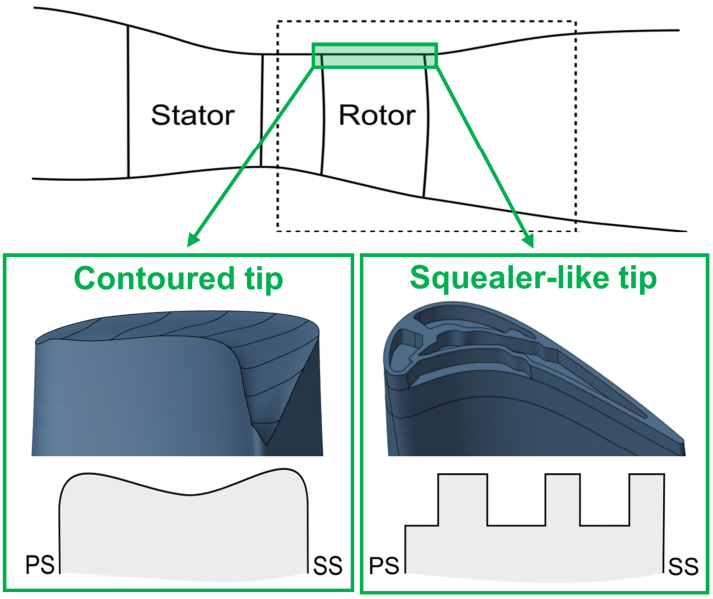

Figure 8.3: Representation of the investigated rotor tip designs.

An illustrative example of the implemented tip design philosophies is given in Fig. 8.3. The rainbow test approach also permits to assess the aerothermal performance of the rotor blades at multiple clearance levels. Here, five sectors mount blades with a

nominal gap size of 1.38% of the blade span, while the blades composing the remaining two sectors are designed to run at a tighter clearance of 0.85% h/H. The 'squealer-like' blade tips feature a cavity depth of 3.4% of the blade span while the rim thickness is 2.0% of the blade span. The contoured blade tips have mild radius variations over the entire tip surface, mostly less than 0.4% of the blade span.

8.1.3 Blade Positioning Optimization and Balancing

Blade Mass Distribution

Every blade was accurately weighted with an estimated error lower than ±0.01% of the total blade mass. The histograms in Fig. 8.4 represent the mass of each individual blade compared to the sector average (left) and to the global average (right). The blade-to-blade variations remain within ±0.5% for the same blade tip design. When considering all the 48 rotor blades, the scattering is significantly larger and reaches almost 4%. The individual masses range from -1.5% below the average blade mass (e.g. squealer type geometries with few rims) to +2.5% above the mean level. The 'heavy' blades belong to the two sectors operating at a tighter clearance, thus carrying an extra mass at the tip radius.

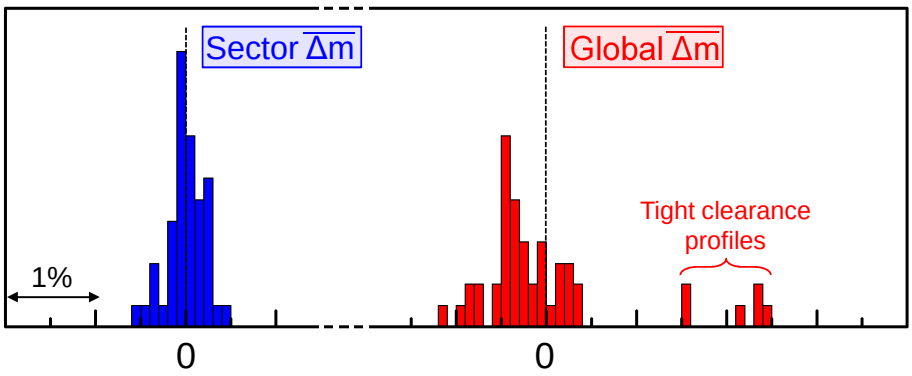

Figure 8.4: Blade weight difference compared to the sector average mass (left) and global mean value (right).

Blade Placement Optimization

A static unbalance, arising from an eccentricity of the center of gravity of the rotating assembly, can generate significant vibrational forces. Avoiding such vibrations is essential to prevent excessive loading on the bearings and thus to reduce fatigue failures and ensure a safe operation at all times. Moreover, if not anticipated during the installation phase, a severe unbalance condition might occur that cannot be corrected using conventional methods that require the addition or removal of material from the rotating parts. For the current turbine configuration, every sector of blades feature a distinct blade tip shape. Additionally, within each sector, blade-to-blade mass variations are observed due to the manufacturing tolerances. Therefore, a significant potential exists for the minimization of the residual unbalance through a proper blade placement. In this view, an optimization strategy was developed to define the ideal relative position of the sectors around the rotor annulus, as well as the position of each single blade within every blade sector.

In the case of a static unbalance, the vibrations are governed by the centrifugal force (F_{centr}=mRω^2), acting on an existing residual unbalance of mass m located at a radius R. This unbalance can be quantified as U=mR. For the turbine rotor, each blade is equivalent to a mass m_i concentrated at its center of gravity R_i, pointing in the direction of the blade position θ_i. Consequently, in order to optimize the total unbalance due to the blade mounting sequence, the vector-sum of the horizontal and vertical unbalance components has to be minimized [169]:

$$U_{tot} = \sqrt{\Big[\sum m_i R_i sin(\theta_i)\Big]^2 + \Big[\sum m_i R_i cos(\theta_i)\Big]^2} \tag{8.1}$$

where the blade weights m_i are measured and the characteristics of the center of mass (R_i and θ_i) are calculated for each blade tip design from the blade CAD drawings. The parameter R_i and θ_i were assumed to remain unaltered by manufacturing variability. A different value of R_i and θ_i was considered for every sector. However,

the maximum variation among the sectors remained limited to ±0.1% of the average radius and ±0.08% of the blade pitch.

The total amount of possible configurations to permute the seven sectors is 6! = 720. Additionally, every blade can be randomly positioned within its own sector, generating additional $7!^6 \cdot 6!$ possibilities for a given sector distribution. Eventually, 48 different ways exist to mount the blade sequence onto the disc itself, resulting in about $4 \cdot 10^{29}$ distinct blade placement sequences. As it is impossible to evaluate directly all options within a finite period of time, a strategy was developed to reduce the amount of unbalance calculations during the optimization.

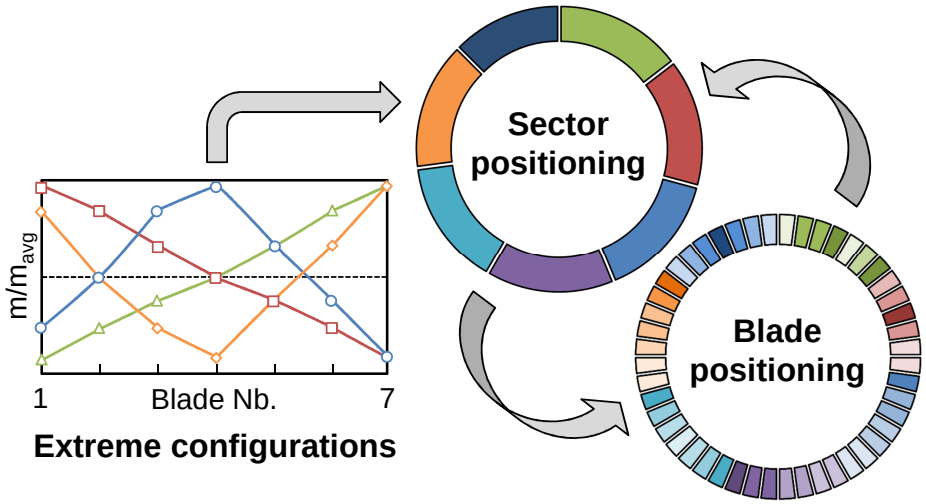

Figure 8.5: Blade positioning optimization strategy.

Fig. 8.5 presents an overview of the adopted methodology for optimum blade placement of a sector-constrained blade set. The key here is not to consider every potential blade sequence inside each sector (i.e. 7! or 6! possibilities), but rather to evaluate only a small amount of 'extreme' configurations per sector. In this case, the blades of each sector were ordered in four different ways according to their mass rank (Fig. 8.5-left). A first 'extreme' configuration places the heaviest blades near the center of the sector ('circles'), a second configuration positions the lightest blades around the sector center ('diamonds'), and for the last two patterns, the mass distri-

bution evolves monotonously, either increasing or decreasing (respectively identified by the 'triangles' and the 'squares' symbols). These four configurations have been chosen to provide a maximum variation in the corresponding rotor unbalance. In particular, while the first two configurations feature a rather low sector unbalance directed towards the center of the segment, the last two sequences would result in a maximum unbalance directed respectively to the right side or to the left side of the sector. This methodology reduces the amount of blade configurations down to $6!{\cdot}4^7 \approx 11.8{\cdot}10^6$, which can be directly evaluated in a couple of seconds on a regular computer.

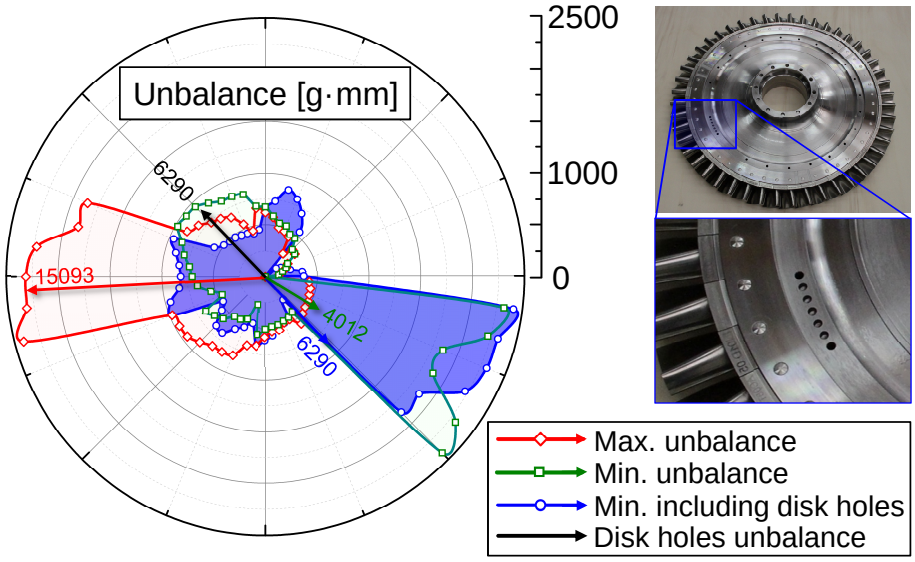

Figure 8.6: Results of the unbalance optimization procedure.

Fig. 8.6 illustrates the results of the blade placement optimization. The polar diagram presents the unbalance along the rotor annulus due to the insertion of the individual blades (where the unbalance has been offset by the minimum unbalance value) and the vectors indicate the resulting unbalance of the full arrangement. The configuration marked with the squares (green) shows the blade placement that provides the minimum possible unbalance (U=4,012 g·mm). The diamond symbols indicate the worst-case scenario with a total unbalance of 15,093 g·mm. Such an

unbalance would require a large balancing mass of almost 60 grams at a radius of 255 mm. In order to allow for a precise balancing, five holes were drilled at the front and back side of the disk, Fig. 8.6-right. The additional holes on the disc creates a specific unbalance of 6,290 g·mm in the opposite direction.

When the disc residual unbalance is included in the blade placement calculation, an optimum blade sequence was found that minimizes the final rotor unbalance down to 0.35 g·mm. This final configuration, indicated with circular labels (blue), was chosen for the eventual rotor assembly.

Field Rotor Balancing

The required balance quality for rigid rotors is specified according to the International Standard ISO 1940/1 [170], also adopted in the American, British and German Standards. For the current rotating turbine rig, the balance quality should satisfy at least G2.5. Combined with the maximum expected rotational speed of the rotor assembly and its total mass, an upper limit for the maximum vibration amplitude of 3.67 μm is demanded.

The vibrations of the rotating turbine are measured with two accelerometers mounted close to the two shaft bearings (Fig. 8.7a). During the operation of the facility, these signals are continuously monitored by means of a field balancing set from Brüel Kjær. The results of the acquired vibration levels during the initial ('unbalanced') run-up of the facility are shown in Fig. 8.7b. At a rotational speed of about 4900 rpm, the vibration levels were judged too high for a long-duration safe operation of the rotating system (vibration amplitudes larger than 5.7 μm), thus in-situ balancing of the rotor assembly was required.

In order to compensate for the residual unbalance, an additional mass can be added to the assembly. To determine the exact angular position and required weight of the balance mass, the four-run methodology was adopted [171]. This strategy allows single-plane balancing of a rotating machine, without the need of phase measurements.

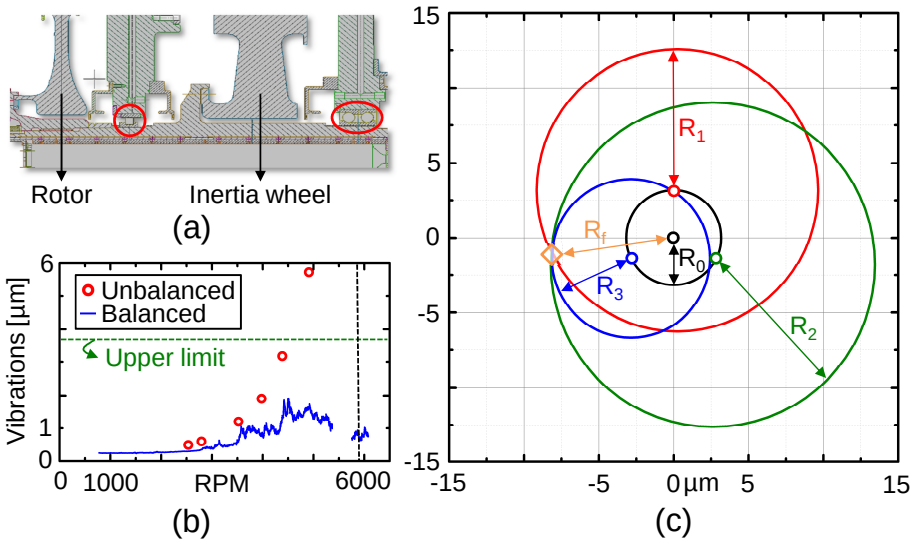

Figure 8.7: Location of the accelerometers (a), vibration results (c) and four-point balancing methodology (c).

After the selection of a proper trial mass, the rotor is spun up sequentially four times to the targeted rotational speed while the vibrational amplitudes are measured (i.e. R_0, R_1, R_2, R_3). The first run the rotor is spun up to speed without any additional balance weight, while in the following three runs the trial mass is attached at three distinct locations along a constant radius around the circumference, ± 120 degrees apart ($\mathrm{R_{balance}} = 275$ mm).

The 4-run balance process is graphically explained in Fig. 8.7c. A circle of radius R_0 is drawn at the center and the angular positions of the three additional tests are indicated with small circular labels. Then, an extra circle for each of the three other tests can be drawn around the latter three marks with a radius equal to the measured vibrations (i.e. R_1, R_2, R_3). The final angular position of the unbalance can be retrieved from the intersection of the last three circles. Additionally, the required weight is found based on the ratio of the vibrational levels:

$$m_f = \frac{R_0}{R_f} m_{trial} \tag{8.2}$$

In order to maintain a safe operation, the four-run procedure was applied at about 4380 rpm. As the vibrations measured in the bearing the furthest away from the rotor generally indicated lower vibrational levels, only the vibration readings from the bearing closest to the disk were used to determine the balance mass characteristics. The vibration levels measured at the end of the balancing procedure after the installation of a 19 g mass are presented in Fig. 8.7b. The maximum vibration amplitudes are below the limit of 3.67 μm recommended for a balance quality level of G2.5, and as low as 1.0 μm at the design speed for aerothermal turbine testing (5900 rpm).

8.2 Tip Clearance Design and Verification

8.2.1 Tip Clearance Control Requirements

Since the turbine performance and the rotor aerodynamics strongly depend on the tip clearance (e.g. the turbine efficiency drops by 2% for a tip gap variation of 1% of the blade span [14]), it is fundamental to accurately set and control the tip gap size during a turbine test.

Current engine manufacturers adopt many distinct strategies, typically categorized by up to what extent touching between the stationary and rotating casing is tolerated. 'No-rub' designs do not allow any contact throughout the whole operation while the 'Just-kiss' and 'Rub-in' approach will permit respectively a slight and heavy contact in which the abradable liner is machined inwards by the rotor tip [172].

In a turbine facility, two different strategies are typically adopted to establish a certain tip clearance in rotation (active tip clearance control is not considered here as a viable solution for transient turbine testing). For wind tunnel testing of tight clearances (e.g. h/H $< 0.5\%$, gaps smaller than 0.4 mm), the turbine is accelerated above the design rotor speed. The blade with the highest tip radius will rub the abradable and thus a constant clearance will be established over the rotor annulus. A lower or higher gap size at nominal speed can be achieved by adjusting the maximum overspeeding.

This procedure has been used successfully in previous turbine test programs where very tight tip clearances could be achieved in rotation thanks to the planned blade-abradable erosion procedure performed at the beginning of the experimental campaign [108, 173]. As the target test running clearance becomes larger and larger, the maximum speed to which the rotor wheel should be spun up (which ultimately sets the radius of the worn abradable liner) is likely to exceed the limits imposed by the mechanical constraints of the rotating assembly.

Therefore, in the case of rotors that operate at larger blade tip clearances ($h/H >$ 0.5%), the rub-in procedure is not viable anymore. In the present test campaign, the

running tip clearance had to be controlled through precise manufacturing and careful mechanical design where the deformation of the components under test conditions is taken into account. As a result, tight dimensional tolerances were imposed on the components of the rotor assembly: the casing ring inner diameter is manufactured with a precision of ±0.01 mm; the tolerance on the radial position of the blade root attachment on the disc is ±0.012 mm and the tip surface shape is controlled within ±0.025 mm. In total, the cumulated dimensional tolerance on the installed tip clearance is ±0.05 mm, i.e. ±0.08% of the blade span.

Furthermore, the actual tip gap established under rotation has to be verified during rig testing by means of accurate casing-to-tip distance measurements at different axial and circumferential locations on the rotor casing ring. These measurements serve to validate the quality of the rotor assembly design, construction and installation as well as to support the results of aerothermal measurements in the turbine rig.

8.2.2 Hot-Cold Conversion

During the operation of the turbine facility, the blades and disk deform under the aerodynamic and centrifugal loads as well as because of the thermal expansion induced by the heating of the rotor surfaces exposed during the test to a blowdown of hot gas. Thus, the difference between the manufactured geometry ('Cold' geometry) and the rotor geometry acquired under rotation ('Hot' geometry) is not negligible.

The aerodynamic forces acting on the blade surfaces induce blade deformations of a small magnitude, typically two orders of magnitude less than the deformation due to centrifugal forces, oriented along the circumferential direction (blade untwist). Coupled aero-elastic effects are also considered of very small intensity and they are neglected in this analysis. An estimation of the thermal dilatation driven by the heat transfer occurring during the short-duration test predicts radial deformations

less than 1 μm. The centrifugal force is therefore the main contributor to the rotor deformation under test conditions.

As a means to quantify accurately the resulting deformation of the blades prior to the manufacturing, a detailed Finite Element (FE) analysis was carried out on the rotating assembly (disk, blades and labyrinth seals), Fig. 8.8a. A simple flat tip was adopted for the study and results indicate an average radial deformation (ΔR) in rotation of about 0.25 mm. Moreover, depending on the location in the overtip region, the local deformation can vary from 0.21 mm on the front suction side of the blade, up to 0.36 mm at the rotor trailing edge.

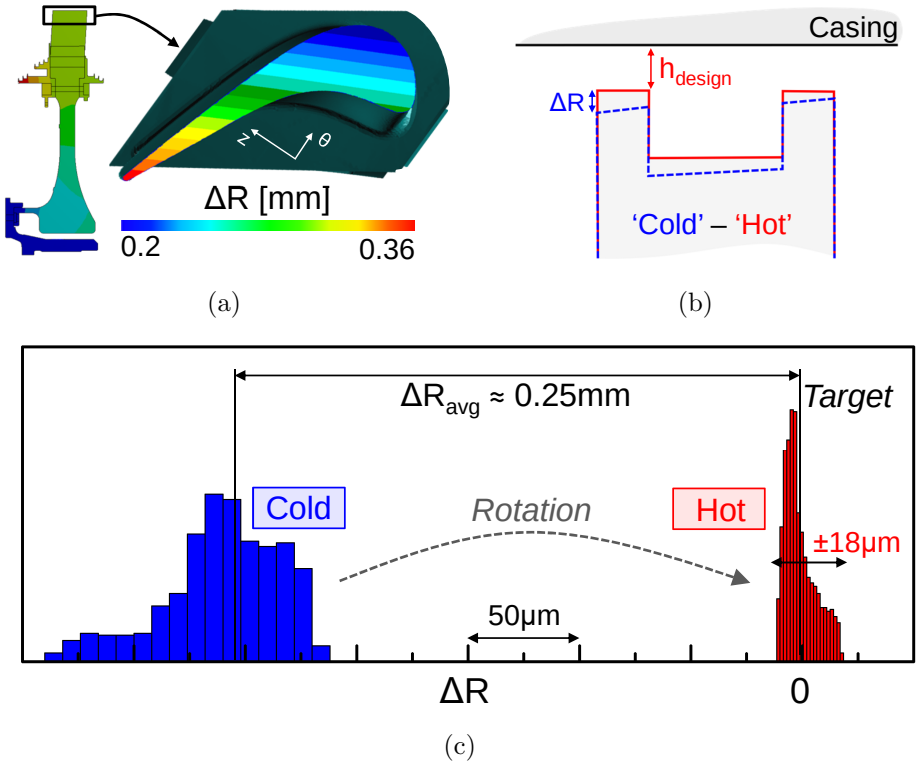

Figure 8.8: Hot-cold blade conversion: Blade FE analysis (a), inverse compensation (b), eventual radial deformation (c).

The maximum radial deformation corresponds to about 40% of the nominal tip clearance and 65% of the tight tip clearance. The deformations in the axial and tangential direction are one order of magnitude smaller than deformations in the

radial direction and their effect on the tip gap geometry and flow characteristics can be disregarded. However, the radial displacement of the tip surface must be compensated during the mechanical design phase to achieve the targeted clearances during the tests and guarantee a safe operation of the facility. Furthermore, the cold-to-hot geometry transformation is needed to compensate for the non-uniform radial deformation of the tip surface. In this particular case, the differential radial deformation of the tip radius can vary as much as 0.25% of the blade span. The final goal of the tip control procedure is to obtain a constant tip radius all over the tip area under rotation, Fig. 8.8b. In fact, not only the height, but also the shape of the tip gap channel plays a key role in the aerodynamics and heat transfer processes in the overtip region [51]. Therefore, the capability to control the tip radius distribution is fundamental to ensure the establishment of engine-representative tip leakage flows in the turbine experiment.

The radius variations shown in the contour plot of Fig. 8.8a suggest that the spatial variations of the tip surface radius are a linear function of the tangential (θ) and axial direction (z):

$$\Delta R(\theta, z) = R_0 + \alpha\theta + \beta z \tag{8.3}$$

where the unknown R_0, α and β can be retrieved using a least-square fit on all the node-data on the tip surface. The analytical model approximates the radius evolution predicted by the FE simulation within 1.5 μm over the whole tip area. Assuming that small changes (i.e., dimensional tolerances) in the blade geometry will not modify the radial deformation field due to centrifugal load, the 'Cold' geometry can be retrieved from the target 'Hot' geometry by applying the reverse deformation and subsequently trimming the blade top surfaces (both rim and cavity surfaces) by the local radial deformation value (Fig. 8.8b).

To verify the inverse deformation methodology, an FE analysis was performed on the 'Cold' geometry of a complex squealer design that underwent blade tip radius compensation based on the deformation data of the flat tip geometry. The results

for the radial deformation are presented in Fig. 8.8c. In this plot, the height of the bars are proportional to the surface area exhibiting the radius deviation (on abscissa) compared to the targeted design value. At rest ('Cold' state), the blades radius is on average about 0.25 mm smaller than the target value, and the tip radius shows variations up to 150 μm over the tip area. When put in rotation ('Hot' state), the tip surface moves towards the design radius within 18 μm. Moreover, the area-average radius is matched within 1 μm, well within the manufacturing tolerances.

This analysis demonstrates the validity of the followed reverse-deformation approach and shows that the deformation field predicted from a flat-tip blade can be reasonably used for the compensation of more complex squealer designs. The radial deformation of the tip is not a function of the tip configuration as long as the blade tip geometry change remains limited to a relatively small portion of the blade span (e.g. $< 4.5\%$ of the blade span).

8.2.3 Clearance Instrumentation

Fig. 8.9 presents an overview of the tip clearance instrumentation used in the current turbine experimental campaign. The distance between the rotating airfoils and the stationary casing is measured by a combination of wear gauges and capacitance-based probes. The rotor casing measurements are performed at three equally spaced circumferential positions. These locations will be further denoted as T, L and R (Fig. 8.2b). Inserts are fit inside these three circumferential slots on the rotor shroud ring and are flush mounted with the abradable liner (Fig. 8.9a). This configuration allows direct access of the sensor head to the rotor casing and blade tips.

Each insert contains five wear gauges, Fig. 8.9b, essentially cylinders of abradable material (the same type as applied on the rotor casing ring) attached to a Monel tube of diameter 1.0 mm and length 15 mm, and mounted on a drilled screw DIN84 M5x10. As the rotor speed is increased, the longest blade gradually machines the abradable pin at the tip of the wear gauge. Before the aerothermal testing program begins, the

rotor dynamics and the actual tip clearance levels are monitored through a controlled procedure where the rotor is spun up to increasing speeds. After each test, the height of the pin extension from the casing endwall is measured by a dial gauge (with a systematic error of ± 0.01 mm) to provide the minimum clearance established at a certain speed. This value can be used as a 'zero' reference to datum the capacitance probe measurements. The purpose of the relatively large sensing area of the wear gauge (tip diameter of 3 mm) is twofold: it reduces the measurement sensitivity to loss of abradable material during spurious events (not related to a blade passage) and it provides a sufficiently large datum surface for precise dial gauge measurements.

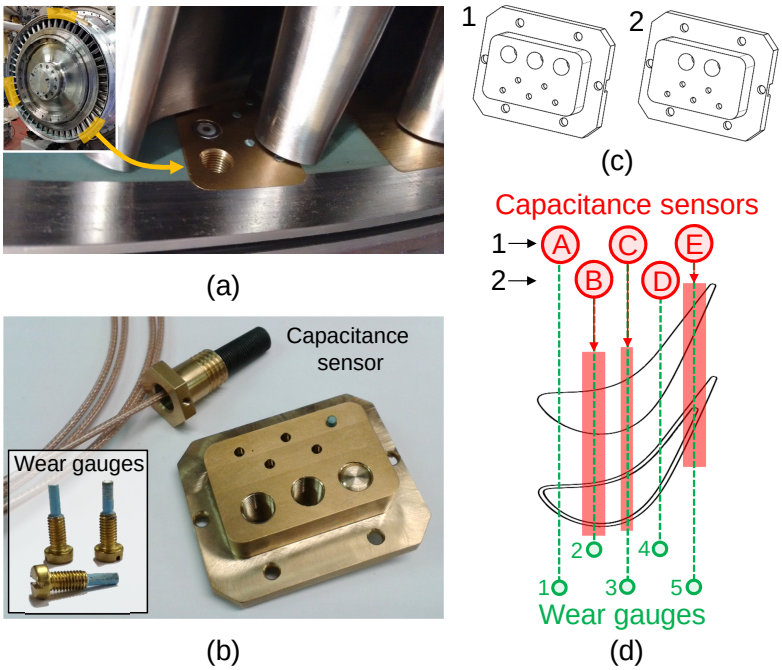

Figure 8.9: Turbine instrumentation location (a), probes and insert types (b,c) and eventual blade coverage (d).

The high-frequency clearance measurements are performed by means of three capacitance-based sensors. The proximity measurement system detects variations of the capacitance between the probe and a moving conducting blade.

Such probes allow high bandwidth measurements, capturing distance fluctuations exceeding 60 kHz (i.e. 13 times higher than the blade passing frequency, 4720 Hz). The sensors performance was demonstrated during prior test campaigns in the same rotating turbine rig [108] and a detailed description of the technique, signal conditioning and data reduction methodology can be found in [173].

The uncertainty in tip clearance is about ± 25 μm at an operating distance of 25% of the probe sensing diameter (approximately 1 mm for a sensor diameter of 5.5 mm). The sensor resolution is approximately 10 μm. The instrument range depends on the sensing head diameter and is roughly equal to the sensors radius. However, the smaller the probe, the higher the spatial resolution as averaging occurs over a reduced surface area. In this view, two probes adopt a sensor diameter of 5.5 mm and the third one is manufactured with a smaller diameter of 2.5 mm. While the 5.5 mm diameter probes can capture the full range of tip clearance variations (about 0.7 mm), the 2.5 mm diameter probe is able to resolve the multiple small-size features that distinguish the different squealer-like and contoured tip designs with an increased accuracy and spatial resolution.

The three capacitive sensors are installed inside two types of inserts, labelled '1' and '2' in Fig. 8.9c, equipped respectively with three and two slots. The combination of these two types of inserts allows placing the wear gauges and the capacitance probes at the same five distinct axial locations distributed between 13% and 88% of the rotor axial chord, Fig. 8.9d. When not equipped with a capacitance sensor, the insert's slots are sealed with special threaded caps to prevent air leakages from the turbine test section. The location of the capacitance probes was selected according to the following measurement requirements:

- Quantify the blade deformation along the rotor axial direction to verify the correct tip gap establishment under rotation.
- Monitor the tip gap distribution along the rotor annulus.

- Maximize the spatial resolution of the tip clearance measurements in blade regions with a high density of tip design features (e.g. squealer with multiple rims, highly ridged contoured surfaces).

Therefore, the single 2.5 mm capacitance probe was positioned at the rotor mid-chord, station 'C' (on insert 'T'), where the seven blade tip designs present the highest variability of tip seal features. The two 5.5 mm probes were installed at two different circumferential locations (insert locations 'L' and 'R') and two distinct axial positions, 'B' and 'E' respectively. The two probes provide discrete tip clearance measurements around the rotor annulus and on blade tip areas where the airfoil radial deformation is predicted to be either the smallest (rotor front suction side, station 'B') or the highest (rotor trailing edge, station 'E'). Table 8.1 summarizes the measurement locations of the tip clearance instrumentation used for the current research.

Table 8.1: Sensor locations.

	Slot	**A**	**B**	**C**	**D**	**E**
	$z/C_{ax,rot}$	13%	32%	51%	69%	88%
Wear Gauges		TLR[1]	TLR	TLR	TLR	TLR
Capacitance sensors						
Ø2.5mm		-	-	T	-	-
Ø5.5mm		-	L	-	-	R

8.2.4 Static Clearance Measurements

Before the first rotor run up takes place, the relative radius variation of all blades was measured at several locations on the tip surface by means of a dial gauge installed on the casing ring. These measurements quantify the manufacturing tolerances and eventual changes in nominal tip radius originating from the blade-disk mounting. Fig. 8.10 illustrates the results of the radius measurements performed at three distinct locations on the blade tip with the rotor at rest. All the measurements are offset

[1]T,L and R refer to the casing insert loacations around the rotor annulus (Fig. 8.2b)

by the relative position of the first airfoil and the different segments characterize the distinct tip shape sectors. The measurement error and repeatability is estimated to be ±0.02 mm for measurements on a squealer rim or cavity. The measurement error increases to ±0.04 mm on the smooth profile of the carved blade due to the difficulty to accurately position the dial indicator head on the tip surface. The blade-to-blade variations remain below 0.1 mm around the average blade radius at each measured location. Moreover, the nominal radius difference expected between blades with nominal and tight tip gap is matched. The last sector (blade 43 to 48) is composed of airfoils with a carved tip profile, designed to run at tight clearance. Due to the strong tip shaping, the pressure side radius is slightly reduced with respect to the leading edge value, while the mid suction side is further decreased by about 0.4 mm. For aerodynamic reasons, the design intent is to create a divergent path for the tip leakage cross-flow.

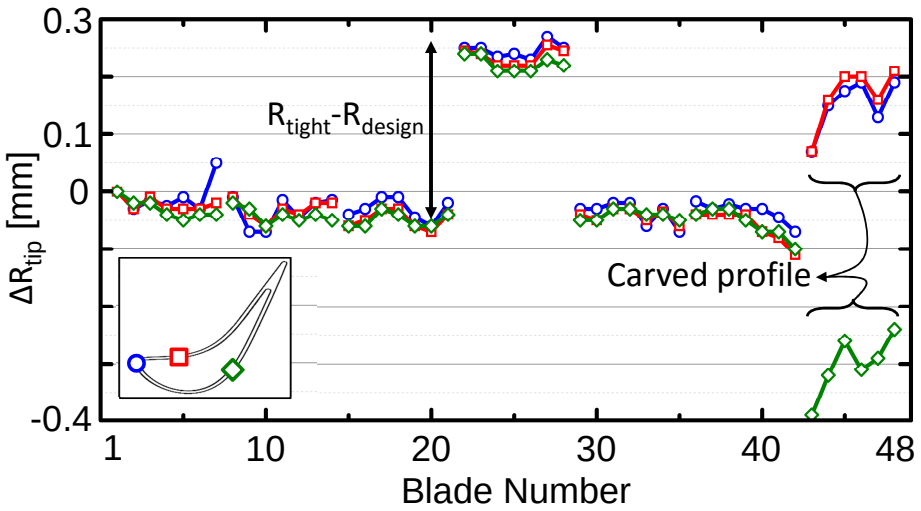

Figure 8.10: Static measurements of the blade radius at three distinct positions on the tip surface.

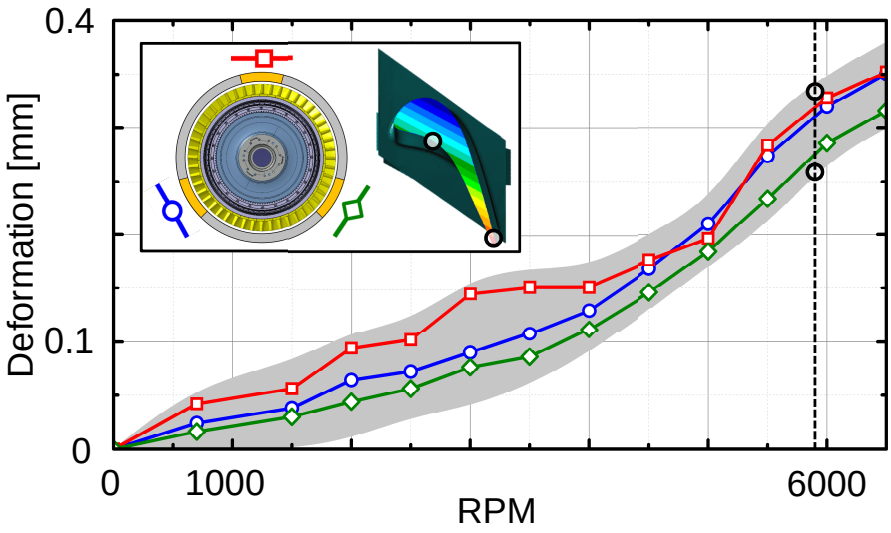

Figure 8.11: Deformation of the blade with increasing RPM.

8.2.5 Verification of Minimum Clearance in Rotation

During the first run-ups, the rotational speed is gradually increased up to the design speed in steps of about 500 rpm. After reaching the speed target, the rotor is brought down to rest again and the height of the consumed wear gauges is measured on the three inserts at each of the five axial locations. Fig. 8.11 presents the deformation of the blade in function of the rotational speed. The three lines indicate the average measured radial elongation for each inserts, while the grey shaded area spans the minimum to maximum deformation observed at each rotational speed. The measured variation of blade radius with rotor speed follow closely a quadratic trend in agreement with the observation that the radial deformation is principally driven by the centrifugal forces. Additionally, the deformation at the design rotational speed (5900 rpm) is compared with the expected value as previously obtained from the FE calculations. The experimental data are in good agreement with the predicted minimum deformation (ΔR_{min}=0.26 mm), occurring at about 40% of the rotor axial chord, and with the maximum deformation (ΔR_{max}=0.33 mm) localized near the tip trailing edge.

For the interested reader, while out of scope for this thesis dissertation, a detail of the unsteady acquired tip clearance signatures can be found in [166] (where the distinct type of profiles can be identified).

8.3 Turbine Instrumentation and CFD Applicability

8.3.1 Aerothermal Instrumentation

The main goal of the future testing program is to detect with high accuracy the variations in the rotor aerothermodynamics introduced by each particular blade tip design. This aim requires the use of very high time and frequency response instrumentation, able to resolve the blade-to-blade flow fluctuations happening at (and far above) the rotor blade passing frequency (∼5kHz). Fig. 8.12 illustrates the eventual instrumentation and measurement locations across the turbine stage.

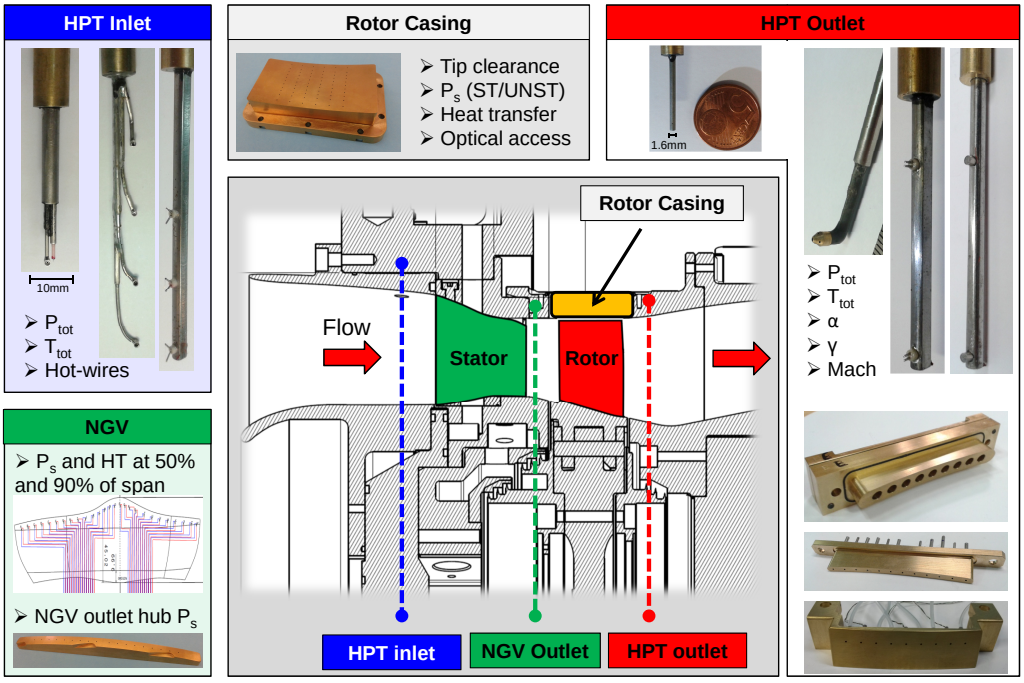

Figure 8.12: Overview of the envisioned aerothermal instrumentation.

The turbine inlet flow field is monitored by endwall static pressure taps and a series of rakes that measure the radial profiles of total pressure (Pitot probes with Kiel heads), total temperature (equipped with bare fast-response thermocouples) [174] and turbulence intensity (hotwire anemometry [175]). The time-averaged and time-resolved static pressure field is also measured at the NGV outlet and at the rotor outlet

tip and hub endwalls using low-frequency response transducers (pneumatic taps) and fast-response piezo-resistive Kulite sensors. The rotor outlet aerodynamic flow field is characterized by a set of high-bandwidth total pressure sensors and directional probes which contain miniaturized pressure sensors with a high frequency range. Two pneumatic 5-hole probes are used to monitor the time-averaged flow direction, speed and pressure. The thermal field is resolved using a combination of cold-wire and thermocouple probes in rake arrangement [160, 162, 176].

The rotor casing is equipped with three capacitance-based tip clearance probes that allow to resolve the blade-to-blade tip gap variations as well as the clearance variations over the blade top section itself (cfr. section 8.2.3 [173]). Additionally, the casing static pressure is sampled by 33 high-frequency pressure sensors (Kulite type XCQ-062) and 33 pneumatic lines connected to a pressure scanner. The fast-response pressure sensors are not flush mounted but recessed inside the metallic block by 0.2 mm to prevent possible damages due to the close proximity of the rotating blades preserving a frequency response above 90 kHz. The sensor locations form a regular array of 6 measurement points in the circumferential direction and 11 measurement points along the axial direction. The number of measurement points allows to reconstruct the casing pressure field with a large spatial resolution over one stator vane pitch and between -5% and 105% of the rotor axial chord in the direction of the machine axis. The endwall heat flux is measured by means of thin film gauges. These type of sensors, first employed by Schultz and Jones [177], have been successfully used for many turbomachinery applications in the form of MACOR substrates placed inside sockets on the blade [83], a full MACOR block equipped with laser-etched sensors for shroud measurements [178] or upon a thin Upilex sheet attached onto the blade surface [179]. For the current campaign, a Upilex sheet was glued on top of the aluminum casing insert. The location of the heat transfer measurement points replicate the location of the pressure instrumentation. Additionally, the heat transfer insert is equipped with flexible heaters mounted on its rear surface. This heating system allows to vary the initial temperature of the metallic support prior to a turbine test from ambi-

ent temperature up to 360K to enable the measurement of the casing adiabatic wall temperature and adiabatic convective heat transfer coefficient [161, 179].

The design of the measurement setup focused on the development of new instrumentation, able to capture the highly unsteady flow features generated by the blade passage in the rotor casing region and at the rotor outlet section.

8.3.2 CFD Data Extraction

In order to estimate the expected measurement ranges (8.3.3), optimize the spatial positioning of the sensors (8.4) and a-priori predict the experimental errors induced by the inherent limited sensor bandwidth (8.5), steady Reynolds-Averaged Navier-Stokes simulations were employed. The adopted simulations are the ones obtained through the 3D optimization routine (cfr. chapter 5) and the full description of the computational domain, mesh specifications and numerical model can be found in section 5.2.

For every one of the seven profiles mounted inside the facility, the relevant aerothermal characteristics were extracted at the main measurement planes of interest: the rotor casing surface and the exit flow field 50% $C_{ax,rot}$ downstream of the blades trailing edge (Fig. 8.13).

Specifically on the rotor shroud, 25 measurement traces of the heat transfer and static pressure are extracted, each at a fixed axial location. These traces (as function of the angular position) represent an estimate of the actual measurement signals in time that the stationary probes in the overtip casing insert will be acquiring. Similarly, 39 signals at a constant radius (uniformly distributed) were extracted in the downstream plane, for all measured aerodynamic quantities (i.e. pressures, temperatures, Mach number and flow angle). Eventually, also the pitchwise-averaged (i.e. the tangentially averaged) values on the casing and downstream plane were obtained, respectively in function of the axial position and the radial location. These values represent the response of the low-frequency instrumentation inside the facility. Ad-

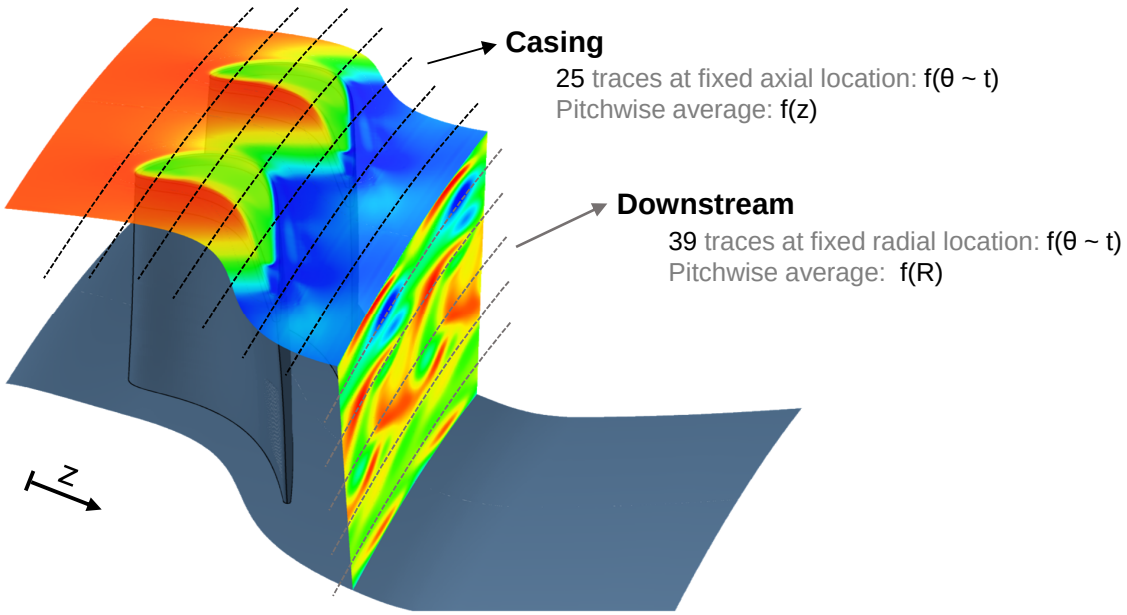

Figure 8.13: Overview of the CFD extraction locations.

ditionally, the minimum and maximum values are dissected for all traces which will indicate the range that the high-frequency sensors are likely to experience.

8.3.3 Analysis of the Measurement Ranges

Casing Measurements

Fig. 8.14 presents the numerical results for the static pressure normalized by the upstream stagnation pressure (a) and the shroud heat flux divided by the average of the simple squealer case (b) for all the installed profiles. Additionally, the trends of 4 specific profiles are highlighted: 2 flat tip geometries running at the design clearance (1.38% h/H - green squares) and tight clearance (0.85% h/H - orange triangles), a simple squealer design (1.38% h/H - blue diamonds) and eventually a fully carved tip shape at the reduced gap size (0.85% h/H - red circles). The graphs on the left of Fig. 8.14 show the pitchwise averaged values of the static pressure and heat load along the axial chord. The shaded area quantifies the observed maximum range over

all investigated profile types. The detailed distributions on the overtip shroud are presented in the contours on the right of Fig. 8.14.

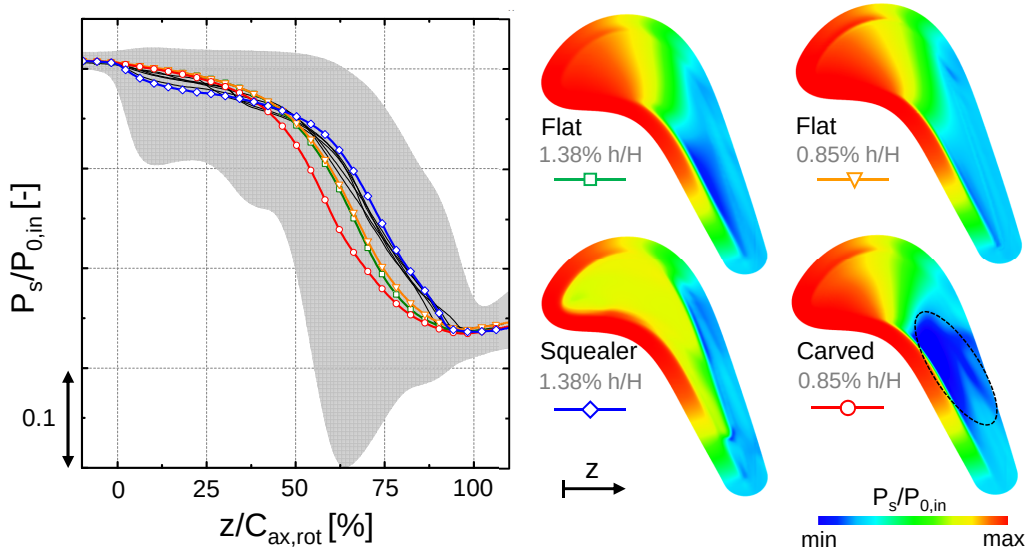

(a)

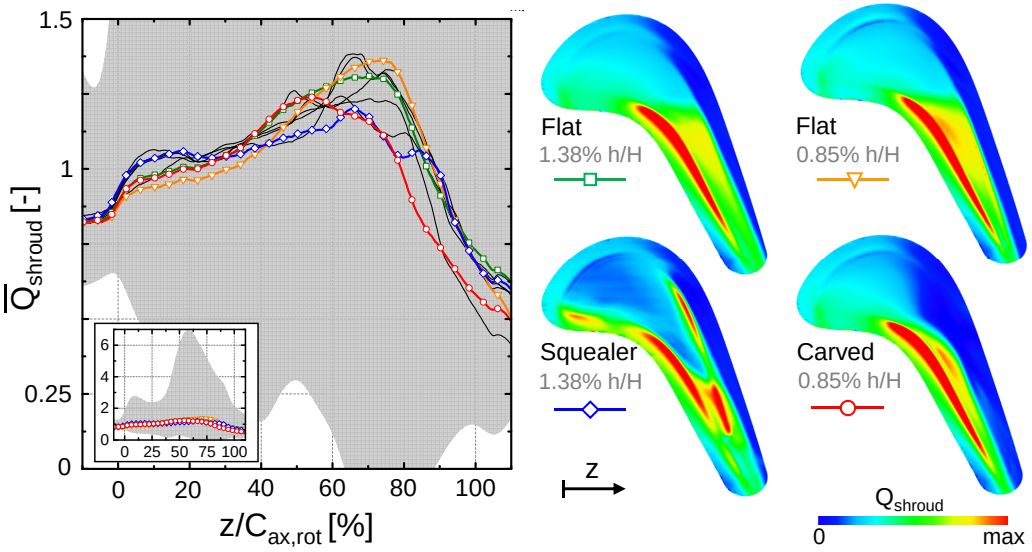

(b)

Figure 8.14: Ranges and expected variability of the casing measurements based on CFD.

The overall average trend of static pressure (Fig. 8.14a) reduces monotonously throughout the rotor passage, accelerating the flow up to a drop in static pressure of

almost 30% of the inlet total pressure. The most significant difference in pitchwise averaged pressure can be observed for the carved profile (red circles) in the last 50% of the rotor blade which reveals considerably lower average values. This can be explained by the supersonic acceleration induced in the highly loaded aft section through a divergent channel (cfr. Fig. 8.14a-right).

The expected pressure variations over the pitchwise traces (i.e. representing unsteady pressure measurements at a constant axial location) account for about 10% of the total pressure in the front section and reach even 40% of the inlet stagnation pressure at a position about 60% of the axial rotor chord.

Interestingly, the flat tip traces do not show a high dependency on the actual clearance levels and mostly differ in the aft section where larger overtip velocities are observed for the higher clearance level (cfr. chapter 3 [1]). As a consequence, lower static pressures can be seen in the contours of Fig. 8.14a-right. The simple squealer geometry on the other hand (blue diamonds), generates a large zone of a rather constant intermediate pressure inside the cavity bath. This results in a reduced static pressure field in the front part of the blade while giving rise to higher pressures in the aft part compared to the other geometries.

The tangentially averaged heat load (Fig. 8.14b-left) shows a common increasing trend for all profiles till about 70% of the blade chord, largely caused by the growing levels of heat transfer observed at the pressure side rim where the flow accelerates into the gap region. In the aft part, the average heat loads decreases again down to 50% to 75% of the average heat flux. The overall profile-to-profile differences in the pitchwise averaged heat transfer do not exceed 30%. The ranges of the heat load fluctuations on the contrary vary considerably. At around 60% of the axial chord, the heat flux can rise locally over 6 times the average value while even dropping below zero in the test facility due to the reduced driving temperatures (i.e. transfer from the casing to the fluid).

Downstream Measurements

Fig. 8.15 presents the estimation of the measurement quantities downstream of the turbine rotor. Consistent with Fig. 8.14, the 4 additional profiles (2 flat ones, a fully carved shape and the simple squealer) are highlighted. On the bottom of Fig. 8.15, a view of the actual distributions of the different flow quantities is provided to emphasize the complexity of the encountered flow structures downstream of the turbine stage.

Based on the pitchwise averaged profiles along the radius, one can observe mainly the upper 50% of the blade span is affected by the altered tip designs. The most significant changes are present in the flow angles, e.g. comparing the two flat tip designs where a difference as high as 40 deg. can be observed at about 90% of the blade span. This is mostly due to the different size and location of the tip leakage vortex which generates either a stronger or weaker local under/overturning. The static and total pressure averages do not show large blade-to-blade variations. However, looking at the downstream structures (Fig. 8.15-bottom), one can see that the pressure is highly tailored by the vortices (particularly P_0). Therefore, the high frequency response sensors downstream of the stage will reveal the clear distinct flow characteristics, indicated by the ranges in total pressure ($\pm 3\%$) and localized static pressure drops of more than 4% in the region of the leakage vortex core. The covered range of angles spans almost 120 deg. over the entire blade height. Therefore, it is essential throughout the experimental campaign to rotate the downstream pressure probes according to the expected average flow angle at the radius of the sensor head to maximize the angle sensitivity. Eventually, significant variations can also be found in the temperature. As a real combustor temperature profile was imposed upstream of the stage, the considerable fluctuations are due to the cold flow which migrates through the secondary vortex structures from the endwalls towards the middle of the passage (Fig. 8.15-bottom right).

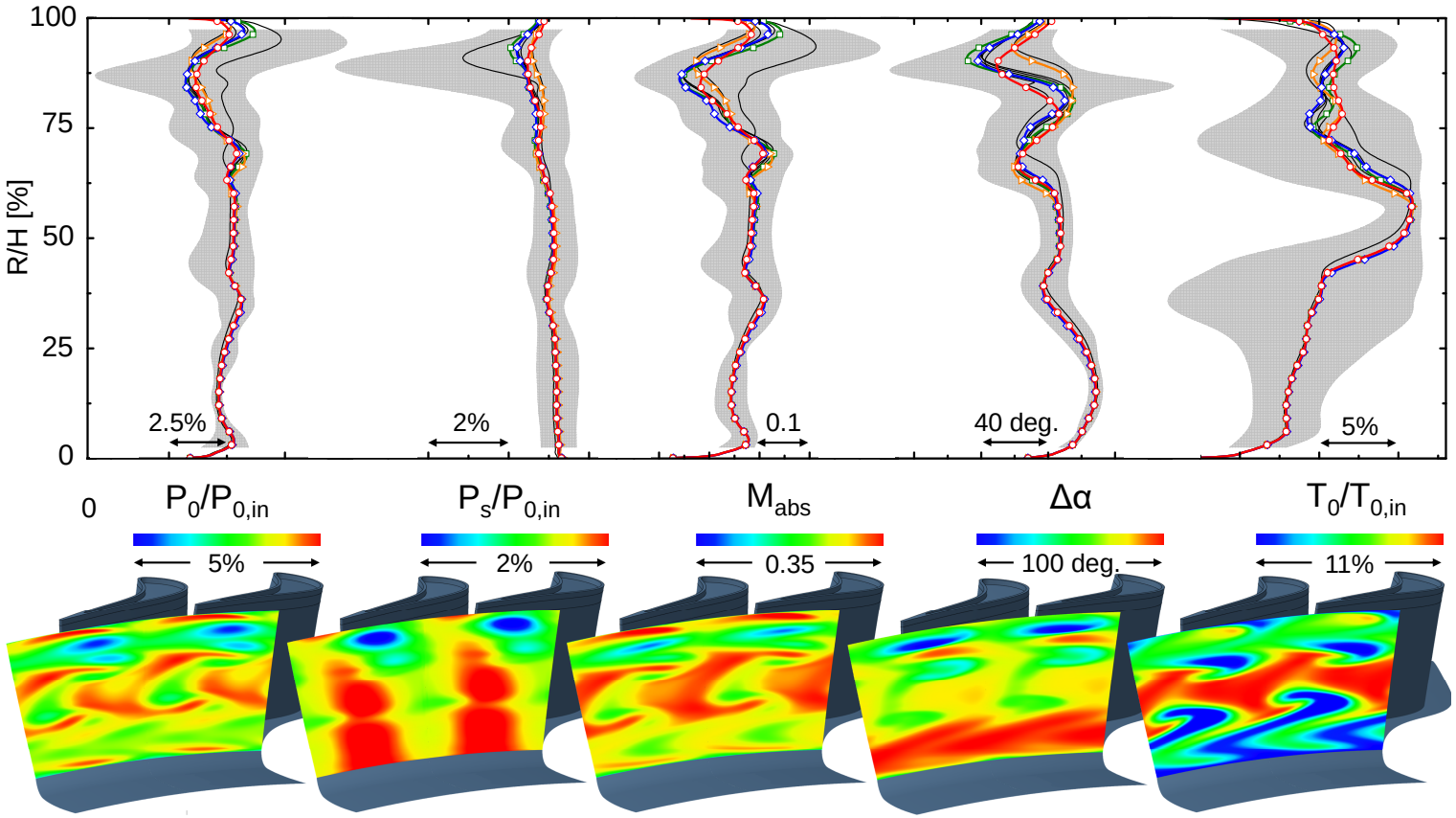

Figure 8.15: Ranges and expected variability of the measurement quantities 50% $C_{ax,rot}$ downstream of the rotor blade.

8.3.4 Sensor Limitations and Temporal/Spatial Resolution Requirements

Both the spatial as well as the temporal resolution are of major importance to accurately resolve the specific flow features developing in small regions with a brief residence time. An insufficient miniaturization of the adopted measurement technique will result in a spatially averaged output signal and consequent inability to capture the small flow features inside the overtip region or downstream vortex development. Additionally, for intrusive measurement techniques, large probes can create a considerable blockage effect, altering the upstream flow field through its potential field. In a similar way, a low cut-off frequency of the sensor will act as a physical low-pass filter onto the acquired traces. It is important to note that both measurement considerations modulate and filter the signal in an analogous way, though in a different dimension, i.e. time and space.

In the following two sections these two aspects are addressed and methodologies are proposed to mitigate and/or a-priori estimate the errors associated with both the spatial (8.4) as well as the temporal (8.5) measurement resolution. The strategies will be illustrated in this dissertation using the data for the commonly adopted squealer geometry, but can however be applied to any type of blade profile.

8.4 Spatial Averaging: Optimization of Sensor Locations

In this section, the effect of the spatial averaging will be quantified and both a single and global optimization strategy is proposed to optimize the probe positioning of the downstream aerodynamic sensors.

First, the errors are quantified when one would use a conventional uniform distribution of the sensor placement (8.4.1). Then, an iterative routine is explained which optimizes the probe location, minimizing the induced error on a single measured quantity (8.4.2). Eventually, in section 8.4.3 a global strategy is presented to obtain an optimal probe positioning, reducing the error on the final efficiency and loss variable, as the result of combined simultaneous measurements of multiple aerodynamic quantities.

8.4.1 Uniformly Distributed Sensor Positioning

The top of Fig. 8.16 presents the error that would be generated along the blade height when one would be measuring the quantity of interest using a uniform sensor placement (or similarly, by performing multiple tests with equidistant probe traverses). The results for 6 different amounts of sensors are illustrated, going from 50 points (blue lines) down to only 5 (red lines). The exact probe locations are additionally included on the left side of Fig. 8.16-top. The bottom of Fig. 8.16 presents the integrated value of the error starting from 3 measurement points up to a total of 50 probe locations.

The 'downsampling' and interpolation procedure is illustrated on the left side of Fig. 8.16-top. The blue line indicates the 'true' pitchwise averaged profile extracted from the high-fidelity CFD simulations using 500 points from hub to shroud. Subsequently, a certain amount of uniformly distributed sensor locations is assumed and the real data is 'probed' at those heights. To retrieve the eventual radial distribution based on the virtually measured points, a Piecewise Cubic Hermite Interpolating Polynomial is used (indicated with 'pchip') [180]. Even though a conventional cubic

spline interpolation would give smoother results (as its construction is based on a continuity of the second derivative), such spline reconstruction often creates large (nonphysical) overshoots. The pchip interpolation however, avoids these overshoots and spurious oscillations. Moreover, throughout this analysis, the pchip method demonstrated consistently to give rise to lower overall errors compared to the use of a spline interpolation. Eventually, the illustrated errors along the blade span in Fig. 8.16-top are the point-wise differences between the pchip interpolated distribution and the 'true' pitchwise averaged values.

The largest errors can be observed near the endwalls and at the locations of the vortex structures, creating steep gradients which are not well captured in case of a low amount of points. The integrated error levels in the lower part of Fig. 8.16 quantify the eventual expected discrepancy. These figures give an indication of the measurement difficulty of a certain quantity, but can additionally provide the experimentalist an idea of the minimum required amount of points satisfying a certain error target. For example, comparing the two pressures, one can observe that after 10 measurement points, there is only few room for improvement in the case of the static pressure. However, to accurately capture the trend in the total pressure, one would need more than twice the amount of points to reach a comparable error level. Similarly, a steeper drop in error with increasing measurement points is observed for the absolute flow angle and temperature as opposed to the Mach number.

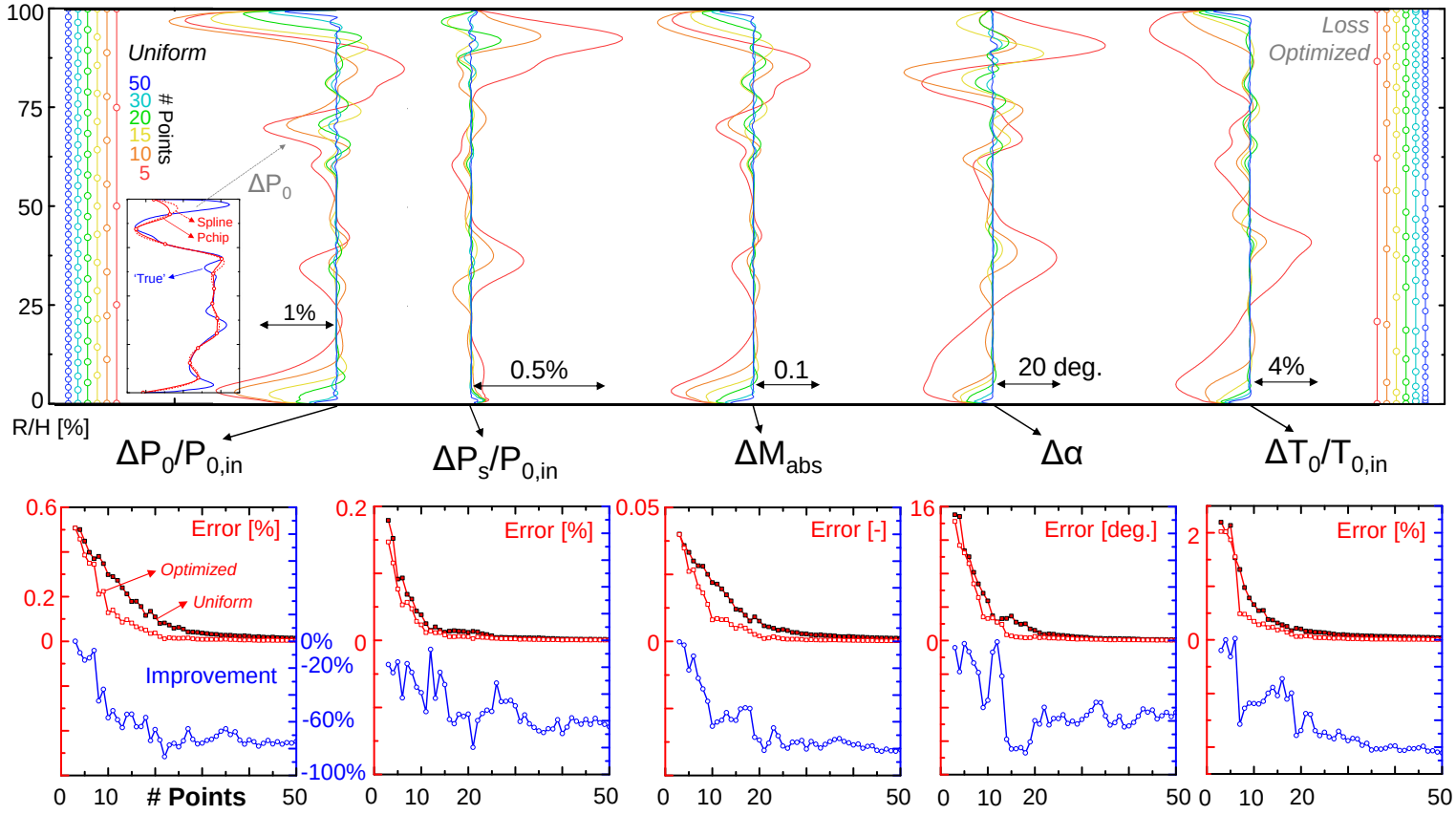

Figure 8.16: Errors on the pitchwise averaged measurement traces with a uniform probe placement and the results of the error improvement after the single optimization strategy.

8.4.2 Radial Optimization of the Sensor Locations

Strategy

Fig. 8.17 presents a new methodology to reposition the probe locations, targeting a minimization of the absolute error on a single measured quantity.

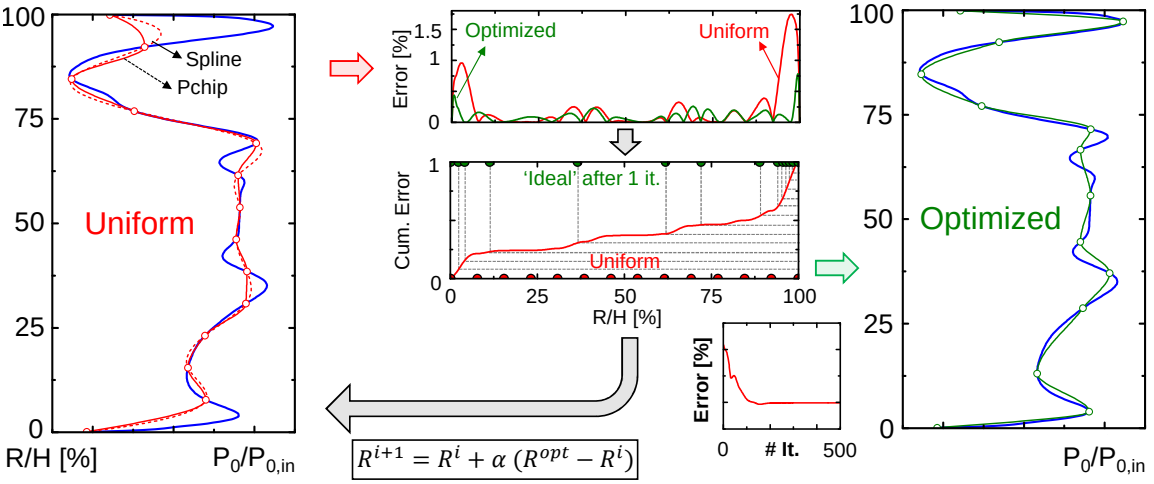

Figure 8.17: Overview of the positioning optimization strategy for a single measurement quantity.

The iterative procedure starts from a certain radial distribution of the probe locations, indicated with R^i for the current iterative step i. In this case, a uniform positioning was chosen as the starting point. First, the error evolution is calculated according to the difference between the interpolated profile (pchip) and the 'true' pitchwise distribution, in the same way as is explained in the previous section. Subsequently, the absolute value of the error along the radius is retrieved (presented on top of Fig. 8.17) from which a cumulative error distribution can be derived in function of the radius (middle of Fig. 8.17). The idea now is to reposition the probe locations towards the regions where the error is the largest. Therefore, one can define an 'ideal' probe location based on a transformation of uniform intervals through the cumulative density function. This is illustrated by the dashed grey lines, uniformly

distributed on the right axis, mapping to a non-uniform probe distribution on the upper horizontal axis. One can observe that this transformation is clustering the points at the locations of the largest errors, while reducing the amount of points in the regions where the accuracy was high already.

However, this 'ideal' distribution (R^{opt}) is typically sub-optimal as the newly proposed positioning will give rise to lower errors in the regions where the points are clustered, but will generally enlarge the errors in the zones where a sparser sampling is proposed. This observation leads to the need of an iterative procedure where this new distribution (R^{i+1}) is re-evaluated, the errors are quantified and a new 'optimal' positioning is proposed. Additionally, as is often done in numerical codes, a relaxation factor α is applied which stabilizes the convergence. This factor controls the differential displacement of each single point towards the current optimal location. Throughout this study, a value for the relaxation factor of 1% (i.e. 0.01) showed to be the best trade-off between ensuring convergence and required amount of iterations. A typical convergence history of the overall error is presented on the bottom of Fig. 8.17. One can see that for this case, 300 iterations are sufficient to reach a stable error.

However, as any conventional type of gradient-based methods, the obtained solution is not a guaranteed global minimum and depends on the initial conditions. Nevertheless, when starting from a simple uniform distribution, this process showed significant and especially consistent improvements for all flow quantities and amount of sensor locations.

Optimization Results

The resulting errors, adopting the optimization routine for each measured quantity was added to the lower graphs in Fig. 8.16 (unfilled squares). The relative improvement of the error compared to a conventional uniform distribution is presented in the lower curves (blue circles).

One can observe that, for every measured quantity and every possible amount of probe locations (i.e. 3-50), the optimization manages to reduce the overall error. Particularly for the total pressure and Mach number, the repositioning allows to reduce the errors significantly when only a few amount of probe locations would be possible: roughly 60% error reduction when using 10 points. The improvements for the static pressure, angle and temperature become particularly apparent from 15 (to 20) measurement points.

8.4.3 Global Optimization for Efficiency and Loss Measurements

The optimization procedure for a single aerodynamic quantity has demonstrated the capability of improving the error levels significantly. However, in a true experimental campaign, most of these aerodynamic quantities are measured using a single probe (e.g. three or five-hole probes which simultaneously retrieve the pressure, Mach and flow angles), or the same measurement grid is used for both the pressure and temperature measurements.

Therefore, this section proposes a global optimization strategy for loss measurements where the distribution is optimized, considering combined acquisitions of multiple aerodynamic quantities.

Measurement of Efficiency and Losses

Accurate measurements of the efficiency are essential to validate new technologies inside experimental rigs. However, several difficulties arise as many formulations require a precise measurement of the mechanical torque as well as massflow [113,181]. Particularly in short duration rigs this is not trivial and complex correction methods are applied to compensate for the occurrence of heat transfer, mechanical losses and injected coolant flows [114, 117].

Therefore, a common way to quantify the aerodynamic losses downstream the turbine stage is via an indirect measurement of the total relative pressure drop across

the rotor (i.e. $P_{02r} - P_{03r}$), non dimensionalized by the downstream dynamic pressure ($P_{03r} - P_3$). This last approach will be adopted to illustrate the global optimization strategy for a loss coefficient defined as:

$$\omega = \frac{P_{02r} - P_{03r}}{P_{03r} - P_3} \tag{8.4}$$

Where the relative downstream pressure (P_{03r}) can be obtained from the measured absolute Mach number, angle, pressure and temperature. In order to calculate the sensitivity to each of the different measurement parameters, a straightforward Monte Carlo approach was adopted which propagates the error through the subsequent equations. Specifically, to retrieve the sensitivity to each of the measured quantities, the other variables were kept constant at their mean levels and 1 million, normally distributed, samples were calculated. The standard deviation was taken as 10% of the expected average measurement range along the entire span.

Note that for simplicity, to retrieve the sensitivity coefficients, the radial component of the velocity was neglected and therefore, retrieving the eventual relative velocity was performed in the cascade plane at mid-span [182].

The resulting (relative) sensitivities of the loss coefficient to variations in the Mach number is 0.717 (%Loss/% of M_3), the temperature 1.010 (%Loss/% of T_{03}), the pressure 3.209 (%Loss/% of P_3) and absolute angle 0.331 (%Loss/% of α).

Optimization Procedure

An overview of the global optimization procedure is presented in Fig. 8.18 and builds upon the single optimization strategy as described in the previous section. However, in this case, a combination of all relevant errors is incorporated simultaneously: M_{abs}, P_s, T_0 and α.

Similar to the single optimization procedure, the error of the interpolated measurement distribution along the radial direction is calculated (Fig. 8.18-left) and the relative errors (compared to their mean value) can be derived ($\delta\overline{M}_{abs}$, $\delta\overline{P}_s$, $\delta\overline{T}_0$ and

$\delta\overline{\alpha}$). Subsequently, the root of sum of squares method [183] is applied to combine all four error contributions ($\delta\overline{S}_i$) to obtain the total loss error $\delta\omega$ using the calculated sensitivities ($\frac{\partial\omega}{\partial\overline{S}_i}$):

$$\delta\omega = \sqrt{\sum_{i=1}^{4}\left(\frac{\partial\omega}{\partial\overline{S}_i}\delta\overline{S}_i\right)^2} \tag{8.5}$$

$$= \sqrt{\left(\frac{\partial\omega}{\partial\overline{M}_{abs}}\delta\overline{M}_{abs}\right)^2 + \left(\frac{\partial\omega}{\partial\overline{P}_s}\delta\overline{P}_s\right)^2 + \left(\frac{\partial\omega}{\partial\overline{T}_0}\delta\overline{T}_0\right)^2 + \left(\frac{\partial\omega}{\partial\overline{\alpha}}\delta\overline{\alpha}\right)^2} \tag{8.6}$$

The upper right graph in Fig. 8.18 illustrates the different error components multiplied with their respective sensitivities (blue, green, black and orange lines) as well as the total estimated error on the loss coefficient along the radial direction (thick red line). Next, based on the total loss evolution, the cumulative distribution function is constructed and identical to the single optimization procedure, an 'ideal' repositioning R^{opt} can be found (i.e. grey dashed lines). Eventually, the probe positions R^i are altered towards the current optimal distribution using the relaxation factor α to find the new distribution R^{i+1} from which the next iteration starts.

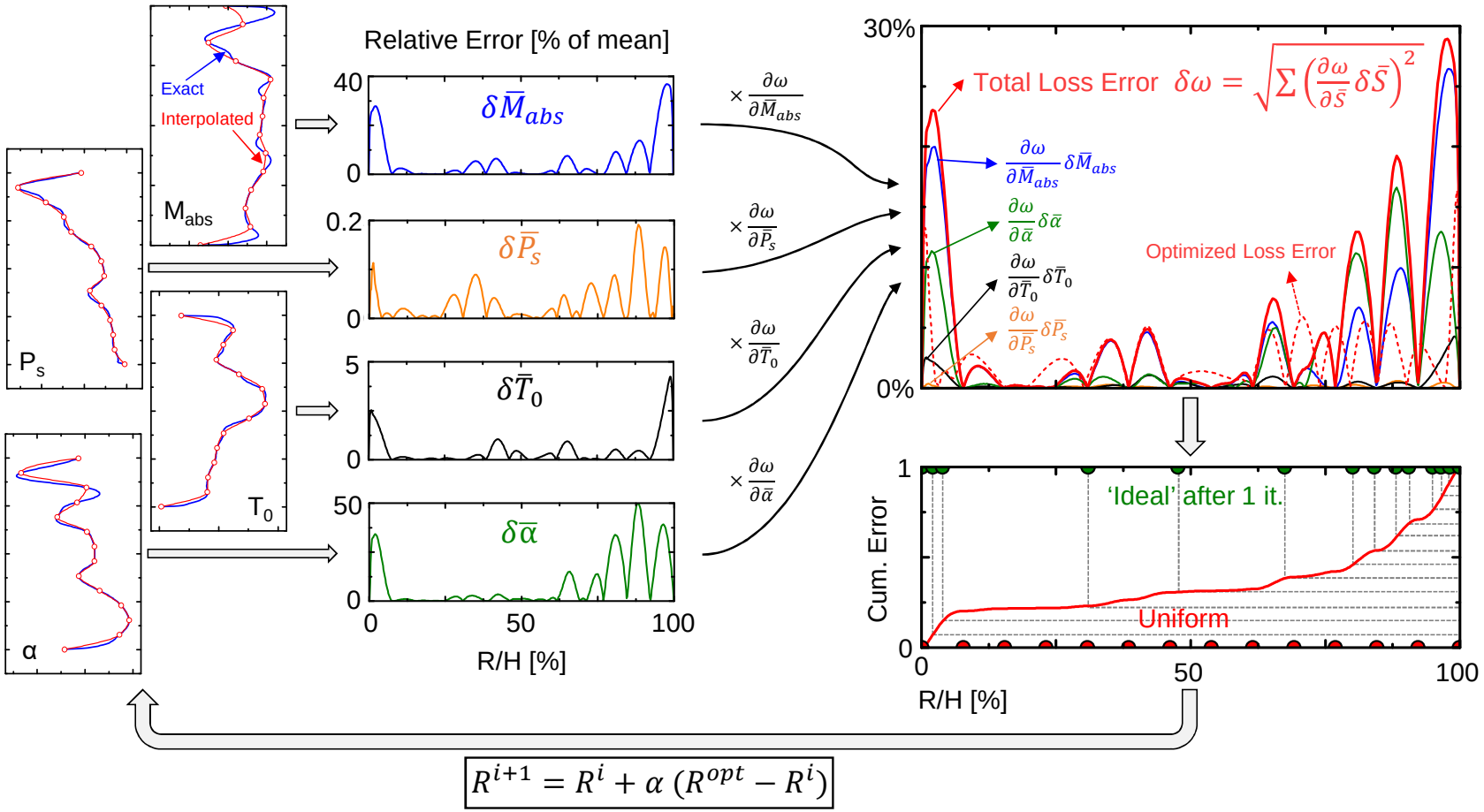

Figure 8.18: Overview of the global positioning optimization strategy for loss measurements.

Global Optimized Positioning Results

Fig 8.19 presents the contribution of each of the measurement errors to the mis-prediction of the total loss coefficient for 3 up to a total of 50 measurement points. On the left, the integrated relative errors of the measured variables are shown in function of the amount of probe locations after the global optimization. The right graph of Fig 8.19 illustrates the different weighted contributions together with the total integrated error on the loss.

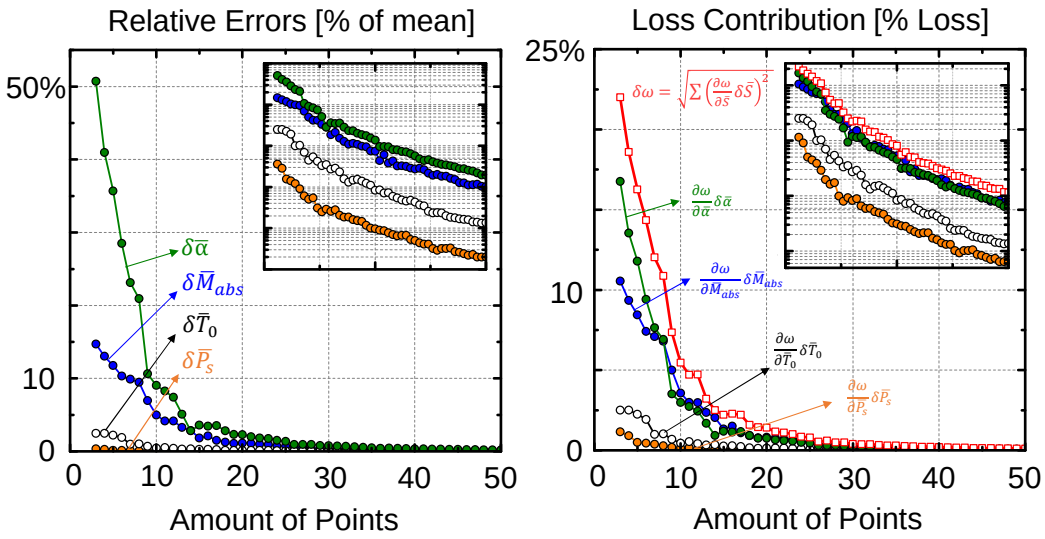

Figure 8.19: Breakdown of the different error contributions to the total loss coefficient after optimization.

Overall, one can observe very large error levels in the eventual loss coefficient, as high as the actual value of the loss itself for a very low amount of measurement points (e.g. < 7). This is due to the fact that all errors along the radius are squared (or for the single optimization strategy the absolute value is taken). This results in large absolute errors as in reality, local under and overpredictions along the blade height would compensate each other. Therefore, the presented values should present absolute maxima.

One can see that the highest contribution to the losses is caused by discrepancies in the flow angle measurements, followed by the correctness of the absolute Mach number. The eventual contribution of the total temperature and static pressure seem to be smaller, mainly due to the low absolute errors after the spatial interpolation on these quantities (cfr. Fig 8.16).

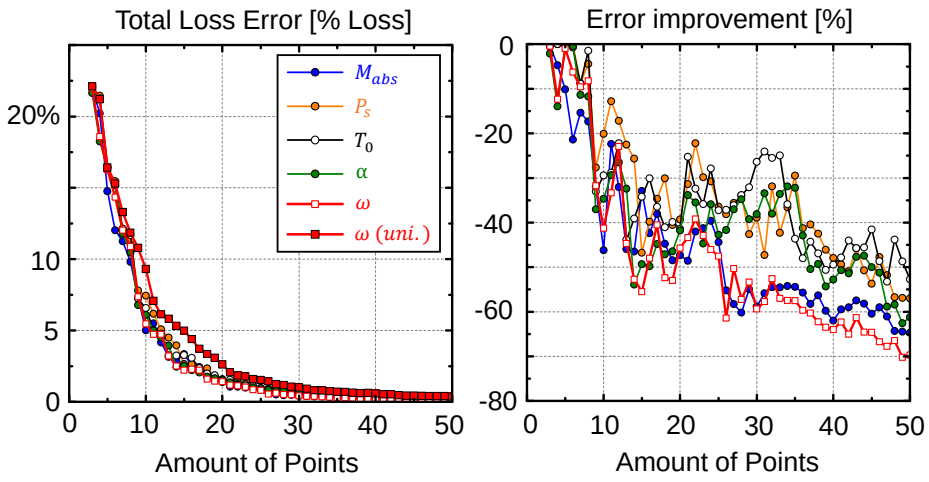

Figure 8.20: Total expected loss error after the global optimization (left) and relative improvement compared to a uniform sampling (right).

Fig 8.20-left eventually illustrates the total error on the losses (ω), compared with what would be obtained via the single optimization strategy, only considering one measurement quantity. The graph on the right presents the relative improvement compared to a uniform spacing of the sensor locations. All optimization strategies, whether it is performed for a single component or combining all quantities, prove to reduce the error compared to a conventional uniform probe distribution. For the majority of the cases, the global optimization strategy tends to generate the largest improvements. However, due to the the fact that the global minimum is not guaranteed, for some cases, the single optimization for either the absolute Mach number or flow angle manages to give slight additional improvements.

The eventual globally optimized distribution of the sensor locations has been included on the vertical axes on the top right of Fig. 8.16.

8.5 Time Averaging: Influence of the Finite Sensor Bandwidth

An insufficient bandwidth of the sensor will result in an inability to capture the small flow features inside the overtip region or downstream vortex development. The measurement device essentially acts as a physical low-pass filter onto the acquired traces and results in the loss of information about the aerothermal field. Techniques to compensate for such insufficient frequency response have been successfully applied (e.g. through the use of inverse transfer functions for hot/cold wires or pressure probes [174]). However, this remains a cumbersome practice, requiring an accurate characterization of the probe/sensors or heavily relies upon the underlying assumptions of the processing methodology. Therefore, it is vital to conduct an a-priori assessment of the required temporal (and spatial) resolution, already during the initial design phase of the experimental campaign.

In this section, a strategy is illustrated which allows to estimate the loss of information due to the finite nature of the sensor frequency response based on RANS simulations.

8.5.1 Procedure Overview

Fig. 8.21 presents the overview of the procedure to predict the captured information by the sensor. From the simulated flow field (e.g. through low-cost steady-state RANS CFD) the time-resolved traces of pressure, temperature or heat flux can be extracted at the envisioned measurement locations during the experiments.

Subsequently, the signal is resampled (/oversampled) according to the finest grid size in order to obtain a uniform spacing of all the virtual measurement points. In the case of the mesh on the casing, the finest grid resolution in the tangential direction is about 0.6 mrad. Taking the rotating frame into account, this spatial discretization translates into a 1MHz frequency. Therefore, the signal was spatially oversampled with a uniform spacing of 0.3 mrad, i.e. 2MHz. Afterwards, this periodic time-series is repeated in order to obtain an accurate frequency resolution for the FFT of 5Hz

(i.e. repetition up to a total length of 0.2s). Eventually, the entire signal is low-pass filtered at 250kHz to remove all spurious (nonphysical) oscillations. Such anti-aliasing filter at 250kHz is also used when acquiring the high-frequency components of the signals inside coming from the experimental turbine facility.

Once the clean, uniform and periodic time-signal is obtained, a filter is applied to mimic the limited sensor bandwidth. Specifically, a 5^{th} order Butterworth filter is applied [184] with a cut-off frequency going from 500Hz to 250kHz in steps of 500Hz. An example of the gradually increased filtering of a static pressure signal is presented on the top right of Fig. 8.21.

Then, a quantitative estimation of the lost portion of the signal can be obtained by comparing the total RMS embedded in the original signal (blue area) with the RMS contained in the difference of the CFD trace with the filtered signal (green area). Eventually, the percentage of the information which is not captured due to the limited sensor capabilities can be plotted in function of the cut-off frequency (Fig. 8.21-bottom left).

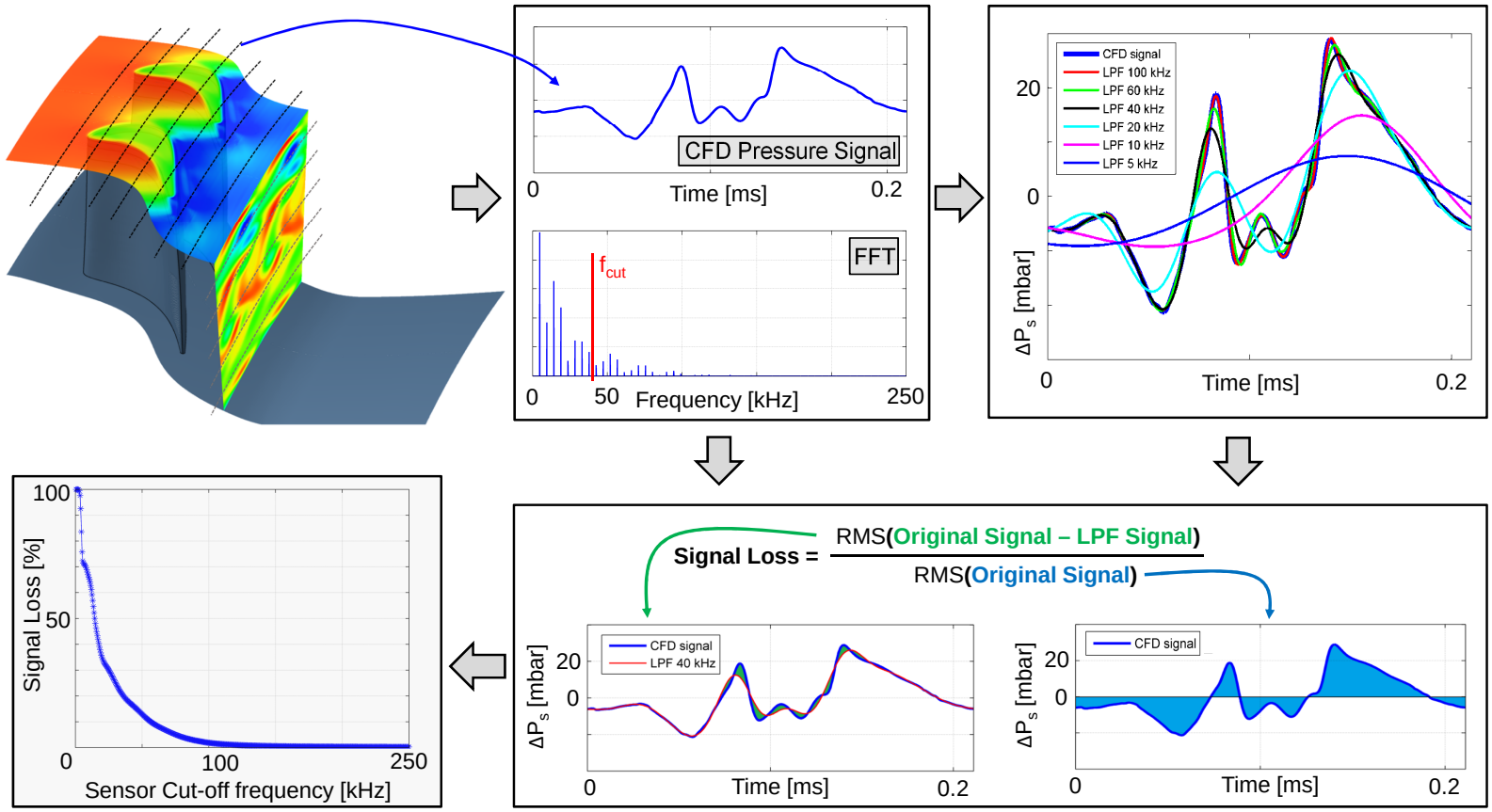

Figure 8.21: Procedure overview to estimate the loss of information due to a limited sensor bandwidth.

8.5.2 Casing Measurements

Fig. 8.22 applies the described procedure for the envisioned measurements of static pressure (top) and heat flux (bottom) on the overtip casing at three axial locations: 20%, 50% and 90% $C_{ax,rot}$. Consistent with Fig. 8.14, the trends of all tip profiles are included and 4 conventional shapes are highlighted (2 flat tip designs, a simple squealer one and a fully carved profile). The contourplots reveal the distribution for a plain tip at the design clearance. Each graph presents the percentage of captured information (i.e. the complement of the signal loss), in function of the sensor bandwidth. Additionally, the FFT included on the bottom right of each figure serves to illustrate the amplitudes in the frequency spectrum, i.e. at each harmonic. The 3 graphs for the FFT of the pressure signals adopt identical scales which allows a direct comparison of the peak amplitudes across the different axial locations. The same holds for the three figures of the heat transfer spectrum.

From the analysis of the static pressure in the front part of the blade (Fig. 8.22-top left), one can conclude that a sensor frequency response of 75 kHz is required to capture a minimum of 90% of the information contained in all tip profiles. The flat tip running at a tight clearance shows to be the most restrictive case (orange triangles). From the FFT at this location, 20% $C_{ax,rot}$ downstream of the rotor leading edge, the simple squealer shows the largest peak amplitudes. However, as the energy is mostly contained in the lower harmonics, the captured information curve rises fast. At mid-chord, the carved profile shows the slowest rising trend, confirmed by the large amount of frequency content contained in the higher harmonics (cfr. FFT). Additionally, based on the frequency spectrum, one can observe that the amplitudes of the fluctuations are almost twice as high as in the front region. In the aft part of the blade (Fig. 8.22-top right), the steep gradients over the thinnest part of the airfoil gives rise to the requirement of a high frequency response. Specifically, the bandwidth would need to exceed 100 kHz in order to sufficiently capture all the embedded information. Furthermore, the spectrum shows reduced amplitudes which

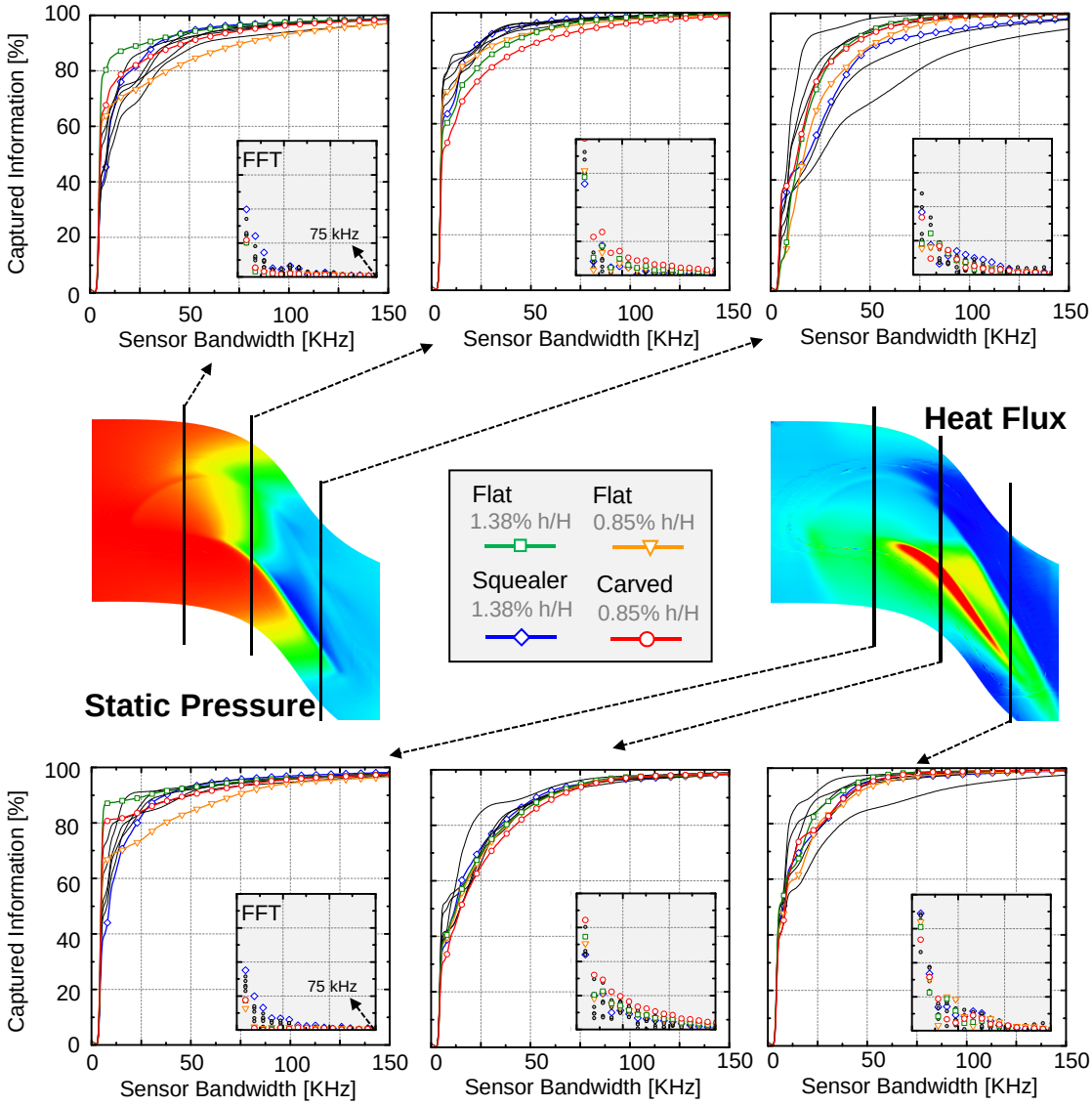

Figure 8.22: Percentage of captured information and FFT at three axial locations on the casing for all tip profiles.

results in additional measurement difficulties. On the heat transfer side, the loss of information can be limited to less than 10% over the entire blade chord when the sensor is capable of monitoring unsteady variations up to 75 kHz. Additionally, from the FFT's, one can observe that the amplitudes of the heat flux fluctuations remain high in the back part of the blade (as opposed to the static pressure trend).

Fig. 8.23 shows a continuous representation of the bandwidth requirements over the entire blade. The horizontal axis depicts the sensor bandwidth from 0 up to 25 times the blade passing frequency (BPF) while the vertical axis progresses from the blade leading to trailing edge. The contours indicate the minimum percentage of captured information over all profiles. Specifically, this means that each horizontal line in Fig. 8.23, represents the minimum curve location from the graphs presented in Fig. 8.22. In this case, the contour is constructed through a cubic interpolation from the data at 21 axial locations (e.g. from which only three were presented in Fig. 8.22). The same procedure has been applied to both the static pressure on the casing as well as the heat flux traces.

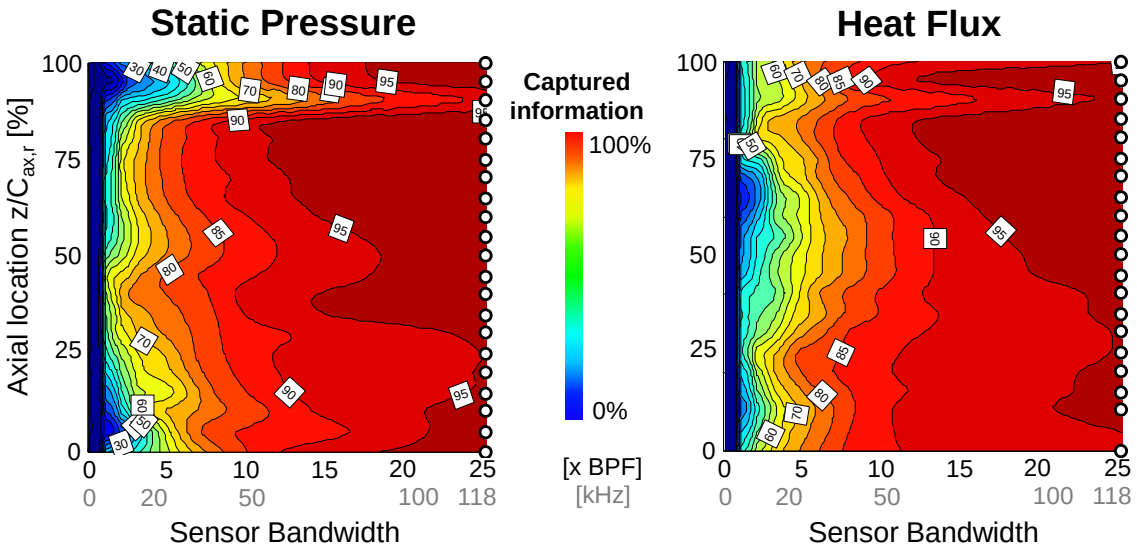

Figure 8.23: Minimum captured information across all profiles due to the limited sensor bandwidth on the casing.

The static pressure contours demonstrate that a bandwidth of 10-15 times the blade passing frequency is more than sufficient over the majority of the blade chord. As identified in Fig. 8.22 already, some distinct geometrical features in the highly loaded thin aft part generate very steep and localized pressure fluctuation, requiring additional bandwidth to fully capture the entire spectrum. A similar trend can be

observed on the heat transfer side (Fig. 8.23-right) where also 10-15 times the BPF is sufficient from the LE up to 80% of the rotor chord and a peak requirement is visible at 90% $C_{ax,rot}$.

8.5.3 Downstream Measurements

Fig. 8.24 illustrates the same methodology as Fig. 8.23, but this time for 5 quantities measured downstream of the turbine stage, i.e. at 50% $C_{ax,rot}$ behind the rotor trailing edge. The horizontal axis represents again the sensor bandwidth while the vertical axis shows the radial position along the blade span. In order to construct the contours of the minimum captured information across all profiles, 39 tangential 'virtual' measurement traces were used with intervals of 2.5% of the blade span.

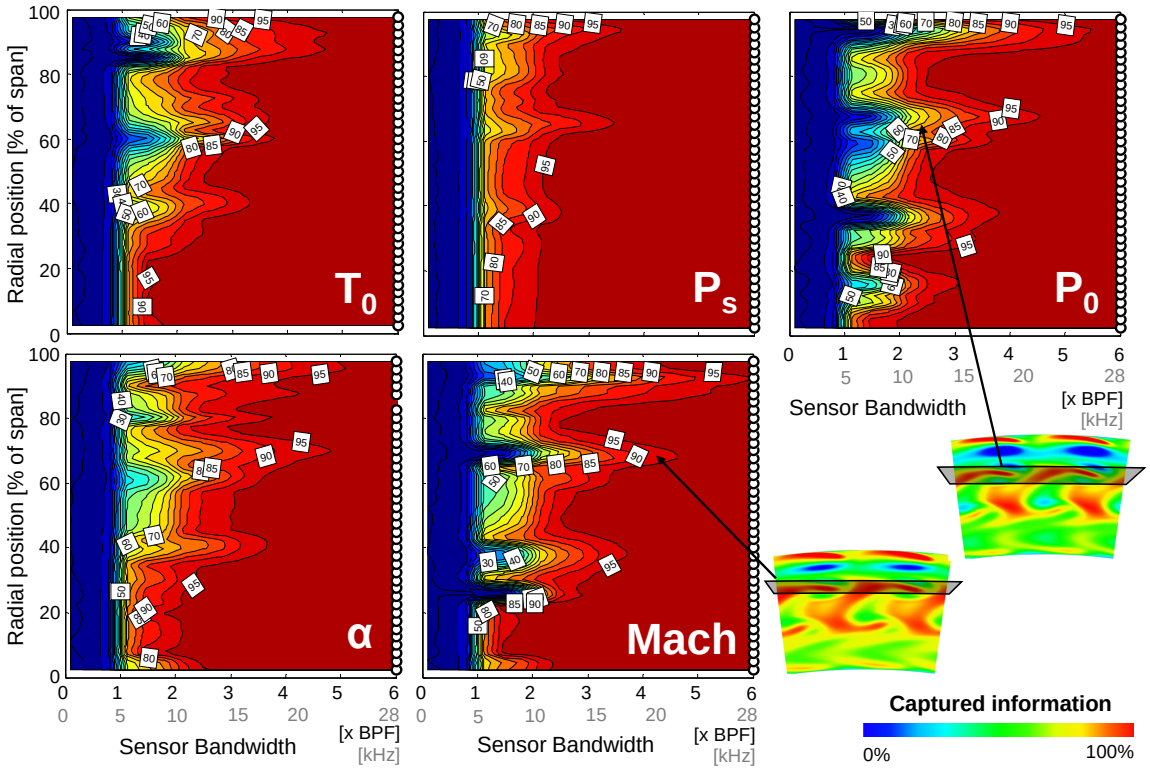

Figure 8.24: Minimum captured information across all profiles due to the limited sensor bandwidth downstream of the stage.

As the flow downstream of the turbine stage mixes out and the variations are mainly due to the remaining vortex structures, the eventual required sensor response is significantly lower than what was shown to be essential on the overtip casing. For all aerothermal measurements, a total bandwidth of 3-4 times the BPF (i.e. 15-20kHz) is more than sufficient to catch the physics over the entire blade height. Interestingly, distinct peaks can be observed in the sensor response around 60-70% of the blade height. This is due to the tangential 'overlapping' of multiple vortex structures which directly doubles the response requirement as illustrated for the Mach number and total pressure on the bottom right of Fig. 8.24.

8.6 Conclusion

This chapter presented the redesign of a high-speed rotating turbine facility at the von Karman Institute for Fluid Dynamics to allow for simultaneous testing of multiple distinct blade (tip) profiles. Important considerations related with the balancing and precise clearance design are highlighted. Furthermore, methodologies were developed to integrate RANS simulations to a priori estimate the measurement errors induced by the finite spatial sampling and inherent limited sensor bandwidth.

The rainbow rotor is composed of seven sectors, each equipped with a distinct tip shape. The weight of each blade was measured prior to the rig assembly, revealing a 4% mass variation. Therefore, a numerical strategy was developed to select the optimal blade and sector placement around the rotor annulus which minimizes the unbalance. The fast procedure calculates the best blade order in a sector-constrained rotor row, considering the measured weight distribution while accounting for any residual disk unbalance. The predicted optimal blade arrangement (featuring a negligible unbalance of 0.35 g·mm) was balanced in situ using the four-run method to achieve a quality grade of G2.5.

In order to guarantee a precise establishment of the gap size, the blade geometries were constructed through an inverse-design methodology to counterbalance the radial deformation caused by the centrifugal loads. The hot-to-cold transformation procedure, validated for a squealer tip design, allows to control the running clearance size and tip shape within a few micrometers and compensates for nonuniform tip deformation fields as high as 0.36mm. Eventually, the rotor components were manufactured with very tight mechanical tolerances, leading to a propagated deviation on the tip radius of $\pm 0.08\%$ of the blade span. Both the static gap height as well as the clearance in rotation were verified using a combination of dial gauges, wear gauges and high-frequency capacitance sensors embedded in the rotor casing ring.

High-fidelity RANS simulations were employed to design and position the aerothermal instrumentation around the rotor row. The expected measurement ranges are

identified and methodologies are proposed to mitigate and estimate the errors associated with the spatial as well as temporal measurement resolution. Specifically, a novel iterative procedure has been developed which optimizes the probe positioning to either reduce the expected errors on a single measured quantity or on the loss variable, as the result of combined measurements of multiple aerodynamic quantities. Furthermore, the effect of the finite nature of the frequency response of the sensors has been simulated using CFD traces extracted on the envisioned measurement locations. After subsequent low-pass filtering, the loss of information can be quantified as a result of the limited bandwidth. The instrumentation on the overtip casing requires a temporal response of about 75 kHz to capture 90% of the unsteady fluctuations across the majority of the blade chord. The downstream aerothermal measurements of the mixing flow are however less demanding and need a proper resolving of only 3 to 4 times the blade passing frequency. Distinct peaks in this requirement were observed at the radial locations where a tangential overlapping of multiple vortex structures occurred.

This part of the research paved the way for a future, elaborate experimental validation of the superior tip geometries in a rotating turbine facility, at engine-matched conditions.

CHAPTER 9. CONCLUSIONS

The present doctoral research aimed to reveal the additional potential within the further modification and optimization of the turbine blade tip shape as a means to control the tip leakage flow aerodynamics and manage the heat load distribution. This work focused on the analysis of three main design strategies for unshrouded turbine blades: tight running clearances, fully contoured tip shapes and squealer-like profiles. Additionally, the use of unsteady upstream shroud coolant injection has been studied and optimized, in an attempt to enhance the overtip flow characteristics in an indirect way. Eventually, the rotating turbine facility at the von Karman Institute has been redesigned to allow simultaneous testing of multiple distinct blade profiles for advanced tip flow research.

The investigation of a turbine rotor operating in the as-yet uninvestigated **tight running clearance** regime down to 0.1% of the blade span demonstrated:

- At tight clearances, the overtip streamlines feature a reversed flow topology where the low-momentum and -energy fluid from the upstream boundary layer is ingested through the gap suction side towards the pressure side. This reversed flow regime was related to the momentum thickness of the incoming boundary layer and the local tangential fluid velocity through comparison with the tip gap size and blade tip peripheral speed respectively.

- An optimal clearance size was identified for the suction side heat load as a trade off between the dominant effect of the tip leakage vortex at high clearances and the scraping of the boundary layer at low gap sizes. Peak levels in the heat transfer onto the tip and shroud are mainly located near the entrance regions of the overtip flow.

The **potential of blade tip contouring** was assessed through a combined simplified quasi-3D strategy and full 3D verification:

- A new optimization strategy was developed, assuming a quasi-3D flow across consecutive 2D planes along streamlines in the overtip region. A multi-objective optimization is performed for five relevant tip flow regimes, targeting the simultaneous reduction of the losses and heat load.

- Tip shapes which perform better at low velocities are not beneficial in a high speed environment. Loss production in the subsonic regime is mainly driven by the gap mass flow while for supersonic channel flows, the specific entropy generation shows a larger impact on the overall gap losses.

- Up to 40% heat load reduction could be achieved through tip-shaping, enhancing a smooth flow acceleration and a proper boundary layer control. Loss reductions were only observed for thin regions of the rotor blade through the creation of a strongly diverging passage.

- A 3D verification of the tip carving strategy confirmed the applicability of the quasi-3D approach for slight alterations of the blade top shape while remaining inherently limited to account for complex 3D tip flows. Significant reductions in heat transfer of 18% up to 36% could be achieved compared to conventional designs.

The **full 3D optimization** of carved and industrial rub-safe profiles has demonstrated the existence of unexplored geometries with aerothermal performances beyond the conventionally employed strategies:

- Two novel optimization methodologies have been developed and implemented. A first strategy creates fully three-dimensional contoured blade designs through a mapping based on a general Bezier surface. The second methodology uses an approach similar to a topology optimization strategy where the tip area was

divided in about 200 distinct blocks, allowing to generate almost every possible rim-cavity layout. In total, over 1500 distinct profiles were simulated during 4 consecutive multi-objective optimizations, targeting the simultaneous increase of the aerodynamic efficiency and the reduction of the overtip heat load.

- In the family of the contoured blade tip geometries, the flat tip continues to represent the prime design choice in terms of efficiency. However, an immediate heat transfer reduction of 5% can be achieved through the creation of a diverging passage in the aft part of the blade. Further heat transfer reduction is accessible through additional carving in the front region. Interestingly, the tighter the clearance, the more aggressive contouring is demanded to achieve the same heat transfer improvements.

- The squealer-like tip optimization showed further aerodynamic improvements and a Pareto front two times less sensitive compared to the carved tip design strategy. Slight variabilities in the turbine operating point were observed and two distinct zones of high aerodynamic performance were identified corresponding to blades with a closed and fully opened aft-section.

- The altered tip designs account for variations in heat transfer up to 50% on the near-tip suction side. The analysis of the RMS value demonstrates that, while the heat flux in the case of the rim-type designs tends to be generally lower due to the larger wetted area, the occurrence of hot spots is considerably increased.

The characterization of the **performance robustness** of the widely adopted squealer-like profile under operational variability and manufacturing tolerances revealed:

- Global performance indicators confirm that corner radius variations induce the smallest effect ($\sim$2% in heat transfer and 0.15% in efficiency). The aerodynamic losses are primarily dominated by changes of tip clearance (i.e. 2% efficiency

change for 1% gap height) and distinct optima for the cavity depth are found whether one would target a reduction in tip, shroud or suction side heat transfer.

- A detailed characterization of the flow topology revealed the generation of a large recirculation zone of low heat transfer in the front part of the blade. Along the suction side, three distinct regions were identified: a first zone acts as an inlet, whereas the two downstream zones allow the flow to leave the gap region. This creates a clear heat transfer signature, separated by the initiation point of the tip leakage vortex and a 'switching point' near the trailing edge.

- The tip heat transfer distribution experiences changes of $\pm 25\%$, mainly caused by tip clearance variations. The shroud thermal load revealed unexpected variations in the aft 30% of the rotor blade, due to the emerging of two parallel stripes of large heat transfer aligned with the SS edge.

The exploration of an indirect control of the rotor aerothermal flow field through the **optimization of shroud purge cooling** resulted in:

- A modern high-pressure turbine stage was successfully scaled from a lab environment towards real engine cruising conditions of a business jet, through a combination of 1D meanline approximations and full 3D CFD simulations.

- A 2-stage multi-objective optimization was performed, simulating over 240 different individuals, parametrizing the purge flow characteristics using 9 design variables.

- Negligible aerodynamic improvements are observed compared with the no-purge case and the additional introduction of a tangential distribution of the purge flow did not reveal significant opportunities. However, the Pareto front reveals heat transfer reductions of 80% with a limited penalty in aerodynamic efficiency. 1% of purge flow reduces the efficiency with 0.07% while sub-optimal purge configurations demonstrate variations as high as 0.4%.

- An increase of 1% in purge flow results in an average reduction of ±30% in tip heat load and ±23% on the shroud and upper quarter of the suction side.

A **high-speed, rotating turbine facility** has been redesigned, paving the way for a future experimental campaign:

- The short-duration rotating turbine facility at the von Karman Institute has been refurbished using a Rainbow Rotor approach, allowing simultaneous testing of multiple distinct blade (tip) profiles mounted in separate sectors around the rotor annulus. A fast numerical strategy was developed to identify the optimal positioning of the heterogeneous blades in the sector constrained rotor row which minimizes the residual unbalance. Eventually, the turbine assembly was balanced in situ using the four-run method, achieving the required quality grade of G2.5.

- The manufactured blade geometries were constructed using an inverse methodology to counterbalance the radial deformation caused by the centrifugal loads. The hot-to-cold transformation procedure allowed to reach the gap target within a few micrometers and compensates for nonuniform tip deformation fields as high as 0.36mm. The eventual static and rotating clearances were verified using a combination of dial gauges, wear gauges and high-frequency capacitance sensors embedded in the rotor casing ring.

- RANS simulations of all installed rotor tip profiles were adopted to estimate and mitigate the errors induced by the finite spatial sampling and conventional uniform probe placement. A novel iterative procedure has been developed which optimizes the sensor positioning to either reduce the expected errors on a single measured quantity or on the loss variable, as the result of combined measurements of multiple aerodynamic quantities.

- Based on low-pass filtered traces extracted from the CFD at the envisioned measurement locations, the loss of information has been quantified due to the

finite nature of the frequency response of the sensors. The results indicate a bandwidth of the casing sensors of 75 kHz is required to capture 90% of the unsteady fluctuations across the majority of the blade chord. Downstream the stage, a proper resolving of the mixing vortex structures can be obtained already with 3 to 4 times the blade passing frequency.

This doctoral research covered the entire span from the initial conception of multiple tip design strategies, through simplified simulation methodologies and more computationally expensive fully three-dimensional multi-objective optimizations, all the way up to the redesign of a high-speed rotating wind tunnel for the validation of the discovered technologies at engine-matched conditions.

Throughout this project, the maximum potential to simultaneously increase the aerodynamic efficiency while reducing the thermal loads was quantified using high-fidelity CFD. New insights into the overtip flow topology and aerothermal characteristics were revealed and analyzed. The complexity and interaction of the overtip structures illustrated the importance and the multi-faceted nature of the tip design problem, not only affecting the local aerodynamic and heat transfer characteristics, but determining the overall performance and durability of the entire machine. Design guidelines for future generation turbines were identified and new unshrouded tip designs were discovered offering increased aerothermal performances beyond the current state-of-the-art, currently implemented in modern gas turbine engines.

LIST OF REFERENCES

LIST OF REFERENCES

[1] C. De Maesschalck, S. Lavagnoli, G. Paniagua, and N. Vinha. Aerothermodynamics of tight rotor tip clearance flows in high-speed unshrouded turbines. *Applied Thermal Engineering*, 65(12):343 – 351, 2014.

[2] C. De Maesschalck, S. Lavagnoli, and G. Paniagua. Blade tip shape optimization for enhanced turbine aerothermal performance. *Journal of Turbomachinery*, 136(4):041016, October 2013.

[3] C. De Maesschalck, S. Lavagnoli, and G. Paniagua. Blade tip carving effects on the aero-thermal performance of a transonic turbine. *Journal of Turbomachinery*, 137(2):021005, September 2014.

[4] C. De Maesschalck, S. Lavagnoli, G. Paniagua, T. Verstraete, R. Olive, and P. Picot. Heterogeneous optimization strategies for carved and squealer-like turbine blade tips. *Journal of Turbomachinery*, 138(12):121011, July 2016.

[5] C. De Maesschalck, C. Lacor, G. Paniagua, L. Lavagnoli, A. Remiot, and Bricteux L. Performance robustness of turbine squealer tip designs due to manufacturing and engine operation. *AIAA Journal of Propulsion and Power*, 2016.

[6] Lecture Series. *Secondary and Tip-Clearance Flows in Axial Turbines*. von Karman Institute for Fluid Dynamics, Rhode-St-Genese, Belgium, 1997.

[7] Lecture Series. *Turbine blade tip design and tip clearance treatment*. von Karman Institute for Fluid Dynamics, Rhode-St-Genese, Belgium, 2004.

[8] A. Ameri. Computational prediction for blade tips. In *ASME Turbine Blade Tip Symposium & Course Week*, 2013.

[9] R. Bunker. Axial turbine blade tips: Function, design, and durability. *Journal of Propulsion and Power*, 22(2):271–285, March 2006.

[10] R. Bunker. Blade tip cooling requirements and design. In *ASME Turbine Blade Tip Symposium and Course Week*, 2013.

[11] J. Denton. The 1993 igti scholar lecture: Loss mechanisms in turbomachines. *Journal of Turbomachinery*, 115(4):621–656, October 1993.

[12] N. Harvey. *Aerothermal Implications of Shroudless and Shrouded Blades*. von Karman Institute for Fluid Dynamics, Rhode-St-Genese, Belgium., 2004.

[13] J. Coull. High pressure turbine blade tip aerodynamics. In *ASME Turbine Blade Tip Symposium and Course Week*, 2013.

[14] S. Yoon, E. Curtis, J. Denton, and J. Longley. The effect of clearance on shrouded and unshrouded turbines at two levels of reaction. *Journal of Turbomachinery*, 136(2):021013, September 2013.

[15] J. Moore and J. Tilton. Tip leakage flow in a linear turbine cascade. *Journal of Turbomachinery*, 110(1):18–26, January 1988.

[16] F. Heyes, H. Hodson, and G. Dailey. The effect of blade tip geometry on the tip leakage flow in axial turbine cascades. *Journal of Turbomachinery*, 114(3):643–651, July 1992.

[17] P. Newton, G. Lock, S. Krishnababu, H. Hodson, W. Dawes, J. Hannis, and C. Whitney. Heat transfer and aerodynamics of turbine blade tips in a linear cascade. *Journal of Turbomachinery*, 128(2):300–309, March 2006.

[18] R. Bunker. A review of turbine blade tip heat transfer. *Annals of the New York Academy of Sciences*, 934(1):64–79, 2001.

[19] J. Bolger. Blade tip and casing surface treatments. In *ASME Turbine Blade Tip Symposium and Course Week*, 2013.

[20] B. Glezer. Engine tip clearance design issues and possible solutions. In *ASME Turbine Blade Tip Symposium and Course Week*, 2013.

[21] S. Lattime and B. Steinetz. High-pressure-turbine clearance control systems: Current practices and future directions. *Journal of Propulsion and Power*, 20(2):302–311, March 2004.

[22] B. Mischo, T. Behr, and R. Abhari. Flow physics and profiling of recessed blade tips: Impact on performance and heat load. *Journal of Turbomachinery*, 130(2):021008, February 2008.

[23] A. Ameri, E. Steinthorsson, and D. Rigby. Effect of squealer tip on rotor heat transfer and efficiency. *Journal of Turbomachinery*, 120(4):753–759, October 1998.

[24] C. Camci, D. Dey, and L. Kavurmacioglu. Aerodynamics of tip leakage flows near partial squealer rims in an axial flow turbine stage. *Journal of Turbomachinery*, 127(1):14–24, February 2005.

[25] H. Nasir, S. Ekkad, D. Kontrovitz, R. Bunker, and C. Prakash. Effect of tip gap and squealer geometry on detailed heat transfer measurements over a high pressure turbine rotor blade tip. *Journal of Turbomachinery*, 126(2):221–228, June 2004.

[26] V. Saxena, H. Nasir, and S. Ekkad. Effect of blade tip geometry on tip flow and heat transfer for a blade in a low-speed cascade. *Journal of Turbomachinery*, 126(1):130–138, March 2004.

[27] N. Key and T. Arts. Comparison of turbine tip leakage flow for flat tip and squealer tip geometries at high-speed conditions. *Journal of Turbomachinery*, 128(2):213–220, March 2006.

[28] J. Kwak, J. Ahn, J. Han, C. Lee, R. Bunker, R. Boyle, and R. Gaugler. Heat transfer coefficients on the squealer tip and near-tip regions of a gas turbine blade with single or double squealer. *Journal of Turbomachinery*, 125(4):778–787, December 2003.

[29] S. Krishnababu, P. Newton, W. Dawes, G. Lock, H. Hodson, J. Hannis, and C. Whitney. Aerothermal investigations of tip leakage flow in axial flow turbines–part i: Effect of tip geometry and tip clearance gap. *Journal of Turbomachinery*, 131(1):011006, October 2008.

[30] D. Dey and C. Camci. Aerodynamic tip desensitization of an axial turbine rotor using tip platform extensions. In *ASME Turbo Expo 2001 Proceedings*, number GT2001-0484, 2001.

[31] A. Saha, S. Acharya, C. Prakash, and R. Bunker. Blade tip leakage flow and heat transfer with pressure side winglet. In *ASME Turbo Expo 2003 Proceedings*, number GT2003-38620, 2003.

[32] Z. Schabowski and H. Hodson. The reduction of over tip leakage loss in unshrouded axial turbines using winglets and squealers. *Journal of Turbomachinery*, 136(4):041001, September 2013.

[33] J. Coull, N. Atkins, and H. Hodson. Winglets for improved aerothermal performance of high pressure turbines. *Journal of Turbomachinery*, 136(9):091007, May 2014.

[34] J. Coull, N. Atkins, and H. Hodson. High efficiency cavity winglets for high pressure turbines. In *ASME Turbo Expo 2014 Proceedings*, 2014.

[35] N. Harvey and K. Ramsden. A computational study of a novel turbine rotor partial shroud. *Journal of Turbomachinery*, 123(3):534–543, February 2000.

[36] N. Harvey, D. Newman, F. Haselbach, and L. Willer. An investigation into a novel turbine rotor winglet: Part idesign and model rig test result. In *ASME Turbo Expo 2006 Proceedings*, number GT2006-585, 2006.

[37] D. ODowd, Q. Zhang, L. He, M. Oldfield, P. Ligrani, B. Cheong, and I. Tibbott. Aerothermal performance of a winglet at engine representative mach and reynolds numbers. *Journal of Turbomachinery*, 133(4):041026, April 2011.

[38] J. Moore, J. Moore, G. Henry, and U. Chaudhry. Flow and heat transfer in turbine tip gaps. *Journal of Turbomachinery*, 111(3):301–309, July 1989.

[39] J. Moore and K. Elward. Shock formation in overexpanded tip leakage flow. *Journal of Turbomachinery*, 115(3):392–399, July 1993.

[40] Q. Zhang, D. ODowd, L. He, A. Wheeler, P. Ligrani, and B. Cheong. Overtip shock wave structure and its impact on turbine blade tip heat transfer. *Journal of Turbomachinery*, 133(4):041001, April 2011.

[41] Q. Zhang, D. ODowd, L. He, M. Oldfield, and P. Ligrani. Transonic turbine blade tip aerothermal performance with different tip gaps–part i: Tip heat transfer. *Journal of Turbomachinery*, 133(4):041027, April 2011.

[42] V. Shyam, A. Ameri, and J. Chen. Analysis of unsteady tip and endwall heat transfer in a highly loaded transonic turbine stage. *Journal of Turbomachinery*, 134(4):041022, July 2011.

[43] A. Wheeler and R. Sandberg. Numerical investigation of the flow over a model transonic turbine blade tip. *Journal of Fluid Mechanics*, 803:119–143, 009 2016.

[44] A. Wheeler and D. Sandberg. Direct numerical simulations of a transonic turbine tip flow. In *13th International Symposium on Unsteady Aerodynamics, Aeroacoustics and Aeroelasticity of Turbomachines, Tokyo, Sept. 1114*, number ISUAAAT13-S9-3, 2012.

[45] A. Wheeler and R. Sandberg. Direct numerical simulations of a transonic tip flow with free-stream disturbances. In *ASME 2013 Turbine Blade Tip Symposium*, number TBTS2013-2037, 2013.

[46] A. Wheeler, N. Atkins, and L. He. Turbine blade tip heat transfer in low speed and high speed flows. *Journal of Turbomachinery*, 133(4):041025, April 2011.

[47] Q. Zhang and L. He. Overtip choking and its implications on turbine blade-tip aerodynamic performance. *Journal of Propulsion and Power*, 27(5):1008–1014, September 2011.

[48] A. Wheeler, T. Korakianitis, and S. Banneheke. Tip-leakage losses in subsonic and transonic blade rows. *Journal of Turbomachinery*, 135(1):011029, October 2012.

[49] L. He, Q. Zhang, and A. Wheeler. Blade tip heat transfer and aero-loss in transonic flow. In *ASME Turbine Blade Tip Symposium and Course Week*, 2013.

[50] V. Shyam and A. Ameri. Comparison of various supersonic turbine tip designs to minimize aerodynamic loss and tip heating. In *ASME 2011 Turbo Expo Conference Proceedings*, number GT2011-46390, 2011.

[51] Q. Zhang and L. He. Tip-shaping for hp turbine blade aerothermal performance management. *Journal of Turbomachinery*, 135(5):051025, June 2013.

[52] *He, L., Zhang, Q., Wheeler, A., and Atkins, N., 2010, Over-Tip-Shaping for Heat Load Reduction, UK Patent No. GB 1017797.0, UKIPO.*

[53] A. Jackson, A. Wheeler, and R. Ainsworth. An experimental and computational study of tip clearance effects on a transonic turbine stage. *International Journal of Heat and Fluid Flow*, 56:335–343, December 2015.

[54] J. Coull and N. Atkins. The influence of boundary conditions on tip leakage flow. *Journal of Turbomachinery*, 137(6):061005, June 2015.

[55] F. Montomoli, M. Massini, and S. Salvadori. Geometrical uncertainty in turbomachinery: Tip gap and fillet radius. *Computers & Fluids*, 46(1):362–368, July 2011.

[56] G. Laskowski, J. Kopriva, V. Michelassi, S. Shankaran, U. Paliath, R. Bhaskaran, Q. Wang, C. Talnikar, Z. Wang, and F. Jia. Future directions of high fidelity cfd for aerothermal turbomachinery analysis and design. In *46th AIAA Fluid Dynamics Conference*, AIAA Aviation. American Institute of Aeronautics and Astronautics, June 2016.

[57] P. Moin. Progress and challenges in numerical simulation of multi-physics turbulent flows in aerospace applications. In *Presentation at Royal Academy of Engineering, Spain*, 2014.

[58] B. Green. *Time-Averaged and Time-Accurate Aerodynamic Effects of Rotor Purge Flow for a Modern, Rotating, High-Pressure Turbine Stage and Low-Pressure Turbine Vane*. PhD thesis, The Ohio State University, The Ohio State University, 2011.

[59] E. Crosh, C. Haldeman, M. Dunn, D. Holmes, and B. Mitchell. Investigation of turbine shroud distortions on the aerodynamics of a one and one-half stage high-pressure turbine. *Journal of Turbomachinery*, 133(3):031002, November 2010.

[60] C. Chahine, T. Verstraete, and L. He. Multidisciplinary design optimization of aero-engine fan blades. In *Proceedings of the 11th ASMO UK / ISSMO / NOED2016 Conference on Numerical Optimisation Methods for Engineering Design, July 18-20th 2016, Munich, Germany*, 2016.

[61] L. Mueller, Z. Alsalihi, and T. Verstraete. Multidisciplinary optimization of a turbocharger radial turbine. *Journal of Turbomachinery*, 135(2):021022, November 2012.

[62] A. Grosvenor, G. Rixon, L. Sailer, M. Matheson, D. Gutzwiller, A. Demeulenaere, M. Gontier, and A. Strazisar. High resolution rans nlh study of stage 67 tip injection physics. In *ASME TurboExpo 2014 Conference Proceedings*, number GT2014-27219, 2014.

[63] A. Grosvenor, A. Zheltovodov, M. Matheson, L. Sailer, M. Krzysztopik, and D. Gutzwiller. Numerical analysis of three complex three-dimensional shock wave / turbulent boundary layer interaction flows. *EUCASS Proceedings Series - Advances in AeroSpace Sciences*, 5:247–284, June 2013.

[64] *Theoretical Manual, Numeca FINE/Open v4, January 2015.*

[65] *Theoretical Manual, Numeca FINE/Turbo v9.1, November 2014.*

[66] P. Spalart and S. Allmaras. A one-equation turbulence model for aerodynamic flows. In *30th Aerospace Sciences Meeting and Exhibit*, Aerospace Sciences Meetings. American Institute of Aeronautics and Astronautics, January 1992.

[67] F. Menter. Two-equation eddy-viscosity turbulence models for engineering applications. *AIAA Journal*, 32(8):1598–1605, August 1994.

[68] G. Ashford and K. Powell. An unstructured grid generation and adaptive solution technique for high-reynolds number compressible flow. In *Von Karman Institute Lecture Series 1996-06*, 1996.

[69] P. Spalart and M. Shur. On the sensitisation of turbulence models to rotation and curvature. *Aerospace Science and Technology*, (5:297-302), 1997.

[70] M. Shur, M. Strelets, A. Travin, and P. Spalart. Turbulence modeling in rotating and curved channels: Assessing the spalart-shur correction. *AIAA Journal*, 38(5):784–792, May 2000.

[71] A. Jameson, W. Schmidt, and E. Turkel. Numerical solution of the euler equations by finite volume methods using runge kutta time stepping schemes. In *14th Fluid and Plasma Dynamics Conference*, Fluid Dynamics and Co-located Conferences. American Institute of Aeronautics and Astronautics, June 1981.

[72] R. Kurz. Gas turbine performance. In *Proceedings of the thirty-fourth turbomachinery symposium*, 2005.

[73] S. Na, R. Dennis, C. Alsup, K. Bryden, and T. Shih. Effects of hot-gas composition on temperature distribution in a flat plate cooled by internal and film cooling. In *Proceedings of ASME TurboExpo 2009*, number GT2009-59727, 2009.

[74] T. Hofer, M. Legrand, L. Pons, and T. Arts. Aerodynamic investigation of the leakage flow for a blade with a squealer tip at transonic conditions. In *8th European Turbomachinery Conference, Graz, Austria, March 2327*, page 14831494, 2009.

[75] T. Hofer and T. Arts. Aerodynamic investigation of the tip leakage flow for blades with different tip squealer geometries at transonic conditions. In *ASME Turbo Expo 2009 Proceedings*, number GT2009-59909, 2009.

[76] S. Naik, C. Georgakis, T. Hofer, and D. Lengani. Heat transfer and film cooling of blade tips and endwalls. *Journal of Turbomachinery*, 134(4):041004, July 2011.

[77] P. Vass and T. Arts. Numerical investigation of high-pressure turbine blade tip flows: analysis of aerodynamics. *Proceedings of the Institution of Mechanical Engineers, Part A: Journal of Power and Energy*, 225(7):940–953, 2011.

[78] P. Vass. *Numerical Investigation of the Tip Leakage Flow in Different High Pressure Turbine Blade Configurations*. PhD thesis, von Karman Institute for Fluid Dynamics, 2012.

[79] G. Paniagua, C. Sieverding, and T. Arts. Review of the von karman institute compression tube facility for turbine research. In *ASME TurboExpo 2013 Conference Proceedings, Paper No. GT2013-95984*.

[80] R. Denos, T. Arts, G. Paniagua, V. Michelassi, and F. Martelli. Investigation of the unsteady rotor aerodynamics in a transonic turbine stage. *Journal of Turbomachinery*, 123(1):81–89, February 2000.

[81] C. Sieverding, T. Arts, R. Denos, and F. Martelli. Investigation of the flow field downstream of a turbine trailing edge cooled nozzle guide vane. *Journal of Turbomachinery*, 118(2):291–300, April 1996.

[82] G. Paniagua, T. Yasa, A. De La Loma, L. Castillon, and T. Coton. Unsteady strong shock interactions in a transonic turbine: Experimental and numerical analysis. *Journal of Propulsion and Power*, 24(4):722–731, July 2008.

[83] F. Didier, R. Denos, and T. Arts. Unsteady rotor heat transfer in a transonic turbine stage. *Journal of Turbomachinery*, 124(4):614–622, November 2002.

[84] T. Verstraete. *Multidisciplinary Turbomachinery Component Optimization Considering Performance, Stress, and Internal Heat Transfer*. PhD thesis, von Karman Institute for Fluid Dynamics, 2008.

[85] T. Verstraete. Cado: a computer aided design and optimization tool for turbomachinery applications. In *Proceedings of the 2nd International Conference on Engineering Optimization, September 6-9, 2010, Lisbon, Portugal*.

[86] T. Verstraete, Z. Alsalihi, and R. Van den Braembussche. Multidisciplinary optimization of a radial compressor for microgas turbine applications. *Journal of Turbomachinery*, 132(3):031004, March 2010.

[87] C. Chahine, J. Seume, and T. Verstraete. The influence of metamodeling techniques on the multidisciplinary design optimization of a radial compressor impeller. In *ASME Turbo Expo 2012 Proceedings*, number GT2012-68358, 2012.

[88] T. Verstraete, S. Amaral, R. Van den Braembussche, and T. Arts. Design and optimization of the internal cooling channels of a high pressure turbine blade–part ii: Optimization. *Journal of Turbomachinery*, 132(2):021014, January 2010.

[89] L. Mueller, T. Verstraete, and T. Arts. Design of the primary liquid-metal pump of the myrrha research reactor. In *Proceedings of the 10th European Conference on Turbomachinery Fluid dynamics & Thermodynamics, ETC10, April 15-19, 2013, Lappeenranta, Finland*, 2013.

[90] J. Holland. *Adaption in Natural and Arti cial Systems.* University of Michigan Press, 1975.

[91] I. Rechenberg. *Evolutionsstrategie - Optimierung technischer Systeme nach Prinzipien der biologischen Evolution.* Fommann-Holzboog, Stuttgart, 1973.

[92] J. Kennedy and R. Eberhart. Particle swarm optimization. In *Proceedings of the IEEE International Conference on Neural Networks*, volume 4, pages 1942–1948 vol.4, Nov 1995.

[93] M. Dorigo, V. Maniezzo, and A. Colorni. Ant system: optimization by a colony of cooperating agents. *IEEE Transactions on Systems, Man, and Cybernetics, Part B (Cybernetics)*, 26(1):29–41, Feb 1996.

[94] K. Price and N. Storn. Differential evolution. *Dr. Dobb's Journal*, pages 18–24, April 1997.

[95] R. Storn and K. Price. Differential evolution - a simple and efficient heuristic for global optimization over continuous spaces. *Journal of Global Optimization*, 11(4):341–359, 1997.

[96] H. Abbass, R. Sarker, and C. Newton. Pde: a pareto-frontier differential evolution approach for multi-objective optimization problems. In *Proceedings of the 2001 Congress on Evolutionary Computation*, volume 2, pages 971–978 vol. 2, 2001.

[97] N. Madavan. Multiobjective optimization using a pareto differential evolution approach. In *CEC '02. Proceedings of the 2002 Congress on Evolutionary Computation*, volume 2, pages 1145–1150, 2002.

[98] M. Rai. *VKI Lecture Series on Introduction to Optimization and Multidisciplinary Design in Aeronautics and Turbomachinery, Brussels, June 2008.*, chapter Single and multiple objective optimization with differential evolution and neural networks.

[99] K. Deb, A. Pratap, S. Agarwal, and T. Meyarivan. A fast and elitist multiobjective genetic algorithm: Nsga-ii. *IEEE Transactions on Evolutionary Computation*, 6(2):182–197, Apr 2002.

[100] Y. Jin. A comprehensive survey of fitness approximation in evolutionary computation. *Soft Computing*, 9(1):3–12, 2005.

[101] T. Simpson, J. Poplinski, P. Koch, and J. Allen. Metamodels for computer-based engineering design: Survey and recommendations. *Engineering with Computers*, 17(2):129–150, 2001.

[102] M. Emmerich, A. Giotis, M. Özdemir, T. Bäck, and K. Giannakoglou. Metamodel-assisted evolution strategies. In *Proceedings of the 7th International Conference on Parallel Problem Solving from Nature*, PPSN VII, pages 361–370, London, UK, UK, 2002. Springer-Verlag.

[103] Y. Ong, P. Nair, and A. Keane. Evolutionary optimization of computationally expensive problems via surrogate modeling. *AIAA Journal*, 41(4):687–696, April 2003.

[104] A. Cochocki and R. Unbehauen. *Neural Networks for Optimization and Signal Processing*. John Wiley & Sons, Inc., New York, NY, USA, 1st edition, 1993.

[105] S. Pierret and R. Van den Braembussche. Turbomachinery blade design using a navier-stokes solver and artificial neural network. *Journal of Turbomachinery*, 121(2):326–332, April 1999.

[106] T. Verstraete and J. Li. Multi-objective optimization of a u-bend for minimal pressure loss and maximal heat transfer performance in internal cooling channels. In s, editor, *ASME 2013 Turbo Expo Conference Proceedings*, number GT2013-95423, 2013.

[107] S. Jeong, M. Murayama, and K. Yamamoto. Efficient optimization design method using kriging model. *Journal of Aircraft*, 42(2):413–420, March 2005.

[108] S. Lavagnoli, G. Paniagua, C. De Maesschalck, and T. Yasa. Analysis of the unsteady overtip casing heat transfer in a high speed turbine. *Journal of Turbomachinery*, 135(3):031027, March 2013.

[109] T. Yasa, G. Paniagua, and R. Denos. Application of hot-wire anemometry in a blow-down turbine facility. *Journal of Engineering for Gas Turbines and Power*, 129(2):420–427, February 2006.

[110] Rolls-Royce plc. *The Jet Engine, 5th Edition*. Wiley, 2015.

[111] R. Bunker. Gas turbine cooling: Moving from macro to micro cooling. In *ASME Turbo Expo 2013 Proceedings*, number GT2013-94277.

[112] F. Heyes and H. Hodson. Measurement and prediction of tip clearance flow in linear turbine cascades. *Journal of Turbomachinery*, 115(3):376–382, July 1993.

[113] T. Yasa. *Efficiency of a HP Turbine Tested in a Compression Tube Facility*. PhD thesis, von Karman Institute for Fluid Dynamics, 2008.

[114] T. Yasa, G. Paniagua, and A. Bussolin. Performance analysis of a transonic high-pressure turbine. *Proceedings of the Institution of Mechanical Engineers, Part A: Journal of Power and Energy*, 221(6):769–778, 2007.

[115] G. Guenette, A. Epstein, and E. Ito. Turbine aerodynamic performance measurements in short duration facilities. In *25th Joint Propulsion Conference*, Joint Propulsion Conferences. American Institute of Aeronautics and Astronautics, July 1989.

[116] R. Keogh, G. Guenette, and T. Sommer. Aerodynamic performance measurements of a fully scaled turbine in a short duration facility. In *ASME TurboExpo 2000 Conference Proceedings*, number GT-486, 2000.

[117] N. Atkins and R. Ainsworth. Turbine aerodynamic performance measurement under nonadiabatic conditions. *Journal of Turbomachinery*, 134(6):061001, August 2012.

[118] C. De Maesschalck, S. Lavagnoli, and G. Paniagua. Blade tip shape optimization for enhanced turbine aerothermal performance. In *ASME Turbo Expo 2013 Proceedings, GT2013-94754*.

[119] C. De Maesschalck, S. Lavagnoli, and G. Paniagua. Blade tip carving effects on the aero-thermal performance of a transonic turbine. In *ASME 2013 Turbine Blade Tip Symposium Proceedings, TBTS2013-2028*.

[120] T. Verstraete. *Introduction to Optimization and Multidisciplinary Design*. von Karman Institute for Fluid Dynamics, Rhode-St-Genese, Belgium, 2010.

[121] T. Booth, P. Dodge, and H. Hepworth. Rotor-tip leakage: Part i–basic methodology. *Journal of Engineering for Power*, 104(1):154–161, January 1982.

[122] C. De Maesschalck. Numerical and exprtimental investigation of turbine overtip flow, research master project report. Technical report, von Karman Institute for Fluid Dynamics, 2012.

[123] G. Farin. *Curves and Surfaces for Computer Aided Geometric Design*. Academic Press, Inc., San Diego, 1993.

[124] D. Montgomery. *Design and Analysis of Experiments*. Wiley, New York, 1997.

[125] A. Shapiro. *The Dynamics and Thermodynamics of Compressible Fluid Flow*. John Wiley and Sons Inc., New York, 1953.

[126] J. Bindon. The measurement and formation of tip clearance loss. *Journal of Turbomachinery*, 111(3):257–263, July 1989.

[127] T. Booth. Importance of tip clearance flows in turbine design. In *Tip clearance effects in axial turbomachines Lecture Series, ed., von Karman Institute for Fluid Dynamics, Brussels*, 1985.

[128] H. Zimmerman and K. Wolff. Air systems correlations part 1: Labyrinth seals. In *ASME paper No. 98-GT-206*, 1998.

[129] I. Celik, U. Ghia, P. Roache, C. Freitas, H. Coleman, and P. Raad. Procedure for estimation and reporting of uncertainty due to discretization in cfd applications. *Journal of Fluids Engineering*, 130(7):078001, July 2008.

[130] S. Salvadori, F. Montomoli, F. Martelli, P. Adami, K. Chana, and L. Castillon. Aerothermal study of the unsteady flow field in a transonic gas turbine with inlet temperature distortions. *Journal of Turbomachinery*, 133(3):031030, February 2011.

[131] C. De Maesschalck, S. Lavagnoli, G. Paniagua, T. Verstraete, R. Olive, and P. Picot. Heterogeneous optimization strategies for carved and squealer-like turbine blade tips. In *ASME Turbo Expo 2015 Proceedings*, number GT2015-42983.

[132] G. Rozvany. A critical review of established methods of structural topology optimization. *Structural and Multidisciplinary Optimization*, 37(3):217–237, 2009.

[133] E. Crosh. *Olive, R., Lavagnoli, S., De Maesschalck, C., and Paniagua, G., 2014, Procede de modelisation dune baignoire dune aube, FR Brevet dInvention, Paper No. FR1456680.*

[134] *Othmer, C., 2006, CFD Topology and Shape Optimization With Adjoint Methods, VDI Fahrzeug- und Verkehrstechnik, 13 Internationaler Kongress Berechnung und Simulation im Fahrzeugbau (Wurzburg), Vol. 1967, p. 61.*

[135] C. Andreasen, A. Gersborg, and O. Sigmund. Topology optimization of microfluidic mixers. *International Journal for Numerical Methods in Fluids*, 61(5):498–513, 2009.

[136] E. Kontoleontos, E. Papoutsis-Kiachagias, A. Zymaris, D. Papadimitriou, and K. Giannakoglou. Adjoint-based constrained topology optimization for viscous flows, including heat transfer. *Engineering Optimization*, 45(8):941–961, 2013.

[137] N. van Dijk, K. Maute, M. Langelaar, and F. van Keulen. Level-set methods for structural topology optimization: a review. *Structural and Multidisciplinary Optimization*, 48(3):437–472, 2013.

[138] C. De Maesschalck, C. Lacor, G. Paniagua, L. Lavagnoli, A. Remiot, and Bricteux L. Performance robustness of turbine squealer tip designs due to manufacturing and engine operation. In *ISABE 2015 Conference Proceedings*, number ISABE2015-20205.

[139] R. Bunker and J. Bailey. Effect of squealer cavity depth and oxidation on turbine blade tip heat transfer. In *Conference Proceedings of the ASME TurboExpo 2001*, number GT2001-0155, 2001.

[140] B. Glezer. Turbine blade tip clearance improvement. In *Proceedings of the International Gas Turbine and Aeroengine Congress and Exposition*, number 91-GT-164, 1991.

[141] N. Atkins. *Hershey, J., Osborn, B., Gardner, D., Ruiz, R. and Herron, W., Aircraft gas turbine engine blade tip clearance control, US Patent 8126628.*

[142] R. Bunker. The effects of manufacturing tolerances on gas turbine cooling. *Journal of Turbomachinery*, 131(4):041018, July 2009.

[143] M. Eldred. Recent advances in non-intrusive polynomial chaos and stochastic collocation methods for uncertainty analysis and design. In *50th AIAA/ASME/ASCE/AHS/ASC Structures, Structural Dynamics, and Materials Conference*, Structures, Structural Dynamics, and Materials and Co-located Conferences. American Institute of Aeronautics and Astronautics, May 2009.

[144] H. Najm. Uncertainty quantification and polynomial chaos techniques in computational fluid dynamics. *Annual Review of Fluid Mechanics*, 41:35–52, 2009.

[145] A. Lange, M. Voigt, K. Vogeler, H. Schrapp, E. Johann, and V. Gummer. Impact of manufacturing variability on multistage high-pressure compressor performance. *Journal of Engineering for Gas Turbines and Power*, 134(11):112601, September 2012.

[146] E. Fadlun, I. Michelizzi, and M. De Iaco. Measurement error influence on gas turbine operability for condition-based maintenance and reliability/availability improvement. In *Conference Proceedings of the ASME TurboExpo 2008*, number GT2008-50749, 2008.

[147] S. Spieler, S. Staudacher, R. Fiola, P. Sahm, and M. Weisschuh. Probabilistic engine performance scatter and deterioration modeling. *Journal of Engineering for Gas Turbines and Power*, 130(4):042507, April 2008.

[148] P. Seshadri, G. Parks, and S. Shahpar. Leakage uncertainties in compressors: The case of rotor 37. *Journal of Propulsion and Power*, 31(1):456–466, September 2014.

[149] F. Montomoli, M. Carnevale, A. D'Ammaro, M. Massini, and S. Salvadori. *Uncertainty Quantification in Computational Fluid Dynamics and Aircraft Engines.* Number ISBN: 978-3-319-14680-5. SpringerBriefs in Applied Sciences and Technology, 2015.

[150] F. Montomoli, A. DAmmaro, and S. Uchida. Uncertainty quantification and conjugate heat transfer: A stochastic analysis. *Journal of Turbomachinery*, 135(3):031014, March 2013.

[151] F. White. *Fluid Mechanics, 4th Edition.* McGraw-Hill Higher Education, New York, 1998.

[152] A. Ameri and R. Bunker. Heat transfer and flow on the first-stage blade tip of a power generation gas turbine: Part 2–simulation results. *Journal of Turbomachinery*, 122(2):272–277, February 1999.

[153] D. Xiu. *Numerical Methods for Stochastic Computations: A Spectral Method Approach.* Princeton University Press, 2010.

[154] B. Adams, M. Ebeida, M. Eldred, J. , Jakeman, L. Swiler, J. Stephens, D. Vigil, T. Wildey, W. Bohnhoff, K. Dalbey, J. Eddy, K. Hu, L. Bauman, and P. Hough. Dakota, a multilevel parallel object-oriented framework for design optimization, parameter estimation, uncertainty quantification, and sensitivity analysis: Version 6.2 user's manual. Technical report, Sandia Technical Report SAND2014-4633, July 2014, Updated May 8, 2015.

[155] M. Zlatinov, C. Sooi Tan, M. Montgomery, T. Islam, and M. Harris. Turbine hub and shroud sealing flow loss mechanisms. *Journal of Turbomachinery*, 134(6):061027, September 2012.

[156] M. Zlatinov. *Secondary Air Interaction with Main Flow in Axial Turbines*. PhD thesis, Massachusetts Institute of Technology, 2011.

[157] M. Bloxham and J. Bons. A global approach to turbomachinery flow control: Passage vortex control. *Journal of Turbomachinery*, 136(4):041003, September 2013.

[158] M. Collins, K. Chana, and T. Povey. Application of film cooling to an unshrouded hp turbine casing. In *ASME TurboExpo 2016 Proceedings*, number GT2016-57387.

[159] O. Tamunobere and S. Acharya. Turbine blade tip cooling with blade rotation–part ii: Shroud coolant injection. *Journal of Turbomachinery*, 138(9):091003, April 2016.

[160] R. Denos. *Etude Aerodymamice et Thermique de l'ecoulement instationnaire dans un rotor de turbine transsonique*. PhD thesis, IVK-University of Poitiers, 1996.

[161] S. Lavagnoli. *On the Aerothermal Flow Field in a Transonic HP Turbine Stage with a Multi-Profile LP Stator Vane*. PhD thesis, von Karman Institute for Fluid Dynamics, 2012.

[162] G. Paniagua. *Investigation of the Steady and Unsteady Performance of a Transonic HP Turbine*. PhD thesis, Universit Libre de Bruxelles, 2002.

[163] C. Cha, S. Hong, P. Ireland, P. Denman, and V. Savarianandam. Experimental and numerical investigation of combustor-turbine interaction using an isothermal, nonreacting tracer. *Journal of Engineering for Gas Turbines and Power*, 134(8):081501, June 2012.

[164] M. Pau, G. Paniagua, D. Delhaye, A. de la Loma, and P. Ginibre. Aerothermal impact of stator-rim purge flow and rotor-platform film cooling on a transonic turbine stage. *Journal of Turbomachinery*, 132(2):021006, January 2010.

[165] M. Pau. *Film cooling and hub disk leakage flow experiments in a fully rotating transonic turbine stage*. PhD thesis, von Karman Institute for Fluid Dynamics, 2009.

[166] S. Lavagnoli, C. De Maesschalck, and V. Andreoli. Design considerations for tip clearance control and measurement on a turbine rainbow rotor with multiple blade tip geometries. In *ASME TurboExpo 2016 Conference Proceedings, Paper No. GT2016-56544*.

[167] S. Lavagnoli, C. De Maesschalck, and V. Andreoli. Design considerations for tip clearance control and measurement on a turbine rainbow rotor with multiple blade tip geometries. *Journal of Engineering for Gas Turbines and Power*, 139(4):042603–042603, November 2016.

[168] S. Lavagnoli, V. Andreoli, V. Villace, and G. Paniagua. High-fidelity model of transient turbine facility for off-design aerothermal testing. In *52nd Aerospace Sciences Meeting*, AIAA SciTech. American Institute of Aeronautics and Astronautics, January 2014.

[169] W. Zhai and W. Gong. Optimal blade placement for large turbofan balancing. In *Proceedings of the Fourth International Conference on Computer Integrated Manufacturing and Automation Technology*, pages 261–266, Oct 1994.

[170] *International Standard ISO 1940-1:2003: Mechanical vibration – Balance quality requirements for rotors in a constant (rigid) state – Part 1: Specification and verification of balance tolerances.*

[171] J. Vance. *Rotordynamics of turbomachinery.* John Wiley & Sons, 1988.

[172] J. Bolger. Blade tip and casing surface treatments. In *Proceedings of the Turbine Blade Tip Symposium & Course Week, Hamburg, Germany, ASME 2013.*

[173] S. Lavagnoli, G. Paniagua, M. Tulkens, and A. Steiner. High-fidelity rotor gap measurements in a short-duration turbine rig. *Mechanical Systems and Signal Processing*, 27:590–603, February 2012.

[174] C. Sieverding, T. Arts, R. Denos, and J. Brouckaert. Measurement techniques for unsteady flows in turbomachines. *Experiments in Fluids*, 28(4):285–321, 2000.

[175] H. Bruun. Hot-wire anemometry: Principles and signal analysis. *Measurement Science and Technology*, 7(10), 1996.

[176] L. Villafane and G. Paniagua. Aero-thermal analysis of shielded fine wire thermocouple probes. *International Journal of Thermal Sciences*, 65:214–223, March 2013.

[177] D. Schultz and T. Jones. Heat-transfer measurements in short-duration hypersonic facilities. Technical Report AD0758590, AGARDograph rept, 1973.

[178] S. Thorpe, S. Yoshino, and R. Ainsworth. Fabrication and calibration techniques for turbine rotor tip heat transfer gauges. In *Proceedings of the XV Symposium on Measuring Techniques for Transonic and Supersonic ows in Cascades and Turbomachines, Florence, Italy, 2000.*, 2000.

[179] J. Solano and G. Paniagua. Novel two-dimensional transient heat conduction calculation in a cooled rotor: Ventilation preheating–blow-down flux. *Journal of Heat Transfer*, 131(8):081601, June 2009.

[180] F. Fritsch and R. Carlson. Monotone piecewise cubic interpolation. *SIAM Journal on Numerical Analysis*, 17(2):238–246, 1980.

[181] P. Beard, T. Povey, and K. Chana. Turbine efficiency measurement system for the qinetiq turbine test facility. *Journal of Turbomachinery*, 132(1):011002–011002, September 2009.

[182] G. Persico. *Unsteady Aerodynamic Stator-Rotor Interaction in High Pressure Turbines*. PhD thesis, Politecnico di Milano, 2006.

[183] H. Coleman and W. Steele. *Experimentation, Validation, and Uncertainty Analysis for Engineers*. Wiley, third ed. edition, 2009.

[184] G. Bianchi and R. Sorrentino. *Electronic Filter Simulation & Design*. McGraw-Hill Education, January 2007.

[185] P. Pritchard and J. Mitchell. *Fox and McDonald's Introduction to Fluid Mechanics, 9th edition*. Wiley, 2015.

[186] F. White. *Fluid Mechanics, 8th edition*. Mc Graw Hill, 2016.

[187] Y. Cengel and J. Cimbala. *Fluid Mechanics: Fundamentals and Applications, 3rd edition*. Mc Graw Hill, 2014.

[188] M. Zucrow and J. Hoffman. *Gas Dynamics, Vol. I*. Wiley, 1976.

[189] J. Anderson. *Modern Compressible Flow: With Historical Perspective, 3rd edition*. Mc Graw Hill, 2012.

[190] H. Schlichting. *Boundary-Layer Theory*. Springer Science and Business Media, 2003.

[191] T. Bergman, A. Lavine, F. Incropera, and D. DeWitt. *Fundamentals of Heat and Mass Transfer, 7th Edition*. Wiley, 2011.

[192] A. Bejan and A. Kraus. *Heat Transfer Handbook*. Wiley, 2003.

[193] M. Moran, H. Shapiro, D. Boettner, and M. Bailey. *Fundamentals of Engineering Thermodyamics, 8th edition*. Wiley, 2014.

[194] A. Bejan. *Advanced Engineering Thermodynamics, 3rd edition*. Wiley, 2006.

[195] S. Dixon and C. Hall. *Fluid Mechanics and Thermodynamics of Turbomachinery, 7th edition*. Butterworth-Heinemann, 2013.

[196] H. Cohen, G. Rogers, and H. Saravanamuttoo. *Gas Turbine Theory*. Longman, 1996.

[197] B. Lakshminarayana. *Fluid Dynamics and Heat Transfer of Turbomachinery*. Wiley, 1995.

[198] T. Arts and M. Lambert de Rouvroit. Aero-thermal performance of a two-dimensional highly loaded transonic turbine nozzle guide vane: A test case for inviscid and viscous flow computations. *Journal of Turbomachinery*, 114(1):147–154, January 1992.

[199] H. Hura, J. Joseph, and D. Halstead. Reynolds number effects in a low pressure turbine. In *Proceedings of ASME Turbo Expo 2012*, number GT2012-68501, 2012.

[200] A. Anderson and R. Moffat. The adiabatic heat transfer coefficient and the superposition kernel function: Part 2–modeling flatpack data as a function of channel turbulence. *Journal of Electronic Packaging*, 114(1):22–28, March 1992.

[201] S. Lavagnoli, C. De Maesschalck, and G. Paniagua. Uncertainty analysis of adiabatic wall temperature measurements inturbine experiments. *Applied Thermal Engineering*, 82:170–181, May 2015.

[202] S. Lavagnoli, C. De Maesschalck, and G. Paniagua. Analysis of the heat transfer driving parameters in tight rotor blade tip clearances. *Journal of Heat Transfer*, 138(1):011705–011705, August 2015.

APPENDICES

APPENDIX A. PATENT SEARCH

An extensive patent research was performed focusing on the worldwide patent publications of the last 15 years of unshrouded turbine tip designs.

Over 50 relevant patents were quickly found, often simultaneously filed in several countries/regions (e.g. US, EP, CA, JP, etc.). The patents were sorted chronologically (based on the publication date) from 1995 up to 2013 and separated per company. The results can be found in Fig. A.1 and A.2, respectively for General Electric and Rolls Royce together with the patents of the other cited companies.

General Electric

GE1 US8083484 B2, Dec. 27, 2011, Turbine rotor blade tips that discourage cross-flow

GE2 US8425183 B2, Apr. 23, 2013, Triforial tip cavity airfoil

GE3 US8186965 B2, May 29, 2012, Recovery tip turbine blade

GE4 EP1079072 B1, Jan. 20, 2010, Blade tip cooling

GE5 US6086328 A, Jul. 11, 2000, Tapered tip turbine blade

GE6 EP1013878 B1, Dec. 1, 2004, Twin rib turbine blade

GE7 EP0916811 B1, Feb. 9, 2005, Ribbed turbine blade

GE8 US5660523 A, Aug. 26, 1997, Turbine blade squealer tip peripheral end wall with cooling passage arrangement

GE9 EP0718467 B1, Mar. 8, 2000, Cooling of turbine blade tip

GE10 US7607893 B2, Oct. 27, 2009, Counter tip baffle airfoil

GE11 US7290986 B2, Nov. 6, 2007, Turbine airfoil with curved squealer tip

GE12 US7281894 B2, Oct. 16, 2007, Turbine airfoil curved squealer tip with tip shelf

GE13 US6672829 B1, Jan. 6, 2004, Turbine blade having angled squealer tip

GE14 US6554575 B2, Apr. 29, 2003, Ramped tip shelf blade

GE15 US6527514 B2, Mar. 4, 2003, Turbine blade with rub tolerant cooling construction

GE16 US6224336 B1, May 1, 2001, Triple tip-rib airfoil

GE17 US6190129 B1, Feb. 20, 2001, Tapered tip-rib turbine blade

GE18 US20120282108 A1, Nov. 8, 2012, Turbine blade with chamfered squealer tip and convective cooling holes

GE19 US7686578 B2, Mar. 30, 2010, Conformal tip baffle airfoil

GE20 US2008044289 A1, Feb. 21, 2008, Tip ramp turbine blade

GE21 US7287959 B2, Oct. 30, 2007, Blunt tip turbine blade

GE22 US2009324422 A1, Dec. 31, 2009, Cascade tip baffle airfoil

GE23 US20100221122 A1, Sep. 2, 2010, Flared tip turbine blade

GE24 US7922455 B2, Apr. 12, 2011, Steam-cooled gas turbine bucker for reduced tip leakage loss

GE25 WO2011002570 A1, Jan. 6, 2011, Rotor blade and method for reducing tip rub loading

GE26 EP2586984 A2, May 1, 2013, Turbine rotor blade and corresponding turbomachine

GE27 US8414265 B2, Apr. 9, 2013, Turbines and turbine blade winglets

GE28 US8157504 B2, Apr. 17, 2012, Rotor blades for turbine engines

GE29 US6027306 A, Feb. 22, 2000, Turbine blade tip flow discouragers

GE30 US6422821 B1, Jul. 23, 2002, Method and apparatus for reducing turbine blade tip temperatures

Rolls Royce

RR1 EP2444592 B1, May 1, 2013, Rotor assembly and corresponding gas turbine engine

RR2 EP2378075 A1, Oct. 19, 2011, Rotor blade and corresponding gas turbine engine

RR3 EP2378074 A1, Oct. 19, 2011, Rotor blade and corresponding gas turbine engine

RR4 EP2378076 A1, Oct. 19, 2011, Rotor blade and corresponding gas turbine engine

RR5 US8133032 B2, Mar. 13, 2012, Rotor blades

RR6 EP2161412 A2, Mar. 10, 2010, Cooling of a blade tip

RR7 US8246307 B2, Aug. 21, 2012, Blade for a rotor

RR8 US7641446 B2, Jan. 5, 2010, Turbine Blade

RR9 US7632062 B2, Dec. 15, 2009, Turbine rotor blades

RR10 US7118329 B2, Oct. 10, 2006, Tip sealing for a turbine rotor blade

RR11 EP0801209 B1, Jan. 8, 2003, Tip sealing for turbine rotor blade

Siemens

S1 US8313287 B2, Nov. 20, 2012, Turbine blade squealer tip rail with fence members

S2 EP1953344 B1, Apr. 11, 2012, Turbine blade

S3 US7513743 B2, Apr. 7, 2009, Turbine blade with wavy squealer tip rail

Safran Aircraft Engines

SN1 US7927072 B2, Apr. 19, 2011, Hollow rotor blade for the turbine of a gas turbine engine

SN2 US7351035 B2, Apr. 1, 2008, Hollow rotor blade for the turbine of a gas turbine engine, the blade being fitted with a bathtub

Florida Turbine Technologies

FTT1 US7494319 B1, Feb. 24, 2009, Turbine blade tip cooling configuration

FTT2 US8469666 B1, Jun. 25, 2013, Turbine blade tip portion with trenched cooling holes

Mitsubishi

M1 US6039531 A, Mar. 21, 2000, Gas turbine blade

M2 US8414262 B2, Apr. 9, 2013, Turbine blade having squealer

Honeywell

H1 US8206108 B2, Jun. 26, 2012, Turbine blades and methods of manufacturing

Pratt and Whitney

PW1 US8092178 B2, Jan. 10, 2012, Turbine blade for a gas turbine engine

United Technologies Corp.

UTC1 EP0781371 B1, Dec. 23, 1998, Dynamic control of tip clearance

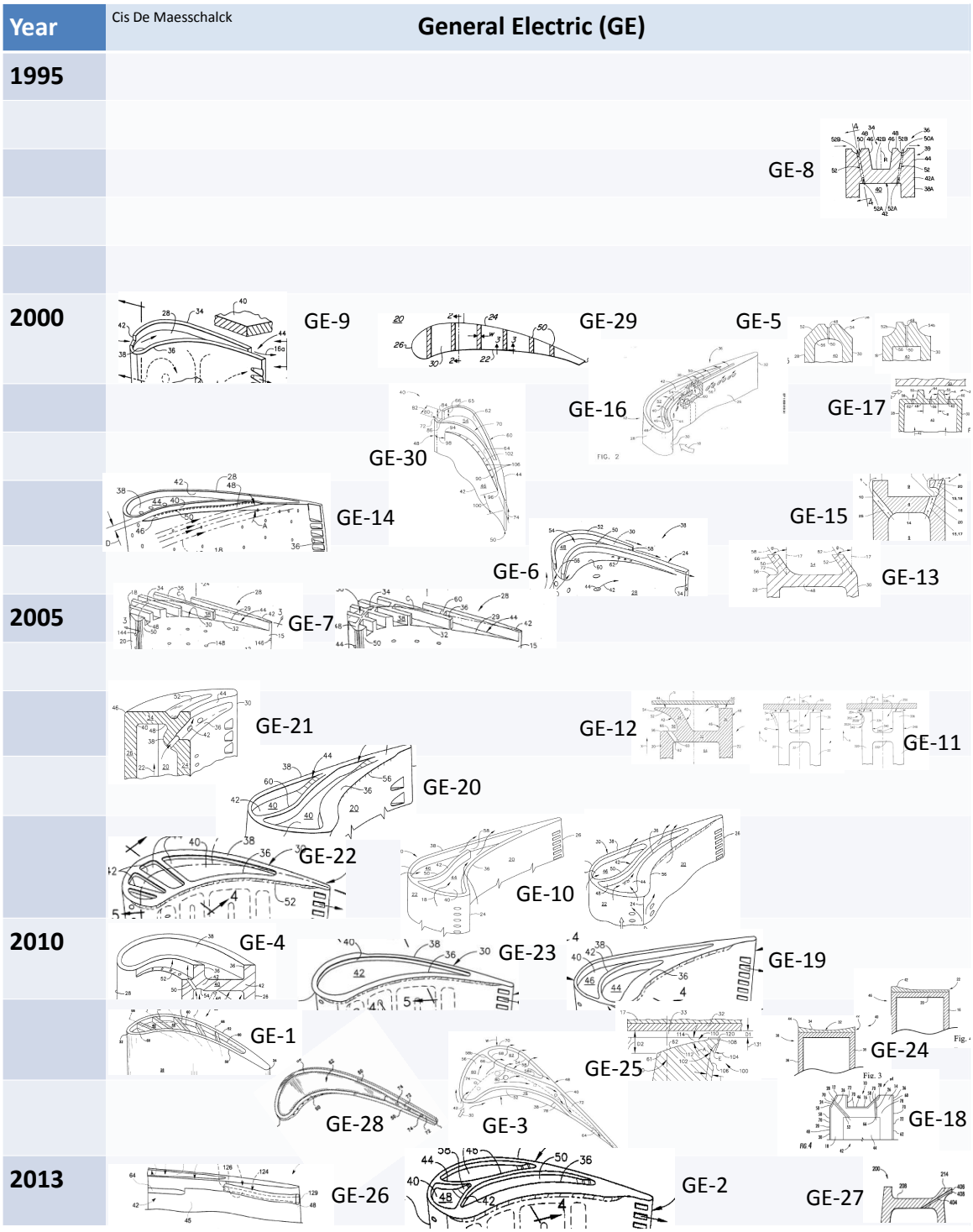

Figure A.1: Overview of the tip design patents from General Electric.

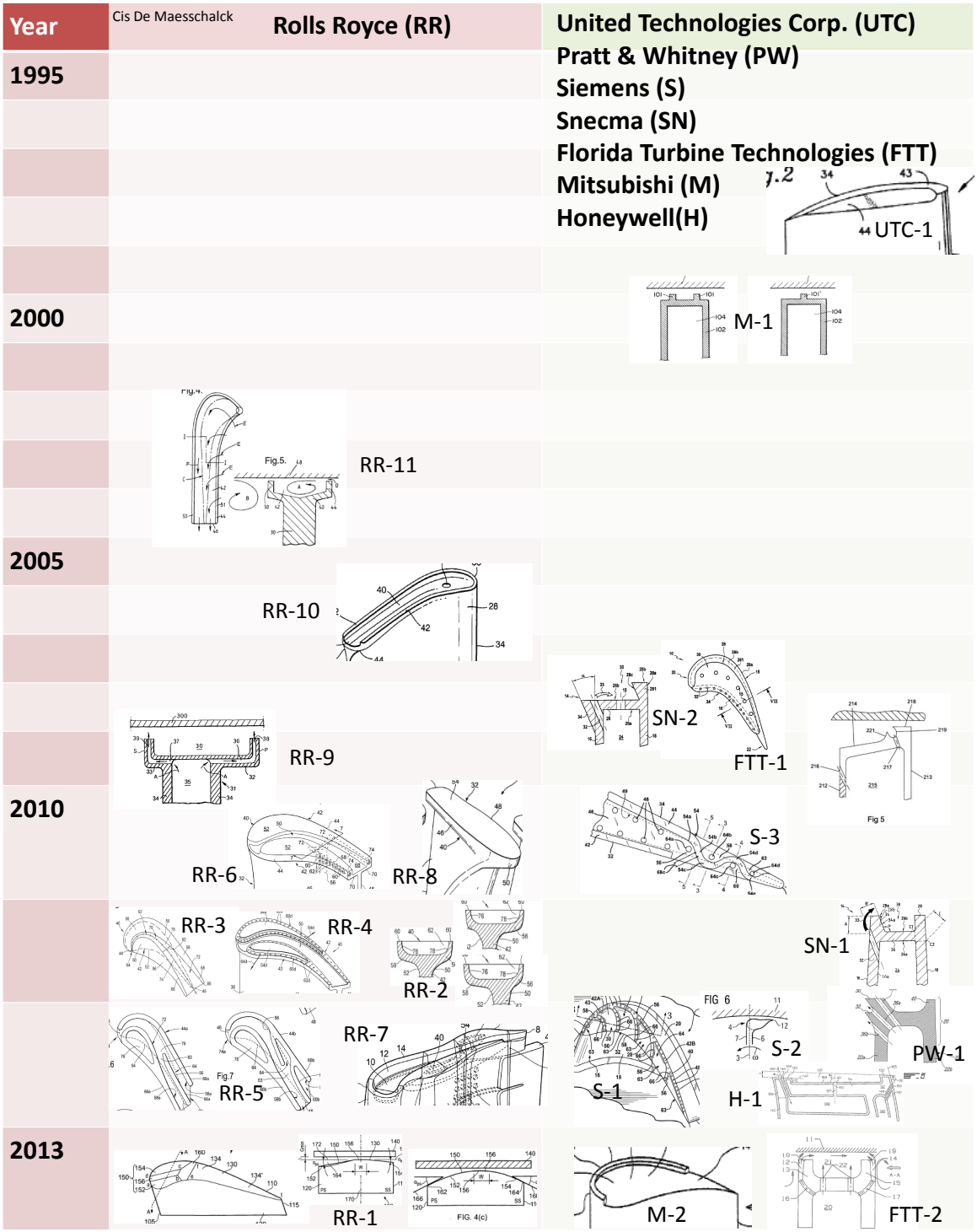

Figure A.2: Overview of the tip design patents from other companies.

APPENDIX B. FUNDAMENTAL CONSIDERATIONS AND THEIR RELEVANCE IN TURBOMACHINERY

Detailed derivations and descriptions of the stated equations below can be found in the majority of the fundamental fluid dynamic textbooks, e.g. Fox and McDonald [185], White [186] or Cengel and Cimbala [187]. For further details on compressible aerodynamics as used throughout the dissertation, the reader is referred to Zucrow and Hoffman [188], Anderson [189] and Shapiro [125]. All aspects regarding the boundary layer can be found in Schlichting [190]. The basic heat transfer concepts are well explained in Incropera et al. [191] and a more advanced, holistic description is provided by Bejan and Kraus [192]. Similarly, essential thermodynamic aspects can be found in Moran et al. [193] and more advanced in Bejan [194]. For specific turbomachinery fundamentals, the reader is referred to Dixon and Hall [195], Cohen et al. [196] and Lakshminarayana [197].

The basic laws of fluid motion and thermodynamics are conventionally described using a Lagrangian approach (i.e. following an identifiable amount of mass throughout space), using the substantial derivative $D()/Dt$ ('material' or 'particle derivative') denoting the differentiation along a particle path.

Of particular importance are **the conservation of mass** (in the absence of nuclear and relativity effects):

$$\frac{D(Mass)}{Dt} = 0 \tag{B.1}$$

The conservation of linear momentum (i.e. Newton's second law of motion), connecting the rate of change of momentum M with the externally applied body and surface forces:

$$\frac{DM}{Dt} = F_{ext} = F_{body} + F_{surf} \tag{B.2}$$

The conservation of Energy (First Law of Thermodynamics) equating the increase in the total energy of the system (E) to the net heat transfer added to the system (Q) reduced with the net work done by the system (W):

$$\frac{DE}{Dt} = \delta\dot{Q} - \delta\dot{W} \tag{B.3}$$

The entropy equation (i.e. Second Law of Thermodynamics):

$$\frac{DS}{Dt} \geq \frac{\delta\dot{Q}}{T} \tag{B.4}$$

However, for many applications (including turbomachinery), the Euler approach is more appropriate to study the effects of the flow through the fluid machinery. In order to relate this control volume formulation, working on a fixed region in space, to the aforementioned Lagrangian approach, the **Reynolds Transport Theorem** is adopted. The latter connects the rate of change of an (intensive) property of a system (n) to the combination of a change of the property inside the control volume (CV) and the net rate leaving the fixed space bounded by the control surface (CS):

$$\frac{D}{Dt}\int_{sys} n\rho dV = \frac{\partial}{\partial t}\int_{CV} n\rho dV + \int_{CS} n\rho \mathbf{V}\cdot d\mathbf{A} \tag{B.5}$$

This results in the integral formulation of the governing equations for fluid flow:

The Continuity Equation

$$\frac{D}{Dt}\int_{sys} \rho dV = 0 = \frac{\partial}{\partial t}\int_{CV} \rho dV + \int_{CS} \rho \mathbf{V}\cdot d\mathbf{A} \tag{B.6}$$

The Momentum Equation

$$\int_{CV} \mathbf{B}\rho dV - \int_{CS} p d\mathbf{A} + \mathbf{F}_{shear} = \frac{\partial}{\partial t}\int_{CV} \rho \mathbf{V} dV + \int_{CS} \mathbf{V}(\rho \mathbf{V}\cdot d\mathbf{A}) \tag{B.7}$$

The Energy Equation

$$\dot{Q} - \dot{W}_{shaft} - \dot{W}_{shear} = \frac{\partial}{\partial t}\int_{CV}\left[\rho\left(u + \frac{V^2}{2} + gz\right)\right]\rho dV + \int_{CS}\left(h + \frac{V^2}{2} + gz\right)(\rho\mathbf{V}\cdot d\mathbf{A}) \tag{B.8}$$

The Entropy Equation

$$\frac{\dot{Q}}{T} \leq \frac{\partial}{\partial t}\int_{CV} s\rho dV + \int_{CS} s(\rho\mathbf{V}\cdot d\mathbf{A}) \tag{B.9}$$

It are the latter equations that are governing the flow through the turbomachinery components and are used, either in their integral or differential form, to construct the CFD codes.

One last conservation equation (though not written explicitly) is the **conservation of angular momentum**. This conservation equation is the rotational equivalent of the linear momentum one and relates the changes in angular momentum to an applied torque. This equation, in conjunction with the energy equation (for a steady, adiabatic case) leads to the Euler Turbine equation, which gives an estimation of the extracted work solely based on the tangential (absolute) velocity components and the peripheral speed:

$$\Delta H = U_2 V_{t,2} - U_1 V_{t,1} \tag{B.10}$$

While the reader is referred to the textbooks quoted above for a deeper understanding of the fundamental governing equations, some important aspects, specifically related to turbomachinery research and high-pressure turbines in particular, are additionally highlighted:

Mach and Reynolds Number. Throughout the operational envelope, the Reynolds number of the turbine stages can vary significantly, e.g. at take-off versus cruising altitudes. While the precise Reynolds number plays an important role in the loss generation and heat transfer [198], its impact on the overall flow topology in the high-pressure turbine stages is limited (considering similar velocity triangles and Mach

numbers). In the case of the low-pressure turbines however, this can give rise to more important alterations arising from the thicker boundary layers, increased viscous losses and risk of separation at higher altitude [199]. For the upstream stages at higher Reynolds, the precise flow field is predominantly determined by the Mach number (i.e. blade pressure loading) which is going to drive the velocity components, blade incidences, possible shock structures at the blades trailing edge and therefore determine the main features throughout the passages.

Isentropic Mach Number. A common way to present the static pressure or equivalently the (blade) pressure loading, is through the use of the 'Isentropic Mach Number' derived from the isentropic flow relation:

$$P_0 = P_s\Big(1 + \frac{\gamma - 1}{2} M_{is}^2\Big)^{\frac{\gamma}{\gamma - 1}} \tag{B.11}$$

Where the total pressure is taken as the upstream (relative) value. The M_{is} therefore represents a Mach number that would be achieved for the given P_s in the absence of losses and gives, more than the raw static pressure, an intuitive idea of the local velocity.

Nusselt Number. For internal flows, the commonly used descriptor for the convective heat load is the Nusselt number, defined as:

$$Nu = \frac{hL}{k} \tag{B.12}$$

where L is the relevant length scale (e.g. axial blade chord) and k the (local) thermal conductivity of the fluid. The convective heat transfer coefficient h is conventionally retrieved based on the Newton cooling law $Q = h(T - T_{ref})$. However, more complex concepts are recently proposed, using increasing sophisticated definitions to take the changing gas properties into account and adopt specific reference temperatures (e.g. adiabatic temperature / heat transfer coefficient) in order to ul-

timately decouple the effect of the local driving temperature and the aerodynamic effects on the heat transfer [200–202].

Relative Quantities. In rotating applications, such as turbomachinery components, it is common to use the 'relative' quantities, or equivalently, adopt the definition of the flow characteristics in a rotating frame of reference. This allows to use very similar calculation and interpretation techniques for the rotating parts (i.e. blades) as are used for the stationary vanes. Specifically, the total relative enthalpy (/temperature) and the total relative pressure are widely used, derived from the static properties using the velocity components in the rotating frame of reference instead of the absolute frame.

VITA

VITA

Cis Guy M. De Maesschalck was born in Kortrijk, Belgium to parents Valere De Maesschalck and Ann Devriendt on September 12, 1988. He has two younger sisters and grew up in Kortrijk. After graduating from the Don Bosco College in 2006, he started his undergraduate studies in electrotechnical-mechanical engineering at the Katholieke Universiteit Leuven. The first year in Kortrijk and the following two in Leuven, Belgium. In 2009, he embarked on a Master study in Mechanical Engineering at the Katholieke Universiteit Leuven. After completing his Master thesis in cooperation with the von Karman Institute for Fluid Dynamics, he pursued there a Master-after-Master program, specializing in the field of Turbomachinery and Propulsion. In October 2012, supported by a personal grant from the Agency for Innovation by Science and Technology (IWT) in Belgium, he started his PhD studies at the Vrije Universiteit Brussel in cooperation with the von Karman Institute under the guidance of Prof. Paniagua and Prof. Lacor. In January 2015, awarded as a Fulbright Scholar and a fellowship from the Belgian American Educational Foundation, Cis additionally enrolled in the PhD program at Purdue University, continuing his research on the design, analysis, optimization and control of rotor tip flows.

Cis will receive his PhD from the School of Mechanical Engineering in December 2016.

LIST OF PUBLICATIONS

LIST OF PUBLICATIONS

Journal Publications

1. S. Lavagnoli, G. Paniagua, **C. De Maesschalck**, T. Yasa, 2013, "Analysis of the unsteady overtip casing heat transfer in a high speed turbine", J. Turbomach. 135(3), 031027

2. **C. De Maesschalck**, S. Lavagnoli, G. Paniagua, 2014,"Blade Tip Shape Optimization for Enhanced Turbine Aerothermal Performance", J. Turbomach, 136(4), 2014

3. **C. De Maesschalck**, S. Lavagnoli, G. Paniagua, N. Vinha, 2014, "Aerothermodynamics of tight rotor tip clearance flows in high-speed unshrouded turbines", Journal of Applied Thermal Engineering, Vol. 65, p. 343-351

4. **C. De Maesschalck**, S. Lavagnoli, G. Paniagua, 2014, "Blade Tip Carving Effects on the Aero-Thermal Performance of a Transonic Turbine", J. Turbomach. 137(2), 021005

5. S. Lavagnoli, **C. De Maesschalck**, G. Paniagua, 2015, "Uncertainty Analysis of Adiabatic Wall Temperature in Turbine Experiments", Journal of Applied Thermal Engineering, Vol. 82, p. 170-181

6. S. Lavagnoli, **C. De Maesschalck**, G. Paniagua, 2015, "Analysis of the Heat Transfer Driving Parameters in Tight Rotor Blade Tip Clearances", ASME J. Heat Transfer 138(1), 011705

7. **C. De Maesschalck**, S. Lavagnoli, G. Paniagua, T. Verstraete, R. Olive, P. Picot, 2016, Heterogeneous Optimization Strategies for Carved and Squealer-like Turbine Blade Tips, J. Turbomach 138(12), 121011

8. S. Lavagnoli, **C. De Maesschalck**, V. Andreoli, 2016, Design Considerations for Tip Clearance Control and Measurement on a Turbine Rainbow Rotor with Multiple Blade Tip Geometries, ASME J. Eng. Gas Turbines Power 139(4), 042603

9. **C. De Maesschalck**, C. Lacor, G. Paniagua, S. Lavagnoli, A. Remiot, L. Bricteux, 2016, "Performance Robustness of Turbine Squealer Tip Designs due to Manufacturing and Engine Operation", AIAA Journal of Propulsion and Power

Conference Publications

1. S. Lavagnoli, G. Paniagua, **C. De Maesschalck**, T. Yasa, 2012, "Analysis of the unsteady overtip casing heat transfer in a high speed turbine", ASME Paper GT2012-69492
2. **C. De Maesschalck**, S. Lavagnoli, G. Paniagua, 2013, "Blade Tip Shape Optimization for Enhanced Turbine Aerothermal Performance", ASME paper GT2013-94754
3. **C. De Maesschalck**, S. Lavagnoli, G. Paniagua, 2013, "Blade Tip Carving Effects on the Aero-Thermal Performance of a Transonic Turbine", ASME Paper TBTS2013-2028
4. S. Lavagnoli, **C. De Maesschalck**, G. Paniagua, 2014, "Analysis of the Heat Transfer Driving Parameters in Tight Rotor Blade Tip Clearances", ASME Paper GT2014-25291
5. S. Lavagnoli, **C. De Maesschalck**, G. Paniagua, 2014, "Uncertainty Analysis of Adiabatic Wall Temperature in Turbine Experiments", Proceedings of the XXII Symposium on Measuring Techniques in Turbomachinery
6. **C. De Maesschalck**, S. Lavagnoli, G. Paniagua, T. Verstraete, R. Olive, P. Picot, 2015, "Heterogeneous Optimization Strategies for Carved and Squealer-like Turbine Blade Tips", ASME Paper GT2015-42983
7. **C. De Maesschalck**, C. Lacor, G. Paniagua, S. Lavagnoli, A. Remiot, L. Bricteux, 2015, "Performance Robustness of Turbine Squealer Tip Designs due to Manufacturing and Engine Operation", ISABE Conference Proceedings (ISABE2015-20205)
8. S. Lavagnoli, **C. De Maesschalck**, G. Paniagua, V. Andreoli, D. Gonzalez Cuadrado, 2016, "Wind Tunnel Testing of Turbine Blade Tip Flows," AIAA Science and Technology Forum and Exposition, San Diego, California
9. S. Lavagnoli, **C. De Maesschalck**, V. Andreoli, 2016, "Design Considerations for Tip Clearance Control and Measurement on a Turbine Rainbow Rotor with Multiple Blade Tip Geometries," ASME Paper GT2016-56544

Other Contributions

1. S. Lavagnoli, **C. De Maesschalck**, G. Paniagua, "Tip Clearance effects in Transonic Turbines", Workshop talk, ASME Turbine Blade Tip Symposium and Workshop, September 2013, Hamburg (Germany)